ENTANGLEMENT OF ATOM-FIELD STATES IN THE ANTI-JAYNES-CUMMINGS INTERACTION: RABI OSCILLATIONS AND QUANTUM TELEPORTATION OF ENTANGLED ATOMIC QUBITS

BY

CHRISTOPHER MAYERO

A THESIS SUBMITTED IN FULFILLMENT OF THE REQUIREMENTS FOR THE DEGREE OF DOCTOR OF PHILOSOPHY IN THEORETICAL PHYSICS

SCHOOL OF PHYSICAL AND BIOLOGICAL SCIENCES

MASENO UNIVERSITY

DECLARATION

This thesis is my own work and has not been presented for a degree award in any other institution.

Christopher MAYERO
PHD/SC/00015/2016

Signature: .... Date:.....................

This thesis has been submitted for examination with our approval as University Supervisors.

1. Prof. Joseph Akeyo OMOLO
   Department of Physics and Material Science
   Maseno University

   Signature:................................ Date.................

2. Dr. Onyango Stephen OKEYO
   Department of Physics and Material Science
   Maseno University

   Signature:................................ Date.................

ACKNOWLEDGMENT

First, I would like to thank God the Almighty Father for giving me wisdom, good health and resilience throughout my PhD (Physics) program at Maseno University, in the Department of Physics and Materials Science. It was a long journey coupled with many challenges but You saw me through and made me reach this far in my studies. May Your name be praised. Secondly, I pass my sincere gratitude to my supervisor Prof. Joseph Akeyo Omolo for believing in me and trusting my ability to undertake this program. Your constant interviews that required proof of all the steps that led to the findings in this work, made me to be chary of mistakes and triumph. I will not forget your humorous word "*gujarati*"as an easy way of telling me to shape my work to standard when my presentation was mixed up. Prof. you are a great man and may God bless you sir. I also thank my second supervisor Dr. Stephen Onyango Okeyo for provision of the relevant computational tool and editor not to mention the reading through of my Thesis findings and delivering pertinent corrections. It may appear trivial, but it perfected the visuals, legibility and accuracy of this Thesis work. Mr. Patrick Muga Owiny', I thank you for the positive contributions during our technical areas discussions and proof reading my second manuscript in time paving way for peer review. It is an effort that made this work a success. Finally, I would want to express my gratitude to Tom Mboya University and Uzima University for their unwavering moral and financial support throughout my education. Most notably, I appreciate Prof. Charles Ochola Omondi of Tom Mboya University and Prof. Fr. Cosmas Ragot of Uzima University for always allowing me the opportunity to contribute my teaching services to the respective Universities even when I was still a PhD(Physics) student. May God richly bless you.

DEDICATION

To my parents and teachers.

ABSTRACT

The quantum Rabi model (QRM), the simplest single-mode spin-boson model, was initially simplified using rotating wave approximation (RWA), yielding the Jaynes-Cummings (JC) model in rotating frame (RF). The QRM was later symmetrised into its rotating JC and counter-rotating (CR) anti-Jaynes-Cummings (AJC) components, yielding an exactly solvable AJC model in the counter-rotating frame (CRF). This work presents the dynamics generated when a two-level atom (fermionic system) interacts with a quantised electromagnetic field mode (bosonic system) in the AJC model. The evolution of the atomic state during the AJC interaction with field mode initially and separately in three basic non-classical states of light is considered. In each respective atom-field interaction, we provided the corresponding extensively studied JC interaction as a comparison. We have shown that when the field mode is in an initial Fock state (idealised light), Rabi oscillations during the AJC interaction occur in the reverse sense relative to that during the JC interaction. In addition, quantum teleportation of a two-atom entangled anti-symmetric state at unit fidelity indicates that maximally entangled atom-field states generated in the AJC interaction are effective quantum channels, and the observed long-lived entanglement during the AJC interaction specify that the atomic qubits exhibit long coherence time vital for computational processes. What is more, two-qubit controlled-NOT (C-NOT) gate operation and single qubit Walsh-Hadamard gate operation is demonstrated each giving standard outcomes as expected. In the former, the target qubit is flipped when the control qubit is in an initial ground state $|g\rangle$ and remain unchanged when the control qubit is in an initial excited state $|e\rangle$ while in the latter the atomic basis states $\{|e\rangle, |g\rangle\}$ were rotated into diagonal basis states $\{|+\rangle, |-\rangle\}$. When the field mode in an initial coherent state is considered during the AJC interaction, fully quantised atom-field interaction is realised since the field is dominantly sub-Poissonian. Finally, when an initial squeezed coherent state is considered during the AJC interaction, at all time intervals the atom-field quantum systems are entangled (mixed), i.e, at no point did the quantum systems evolve to pure state, the degree of mixedness increased with every increase in the squeeze parameter and ringing revivals at an expected collapse phase are observed when higher values of squeeze parameter is applied. This thesis work presents the first ever demonstration of quantum Rabi oscillations, entanglement dynamics, successful quantum teleportation, photon statistics and effective quantum gate operations in an AJC interaction between a two-level atom and a quantised electromagnetic field mode. In contrast to the standard JC interaction which has generally been

used in quantum information theory (QIT) and quantum computation, the AJC interaction provides the advantage of starting with both an atom and field mode each in an initial ground state, i.e, an atom in spin-down state and field mode in vacuum state, a property which is essentially unachievable in the JC interaction when an initial Fock state is considered. We now recommend application of the AJC model in the emerging field of quantum technology, which has a potential to revolutionise a wide range of industries and applications, from finance and logistics to healthcare and energy. More specifically, the results of this work in its present form, will be of immense contribution to QIT and physical realisation of quantum computation.

CONTENTS PAGE

LIST OF PUBLICATIONS

Paper 1:

Mayero, C. , Omolo, J.A. and Okeyo, O.S. Rabi Oscillations, Entanglement and Teleportation in the Anti-Jaynes-Cummings Model. *J. Mod. Phys.*, 12 (**4**): 408-432, 2021.
`https://doi.org/10.4236/jmp.2021.124029`

Paper 2:

Mayero, C. and Owiny, P. Effects of Frequency Detuning and Excitation Quantum Number on the Dynamics of Entanglement in the Jaynes-Cummings Polariton Model. *Quantum Phys. Lett.*, 10 (**1**): 23–30, 2021.
`http://dx.doi.org/10.18576/qpl/100101`

Paper 3:

Mayero, C., Omolo, J.A. and Okeyo, O.S. Theoretical Realization of a Two Qubit Quantum Controlled-Not Logic Gate and a Single Qubit Quantum Hadamard Logic Gate in the Anti-Jaynes-Cummings Model. *Int. J. Appl. Math. Theor. Phys.*, 7 (**4**):105-111, 2021.
`http://dx.doi.org/10.11648/j.ijamtp.20210704.13`

Paper 4:

Mayero, C. Photon statistics and quantum field entropy in the anti-Jaynes-Cummings model: a comparison with the Jaynes-Cummings interaction. *Quantum Inf Process* **22**, 182 (2023).
`https://doi.org/10.1007/s11128-023-03912-7`

LIST OF ABBREVIATIONS

AJC anti-Jaynes-Cummings

BSB Blue-sideband

C-NOT controlled-NOT

cQED Circuit quantum electrodynamics

CQED Cavity quantum electrodynamics

DSC Deep strong coupling

EM Electromagnetic

EPR Einstein-Podolsky-Rosen

JC Jaynes-Cummings

LOCC Local operation and classical communication

MUS Minimum uncertainty state

NMR Nuclear magnetic resonance

OP Original protocol

QIP Quantum information processing

QIT Quantum information theory

QKD Quantum key distribution

QRM Quantum Rabi model

QTY Quantity

Qubit Quantum bit

RM Rabi model

RSB Red-sideband

RWA Rotating wave approximation

USC Ultrastrong coupling

LIST OF FIGURES

xvii

LIST OF TABLES

CHAPTER 1
INTRODUCTION

1.1 Background of the study

The quantum Rabi model (QRM) [1–3] describes a two-level system coupled to a single-mode quantised light field. Despite its simplicity, the QRM exhibits rich physics and has found applications in quantum optics [4], condensed matter physics [5], molecular physics and superconducting circuit quantum electrodynamics (cQED) [6, 7].

The QRM is composed of a rotating wave component identified as the Jaynes-Cummings (JC) model and a counter(anti)-rotating (CR) wave component identified as the anti-Jaynes-Cummings (AJC) model.

Exact analytical solution of the JC model was obtained through diagonalisation with the conserved excitation number operator as early as 1963 [8], while exact analytical solution of the corresponding AJC model was obtained much later after discovery of the conserved excitation number operator in 2017 [9–12].

It is important to note that both JC and AJC Hamiltonians are now expressible in terms of the respective excitation number and qubit state transition operators which now provide description of the dynamics through normalised non-orthogonal qubit state vectors or orthornormal eigenstate vectors.

Exact solutions of the eigenvalue equation of the full QRM obtained in 2011 [3] and in subsequent studies [13–15] take complicated forms which have made them too difficult to develop the general time evolving states of QRM. Hence JC and AJC are studied separately [9].

Recently it was discovered that JC and AJC are duality conjugates [16], with JC describing red-sideband (RSB) and AJC describing blue-sideband (BSB) transitions

Noting that fundamental features namely; collapses and revivals in the atomic inversion [17], generation of Schrödinger cat states of the quantised field [18, 19], transfer of atomic coherence to the quantised field [20], vacuum-field Rabi oscillations in a cavity [21] and many more have been extensively studied in the JC model in both theory and experiment in quantum optics, we now focus attention on the AJC model which has not received much attention over the years due to the assumed lack of a conserved excitation number operator.

In the subsequent sections in this chapter we introduce mathematical concepts of this

study, statement of the problem, objectives, justification and scope of this study.

1.2 Qubits

1.2.1 Single qubits

A qubit is a quantum system having two orthogonal states [22–25]. It is the quantum analogue to the term bit in information theory and it can hold one bit by preparing it either in a state $|0\rangle$ or $|1\rangle$. However, due to superposition principle in quantum mechanics, a qubit can also be prepared in any superposition state of the form

$$|\psi\rangle = \alpha|0\rangle + \beta|1\rangle \qquad (1.2.1)$$

where the qubit $|\psi\rangle$ is defined in a two-dimensional state space $\mathbb{C}^2$ (Hilbert space[1]) and $|0\rangle, |1\rangle$ are the orthonormal basis for the space. The parameters α, β are the qubit state probability amplitudes, generally considered complex.

Noting that $|\psi\rangle$ must be a unit vector the inner product gives normalisation relation

$$\langle\psi|\psi\rangle = 1 \quad \Rightarrow \quad |\alpha|^2 + |\beta|^2 = 1 . \qquad (1.2.2)$$

The states can be represented by column vectors

$$|0\rangle = \begin{pmatrix} 1 \\ 0 \end{pmatrix} \quad ; \quad |1\rangle = \begin{pmatrix} 0 \\ 1 \end{pmatrix} \quad \Rightarrow \quad |\psi\rangle = \begin{pmatrix} \alpha \\ \beta \end{pmatrix} . \qquad (1.2.3)$$

In the Bloch sphere picture [2], Eq. (1.2.1) can be expressed as

$$|\psi\rangle = e^{i\gamma} \left\{ \cos\left(\frac{\theta}{2}\right) |0\rangle + e^{i\phi} \sin\left(\frac{\theta}{2}\right) |1\rangle \right\} . \qquad (1.2.4)$$

Here, the global phase factor $e^{i\gamma}$ in Eq. (1.2.4) has no observable effect [23] and is therefore easily omitted.

A Bloch vector $\vec{r}$ is a vector in an arbitrary direction, which is defined in terms of the

---

[1]Associated to any isolated physical system is a complex vector space with inner product known as a Hilbert space or the state space of the system. The system is described by its state vector, which is a unit vector in the system's state space [22]

[2]Named after the Physicist Felix Bloch [26]

polar θ and azimuthal ϕ angles as [23]

$$\vec{r} = (r_x,\, r_y,\, r_z) = (\cos\phi\,\sin\theta,\, \sin\phi\,\sin\theta,\, \cos\theta)\,. \qquad (1.2.5)$$
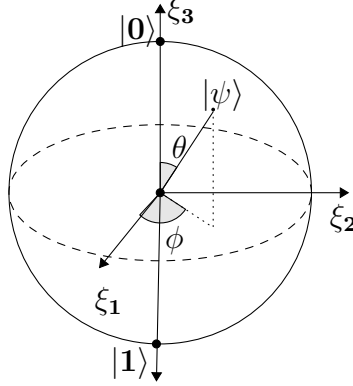
Figure 1.1: The Bloch sphere representation of a qubit. The basis states $|0\rangle$, $|1\rangle$ are located at the North and South poles. The various possible superpositions of the two can then be converted to unique coordinates on the sphere.

As shown in Fig. 1.1, angle θ is the angle between the Bloch vector and the z-axis while ϕ is the angle between the Bloch vector's orthogonal projection on the equatorial plane and the positive x-axis measured counter-clockwise. The state of a qubit is then visualised as a point with polar coordinates θ and ϕ on a unit sphere.

1.3 The density operator (density matrix)

In order to relate unitary operations on a qubit state $|\psi\rangle$ in Eq. (1.2.4) to rotations on Bloch sphere, it is convenient to use the corresponding density operator $\hat{\rho}$, defined as

$$\hat{\rho} = |\psi\rangle\langle\psi| = |\psi\rangle \otimes \langle\psi| \qquad (1.3.1)$$

where we note the Hermitian conjugation

$$\langle\psi| = |\psi\rangle^{\dagger}\,. \qquad (1.3.2)$$

Substituting $|\psi\rangle$ from Eq. (1.2.4) into Eq. (1.3.1) gives the form

$$\hat{\rho} = |\psi\rangle \otimes \langle\psi| = \begin{pmatrix} \cos(\frac{\theta}{2}) \\ e^{i\phi}\sin(\frac{\theta}{2}) \end{pmatrix} \otimes \begin{pmatrix} \cos(\frac{\theta}{2}) & e^{-i\phi}\sin(\frac{\theta}{2}) \end{pmatrix}\,. \qquad (1.3.3)$$

3

By definition of outer product Eq. (1.3.3) takes the 2×2 matrix form

$$\hat{\rho} = \begin{pmatrix} \cos^2(\frac{\theta}{2}) & e^{-i\phi}\cos(\frac{\theta}{2})\sin(\frac{\theta}{2}) \\ e^{i\phi}\cos(\frac{\theta}{2})\sin(\frac{\theta}{2}) & \sin^2(\frac{\theta}{2}) \end{pmatrix} \qquad (1.3.4)$$

and using standard trigonometric identities Eq. (1.3.4) gives the form

$$\hat{\rho} = \frac{1}{2}\begin{pmatrix} 1+\cos\theta & \cos\phi\sin\theta - i\sin\phi\sin\theta \\ \cos\phi\sin\theta + i\sin\phi\sin\theta & 1-\cos\theta \end{pmatrix}. \qquad (1.3.5)$$

Regrouping Eq. (1.3.5) in terms of the Pauli basis $\{I, \sigma_x, \sigma_y, \sigma_z\}$ defined as [22, 23]

$$I = \begin{pmatrix} 1 & 0 \\ 0 & 1 \end{pmatrix} \quad ; \quad \sigma_x = \begin{pmatrix} 0 & 1 \\ 1 & 0 \end{pmatrix} \quad ;$$

$$\sigma_y = \begin{pmatrix} 0 & -i \\ i & 0 \end{pmatrix} \quad ; \quad \sigma_z = \begin{pmatrix} 1 & 0 \\ 0 & -1 \end{pmatrix} ,$$

$$(1.3.6)$$

we obtain

$$\hat{\rho} = \frac{1}{2}(I + \sigma_x \cos\phi \sin\theta + \sigma_y \sin\phi \sin\theta + \sigma_z \cos\theta) \qquad (1.3.7)$$

which we now express in the form

$$\hat{\rho} = \frac{1}{2}(I + \vec{r}\cdot\vec{\sigma}) \qquad (1.3.8)$$

where

$$\vec{\sigma} = (\sigma_x, \sigma_y, \sigma_x) \equiv \sigma_x\hat{i} + \sigma_y\hat{j} + \sigma_z\hat{k} , \qquad (1.3.9)$$

is the Pauli matrix vector and $\vec{r}$ [27] is the unit Bloch vector defined in Eq. (1.2.5).

1.3.1 Properties of the density matrix

First, the density matrix is a Hermitian operator [25]

$$\hat{\rho} = \hat{\rho}^{\dagger} . \qquad (1.3.10)$$

Second, the density matrix is normalised, satisfying

$$tr(\hat{\rho}) = \sum_i p_i \; tr(|\psi_i\rangle\langle\psi_i|) = \sum_i p_i \; \langle\psi_i|\psi_i\rangle = \sum_i p_i = 1 \; . \qquad (1.3.11)$$

Besides normalisation, the density matrix is positive semi-definite satisfying

$$\hat{\rho} \geq 0 \; . \qquad (1.3.12)$$

This is established for an arbitrary quantum state $|\phi\rangle$ in the form

$$\langle\phi|\hat{\rho}|\phi\rangle = \sum_i p_i \; |\langle\phi|\psi\rangle|^2 \geq 0 \; . \qquad (1.3.13)$$

Hermitian means that the density matrix can be diagonalised by some orthonormal basis $|\lambda_k\rangle$ as

$$\hat{\rho} = \sum_k \lambda_k \; |\lambda_k\rangle\langle\lambda_k| \qquad (1.3.14)$$

for certain eigenvalues λ_k.

The purity of the quantum state $\hat{\rho}$ specified by eigenvalues λ_k is defined as [25]

$$tr(\hat{\rho}^2) = \sum_k {\lambda_k}^2 \leq 1 \; . \qquad (1.3.15)$$

The equality $tr(\hat{\rho}^2) = 1$ means $\hat{\rho}$ is a pure state. In that case it can be written as $\hat{\rho} = |\psi\rangle\langle\psi|$ so it will have one eigenvalue equal to one and all other eigenvalues equal to zero. For a mixed state $\hat{\rho} = p_i \; |\psi_i\rangle\langle\psi_i|$ the purity of the quantum state $tr(\hat{\rho}^2) < 1$ with $\sum_{i=1}^n p_i = 1$. It has also been shown in [28] that purity parameter $tr(\hat{\rho}^2)$ can be determined using components r_x, r_y, r_z of the Bloch vector $\vec{r}$ according to

$$tr(\hat{\rho}^2) = \frac{1}{2}\left(1 + \vec{r}\cdot\vec{r}\right) = \frac{1}{2}\left[1 + \left(r_x^2 + r_y^2 + r_z^2\right)\right] \; . \qquad (1.3.16)$$

1.4   Sub-Poissonian photon statistics

One of the best known nonclassical effects is the sub-Poissonian photon statistics of the light field [29–32].

Following Mandel [29] we introduce the Q parameter in the Fock space $\mathbb{H}_f$ in the

general form

$$Q = \frac{\langle (\triangle \hat{n})^2 \rangle - \langle \hat{n} \rangle}{\langle \hat{n} \rangle} \quad ; \quad \Delta \hat{n} = \sqrt{\langle \hat{n}^2 \rangle - \langle \hat{n} \rangle^2} \, , \qquad (1.4.1)$$

which characterises the departure from the Poissonian photon statistics. In Eq. (1.4.1) $\langle (\Delta \hat{n})^2 \rangle$ is the photon number variance, $\langle \hat{n} \rangle$ is the mean photon number and $\hat{n}$ is the photon number operator.

We take note that the sign of the Mandel parameter determines the nature of deviation of excitation statistics from the Poisson statistics. More precisely, the Mandel parameter is positive ($Q > 0$) when the statistic is super-Poissonian, zero ($Q = 0$) when Poissonian and negative ($Q < 0$) when sub-Poissonian with values ranging between 0 and -1 during which the phenomenon of anti-bunching occurs [30] a clear manifestation of quantum effect. In the Poissonian distribution (coherent state), the mean $\langle \hat{n} \rangle$ and the variance $\langle (\Delta \hat{n})^2 \rangle$ of the distribution have the same value, super-Poissonian (classical) the variance is higher than the mean and sub-Poissonian (non-classical) the variance is smaller than the mean.

1.5 Non-classical states of light

The three basic non-classical states of light [28, 33, 34] are the Fock states, coherent states and squeezed states. The last two are minimum uncertainty states (MUSs) i.e, states for which the uncertainty relation for the variances of quadrature operators given by

$$\langle (\triangle \hat{a}_1)^2 \rangle \langle (\triangle \hat{a}_2)^2 \rangle \geq \frac{1}{16} \qquad (1.5.1)$$

holds. The quadrature operators $\hat{a}_1$ and $\hat{a}_2$ corresponding to creation $(\hat{a}^\dagger)$ and annihilation $(\hat{a})$ operators of the field mode are defined as

$$\hat{a}_1 = \frac{\hat{a} + \hat{a}^\dagger}{2} \quad ; \quad \hat{a}_2 = \frac{\hat{a} - \hat{a}^\dagger}{2i} \, . \qquad (1.5.2)$$

The states can be formally obtained by applying group theoretical methods by which one can describe wide classes of non-classical states of light [35–38].

We present briefly the theory of Fock, coherent and squeezed states. In this Thesis, time evolution of a two-level atom in the AJC, JC interaction mechanisms respectively with the field mode initially in Fock state, coherent state and squeezed state is considered.

1.5.1 Fock states

The photon number (Fock) state $|n\rangle$ [28, 33, 34] is the eigenstate of the field Hamiltonian defined in terms of the photon creation $\hat{a}^\dagger$ and annihilation operators $\hat{a}$ in the form

$$\hat{H} = \hbar\omega \left(\hat{a}^\dagger \hat{a} + \frac{1}{2} \right) \tag{1.5.3}$$

Although the annihilation and creation operators do not themselves describe physical variables, their normal ordered product $\hat{n} = \hat{a}^\dagger \hat{a}$ is the excitation number operator that describes the number of excitations n in a single-mode field $|n\rangle$

$$\hat{n}|n\rangle = n|n\rangle \ . \tag{1.5.4}$$

The Fock states can be generated from the vacuum state $|0\rangle$ of the field mode by multiple actions of the creation operator $\hat{a}^\dagger$

$$|n\rangle = \frac{(\hat{a}^\dagger)^n}{\sqrt{n!}}|0\rangle \ . \tag{1.5.5}$$

The number states describe a state of precisely defined energy, that is, of a precisely given number of photons. Therefore the Mandel Q-parameter [29–32] for the Fock state is equal to -1 [39], because the photon number distribution of the Fock state has zero width. On the other hand, the Fock state does not describe a well-defined field, because the mean field is zero for any value of n. Despite this, the mean square of the field is not equal to zero, since it is one component of field mode energy. The Fock states have large quadrature fluctuations and for any $n > 0$ they are superfluctuant and do not belong to the class of the MUSs.

1.5.2 Coherent states

The coherent state introduced by Glauber [40] and Sudarshan [41] is defined as the eigen state $|\alpha\rangle$ of the annihilation operator $\hat{a}$ of a quantised field mode and yields Poissonian photon statistics. The main motivation behind their study being the correspondence principle well articulated in [42] - quantum phenomena resembles classical phenomena in high energy limit. They noted that the electron wavefunctions inside a hydrogen atom did not have a classical analogue and so little was known about these wavefunctions. But in quantum electrodynamics (QED) and quantum optics, the wavefunctions have to be connected with classical electromagnetic (EM) oscillations. This connection was then

established through introduction of the coherent state $|\alpha\rangle$ of quantised light.

For a single mode of quantised light, the coherent state is defined by

$$\hat{a}|\alpha\rangle = \alpha|\alpha\rangle, \tag{1.5.6a}$$

where the eigenvalue α is complex.

Expanding the coherent state in Fock basis

$$|\alpha\rangle = \sum_{n=0}^{\infty} c_n|n\rangle \tag{1.5.6b}$$

we easily get

$$
\begin{aligned}
\hat{a}|\alpha\rangle &= \sum_{n=1}^{\infty} c_n\sqrt{n}|n-1\rangle \\
&= \alpha\sum_{n=0}^{\infty} c_n|n\rangle,
\end{aligned}
\tag{1.5.6c}
$$

from which we get the following recursion relation

$$c_n\sqrt{n} = \alpha c_{n-1}. \tag{1.5.6d}$$

The solution of Eq. (1.5.6d) gives

$$c_n = \frac{\alpha^n}{\sqrt{n!}}c_p. \tag{1.5.6e}$$

The solution of c_p in Eq. (1.5.6e) is found from normalisation

$$\langle\alpha|\alpha\rangle = 1 = |c_p|^2\sum_{n=0}^{\infty}\frac{|\alpha|^{2n}}{n!} = |c_p|^2 e^{|\alpha|^2} \tag{1.5.6f}$$

so that we can now write the expansion

$$|\alpha\rangle = e^{-\frac{|\alpha|^2}{2}}\sum_{n=0}^{\infty}\frac{|\alpha|^n}{\sqrt{n!}}|n\rangle \ . \tag{1.5.6g}$$

Coherent states are MUSs such that, $(\Delta\hat{x})^2(\Delta\hat{p})^2 = \frac{\hbar^2}{4}$ where, $\hat{x}$, $\hat{p}$ are position and momentum operators. Coherent states are overcomplete and nonorthogonal [25, 43].

1.5.3 Squeezed states

Squeezed states, just like the coherent states, $|\alpha\rangle$, introduced in Sec. 1.5.2 are MUSs. A generalised state, the squeezed state, can remain a MUS if one of the variances is compressed (squeezed) at the expense of an expansion of the complementary variance [28]. The modified variances are conveniently written as

$$\langle(\triangle\hat{a}_1)^2\rangle = \frac{1}{4}e^{-2r} \quad ; \quad \langle(\triangle\hat{a}_2)^2\rangle = \frac{1}{4}e^{2r} \tag{1.5.7}$$

where r, is the squeeze parameter.

The squeezed state, $|\alpha, \zeta\rangle$, has the number state decomposition

$$
\begin{aligned}
|\alpha, \zeta\rangle = \hat{D}(\alpha)\hat{S}(\zeta)|0\rangle \quad =& \quad \frac{1}{\sqrt{\cosh(r)}} \exp\left[-\frac{1}{2}|\alpha|^2 - \frac{1}{2}\alpha^{*2}e^{i\theta}\tanh(r)\right] \\
&\times \sum_{n=0}^{\infty} \frac{\left[\frac{1}{2}e^{i\theta}\tanh(r)\right]^{\frac{n}{2}}}{\sqrt{n!}} H_n\left[\gamma\left(e^{i\theta}\sinh(2r)\right)^{-\frac{1}{2}}\right] \otimes |n\rangle
\end{aligned}
$$

$$\tag{1.5.8a}$$

where, $\hat{D}(\alpha) = \exp(\alpha\hat{a}^\dagger - \alpha^*\hat{a})$, is the displacement operator, $\hat{S}(\zeta) = \exp\left[\frac{1}{2}(\zeta^*\hat{a} - \zeta\hat{a}^\dagger)\right]$, is the squeeze operator, ζ, is the complex squeeze parameter [28, 44, 45] defined in the form

$$\zeta = r\,\exp(i\theta) \quad ; \quad 0 \le r < \infty \quad ; \quad 0 \le \theta \le 2\pi \tag{1.5.8b}$$

and

$$\gamma = \alpha\cosh(r) + \alpha^*e^{i\theta}\sinh(r) \,. \tag{1.5.8c}$$

The squeeze operator, $\hat{S}(\zeta)$, is a kind of a two-photon generalisation of the displacement operator, $\hat{D}(\alpha)$. Evidently, $\hat{a}^{\dagger 2}$, $\hat{a}^2$, in the operator, $\hat{S}(\zeta)$, implies that when the operator, $\hat{S}(\zeta)$, acts on a vacuum field, $|0\rangle$, photons will be created and destroyed in pairs.

1.5.3.1 Averages of creation, annihilation and photon number operators

The action of the product of displacement and squeeze operators, $\hat{D}(\alpha)\hat{S}(\zeta)$, on the creation, $\hat{a}^\dagger$, and separately annihilation, $\hat{a}$, operators, determines the average of the photon creation $\langle\hat{a}^\dagger\rangle$, photon annihilation, $\langle\hat{a}\rangle$, operators respectively and consequently the average of the photon number operator, $\langle\hat{n}\rangle$.

When, $\zeta = 0$, the squeezed coherent state, $|\alpha, \zeta\rangle$, in Eq. (1.5.8a) reduces to the single-mode field coherent state, $|\alpha\rangle$, specified in Eq. (1.5.6g) and the displacement operator effects the following transformations [28]

$$\hat{D}^\dagger(\alpha)\hat{a}\hat{D}(\alpha) = \hat{a} + \alpha \quad ; \quad \hat{D}^\dagger(\alpha)\hat{a}^\dagger\hat{D}(\alpha) = \hat{a}^\dagger + \alpha^* . \tag{1.5.9a}$$

To derive the transformations, $\hat{S}^\dagger(\zeta)\hat{a}\hat{S}(\zeta)$, $\hat{S}^\dagger(\zeta)\hat{a}^\dagger\hat{S}(\zeta)$, we apply the Baker-Housdorff (BH) lemma [46]

$$e^A B e^{-A} = B + [A, B] + \frac{1}{2!}[A, [A, B]] + \frac{1}{3!}[A, [A, [A, B]]] + \dots, \tag{1.5.9b}$$

while keeping in mind that, $\hat{S}^\dagger(\zeta) = \hat{S}(-\zeta)$, and consider

$$A \;=\; \frac{1}{2}\left(\zeta\hat{a}^{\dagger 2} - \zeta^*\hat{a}^2\right) \quad ; \quad B = \hat{a} , \; \hat{a}^\dagger \tag{1.5.9c}$$

to obtain

$$\begin{aligned}
\hat{S}^\dagger(\zeta)\hat{a}\hat{S}(\zeta) &= \hat{a}\cosh(r) - \hat{a}^\dagger e^{i\theta}\sinh(r) \quad ; \\
\hat{S}^\dagger(\zeta)\hat{a}^\dagger\hat{S}(\zeta) &= \hat{a}^\dagger\cosh(r) - \hat{a}e^{-i\theta}\sinh(r) .
\end{aligned} \tag{1.5.9d}$$

The average of annihilation, creation operators are derived by applying the transformations in Eqs. (1.5.9a) and (1.5.9d) according to

$$\begin{aligned}
\langle\hat{a}\rangle &= \langle\alpha, \zeta|\hat{a}|\alpha, \zeta\rangle \\
&= \langle 0|\hat{S}^\dagger(\zeta)\hat{D}^\dagger(\alpha)\hat{a}\hat{D}(\alpha)\hat{S}(\zeta)|0\rangle \\
&= \langle 0|\hat{S}^\dagger(\zeta)\left[\hat{a} + \alpha\right]\hat{S}(\zeta)|0\rangle \\
&= \alpha
\end{aligned}$$

$$\tag{1.5.9e}$$

and

$$\begin{aligned}
\langle\hat{a}^\dagger\rangle &= \langle\alpha, \zeta|\hat{a}^\dagger|\alpha, \zeta\rangle \\
&= \langle 0|\hat{S}^\dagger(\zeta)\hat{D}^\dagger(\alpha)\hat{a}^\dagger\hat{D}(\alpha)\hat{S}(\zeta)|0\rangle \\
&= \langle 0|\hat{S}^\dagger(\zeta)\left[\hat{a}^\dagger + \alpha^*\right]\hat{S}(\zeta)|0\rangle \\
&= \alpha^* .
\end{aligned} \tag{1.5.9f}$$

The average photon number for the squeezed state in Eq. (1.5.8a) now takes the final form

$$
\begin{aligned}
\langle \hat{n} \rangle = \langle \hat{a}^\dagger \hat{a} \rangle &= \langle \alpha, \zeta | \hat{a}^\dagger \hat{a} | \alpha, \zeta \rangle \\
&= \langle 0 | \hat{S}^\dagger \hat{D}^\dagger \hat{a}^\dagger \hat{D} \hat{D}^\dagger \hat{a} \hat{D} \hat{S} | 0 \rangle \\
&= \langle 0 | \hat{S}^\dagger \left(\hat{a}^\dagger + \alpha^* \right) \left(\hat{a} + \alpha \right) \hat{S} | 0 \rangle \\
&= \langle 0 | \hat{S}^\dagger \hat{a}^\dagger \hat{S} \hat{S}^\dagger \hat{a} \hat{S} | 0 \rangle + |\alpha|^2 \\
&= |\alpha|^2 + \sinh^2(r)
\end{aligned}
\tag{1.5.9g}
$$

such that $|\alpha|^2$, $\sinh^2(r)$ are the respective coherent and squeeze contributions to the average number of photons, $\langle \hat{n} \rangle$, in a squeezed coherent state. Also note that if, $|\alpha|^2 \gg \sinh^2(r)$, the coherent part of the state dominates the squeezed part.

1.5.3.2 Photon number distribution (P(n))

The photon number distribution, is the probability of finding n-photons in the field. It is obtained from Eq. (1.5.8a) as the absolute square of its probability amplitude in the form

$$
\begin{aligned}
P(n) &= |\langle n | \alpha, \zeta \rangle|^2 \\
&= \frac{\left(\frac{1}{2} \tanh(r) \right)^n}{n! \cosh(r)} \exp \left[-|\alpha|^2 - \frac{1}{2} \left(\alpha^{*2} e^{i\,\theta} + \alpha^2 e^{-i\,\theta} \right) \tanh(r) \right] \\
&\quad \times \left| H_n \left[\gamma \left(e^{i\,\theta} \sinh(2s) \right)^{-\frac{1}{2}} \right] \right|^2 ,
\end{aligned}
\tag{1.5.10}
$$

where it is evident that the distribution is dependent on the phase of α.

1.6 Evolution of quantum systems

The evolution of a closed quantum system is described by a unitary transformation [25]. That is, the state $|\psi\rangle$ of the system at a time t_1 is related to the state $|\psi'\rangle$ of the system at a time t_2 by a unitary operator $\hat{U}(t)$ which depends on times t_1 and t_2. The corresponding equation is the Schrödinger equation

$$
i\hbar \frac{\partial}{\partial t} |\psi\rangle = \hat{H} |\psi\rangle
\tag{1.6.1a}
$$

$\hat{H}$ is the Hamiltonian operator. Solving Eq. (1.6.1a), $|\psi\rangle$ evolves with time according to

$$|\psi(t)\rangle = \hat{U}(t)|\psi(0)\rangle \tag{1.6.1b}$$

where

$$\hat{U}(t) = e^{-i\frac{\hat{H}t}{\hbar}} \ . \tag{1.6.1c}$$

The time evolution operator $\hat{U}(t)$ in Eq. (1.6.1c) must be unitary, meaning that it preserves the norm of a state, hence $\hat{U}^\dagger \hat{U} = 1$.

1.7 Quantum gates

1.7.1 Single qubit gates

Quantum circuits are constructed from elementary gates [23, 47, 48], much like classical circuits. The important quantum gates which act on single qubits are shown in Fig. 1.2.

$$\boxed{X} \qquad \boxed{Y} \qquad \boxed{Z} \qquad \boxed{H} \qquad \boxed{S} \qquad \boxed{T}$$
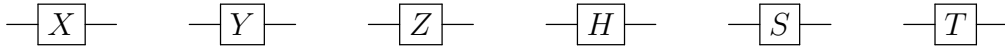
Figure 1.2: Important single qubit gates

In addition to the Pauli X, Y and Z gates in Eq. (1.3.6) we have the phase gate S and the $\frac{\pi}{8}$ gate T, with unitary transforms

$$S = \begin{pmatrix} 1 & 0 \\ 0 & i \end{pmatrix} \quad ; \quad T = \begin{pmatrix} 1 & 0 \\ 0 & \sqrt{i} \end{pmatrix} \tag{1.7.1}$$

which are obtained as $S = \sqrt{Z}$ and $T = \sqrt{S}$, respectively. These gates are important in fault tolerance quantum circuits. The Hadamard gate H also known as the Walsh-Hadamard gate is a single qubit gate [22, 23, 48]. The Hadamard transformation is defined as

$$H = \frac{X + Z}{\sqrt{2}} = \frac{1}{\sqrt{2}} \begin{pmatrix} 1 & 1 \\ 1 & -1 \end{pmatrix} \tag{1.7.2}$$

where it transforms atomic (field) computational basis states, $\{|e\rangle(|0\rangle), |g\rangle(|1\rangle)\}$ according

to

$$H|e\rangle \;\;\to\;\; \frac{|e\rangle + |g\rangle}{\sqrt{2}} = |+\rangle \;;\; H|g\rangle \to \frac{|e\rangle - |g\rangle}{\sqrt{2}} = |-\rangle \;;\; |e\rangle = \begin{pmatrix} 1 \\ 0 \end{pmatrix} \;;\; |g\rangle = \begin{pmatrix} 0 \\ 1 \end{pmatrix}$$

$$H|0\rangle \;\;\to\;\; \frac{|0\rangle + |1\rangle}{\sqrt{2}} = |+\rangle \;;\; H|1\rangle \to \frac{|0\rangle - |1\rangle}{\sqrt{2}} = |-\rangle \;;\; |0\rangle = \begin{pmatrix} 1 \\ 0 \end{pmatrix} \;;\; |1\rangle = \begin{pmatrix} 0 \\ 1 \end{pmatrix} \,.$$

$$(1.7.3)$$

into diagonal (Hadamard) basis states [49], $\{|+\rangle, |-\rangle\}$. Single qubit gates act upon single qubits of the form in Eqs. (1.2.4) and (1.7.3).

In the Bloch Sphere representation, unitary operations on a single qubit act as rotations of the Bloch vector $R_x(\theta)$, $R_y(\theta)$, $R_z(\theta)$ [23, 47]. These operations keep the radius of the sphere constant hence the name rigid operations. In this sense, each point on a Bloch sphere goes to another point on the sphere after undergoing a unitary operation. Thereby, rotations about the x, y and z axes take the forms

$$
\begin{aligned}
R_x(\theta) &= e^{-i\frac{\theta}{2}\sigma_x} = \cos\left(\frac{\theta}{2}\right) I - i\sin\left(\frac{\theta}{2}\right)\sigma_x = \begin{pmatrix} \cos(\frac{\theta}{2}) & -i\sin(\frac{\theta}{2}) \\ -i\sin(\frac{\theta}{2}) & \cos(\frac{\theta}{2}) \end{pmatrix} \;\;; \\[6pt]
R_y(\theta) &= e^{-i\frac{\theta}{2}\sigma_y} = \cos\left(\frac{\theta}{2}\right) I - i\sin\left(\frac{\theta}{2}\right)\sigma_y = \begin{pmatrix} \cos(\frac{\theta}{2}) & -i\sin(\frac{\theta}{2}) \\ \sin(\frac{\theta}{2}) & \cos(\frac{\theta}{2}) \end{pmatrix} \;\;; \\[6pt]
R_z(\theta) &= e^{-i\frac{\theta}{2}\sigma_z} = \cos\left(\frac{\theta}{2}\right) I - i\sin\left(\frac{\theta}{2}\right)\sigma_z = \begin{pmatrix} e^{-i\frac{\theta}{2}} & 0 \\ 0 & e^{i\frac{\theta}{2}} \end{pmatrix} \;\;,
\end{aligned}
$$

$$(1.7.4)$$

where σ_x, σ_y, σ_z are Pauli matrices and I the identity matrix defined in Eq. (1.3.6). More generally, the rotation of the Bloch vector by θ around real unit vector $\hat{n} = (n_x, n_y, n_z)$ is given by

$$R_{\hat{n}} = exp\left(-i\theta\hat{n}\cdot\frac{\vec{\sigma}}{2}\right) = \cos\left(\frac{\theta}{2}\right) I - i\sin\left(\frac{\theta}{2}\right)(n_x\sigma_x + n_y\sigma_y + n_z\sigma_z) \qquad (1.7.5)$$

where $\vec{\sigma}$ denotes the three-component vector of Pauli matrices called the Pauli matrix vector defined in Eq. (1.3.9).

An important result, sometimes known as the *Bloch's theorem* or the Bloch decomposition, is that any single qubit gate, U, can be written as the product of three rotations (and the overall scalar phase that is mostly irrelevant): for all $U \in U(2), \exists\ \alpha,\ \beta,\ \gamma$ such

that $U = e^{i\alpha} R_z(\beta) R_y(\gamma) R_z(\delta)$ [47, 48].

1.7.2 Two qubit gates

A two qubit gate which is a member of the universal gate set is the controlled-NOT (C-NOT) gate. We define a quantum C-NOT gate as that which affects the unitary operation on two qubits which in a chosen orthonormal basis in $\mathbb{C}^2$ gives the C-NOT operation obtained as

$$|a\rangle|b\rangle \rightarrow |a\rangle|a \oplus b\rangle \tag{1.7.6}$$

where, $|a\rangle$, is the control qubit, $|b\rangle$, is the target qubit and, $\oplus$, indicates addition modulo 2 [22, 23, 50]. As an example, it flips the second qubit (target qubit) if the first qubit (control qubit) is $|1\rangle$ and when the control qubit is $|0\rangle$, the target qubit remains unchanged as shown in Fig. 1.3.

$$
|1\rangle \;\longrightarrow\!\!\bullet\!\!\longrightarrow\; |1\rangle \qquad\qquad |0\rangle \;\longrightarrow\!\!\bullet\!\!\longrightarrow\; |0\rangle
$$
$$
|1\rangle \;\longrightarrow\!\!\oplus\!\!\longrightarrow\; |0\rangle \qquad\qquad |1\rangle \;\longrightarrow\!\!\oplus\!\!\longrightarrow\; |1\rangle
$$
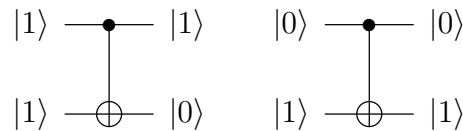
Figure 1.3: C-NOT gate operations

The C-NOT gate transforms superposition into entanglement, thus acting as a measurement gate [22, 23, 50]; it is fundamental in performing algorithms in quantum computers [51]. Transformation to a separable state (product state) is realised by applying the C-NOT gate again. In this case, it is used to implement Bell (state) measurement on the two qubits [52].

A useful operator representation of the C-NOT gate is

$$
\begin{aligned}
U_{C-NOT} &= |0\rangle\langle 0| \otimes I + |1\rangle\langle 1| \otimes X \\
&= \begin{pmatrix} 1 & 0 & 0 & 0 \\ 0 & 1 & 0 & 0 \\ 0 & 0 & 0 & 1 \\ 0 & 0 & 1 & 0 \end{pmatrix}
\end{aligned}
$$

$$\tag{1.7.7}$$

which captures the coherent quantum nature of the C-NOT gate. In the quantum C-NOT gate, the second operation is controlled on the basis state of the first qubit hence the choice of the name "controlled-NOT".

Another two qubit gate which is useful is the SWAP gate which interchanges two states without entanglement [47, 48]

$$U_s|\psi, \phi\rangle = U_s(|\psi\rangle \otimes |\phi\rangle) = |\phi, \psi\rangle \ . \tag{1.7.8}$$

The operator representation of this gate in the basis, $\{|0\rangle, |1\rangle\}$, is

$$U_s = |00\rangle\langle00| + |01\rangle\langle10| + |10\rangle\langle01| + |11\rangle\langle11| \ . \tag{1.7.9}$$

The schematic diagram of the SWAP gate is shown in Fig. 1.4
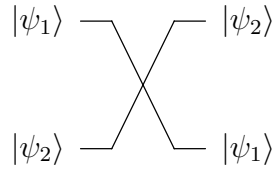
Figure 1.4: SWAP gate operations

1.7.3   Three qubit gates

Three qubit gates can as well be defined. These are the Toffoli gate or the Controlled - Controlled NOT (CCNOT) gate and the Fredkin gate or the Controlled SWAP (CSWAP) gate [47, 48]. The CCNOT gate has two qubits as the control and a third qubit as the target. In this case the target qubit is flipped only when both the control qubits are $|1\rangle$. This gate is reversible. The representation of the general CCNOT gate is shown in Fig. 1.5
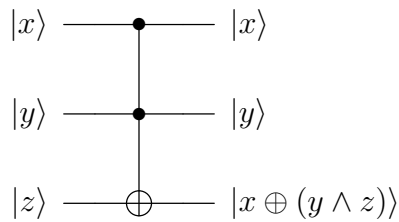
Figure 1.5: Toffoli gate operations

The operator representation of this gate in the basis, $\{|0\rangle, |1\rangle\}$, is

$$U_{CCNOT} = (|00\rangle\langle00| + |01\rangle\langle01| + |10\rangle\langle10|) \otimes I + |11\rangle\langle11| \otimes X \tag{1.7.10}$$

where the operators act on the three qubits in the order in which the relation in Eq. (1.7.10) is written.

The CSWAP gate is a three qubit gate which interchanges two target qubits if the control qubit is $|1\rangle$. The diagramatic representation of the general CSWAP gate is shown in Fig. 1.6

$$|\psi_1\rangle \quad\underline{}\bullet\underline{}\quad |\psi_1\rangle$$
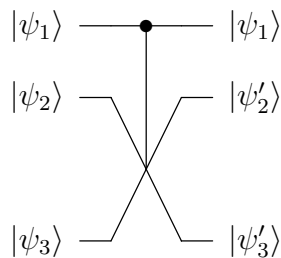
Figure 1.6: Fredkin gate operations

Its explicit operator form is

$$U_{CSWAP} = |0\rangle\langle 0| \otimes I_4 + |1\rangle\langle 1| \otimes U_{SWAP} \ . \tag{1.7.11}$$

1.8   Bipartite entanglement and Bell states

Entanglement, once described by Einstein as a "telepathically" working interaction [53, 54] and used to criticise quantum mechanics for its counter-intuitiveness [55], can today be observed in experiments. In quantum computing, entanglement is a source of exponential speed up of algorithms [56–58] and its existence is a necessary condition for teleportation [59] and quantum cryptography [60–62].

The effect can take place between any two quantum objects. If the two objects are entangled, their state is best described by one common wave function. Upon measurement of one of the object's properties the other one will show either the complimentary value or the same value, depending on which Bell state [59] the system is in. The main point is that the state of the second quantum object is exactly determined once the first has been measured. In theory, entanglement does not weaken if the distance between the two quantum objects increases but remains the same at arbitrary distance [63]. It was shown by Bell [64], that the effect of entanglement is independent of the basis in which the measurement is carried out. Thus, it became unavoidable to state that entanglement is indeed a phenomenon, which can neither be explained by classical means nor limited relativistically by the speed of light, c.

A special case of a measurement is a projective measurement in the Bell state basis [23, 25, 64, 65]. Considering two states $|\psi\rangle_1$, $|\psi\rangle_2$ in separate remote locations defined as

$$|\psi\rangle_1 = \alpha_1|0\rangle + \beta_1|1\rangle \quad ; \quad |\psi\rangle_2 = \alpha_2|0\rangle + \beta_2|1\rangle \ , \tag{1.8.1a}$$

the combined state of the system, $|\Psi\rangle_c$, is determined according to

$$
\begin{aligned}
|\Psi\rangle_c &= |\psi\rangle_1 \otimes |\psi\rangle_2 \\
&= (\alpha_1\alpha_2|00\rangle + \beta_1\beta_2|11\rangle) + (\alpha_1\beta_2|01\rangle + \beta_1\alpha_2|10\rangle) \ . \tag{1.8.1b}
\end{aligned}
$$

Symmetrising and re-organising Eq. (1.8.1b), we obtain

$$
\begin{aligned}
|\Psi\rangle_c &= \frac{1}{2}(\alpha_1\alpha_2 + \beta_1\beta_2)(|00\rangle + |11\rangle) + \frac{1}{2}(\alpha_1\alpha_2 - \beta_1\beta_2)(|00\rangle - |11\rangle) \\
&+ \frac{1}{2}(\alpha_1\beta_2 + \beta_1\alpha_2)(|01\rangle + |10\rangle) + \frac{1}{2}(\alpha_1\beta_2 - \beta_1\alpha_2)(|01\rangle - |10\rangle) \\
&= \frac{1}{\sqrt{2}}(\alpha_1\alpha_2 + \beta_1\beta_2)|\Phi^+\rangle + \frac{1}{\sqrt{2}}(\alpha_1\alpha_2 - \beta_1\beta_2)|\Phi^-\rangle \\
&+ \frac{1}{\sqrt{2}}(\alpha_1\beta_2 + \beta_1\alpha_2)|\Psi^+\rangle + \frac{1}{\sqrt{2}}(\beta_1\alpha_2 - \alpha_1\beta_2)|\Psi^-\rangle \ . \tag{1.8.1c}
\end{aligned}
$$

The combined system in Eq. (1.8.1c) is now in terms of four (maximally entangled) Bell states $|\Psi^\pm\rangle$, $|\Phi^\pm\rangle$, expressed in computational basis as

$$
\begin{aligned}
|\Psi^+\rangle &= \frac{1}{\sqrt{2}}(|10\rangle + |01\rangle) \quad ; \quad |\Psi^-\rangle = \frac{1}{\sqrt{2}}(|10\rangle - |01\rangle) \quad ; \\
|\Phi^+\rangle &= \frac{1}{\sqrt{2}}(|00\rangle + |11\rangle) \quad ; \quad |\Phi^-\rangle = \frac{1}{\sqrt{2}}(|00\rangle - |11\rangle) \ . \tag{1.8.1d}
\end{aligned}
$$

In most experimental set-ups measurements are preferably done in the computational basis $\{|0\rangle, |1\rangle\}$. Therefore, in order to perform a measurement in the Bell basis, the basis states, $\{|\Psi^+\rangle, |\Psi^-\rangle, |\Phi^+\rangle, |\Phi^-\rangle\}$, must be mapped onto the computational basis states of two qubits, $\{|00\rangle, |01\rangle, |10\rangle, |11\rangle\}$. This is achieved by first applying a C-NOT (U_{C-NOT}^{12}) where qubit 1 is the control qubit and qubit 2 is the target qubit, and then a Hadamard operation H to qubit 1. It is important to note that this operation works in both directions, i.e., starting from computation basis states, applying a Hadamard operation first and then the C-NOT gate, will generate Bell states.

In recent years it has been shown experimentally that the effects of entanglement are transmitted at a speed at least of the order $c \cdot 10^3$ [66, 67]. In summary the actual transfer of information is limited, since it can only happen by means of quantum teleportation

[68].

1.8.1 Bell state projection

Projection of a state, $|\Lambda\rangle$, onto another state, $|\Sigma\rangle$, is defined as [22]

$$P_\Sigma := \langle\Sigma|\Lambda\rangle|\Sigma\rangle \tag{1.8.2}$$

where, P_Σ, stands for projection onto $|\Sigma\rangle$ and not probability. Further, the term, $\langle\Sigma|\Lambda\rangle$, is an inner product between the two states, $|\Sigma\rangle$, $|\Lambda\rangle$. As an example, the projection into Bell basis of the state, $|\Psi\rangle_c$, in Eq. (1.8.1c) onto, $|\Phi^+\rangle$, also defined in Eq. (1.8.1d) is

$$\langle\Phi^+|\Psi\rangle_c = \frac{1}{\sqrt{2}}(\alpha_1\alpha_2 + \beta_1\beta_2)|\Phi^+\rangle \quad ; \quad \langle\Sigma|\Lambda\rangle = \frac{1}{\sqrt{2}}(\alpha_1\alpha_2 + \beta_1\beta_2) . \tag{1.8.3}$$

It is clear from Eq. (1.8.3) that the system, $|\Psi\rangle_c$, collapses (projected) onto the Bell state basis, $|\Phi^+\rangle$. Meaning that projection of a quantum state results from measurement of a system's observables (eigenstates). In this case, the Bell state basis, $\{|\Psi+\rangle, |\Psi^-\rangle, |\Phi^+\rangle, |\Phi^-\rangle\}$, for state, $|\Psi\rangle_c$.

1.8.2 Quantifying entangled states of two qubits

As stated in Sec. 1.8, for entangled states the subsystems are no longer independent. This means that a measurement performed on one subsystem will result in a state reduction in both subsystems with strongly correlated measurement results.

A quantitative discussion of entanglement is possible by defining entanglement measures. For a bipartite system, a criterion exists to determine whether or not a state is separable, which relies on the behaviour of the partial transpose. The partial transpose is defined by [69]

$$\hat{\rho}^{PT} = (\sigma_x \otimes I) \cdot \hat{\rho} . \tag{1.8.4}$$

It has been shown that a mixed state, $\hat{\rho}$, is entangled if and only if its partial transpose, $\hat{\rho}^{PT}$, has a negative eigenvalue [70].

Using Schmidt decomposition [71], any pure state, $|\Psi_{ab}\rangle$, can be written as

$$|\Psi_{ab}\rangle = \sum_{i=1}^{n} c_i \, |\alpha_i\rangle \otimes |\beta_i\rangle \tag{1.8.5}$$

where, $\{\alpha_i\}$, and $\{\beta_i\}$, are orthonormal basis of the subsystems a and b, respectively, and the coefficients, $\{c_i\}$, are positive, real numbers. An entanglement measure for such a state is given by the entropy of one of the subsystems

$$
\begin{aligned}
E(\Psi_{ab}) &= S(tr_a|\Psi_{ab}\rangle\langle\Psi_{ab}|) = S(tr_b|\Psi_{ab}\rangle\langle\Psi_{ab}|) = -\sum_{i=1}^{n} c_i^2 \log_2 c_i^2 \quad ; \\
\hat{\rho}_a &= tr_b\left(|\Psi_{ab}\rangle\langle\Psi_{ab}|\right) \quad ; \quad \hat{\rho}_b = tr_a\left(|\Psi_{ab}\rangle\langle\Psi_{ab}|\right) \; .
\end{aligned}
$$

(1.8.6)

The entropies of the subsystems are defined through their respective reduced density operators by

$$
S(\hat{\rho}_j) = -tr(\hat{\rho}_j \log_2 \hat{\rho}_j) \quad ; \quad j : a(b)
$$

(1.8.7)

where in general

$$
S(\hat{\rho}) = -tr(\hat{\rho} \log \hat{\rho}) \quad ; \quad \hat{\rho} = |\Psi_{ab}\rangle\langle\Psi_{ab}|
$$

(1.8.8)

is the von Neumann entropy [23, 28, 72–76]. It follows that $0 \leqslant S(\hat{\rho}) \leqslant 1$, where $S(\hat{\rho}) = 0$ if and only if $\hat{\rho}$ is a pure state and $0 \leq E(\Psi_{ab}) \leq 1$ where the limit 0 is achieved if the pure state is a product (or separable) and 1 is achieved for maximally entangled states.

In addition, for pure states including mixed states where the Bloch vector [27] in Eq. (1.2.5) assumes values $|\vec{r}| \leqslant 1$, the density operator well defined in Eqs. (1.3.1), (1.3.3) - (1.3.5) and (1.3.8) has two eigenvalues, $\pi_1 = \frac{1}{2}[1 - |\vec{r}|], \pi_2 = \frac{1}{2}[1 + |\vec{r}|]$, and so for each subsystem its easy to obtain the von Neumann entropy in the form

$$
S(\hat{\rho}_j) = -\pi_1 \log_2 \pi_1 - \pi_2 \log_2 \pi_2 \quad ; \quad j : a(b) \; .
$$

(1.8.9)

Whenever $|\vec{r}| = 1$ for pure states, we have $S(\hat{\rho}_j) = 0$.

The definition of the quantity, $E(\Psi_{ab})$, is connected to the question of how many singlet pairs of the type, $|\Psi^-\rangle = (|0_a\rangle|1_b\rangle - |1_a\rangle|0_b\rangle)$, are necessary to create n copies of a given bipartite state, $|\Psi_{ab}\rangle$. It has been shown that approximately $nE(\Psi_{ab})$ singlet states are necessary to perform this task [73].

Considering the result obtained for pure states, it is reasonable to estimate the number

of singlets necessary to create n copies of $\hat{\rho}$ as

$$n \sum_{i=1}^{N} p_i \, E(\Psi_i) \qquad (1.8.10)$$

However the quantity, $\sum p_i \, E(\Psi_i)$, is still not a good measure of entanglement, since it depends on particular decomposition of $\hat{\rho}$. This line of reasoning leads to the definition of entanglement of formation [77]

$$E_f(\hat{\rho}) = \inf \sum_j p_j E(\Psi_j) \qquad (1.8.11)$$

Here the infimum of $\sum p_j \, E(\Psi_j)$ over all possible decompositions of $\hat{\rho}$ into pure states is taken as an entanglement measure. The definition of entanglement of formation involves an optimization problem to find the infimum, which in the case of higher dimensional systems is an unsolved problem. However for bipartite systems an algebraic solution is known, which allows calculation of entanglement of formation from the given density matrix [77, 78]. More precisely, in the bipartite case, with two subsystems labeled a and b, the concurrence is widely used in practical situations. For pure states of two spins, this quantity can be written as

$$C(|\psi_{ab}) = |\langle \psi_{ab} | \tilde{\psi}_{ab} \rangle| \qquad (1.8.12)$$

where, $|\tilde{\psi}_{ab}\rangle \equiv \hat{\sigma}_x^{\otimes 2} |\psi_{ab}^*\rangle$, is referred to as the 'spin-flipped' state vector [77]. The concurrence of a mixed two-qubit state , $C(\hat{\rho}_{ab})$, can be expressed in terms of the minimum average pure-state concurrence, $C(|\psi_{ab}\rangle)$, where the required minimum is taken over all possible ways of decomposing the ensemble, $\hat{\rho}_{ab}$, into a mixture of pure states, $|\psi_{ab}\rangle$. The concurrence of a general two-spin state is then [69]

$$C(\rho_{ab}) = \max\{0, \lambda_1 - \lambda_2 - \lambda_3 - \lambda_4\} \qquad (1.8.13)$$

where λ_i are real square roots of eigenvalues of the matrix $\hat{\tilde{\rho}}_{ab}$, ordered by decreasing size, and are non-negative. The entanglement of formation, $E_f(\hat{\rho}_{ab})$, of a mixed bipartite state, $\hat{\rho}_{ab}$, of a pair of two-level systems (qubits) is defined in the large number limit of identical copies of the two-level system as the minimum number required to form the state, $\hat{\rho}_{ab}$, by local operations and classical communication (LOCC) on this collection copies. This quantity has the form of the binary entropy function, expressed in terms of concurrence

[69, 77]

$$E_f(\hat{\rho}_{ab}) = h \left\{ \frac{1 + \sqrt{1 - C^2(\hat{\rho}_{ab})}}{2} \right\} \tag{1.8.14}$$

where

$$h(x) = -x \log_2 x - (1 - x) \log_2 (1 - x) . \tag{1.8.15}$$

The square of concurrence of a state is often referred to as a *tangle.*

A practical entanglement measure quantifying bipartite-state entanglement in a few important quantum system sizes is negativity. Negativity is defined in terms of the transpose of the density matrix representation of the statistical operator, as follows [24, 69, 70]

$$N(\hat{\rho}) = \frac{1}{2}(\|\hat{\rho}^{T_a}\| - 1) = \left| \sum_i \lambda_i \right| \tag{1.8.16}$$

where, $\hat{\rho}^{T_a}$, is the partial transpose of a given bipartite state, $\hat{\rho}_{ab}$, with respect to subsystem, a, and, $\|\cdot\|$, is the trace-norm and i runs over the subset of negative eigenvalues of this density matrix; the operator, $\hat{\rho}^{T_a}(or\ \hat{\rho}^{T_b})$, is positive if and only if the statistical operator, $\hat{\rho}$, is separable else entangled [70, 79, 80]. Negativity becomes, $N(\hat{\rho}_{ab}) = \frac{1}{2}$, for a maximally entangled two-qubit state and, $N(\hat{\rho}_{ab}) = 0$, for any separable state. In this sense, $N(\hat{\rho}_{ab})$, is the actual measure of negativity.

Another important and more practical mixed state entanglement quantifier is the logarithmic negativity [24, 69] which is based upon the negativity after partial transposition [70, 79, 80]. The logarithmic negativity is defined as follows

$$E_N(\hat{\rho}_{ab}) \equiv \log_2 \left\| \hat{\rho}^{T_b} \right\| \tag{1.8.17}$$

where, $\|\cdot\|$, is the trace norm and, ρ^{T_b}, is the partial transpose of a given bipartite state, ρ_{ab}, with respect to subsystem b. This measure is an entanglement monotone, that is, it does not increase under LOCC, and in addition it is additive. The trace norm of the partial transpose corresponds to the sum of modulus of its eigenvalues.

Logarithmic negativity can also be expressed as follows

$$E_N(\hat{\rho}_{ab}) = -2 \sum_i \lambda_i \tag{1.8.18}$$

where it is defined in terms of negative eigenvalues, λ_i, of the partial transpose of the state, $\hat{\rho}_{ab}$. For a separable two-qubit state, $\hat{\rho}_{ab}$, we always obtain, $\left\| \hat{\rho}^{T_b} \right\| = 1$, and for a

maximally entangled two-qubit state, $\left\|\hat{\rho}^{T_b}\right\| = 2$. Thus a maximally entangled state gives, $E_N(\hat{\rho}_{ab}) = 1$, whereas the separable state, $E_N(\hat{\rho}_{ab}) = 0$. In general any entanglement measure should be an entanglement monotone and should vanish for separable states.

In summary, since the trace norm of the partial transpose effectively expresses to what extent $\hat{\rho}^{T_b}$ fails to represent a physical state, it can be considered a quantitative version of the partial transpose criterion.

Characterising quantum entanglement in all but even the simplest of cases, the bipartite system of qubits, is challenging not to mention understanding the relevant experimental quantities related to entanglement. It may not be necessary, however, to quantify the entanglement of a state in order to quantify the quantum information processing significance of a state. For example, Horodecki $et.al$ [81] demonstrated that the maximum teleportation fidelity for a general two qubit system is given by

$$F_{\hat{\rho}} = \frac{2f_{\hat{\rho}} + 1}{3} \tag{1.8.19a}$$

where $f_{\hat{\rho}}$ is the fully entangled fraction in the form [75]

$$f_{\hat{\rho}} = \max_{|\Psi\rangle}\langle\Psi|\hat{\rho}|\Psi\rangle = \left\{tr\sqrt{\hat{\rho}^{\frac{1}{2}}_{expected}\hat{\rho}_{measured}\hat{\rho}^{\frac{1}{2}}_{expected}}\right\}^2 , \tag{1.8.19b}$$

and is defined as the overlap between a mixed state, $\hat{\rho}$, and a maximally entangled state, $|\Psi\rangle$, maximised over all $|\Psi\rangle$. Unlike entanglement, the fully entangled fraction does not have a clear experimental interpretation as the optimal ability to teleport but it is clear that the degree to which fully entangled fraction is greater than a half ($f_{\hat{\rho}} > \frac{1}{2}$; $F_{\hat{\rho}} > \frac{2}{3}$) can be used to quantify the teleporting ability of a state over the best classical limit ($F_{\hat{\rho}} = \frac{2}{3}$) defined for classical teleportation protocols.

1.9   Statement of the problem

The quantum Rabi model (QRM), the simplest model that describes the interaction between a two-level atom (fermionic system) and a quantised single mode of electromagnetic radiation (bosonic system), could not be solved exactly under the assumption that the counter(anti)-rotating terms (CRTs), $\hat{a}\hat{s}_-$, $\hat{a}^\dagger\hat{s}_+$, which simultaneously de-excite and excite atom-field states, do not conserve energy. The CRTs were dropped by a mathematical method called RWA to solve the QRM, yielding an exactly solvable simplified form of the QRM in the RF termed the JC model.

The QRM was recently re-organised into a two-component, JC Hamiltonian in

the rotating frame (RF) and the anti-Jaynes-Cummings (AJC) Hamiltonian in the counter(anti)-rotating frame (CRF), and the AJC Hamiltonian was solved exactly after discovery of the AJC conserved excitation number operator.

The JC Hamiltonian is now defined as the one that generates dynamics when the atomic spin couples to the rotating positive frequency component of the field mode, allowing algebraic operations to be performed using normal-operator-ordering, whereas the AJC Hamiltonian generates dynamics when the atomic spin couples to the CR negative frequency component of the field mode, allowing algebraic operations to be performed using anti-normal-operator ordering. The AJC and JC interactions can now be investigated independently.

Noting that the JC model has been successful in accurately predicting a wide range of experiments and has correctly described most observed effects when a two-level system couples to a bosonic mode, we now focus attention on the AJC model and proceed here to present a first time clear algebraic properties, dynamics and application in QIP (a combination of QIT and quantum computation) of the AJC model when a two-level atom interacts with a quantised field mode.

1.10 Objectives of the study

The objectives of this study are to;

1. demonstrate Rabi oscillations between stationary basic AJC qubit state vectors in the AJC interaction mechanisms,

2. demonstrate time evolution of degree of entanglement (DEM) of a coupled time evolving AJC qubit state vectors formed in the AJC interaction mechanism,

3. create maximally entangled AJC qubit states in the AJC interaction mechanism,

4. analyse time evolution of atomic population inversion, DEM and photon statistics to provide a clear visualisation of the AJC processes and its non-classicality,

5. demonstrate teleportion of maximally entangled two-atom qubit state in the AJC interaction mechanisms and

6. demonstrate how to realise a quantum C-NOT gate operation and a quantum Hadamard gate operation in the AJC process.

1.11 Justification of the study

Experiments in the full QRM conducted in the so called deep strong coupling (DSC) [82, 83] and Ultrastrong coupling (USC) regimes [6, 84, 85], respectively, have demonstrated that the contribution of CRTs in atom-field interaction is significant, implying that RWA is invalid. It is in these coupling regimes that the dynamics of the absolute ground state, $\mid g, 0 \rangle$, and effects of the residual sum-frequency detuning, $\bar{\delta} = 2\omega$, could be explained [86].

In this study, the AJC Hamiltonian drives an initial atom-field ground state, $\mid g, 0 \rangle$, into a time-evolving entangled state, based on the physical interpretation of the AJC interaction [9, 10, 16] as that which couples a two-level system to the CR negative frequency component of the field mode. Again, we remark that in [87, 88], the experiments have revealed dynamical effects arising from interactions involving negative frequency radiation.

It is now possible to visualise the key effects of the CRTs in the dynamics generated by the AJC Hamiltonian, which is an exactly solvable form of the QRM in the CRF, independent of the entire QRM generated dynamics. This model, AJC model, is the cornerstone in this Thesis.

1.12 Significance of the study

We have presented a first-time dynamical analysis of an exactly solvable AJC model which is nothing short of inspiring. Whereas the JC model as a building block of QRM has been extensively studied for its fundamental interaction properties both in theory and in experiments in quantum optics, this work emphasises that the energy conserving AJC model as a building block of QRM, can be effectively applied in QIP.

Utilisation of quantum mechanics and quantum optics, accepted quantum information theory (QIT) probing techniques of purity of states, degree of entanglement (DEM) and fidelity, and quantum computation principles, we have established that there are obvious parallels and positive differences in comparison to the extensively studied exactly solvable JC model. By studying the AJC process independently it is now demonstrated that indeed in this interaction starting from an absolute atom-field ground state, there exists Rabi oscillations and you can easily create maximally entangled anti-symmetric atom-field qubit states of profound interest in QIP due to their important properties. To mention, the anti-symmetric qubit states are invariant under local unitary transformation, they exhibit perfect correlation when simultaneous measurements of all particles in a commonly

chosen measurement basis is applied and they can be generated in an iterative manner by a sequence of C-NOT gates. In addition, totally anti-symmetric states can as well be used in different tasks which are of interest for quantum communication. This include quantum mechanical key sharing protocol, security of the quantum key sharing protocol, protocol for quantum state sharing and comparison of two quantum states. All these is because of high symmetry and peculiar correlation properties of the anti-symmetric quantum states. We have shown that direct atom-field interaction in the JC process, results in symmetric atom-field states for which correlations of quantum states during measurement are not easily determined.

Further, according to DiVincenzo criteria [89], storing and processing quantum information requires a scalable physical system (a system that is able to handle an increasing number of qubits in a stable manner) with well-defined qubits, which can be initialised to well-defined qubit state vectors, and have long lived quantum states in order to ensure long coherence times during the computational process, i.e, much longer than the quantum gate operation time. The necessity to coherently manipulate the stored quantum information requires a set of universal gate operations between the qubits which must be manipulated using controllable interactions of quantum systems. Finally, determining reliably the outcome of a quantum computation requires an efficient measurement procedure.

With reference to the DiVincenzo criteria for storing and processing of quantum information together with the problem statement well articulated in Sec. 1.9, we have discussed QIP (a combination of QIT and quantum computation) in the AJC interaction with particular emphasis on entanglement, realisation of efficient quantum C-NOT, Walsh-Hadamard gate operations and quantum teleportation of an entangled two-atom state. The precise and verifiable outcomes, demonstrates the accuracy with which each item is arrived at with reference to the critera according to DiVincezo. The results of this work will therefore provide significant contribution when applying qubit technologies (photonic qubits, trapped ion qubits, cold atom qubits, nuclear magnetic resonance, quantum dot qubits, defect based qubits, super-conducting qubits and topological qubits); in quantum technologies (quantum communication, quantum computation, quantum simulation, quantum sensing and quantum metrology); on the conceptual understanding of quantum teleportation and how to easily realise anti-symmetric quantum channels Sec. 3.2.1 and Sec. 3.2.2.3; on how to easily realise a long-lived qubit coherence time Sec. 3.2.2.2; how to realise universal gate operation through controlled interaction Sec. 3.2.3 and Sec. 3.2.4; on how to easily realise a fully quantised qubit field interaction in an open quantum sys-

tem when a coherent field mode is considered Sec. 3.3 and Sec 3.4 and most importantly entanglement. A major goal of QIS is to characterise and quantify quantum entanglement and to formulate new ways in which it can be exploited and manipulated. This we have explicitly presented in Secs. $4.1.2, 4.1.3, 4.1.4, 4.2$ and 4.3. We take note here that entanglement is a key resource that enables quantum communication protocols such as quantum teleportation Sec. 4.1.2, superdense coding and quantum key distribution (QKD).

1.13 Scope of the study

Whilst the effect of CRTs have been observed in experiments involving the full QRM through application of USC/DSC coupling regimes, the approach taken here is fundamentally different. Indeed, we are studying atom-field interaction in an exactly solvable AJC model where the coupling terms $\hat{a}^{\dagger}\hat{s}_{+}$, $\hat{a}\hat{s}_{-}$ simultaneously excite, de-excite atom, field interacting quantum systems. The aim of this study, is to demonstrate that important quantum features such as Rabi oscillations and photon anti-bunching exist during this interaction; entanglement of atom-field states as a quantum phenomenon can be realised; and applications in quantum computation (quantum gates) and quantum information processing (teleportation) is feasilble using qubits that are generated during the AJC interaction. The scope of this study is limited to application of standard methods in quantum optics in analysis of Rabi oscillations between the interacting atom-field quantum systems, entanglement of the atom-field quantum states, time evolution of degree of entanglement, purity of states and photon anti-bunching in the exactly solvable AJC model. Analytical description of the AJC model is left in its original form and applied as it is.

For purposes of comparing the AJC dynamics to that of the well-known JC interaction, we have provided the corresponding analysis during the JC interaction involving a two-level atom and quantised light mode separately in Fock state, coherent state and squeezed state in Appendices A, B and C respectively.

CHAPTER 2
LITERATURE REVIEW

2.1 Studies of the Rabi model

The Quantum Rabi Model (QRM) [3, 9, 11, 12, 15] describes the most fundamental light-matter interaction involving quantised light and quantised matter. It is different from the semiclassical Rabi model (RM) [1], where light is treated classically. In its semiclassical form, the RM was formulated to describe the effect of a rapidly varying weak magnetic field on an oriented atom possessing nuclear spin. It was applied with success to explain the challenging experimental data taken by R. Frisch and E. Segre' [90].

The QRM is used to describe the dipolar coupling between a two-level system (typically an atom assumed to have only two discrete states) and a bosonic field mode. Although it plays a central role in the dynamics of a collection of quantum optics and condensed matter systems [91], such as cavity quantum electrodynamics (CQED) [92–94], quantum dots [95–97], trapped ions [98–100], or circuit quantum electrodynamics (cQED) [101, 102], only recently has analytical solution of the QRM in all coupling regimes been proposed [3, 13–15, 103].

In most cases the QRM, $\hat{H}_R = \frac{1}{2}\hbar\omega(\hat{a}^\dagger\hat{a} + \hat{a}\hat{a}^\dagger) + \hbar\omega_0\hat{s}_z + \hbar\lambda(\hat{a} + \hat{a}^\dagger)(\hat{s}_+ + \hat{s}_-)$, is further simplified by making the rotating-wave approximation (RWA) where the coupling terms that simultaneously excite, $\hat{a}^\dagger\hat{s}_+$, or de-excite, $\hat{a}\hat{s}_-$, the atom and the field are neglected. This quantum version of the RM determined by application of the RWA is known as the Jaynes-Cummings (JC) model, $\hat{H} = \hbar(\omega\hat{a}^\dagger\hat{a} + \omega_0\hat{s}_z + 2\lambda(\hat{a}\hat{s}_+ + \hat{a}^\dagger\hat{s}_-))$, [8]. Typically the RWA is valid when the ratio between the coupling strength, λ, and the mode frequency, ω, is small [104]. Its dynamics is integrable[1] and splits the space of quantum states in an infinite sequence of state doublets. The reason the JC model has been so successful is not merely because it can be solved exactly, but how it accurately predicts a wide range of experiments. Analytical solutions of this model have brought clarity and intuition to several important problems and experimental results in modern physics. In this sense, the JC model is able to correctly describe most observed effects where an effective two-level system couples to a bosonic mode, be it in more natural systems as CQED [105–107] or in simulated versions as trapped ions [100, 108] and cQED [101, 102, 109]. However,

---

[1]Integrable means that the time dependence of most of the interesting properties can be described by explicit analytical expressions

when the interaction grows in strength until the ultrastrong coupling (USC) [6, 84, 85] and deep strong coupling (DSC) [82, 83] regimes, the RWA is no longer valid.

Experiments on the full QRM have made outstanding breakthroughs, determining details of the dynamics into the USC and DSC regimes, however in both theoretical and experimental advances information on the solvability of the AJC interaction has received little or no attention. Recently Omolo, J.A. [9] reorganised the QRM and showed that the AJC model has a conserved excitation number operator, $\hat{\bar{N}}$, which generates $U(1)$ symmetry of the counter-rotating frame (CRF). In further developments of his reorganisation [10–12] he presented explicitly how the effective AJC Hamiltonian, $\hat{\bar{H}}$, generates dynamical evolution from the initial (absolute) ground state, $|g, 0\rangle$, into a time evolving entangled state in CRF. A similar observation was made independently in [104] while discussing accessible regimes of the QRM. In [104], the author discussed briefly that when the qubit frequency, ω_0, and the mode frequency, ω, are of opposite sign such an interaction will give rise to the AJC Hamiltonian as terms that rotate at frequencies, $|\omega_0 - \omega|$, can be neglected.

In this Thesis, we apply the reformulation developed in [9–12] to study and present a clear visualisation of the AJC dynamics and possible applications in quantum information processing (QIP) as a combination of QIT and quantum computation.

2.2 Entanglement and teleportation

Quantum entanglement is a fundamental resource in quantum information processing such as quantum cryptography [61], quantum computation [57] and quantum teleportation [59]. For implementation of quantum computation and teleportation the main ingredient is the conditional quantum dynamics, in which one subsystem undergoes a coherent evolution depending on the state of another system.

Quantum teleportation, proposed by Bennett *et al* [59] and experimentally realised by Bouwmeester *et al* [110] and Boschi *et al* [111], is a process to transmit an unknown state to a remote location via a quantum channel aided by some classical communication. Teleportation of entangled states have been suggested for different theoretical schemes; Shi, *et al* [112] showed probabilistic teleportation of two-particle entangled state by pure entangled three-particle state, Lee, H. W. [113] presented a set up for a direct, total teleportation of a single-particle entangled state, Sibasish *et al* [114] investigated the teleportation of the bipartite entangled states through mixture of Bell states, Lee, J. [115] proposed a scheme for entanglement teleportation to incorporate multipartite entanglement of four qubits as a quantum channel. Lu *et al* [116] proposed a scheme of

teleporting a two-particle entangled state and Chimczak *et al* [117] proposed a scheme to teleport an entangled -type three-level atoms via photons.

Recall that if two subsystems are entangled as presented in Sec. 1.8, the whole state vector cannot be separated into a product of the states of the two subsystems. This means that the two subsystems are no longer independent even if they are far spatially separated. A measurement on one subsystem gives information about the other subsystem and provides possibilities of manipulating it [78]. The generation of entangled states for two or more particles is fundamental to demonstrate quantum non-locality [118, 119]. In prior work, two particle entangled states have been realised in both cavity quantum electrodynamics and ion traps; Hagley *et al* [120] prepared pairs of atoms in an entangled state of the Einstein-Podolsky-Rosen (EPR) type by exchange of a single photon between atoms in a high Q cavity, Turchette *et al* [121] used conditional quantum logic transformations to entangle and manipulate the qubits of two trapped ions, specified by Raman processes and sideband transitions and Roos *et al* [122] reported on the programmed generation of arbitrary Bell states of two atomic ions specified by sideband transitions. Recently Omolo, J.A. [11, 12] used polariton and antipolariton qubit state transition operations to entangle qubits which are useful in quantum teleportation as we shall demonstrate in this Thesis. Further, the qubit state transition operators developed in [11, 12], effectively carry out two qubit C-NOT and a single qubit Hadamard quantum logic gate operations, a process useful in Bell state measurement which we shall demonstrate herein. In this approach, despite clarity and ease of interpretation of the well defined qubit state transitions, an excessively large dimensionless coupling ratio, $\frac{\lambda}{\delta}$, is necessary for experimental realisation of the C-NOT gate, since achieving transitions between atomic basis states in an almost resonant atom-field interaction is a prerequisite.

Haroche, S. and Wineland, D.J. in 2012 were jointly awarded a Nobel Prize in Physics for ground-breaking experimental methods that enable measuring and manipulation of individual quantum systems [123]. Wineland, D. trapped electrically charged atoms (ions), controlled and measured them with photons. Haroche, S., took the opposite approach: he controlled and measured trapped photons by sending atoms through a trap.

In 2022 the Nobel Prize in Physics was announced for experiments with entangled photons, establishing the violation of Bell inequalities and pioneering quantum information science (QIS) [124]. Aspect, A., Clauser, J. and Zeilinger, A. emerged the winners. Clauser, J., developed John Bell's ideas, leading to a practical experiment. When he took the measurements, they supported quantum mechanics by clearly violating a Bell inequality. This means that quantum mechanics cannot be replaced by a theory that

uses hidden variables. Some loopholes remained after Clauser's experiment. Aspect, A., developed a setup that closed the important loophole. He was able to switch the measurement settings after an entangled pair had left it's source, so the setting that existed when they were emitted could not affect the result. Using refined tools, Zeilinger, A., used the entangled quantum states, and demonstrated quantum teleportation.

2.3 Geometry of state spaces

The geometry of state spaces is an important subject in quantum theories [125–130] that find applications in diverse branches of contemporary physics as dynamical control of quantum systems [131–136] and quantum information [137], among others. Quantum states cannot always be represented by vectors in a Hilbert space [125]. The most realistic approach uses density operators to represent the state of a quantum system since it is usually prepared in a statistical ensemble of pure states , better than in a given pure state [138]. This situation provides an indication of the geometry involved since the density operator is expressed as a convex combination of orthogonal projectors that map the Hilbert space into a one-dimensional subspace. Using a geometric approach the dynamics of the two-level pure states is reduced to rotations and reflections of the 2-sphere (Bloch sphere) [135]. This condition is useful, as an example, to determine the (classical) magnetic fields that must be applied to a spin-1/2 particle in order to control the time-evolution of its quantum state [133, 134]. For instance the particle can be compelled to evolve cyclically [133, 134] in a process that is known as evolution loop [131].

Entanglement being the main ingredient in quantum information, quantum communication (that includes quantum teleportation and quantum crytography), quantum computers and simulators, analysis of entangled states in a Hilbert space, using specific entanglement measures and Bloch spheres has been done in [139–144]. Independently, n-single qubit Bloch spheres with superimposed correlation axes to geometrically represent each qubit in a bipartite and multipartite system or analysing atom-field interaction in the semi-classical picture is considered. Though accurate, geometric analysis of entanglement and qubit state transitions may prove tedious, in particular, in [140, 141] the entanglement measures they chose vanish not only for product states but also for some entangled states, while in [139] in the case of quantised field, it was only possible to represent bipartite entanglement geometrically in terms of the length of the Bloch vector along the z-axis by tracing out the field system.

In this Thesis, the time-evolving atom-field bipartite qubit state vectors are represented

as density operators and expressed in Pauli matrix basis, with the coefficients making up the Bloch vector. We then applied the entanglement Bloch sphere approach articulated in [145–147] to analyse separability and entanglement in the Bloch sphere picture of (definite) bipartite atom-field states through time evolution of the time-evolving Bloch vector. We fully charaterised the set of separable and entangled states on a single Bloch sphere at different parameter values of sum-frequency $\bar{\delta}$ (AJC) and separately frequency detuning δ (JC). The simplicity of this approach, makes it easy to geometrically analyse requisite fundamental quantum mechanical features during the atom-field interaction. Recall that the Bloch vector has a simple geometry of a vector inside a unit Bloch sphere, whose magnitude indicates the state's purity, and whose rotations are unitary transformations.

2.4 Quantum Hadamard and quantum controlled-NOT (C-NOT) logic gates

In quantum computation as introduced in Sec. 1.7, quantum bits (qubits) [22, 23] are the elementary information carriers. The quantum gates [22, 23, 148] defined therein can manipulate arbitrary multi-partite quantum states [149] including arbitrary superposition of the computational basis states, which are frequently also entangled. Thus the logic gates of quantum computation are considerably more varied than the logic gates of classical computation. In addition, a quantum computer can solve problems exponentially faster than any classical computer [57], since exploiting superposition principle and entanglement allow the computer to manipulate and store more bits of information than a classical computer.

We note here that the JC model has been applied extensively in implementing C-NOT and Hadamard quantum gate operations which together form a universal set for quantum computation [150–152]. Domokos *et al* [153] showed that using induced transitions between dressed states, it is possible to implement a C-NOT gate in which a cavity containing at most one photon is the control qubit and the atom is the target qubit. Later, Vitali, D. *et al* [154] proposed a scheme of implementing a C-NOT gate between two distinct but identical cavities, acting as control and target qubits respectively. By passing an atom prepared initially in ground state consecutively between the two cavities a C-NOT (*cavity → atom*) and a C-NOT (*atom → cavity*) is realised with the respective classical fields. Saif, F. *et al* [155] presented a study of quantum computing by engineering non-local quantum universal gates based on interaction of a two-level atom with two modes of electromagnetic field in high Q superconducting cavity. The two-level atom

acted as the control qubit and the two-mode electromagnetic field served as the target qubit. In this Thesis, we demonstrate a theoretical approach of realising a quantum C-NOT logic gate in the AJC model noting that the important discovery and proof of a conserved excitation number operator of the AJC Hamiltonian [9] and the introduction of the polariton qubit model confirm that the dynamics generated by the AJC Hamiltonian is exactly solvable, as demonstrated in [9–12]. In this approach, we implement a quantum C-NOT gate operation between two cavities defined in a two-dimensional Hilbert space spanned by the state vectors, $|v\rangle_1 = |1_a, 0_b\rangle$, and, $|v\rangle_2 = |0_a, 1_b\rangle$. as target qubits. Here, $|v\rangle_1$, expresses the presence of one photon in mode a, when there is no photon in mode b, and, $|v\rangle_2$, indicates that mode a is in vacuum state and one photon is present in mode b. The control qubit in this respect is a two-level atom. The important difference with the approach used in [155] is the model, i.e., while the initial absolute atom-field ground state, $|g, 0\rangle$, in the AJC interaction is affected by atom-cavity coupling, the ground state, $|g, 0\rangle$, in the JC model [155] is not affected by atom-cavity coupling. A similar result was determined independently in [12]. Further, with precise choice of interaction time in the AJC qubit state transition operations defined in the AJC qubit sub-space spanned by normalised but non-orthogonal basics qubit state vectors [11, 12], C-NOT gate operations are realised between the two cavities.

Vitali, D. *et al* [154] showed that one qubit operations can be implemented on qubits represented by two internal atomic states because it amounts to applying suitable Rabi pulses. He demonstrated that the most practical solution on implementing one qubit operations on two Fock states is sending the atoms through the cavity. If the atom inside the cavity undergoes a $\frac{\pi}{2}$ pulse one realises a Hadamard-phase gate. Saif, F. *et al* [155] also showed that it is possible to realise Hadamard operation by a controlled interaction between a two-mode high Q electromagnetic cavity field and a two-level atom. In this approach, the two-level atom is the control qubit, whereas the target qubit is made up of two modes of cavity field. Precision of the gate operations is realised by accurate selection of interaction times of the two-level atom with the cavity mode. In this Thesis, we show that Hadamard operation in the AJC interaction is possible for a specified initial atomic state by setting a specific sum frequency and photon number in the AJC qubit state transition operation [11, 12], noting that the interaction components of the AJC Hamiltonian generates state transitions.

2.5 Non-classicality of both field states and atomic states

Non-classicality of both field and atomic states [156–158] is a fundamental quantum feature and crucial resource, which is indispensable in quantum information tasks. For optical fields, the Glauber coherent states and mixture of them [44] are conventionally identified as classical states in quantum optics, while the Fock states, squeezed states, cat states are regarded as non-classical ones [29, 159]. Similarly for atomic spin systems, the atomic coherent states and their mixtures are conventionally regarded by some authors as classical, while all other states are non-classical [160, 161]. Various measures and witnesses of non-classicality for atomic systems have been proposed, including distance based non-classicality [162, 163], non-classicality witness based on the atomic quadrature measurements and expectations [164, 165] and non-classicality quantifier based on Wigner-Yanase skew information [166].

In a broad sense, the notion of non-clssicality (quantumness) goes beyond the the mentioned conventions above. Different research articles provide different interpretations dependent on the context. From mathematical and physical point of view, the qubit (a two-level system e.g. a two-level atom) is a quantum object fundamentally different from the classical bit, and the non-classical (quantum) features in spin-$\frac{1}{2}$ states are a fundamental resource in quantum technologies. Consequently in this Thesis work, considering the mathematical and physical interpretation of non-classicality of the atomic states, we strictly regard a two-level atom as a fully quantum object and study the nature of the field statistics by applying the Mandel Q-parameter [29, 159], to determine the extent in which the field is sub-Poissonian. Remember that the Mandel Q-parameter measures the deviation of photon statistics from the Poissonian statistics $Q = 0$. A positive value of the Mandel Q-parameter $Q > 0$ specifies a classical field, i.e., bunched, while a negative value of the Mandel Q-parameter $Q < 0$ specifies a fully quantised field, i.e, anti-bunched. If an initial coherent and separately a squeezed coherent state is anti-bunched in the dynamics generated by the AJC Hamiltonian when a two-level atom couples to a field mode, then we quantify the interaction as non-classical, else, classical. This means, non-classicality captures the quantum aspect of the qubit and field states during their interaction.

CHAPTER 3
METHODOLOGY

3.1 The model

The quantum Rabi model of a quantised electromagnetic field mode interacting with a two-level atom is generated by the Hamiltonian [9]

$$\hat{H}_R = \frac{1}{2}\hbar\omega(\hat{a}^\dagger\hat{a} + \hat{a}\hat{a}^\dagger) + \hbar\omega_0\hat{s}_z + \hbar\lambda(\hat{a} + \hat{a}^\dagger)(\hat{s}_+ + \hat{s}_-) \qquad (3.1.1)$$

noting that the free field mode Hamiltonian is expressed in normal and anti-normal order form, $\frac{1}{2}\hbar\omega(\hat{a}^\dagger\hat{a} + \hat{a}\hat{a}^\dagger)$. Here, ω , $\hat{a}$, $\hat{a}^\dagger$ are quantised field mode angular frequency, annihilation and creation operators, while ω_0, $\hat{s}_z$, $\hat{s}_+$, $\hat{s}_-$ are atomic state transition angular frequency and operators. The Rabi Hamiltonian in Eq. (3.1.1) is expressed in a symmetrised two-component form [9, 11, 12]

$$\hat{H}_R = \frac{1}{2}(\hat{H} + \hat{\overline{H}}) \qquad (3.1.2)$$

where, $\hat{H}$, is the standard JC Hamiltonian interpreted as a polariton qubit Hamiltonian expressed in the form [9]

$$\begin{aligned}
\hat{H} &= \hbar\omega\hat{N} + 2\hbar\lambda\hat{A} - \frac{1}{2}\hbar\omega \quad ; \quad \hat{N} = \hat{a}^\dagger\hat{a} + \hat{s}_+\hat{s}_- \\
\hat{A} &= \alpha\hat{s}_z + \hat{a}\hat{s}_+ + \hat{a}^\dagger\hat{s}_- \quad ; \quad \alpha = \frac{\omega_0 - \omega}{2\lambda}
\end{aligned} \qquad (3.1.3)$$

while, $\hat{\overline{H}}$, is the AJC Hamiltonian interpreted as an anti-polariton qubit Hamiltonian in the form [9]

$$\begin{aligned}
\hat{\overline{H}} &= \hbar\omega\hat{\overline{N}} + 2\hbar\lambda\hat{\overline{A}} - \frac{1}{2}\hbar\omega \quad ; \quad \hat{\overline{N}} = \hat{a}\hat{a}^\dagger + \hat{s}_-\hat{s}_+ \quad ; \\
\hat{\overline{A}} &= \overline{\alpha}\hat{s}_z + \hat{a}\hat{s}_- + \hat{a}^\dagger\hat{s}_+ \quad ; \quad \overline{\alpha} = \frac{\omega_0 + \omega}{2\lambda} \ .
\end{aligned} \qquad (3.1.4)$$

In Eqs. (3.1.3) and (3.1.4), $\hat{N}$, $\hat{\overline{N}}$ and $\hat{A}$, $\hat{\overline{A}}$ are the respective polariton and anti-polariton qubit conserved excitation numbers and state transition operators.

In Sec. 3.2 we provide the general dynamics of the AJC model when a two-level atom

interacts with a field-mode of frequency, $-\omega$, in Fock state introduced in Sec. 1.5.1 of this Thesis. To be exact, in Sec. 3.2.1 we present the method applied in this Thesis in analysis of Rabi oscillations between basic stationary qubit state vectors in the Bloch sphere picture during the AJC interactions and in Sec. 4.1.2 how to determine entanglement properties, teleportation of maximally entangled two-atom states and dynamical evolution of entanglement is proffered. Further, in Sec. 3.3 the method applied here in analysis of interaction properties during the AJC interaction of a two-level atom and a field-mode in an initial coherent state introduced in Sec. 1.5.2 is provided. More precisely, we introduce explicitly purity of states and atomic population inversion in Sec. 3.3.1, degree of entanglement in Sec. 3.3.2 and finally in Sec. 3.3.3, how to determine the nature of photon statistics during the AJC atom-field interaction. We conclude in Sec. 3.4 by presenting the approach adopted here in studying the dynamical properties during the AJC process when a two-level atom interacts with a field mode initially in a squeezed coherent state introduced in this work in Sec. 1.5.3. Just to highlight, in Sec. 3.4.1 how to analyse photon statistics during the atom-field quantum systems interaction is presented and we close in Sec. 3.4.2 by showing clear steps applied in this Thesis in studying photon statistics, atomic population inversion and degree of entanglement.

3.2 AJC dynamics

Let us now consider the AJC dynamics. It was shown explicitly in [9] that in the AJC interaction process, only an atom in an initial ground state, $|g\rangle$, entering a field mode in Fock state in an initial vacuum state, $n = 0$, couples to the anti-rotating (CR) negative frequency field mode. An atom in an initial excited state, $|e\rangle$, will not couple ($\lambda = 0$) to the CR field mode in an initial vacuum state, $n = 0$, and will just propagate as a free wave.

Recollecting that quantum gates are reversible, interaction of an atom in excited state, $|e\rangle$, with a single-photon field mode, $|1\rangle$, during the AJC process will be requisite in the implementation of a single qubit Walsh-Hadamard and two qubit C-NOT quantum gate processes. We now consider the general case where the atom is initially in ground or excited state $|g\rangle$, $|e\rangle$ and the field mode in number state, $|n\rangle$, $n = 0, 1, 2, 3, ...$. The initial atom-field qubit states are, $|\psi_{gn}\rangle = |g, n\rangle$; $|\psi_{en}\rangle = |e, n\rangle$. Applying separately the state transition operator, $\widehat{\overline{A}}$, from Eq. (3.1.4) to the initial atom-field n-photon excited state vector, $|\psi_{en}\rangle$, and initial n-photon ground state vector, $|\psi_{gn}\rangle$, the basic qubit state

vectors satisfy the respective qubit state algebraic operations [12]

$$\hat{\overline{A}}|\psi_{en}\rangle = \overline{A}_{en}|\overline{\phi}_{en}\rangle \quad ; \quad \hat{\overline{A}}|\overline{\phi}_{en}\rangle = \overline{A}_{en}|\psi_{en}\rangle,$$
$$\hat{\overline{A}}|\psi_{gn}\rangle = \overline{A}_{gn}|\overline{\phi}_{gn}\rangle \quad ; \quad \hat{\overline{A}}|\overline{\phi}_{gn}\rangle = \overline{A}_{gn}|\psi_{gn}\rangle. \tag{3.2.1}$$

In Eq. (3.2.1)

$$|\psi_{en}\rangle = |e,n\rangle \quad ; \quad |\psi_{gn}\rangle = |g,n\rangle \tag{3.2.2}$$

are the initial uncoupled qubit state vectors while

$$|\overline{\phi}_{en}\rangle = \overline{c}_{en}|e,n\rangle + \overline{s}_{en}|g,n-1\rangle \quad ; \quad |\overline{\phi}_{gn}\rangle = -\overline{c}_{gn}|g,n\rangle + \overline{s}_{gn}|e,n+1\rangle \tag{3.2.3}$$

are the transition coupled qubit state vectors with dimensionless interaction parameters, $\overline{c}_{en}$, $\overline{c}_{gn}$, $\overline{s}_{en}$, $\overline{s}_{gn}$, and Rabi frequencies, $\overline{R}_{en}$, $\overline{R}_{gn}$, defined as

$$\overline{c}_{en} = \frac{\overline{\delta}}{2\overline{R}_{en}} \quad ; \quad \overline{s}_{en} = \frac{2\lambda\sqrt{n}}{\overline{R}_{en}} \quad ; \quad \overline{R}_{en} = 2\lambda\overline{A}_{en} \quad ; \quad \overline{A}_{en} = \sqrt{n + \frac{\overline{\delta}^2}{16\lambda^2}} \quad ,$$

$$\overline{c}_{gn} = \frac{\overline{\delta}}{2\overline{R}_{gn}} \quad ; \quad \overline{s}_{gn} = \frac{2\lambda\sqrt{n+1}}{\overline{R}_{gn}} \quad ; \quad \overline{R}_{gn} = 2\lambda\overline{A}_{gn} \quad ; \quad \overline{A}_{gn} = \sqrt{(n+1) + \frac{\overline{\delta}^2}{16\lambda^2}} \tag{3.2.4}$$

where we have introduced sum frequency, $\overline{\delta} = \omega_0 + \omega$, to redefine $\overline{\alpha}$ in Eq. (3.1.4).

In the AJC qubit computational subspace spanned by normalised but non-orthogonal basic qubit state vectors, $|\psi_{en}\rangle$, $|\overline{\phi}_{en}\rangle$, and, $|\psi_{gn}\rangle$, $|\overline{\phi}_{gn}\rangle$, respectively, the basic qubit normalised state transition operators, $\hat{\overline{\varepsilon}}_e$, $\hat{\overline{\varepsilon}}_g$, and identity operators, $\hat{\overline{I}}_e$, $\hat{\overline{I}}_g$, are introduced according to the definitions [12]

$$\hat{\overline{\varepsilon}}_e = \frac{\hat{\overline{A}}}{\overline{A}_{en}} \quad ; \quad \hat{\overline{I}}_e = \frac{\hat{\overline{A}}^2}{\overline{A}_{en}^2} \quad \Rightarrow \quad \hat{\overline{I}}_e = \hat{\overline{\varepsilon}}_e^2 \quad ,$$

$$\hat{\overline{\varepsilon}}_g = \frac{\hat{\overline{A}}}{\overline{A}_{gn}} \quad ; \quad \hat{\overline{I}}_g = \frac{\hat{\overline{A}}^2}{\overline{A}_{gn}^2} \quad \Rightarrow \quad \hat{\overline{I}}_g = \hat{\overline{\varepsilon}}_g^2 \tag{3.2.5}$$

with respective algebraic properties

$$e^{i\varphi\hat{\bar{\varepsilon}}_e} \;=\; \cos(\varphi)\hat{\bar{I}}_e + i\sin(\varphi)\hat{\bar{\varepsilon}}_e \quad ; \quad e^{-i\theta\hat{\bar{\varepsilon}}_g} = \cos(\theta)\hat{\bar{I}}_g - i\sin(\theta)\hat{\bar{\varepsilon}}_g$$

$$(3.2.6)$$

which are useful in evaluating time evolution operators.

Substituting the operators $\hat{\bar{\varepsilon}}_e$, $\hat{\bar{I}}_e$ and $\hat{\bar{\varepsilon}}_g$, $\hat{\bar{I}}_g$ in Eq. (3.2.5) into Eq. (3.2.1) generates the respective basic qubit state transition algebraic operations

$$\hat{\bar{\varepsilon}}_e|\psi_{en}\rangle \;=\; |\overline{\phi}_{en}\rangle \quad ; \quad \hat{\bar{\varepsilon}}_e|\overline{\phi}_{en}\rangle = |\psi_{en}\rangle \quad ; \quad \hat{\bar{I}}_e|\psi_{en}\rangle = |\psi_{en}\rangle \quad ; \quad \hat{\bar{I}}_e|\overline{\phi}_{en}\rangle = |\overline{\phi}_{en}\rangle \quad ;$$

$$\hat{\bar{\varepsilon}}_g|\psi_{gn}\rangle \;=\; |\overline{\phi}_{gn}\rangle \quad ; \quad \hat{\bar{\varepsilon}}|\overline{\phi}_{gn}\rangle = |\psi_{gn}\rangle \quad ; \quad \hat{\bar{I}}_g|\psi_{gn}\rangle = |\psi_{gn}\rangle \quad ; \quad \hat{\bar{I}}_g|\overline{\phi}_{gn}\rangle = |\overline{\phi}_{gn}\rangle \; .$$

$$(3.2.7)$$

The respective AJC qubit Hamiltonian, $\hat{\overline{H}}_e$, $\hat{\overline{H}}_g$, defined within the qubit computational subspace spanned by the respective basic qubit state vectors, $|\psi_{en}\rangle$, $|\overline{\phi}_{en}\rangle$, and, $|\psi_{gn}\rangle$, $|\overline{\phi}_{gn}\rangle$, specified for initial atomic basis states, $|e\rangle$, $|g\rangle$, in n-photon field modes respectively are then expressed in terms of the basic qubit normalised state transition operators, $\hat{\bar{\varepsilon}}_e$, $\hat{\bar{\varepsilon}}_g$, and identity operators, $\hat{\bar{I}}_e$, $\hat{\bar{I}}_g$, in the forms [12]

$$\hat{\overline{H}}_e \;=\; \hbar\omega\left(n+\frac{1}{2}\right)\hat{\bar{I}}_e + \hbar\overline{R}_{en}\hat{\bar{\varepsilon}}_e \quad ; \quad \hat{\overline{H}}_g = \hbar\omega\left(n+\frac{3}{2}\right)\hat{\bar{I}}_g + \hbar\overline{R}_{gn}\hat{\bar{\varepsilon}}_g \; .$$

$$(3.2.8)$$

Considering now an atom in an initial ground state, $|g\rangle$, in an n-photon field mode, $|n\rangle$, the initial atom-field state as presented earlier and in Eq. (3.2.2) is, $|\psi_{gn}\rangle = |g,n\rangle$. We use the form of the AJC Hamiltonian, $\hat{\overline{H}}_g$, in Eq. (3.2.8) to determine the general time evolving state vector describing Rabi oscillations in the AJC dynamics in Sec. 3.2.1 below.

3.2.1 Rabi oscillations between the basic AJC qubit state vectors $|\psi_{gn}\rangle$ and $|\overline{\phi}_{gn}\rangle$

The general dynamics generated by the AJC Hamiltonian, $\hat{\overline{H}}_g$, in Eq. (3.2.8) specified for an initial atom-field qubit state, $|g,n\rangle$, defining an atomic ground state in n-photon field, is described by a time evolving AJC qubit state vector, $|\overline{\Psi}_{gn}(t)\rangle$, obtained from the

time-dependent Schrödinger equation in the form [12]

$$|\overline{\Psi}_{gn}(t)\rangle = \hat{\overline{U}}_g(t)|\psi_{gn}\rangle \quad ; \quad \hat{\overline{U}}_g(t) = e^{-\frac{i}{\hbar}\hat{\overline{H}}_g t} \tag{3.2.9}$$

where, $\hat{\overline{U}}_g(t)$, is the time evolution operator. Substituting $\hat{\overline{H}}_g$ from Eq. (3.2.8) into Eq. (3.2.9) and applying appropriate algebraic properties [12], we use the algebraic property relation, $e^{-i\theta\hat{\overline{\varepsilon}}_g}$, on exponentiation of $\hat{\overline{\varepsilon}}_g$ given in Eq. (3.2.6) to express the time evolution operator in its final form

$$\hat{\overline{U}}_g(t) = e^{-i\omega t(n+\frac{3}{2})}\left\{\cos(\overline{R}_{gn}t)\hat{\overline{I}}_g - i\sin(\overline{R}_{gn}t)\hat{\overline{\varepsilon}}_g\right\} \ , \tag{3.2.10}$$

which we substitute into equation Eq. (3.2.9) and use the qubit state transition operations, $\hat{\overline{\varepsilon}}_g|\psi_{gn}\rangle = |\overline{\phi}_{gn}\rangle \quad ; \quad \hat{\overline{\varepsilon}}|\overline{\phi}_{gn}\rangle = |\psi_{gn}\rangle \quad ; \quad \hat{\overline{I}}_g|\psi_{gn}\rangle = |\psi_{gn}\rangle \quad ; \quad \hat{\overline{I}}_g|\overline{\phi}_{gn}\rangle = |\overline{\phi}_{gn}\rangle$, in Eq. (3.2.7) to obtain the time-evolving AJC qubit state vector for an initial atomic ground state in n-photon field in the form

$$|\overline{\Psi}_{gn}(t)\rangle = e^{-i\omega t(n+\frac{3}{2})}\left\{\cos(\overline{R}_{gn}t)|\psi_{gn}\rangle - i\sin(\overline{R}_{gn}t)|\overline{\phi}_{gn}\rangle\right\} \ . \tag{3.2.11}$$

This time evolving state vector describes Rabi oscillations between the basic qubit states, $|\psi_{gn}\rangle$ and $|\overline{\phi}_{gn}\rangle$, at Rabi frequency, $\overline{R}_{gn}$.

In order to determine the length of the AJC Bloch vector associated with the state vector in Eq. (3.2.11), we introduce the density operator

$$\hat{\overline{\rho}}_{gn}(t) = |\overline{\Psi}_{gn}(t)\rangle\langle\overline{\Psi}_{gn}(t)| \tag{3.2.12a}$$

which we expand to obtain

$$\begin{aligned}\hat{\overline{\rho}}_{gn}(t) &= \cos^2(\overline{R}_{gn}t)|\psi_{gn}\rangle\langle\psi_{gn}| + \frac{i}{2}\sin(2\overline{R}_{gn}t)|\psi_{gn}\rangle\langle\overline{\phi}_{gn}| - \frac{i}{2}\sin(2\overline{R}_{gn}t)|\overline{\phi}_{gn}\rangle\langle\psi_{gn}| \\ &+ \sin^2(\overline{R}_{gn}t)|\overline{\phi}_{gn}\rangle\langle\overline{\phi}_{gn}| \ .\end{aligned}$$
$$\tag{3.2.12b}$$

Defining the coefficients of the projectors in Eq. (3.2.12b) as

$$\begin{aligned}\overline{\rho}_{gn}^{11}(t) &= \cos^2(\overline{R}_{gn}t) \quad ; \quad \overline{\rho}_{gn}^{12}(t) = \frac{i}{2}\sin(2\overline{R}_{gn}t) \quad ; \\ \overline{\rho}_{gn}^{21}(t) &= -\frac{i}{2}\sin(2\overline{R}_{gn}t) \quad ; \quad \overline{\rho}_{gn}^{22}(t) = \sin^2(\overline{R}_{gn}t)\end{aligned}$$
$$\tag{3.2.12c}$$

we interpret the coefficients in Eq. (3.2.12c) as elements of a 2×2 density matrix, $\hat{\bar{\rho}}_{gn}(t)$, expressed in terms of standard Pauli operator matrices I, σ_x, σ_y and σ_z in Eq. (1.3.6) as

$$\hat{\bar{\rho}}_{gn}(t) = \begin{pmatrix} \bar{\rho}_{gn}^{11}(t) & \bar{\rho}_{gn}^{12}(t) \\ \bar{\rho}_{gn}^{21}(t) & \bar{\rho}_{gn}^{22}(t) \end{pmatrix} = \frac{1}{2}\left(I + \vec{\bar{\rho}}_{gn}(t) \cdot \vec{\sigma}\right) \tag{3.2.12d}$$

where we recall from Sec. 1.3 $\vec{\sigma} = (\sigma_x, \sigma_y, \sigma_z)$ is the Pauli matrix vector and we have introduced the time-evolving AJC Bloch vector, $\vec{\bar{\rho}}_{gn}(t)$, obtained in the form

$$\vec{\bar{\rho}}_{gn}(t) = \left(\bar{\rho}_{gn}^x(t),\, \bar{\rho}_{gn}^y(t),\, \bar{\rho}_{gn}^z(t)\right) \tag{3.2.12e}$$

with components defined as

$$
\begin{aligned}
\bar{\rho}_{gn}^x(t) &= tr(\hat{\bar{\rho}}_{gn}(t)\sigma_x) = tr\begin{pmatrix} \frac{i}{2}\sin(2\overline{R}_{gn}t) & \cos^2(\overline{R}_{gn}t) \\ \sin^2(\overline{R}_{gn}t) & -\frac{i}{2}\sin(2\overline{R}_{gn}t) \end{pmatrix} = 0 \quad ; \\
\bar{\rho}_{gn}^y(t) &= tr(\hat{\bar{\rho}}_{gn}(t)\sigma_y) = tr\begin{pmatrix} -\frac{1}{2}\sin(2\overline{R}_{gn}t) & -i\cos^2(\overline{R}_{gn}t) \\ i\sin^2(\overline{R}_{gn}t) & -\frac{1}{2}\sin(2\overline{R}_{gn}t) \end{pmatrix} = -\sin(2\overline{R}_{gn}t) \quad ; \\
\bar{\rho}_{gn}^z(t) &= tr(\hat{\bar{\rho}}_{gn}(t)\sigma_z) = tr\begin{pmatrix} \cos^2(\overline{R}_{gn}t) & -\frac{i}{2}\sin(2\overline{R}_{gn}t) \\ -\frac{i}{2}\sin(2\overline{R}_{gn}t) & -\sin^2(\overline{R}_{gn}t) \end{pmatrix} = \cos(2\overline{R}_{gn}t) \quad .
\end{aligned}
$$

$$\tag{3.2.12f}$$

The AJC Bloch vector in Eq. (3.2.12e) takes the explicit form

$$\vec{\bar{\rho}}_{gn}(t) = \left(0,\, -\sin(2\overline{R}_{gn}t),\, \cos(2\overline{R}_{gn}t)\right) \tag{3.2.12g}$$

which has unit length obtained easily as

$$|\vec{\bar{\rho}}_{gn}(t)| = 1 . \tag{3.2.12h}$$

The property that the AJC Bloch vector, $\vec{\bar{\rho}}_{gn}(t)$, is of unit length shows that the general time evolving AJC state vector, $|\overline{\Psi}_{gn}(t)\rangle$, in Eq. (3.2.11) is a pure state.

The AJC Bloch vector, $\vec{\bar{\rho}}_{gn}(t)$, in effect describes the geometric configuration of states in the Bloch sphere picture, where we adopt class 4 Bloch-sphere entanglement of a quantum rank-2 bipartite state, [145, 147] to bring a clear visualisation of this interaction in comparison to the familiar JC interaction process in standard literature.

3.2.2 Entanglement properties, teleportation of a two-atom singlet state and dynamical evolution of entanglement generated in the AJC interaction

In this section we show how to apply the von Neumann entropy measure in analysis of entanglement properties and dynamical evolution of entanglement during this interaction. We close by providing the algorithm adopted in carrying out teleportation similar to the JC case in the literature, quantum C-NOT and Hadamard gates.

3.2.2.1 Entanglement properties of AJC qubit states

The von Neumann entropy introduced in Sec. (1.8.2) is a measure of entanglement in a pure bipartite system of qubits similar to concurrence in the same section. We re-write explicitly the von Neumann entropy of a quantum state, $\hat{\rho}_{ab}$, defined in Eq. (1.8.8) as

$$S(\hat{\rho}_{ab}) = -tr\left(\hat{\rho}_{ab} \log_d \hat{\rho}_{ab}\right) = -\sum_i \lambda_i \log_d \lambda_i \qquad (3.2.13)$$

where the logarithm is taken to base d, d being the dimension of the Hilbert space containing $\hat{\rho}_{ab}$ and $\lambda_i s$ are the eigenvalues of $\hat{\rho}_{ab}$. As presented in Sec. 1.8.2, $0 \leqslant S(\hat{\rho}_{ab}) \leqslant 1$, where $S(\hat{\rho}_{ab}) = 0$ if and only if $\hat{\rho}_{ab}$ is a pure state.

Further as stated in Sec. 1.8.2, the von Neumann entropy of the reduced density matrices of a bipartite pure state, $\hat{\rho}_{ab} = |\psi_{ab}\rangle\langle\psi_{ab}|$, is a good and convenient entanglement measure, $E(\hat{\rho}_{ab})$, defined in Eq. (1.8.6). We re-write explicitly the entanglement measure in Eq. (1.8.6) defined as the entropy of either of the quantum subsystem a, b as

$$\begin{aligned} E(\hat{\rho}_{ab}) &= -tr(\hat{\rho}_a \log_2 \hat{\rho}_a) = -tr(\hat{\rho}_b \log_2 \hat{\rho}_b) = -\sum_i \eta_i \log_2 \eta_i \quad ; \\ \hat{\rho}_a &= tr_b(\hat{\rho}_{ab}) \quad ; \quad \hat{\rho}_b = tr_a(\hat{\rho}_{ab}) \ , \end{aligned}$$
$$(3.2.14)$$

where for all states we have $0 \leq E(\hat{\rho}_{ab}) \leq 1$ and $\eta_i s$ are the eigenvalues of $\hat{\rho}_j$, $j : a(b)$. Here the limit 0 is achieved in a pure state defined as a product $|\psi_{ab}\rangle = |\psi_a\rangle \otimes |\psi_b\rangle$ and 1 is achieved for a maximally entangled states, noting in this case the reduced density matrices are maximally mixed states.

The AJC stationary initial qubit state vector, $|\psi_{gn}\rangle$, is defined in Eq. (3.2.2) in the form $(n = 0, 1, 2, ...)$

$$|\psi_{gn}\rangle = |g, n\rangle = |g\rangle \otimes |n\rangle \ . \qquad (3.2.2')$$

In order to quantify the AJC initial qubit state vector as pure or mixed, entangled or product state we first determine the density operator $\hat{\rho}_{gn}$ of $|\psi_{gn}\rangle$ in Eq. (3.2.2) by substituting $|\psi_{gn}\rangle$ into Eq. (1.3.1) to obtain

$$\hat{\rho}_{gn} = |g,n\rangle\langle g,n| \ . \tag{3.2.15a}$$

We then determine the atom (a), field (f) reduced density operators $\hat{\rho}_{a(f)}$ of $\hat{\rho}_{gn}$ in Eq. (3.2.15a) by tracing over the field (atom) states respectively to obtain

$$\hat{\rho}_{a(f)} = tr_{f(a)}(\hat{\rho}_{gn}) \Rightarrow \hat{\rho}_a = |g\rangle\langle g| \quad ; \quad \hat{\rho}_f = |n\rangle\langle n| \ . \tag{3.2.15b}$$

To quantify the initial atom-field state as pure or mixed, we substitute Eq. (3.2.15b) into Eq. (1.3.15) and separately Eq. (3.2.14). In this case, the pure initial state corresponds to $tr(\hat{\rho}_{a(f)}^2) = 1$, $E(\hat{\rho}_{gn}) = 0$. Recall that in a bipartite system of qubits as presented earlier in Sec. 1.3.1, for a quantum state $\hat{\rho}_{ab}$, $tr(\hat{\rho}_{a(b)}^2) \leqslant 1$ quantifies a quantum state as pure or mixed. This means that for a pure state $tr(\hat{\rho}_{a(b)}^2) = 1$, $E(\hat{\rho}_{ab}) = 0$. That of a mixed state conforms to $tr(\hat{\rho}_{a(b)}^2) = \frac{1}{n}$, $0 < E(\hat{\rho}_{ab}) < 1$ where for a maximally mixed state $n = 2$, $E(\hat{\rho}_{ab}) = 1$.

We then proceed to analyse entanglement properties of the AJC stationary transition qubit state vectors $|\overline{\phi}_{gn}\rangle$. The AJC stationary transition qubit state vector $|\overline{\phi}_{gn}\rangle$ is defined in Eq. (3.2.3). In order to quantify if it is a pure or mixed state we first determine its density operator by substituting $|\overline{\phi}_{gn}\rangle$ in Eq. (3.2.3) into Eq. (1.3.1). The density operator takes the form

$$\begin{aligned} \hat{\overline{\rho}}_{gn} &= |\overline{\phi}_{gn}\rangle\langle\overline{\phi}_{gn}| \\ &= |\overline{c}_{gn}|^2 \, |g,n\rangle\langle g,n| - \overline{c}_{gn}\overline{s}_{gn}^* |g,n\rangle\langle e,n+1| - \overline{c}_{gn}^*\overline{s}_{gn}|e,n+1\rangle\langle g,n| \\ &\quad + |\overline{s}_{gn}|^2 \, |e,n+1\rangle\langle e,n+1| \ . \end{aligned} \tag{3.2.16a}$$

The density operator in Eq. (3.2.16a) has an expanded basis
$\{|e,n\rangle \ , \ |e,n+1\rangle \ , \ |g,n\rangle \ , \ |g,n+1\rangle\}$. We sum up the projectors (matrices)
$|\overline{c}_{gn}|^2 \, |g,n\rangle\langle g,n| \ , \ -\overline{c}_{gn}\overline{s}_{gn}^*|g,n\rangle\langle e,n+1| \ , \ -\overline{c}_{gn}^*\overline{s}_{gn}|e,n+1\rangle\langle g,n| \ , \ |\overline{s}_{gn}|^2 \, |e,n+1\rangle\langle e,n+1|$
where $|\overline{c}_{gn}|^2 \ , \ \overline{c}_{gn}\overline{s}_{gn}^* \ , \ \overline{c}_{gn}^*\overline{s}_{gn} \ , \ |\overline{s}_{gn}|^2$ represent the respective probabilities in which the transition stationary state $|\overline{\phi}_{gn}\rangle$ is projected by the respective projectors in $\hat{\overline{\rho}}_{gn}$.

As an illustration, in the case of an initial vacuum field, $|0\rangle$, the projector $|\bar{c}_{gn}|^2|g,n\rangle\langle g,n|$ in Eq. (3.2.16a) takes the form, $|\bar{c}_{g0}|^2|g,0\rangle\langle g,0|$, which we express as a matrix, by first obtaining the vector form of $|g,0\rangle$ through tensor product, according to

$$|g\rangle \otimes |0\rangle = \begin{pmatrix} 0 \\ 1 \end{pmatrix} \otimes \begin{pmatrix} 1 \\ 0 \end{pmatrix} = \begin{pmatrix} 0 \\ 0 \\ 1 \\ 0 \end{pmatrix}$$

and proceed to evaluate the outer product

$$|\bar{c}_{g0}|^2|g,0\rangle\langle g,0| = |\bar{c}_{g0}|^2 \begin{pmatrix} 0 \\ 0 \\ 1 \\ 0 \end{pmatrix} \begin{pmatrix} 0 & 0 & 1 & 0 \end{pmatrix} = |\bar{c}_{g0}|^2 \begin{pmatrix} 0 & 0 & 0 & 0 \\ 0 & 0 & 0 & 0 \\ 0 & 0 & 1 & 0 \\ 0 & 0 & 0 & 0 \end{pmatrix}$$

which is a 4×4 projector matrix.

The final matrix representation of $\hat{\bar{\rho}}_{gn}$, specified in Eq. (3.2.16a), is then expressed in the form

$$\hat{\bar{\rho}}_{gn} = \begin{pmatrix} 0 & 0 & 0 & 0 \\ 0 & |\bar{s}_{gn}|^2 & -\bar{c}_{gn}^*\bar{s}_{gn} & 0 \\ 0 & -\bar{c}_{gn}\bar{s}_{gn}^* & |\bar{c}_{gn}|^2 & 0 \\ 0 & 0 & 0 & 0 \end{pmatrix} \tag{3.2.16b}$$

to evaluate its eigenvalues $\lambda_i\,|_{i=1,2,3,4}$ determined at a value of sum frequency $\bar{\delta} = \delta + 2\omega$ (easily obtained according to; $\bar{\delta} = \omega_0 + \omega = \omega_0 + \omega + (\omega - \omega) = \delta + 2\omega$; $\delta = \omega_0 - \omega$). While noting the definitions of interaction parameters $\bar{c}_{gn}$, $\bar{s}_{gn}$ and Rabi frequency $\bar{R}_{gn}$ in Eq. (3.2.4) we obtain the eigenvalues

$$\{\lambda_1, \lambda_2, \lambda_3, \lambda_4\} = \left\{(|\bar{c}_{gn}|^2 + |\bar{s}_{gn}|^2), 0, 0, 0\right\} = \{1, 0, 0, 0\} \quad ; \quad |\bar{c}_{gn}|^2 + |\bar{s}_{gn}|^2 = 1 \ . \tag{3.2.16c}$$

We substitute the resulting eigenvalues $\lambda_i\,|_{i=1,2,3,4}$ in Eq. (3.2.16c) into Eq. (3.2.13) to

quantify purity of the stationary transition qubit state $|\overline{\phi}_{gn}\rangle$ according to

$$
\begin{aligned}
S(\hat{\overline{\rho}}_{gn}) &= -\lambda_1 \log_2 \lambda_1 - \lambda_2 \log_2 \lambda_2 - \lambda_3 \log_2 \lambda_3 - \lambda_4 \log_2 \lambda_4 \\
&= -1 \log_2 1 - 0 \log_2 0 - 0 \log_2 0 - 0 \log_2 0 \\
&= 0 \ .
\end{aligned}
\tag{3.2.16d}
$$

Recollecting that $S(\hat{\overline{\rho}}_{gn})$ values should range in the closed interval $[0,1]$, where 0 quantifies a pure state and 1 a maximally mixed state, else if $0 < S(\hat{\overline{\rho}}_{gn}) < 1$ partially mixed, the von Neumann entropy, $S(\hat{\overline{\rho}}_{gn})$, in Eq. (3.2.16d) of the bipartite transition qubit state assumes $S(\hat{\overline{\rho}}_{gn}) = 0$, quantifying $|\overline{\phi}_{gn}\rangle$ as a pure state.

Further as an additional measure, to quantify the stationary transition qubit state $|\overline{\phi}_{gn}\rangle$ as a product, entangled or maximally entangled we first determine the reduced density operators $\hat{\overline{\rho}}_{a(f)}$ of the atom (field) states by tracing $\hat{\overline{\rho}}_{gn}$ in Eq. (3.2.16a) over the field (atom) states respectively according to Eq. (3.2.15b)

$$
\hat{\overline{\rho}}_{a(f)} = tr_{f(a)}(\hat{\overline{\rho}}_{gn})
\tag{3.2.15b'}
$$

to obtain

$$
\begin{aligned}
\hat{\overline{\rho}}_a &= tr_f(\hat{\overline{\rho}}_{gn}) = |\overline{c}_{gn}|^2 |g\rangle\langle g| \ tr_f |n\rangle\langle n| - \overline{c}_{gn}\overline{s}_{gn}^* |g\rangle\langle e| \ tr_f |n\rangle\langle n+1| \\
&\quad - \overline{c}_{gn}^* \overline{s}_{gn} |e\rangle\langle g| \ tr_f |n+1\rangle\langle n| + |\overline{s}_{gn}|^2 |e\rangle\langle e| \ tr_f |n+1\rangle\langle n+1| \\
&= |\overline{c}_{gn}|^2 |g\rangle\langle g|\langle n|n\rangle - \overline{c}_{gn}\overline{s}_{gn}^* |g\rangle\langle e|\langle n+1|n\rangle \\
&\quad - \overline{c}_{gn}^* \overline{s}_{gn} |e\rangle\langle g|\langle n|n+1\rangle + |\overline{s}_{gn}|^2 |e\rangle\langle e|\langle n+1|n+1\rangle \\
&= |\overline{c}_{gn}|^2 |g\rangle\langle g| + |\overline{s}_{gn}|^2 |e\rangle\langle e| \quad ; \quad \delta_{ij} = \begin{cases} 1, & \text{if } i = j \\ 0, & \text{if } i \neq j \end{cases} \\
&= \begin{pmatrix} |\overline{s}_{gn}|^2 & 0 \\ 0 & |\overline{c}_{gn}|^2 \end{pmatrix} \ .
\end{aligned}
\tag{3.2.17}
$$

Similarly the reduced density matrix of the field $\hat{\bar{\rho}}_f$ is obtained as follows

$$
\begin{aligned}
\hat{\bar{\rho}}_f &= tr_a(\hat{\bar{\rho}}_{gn}) = |\bar{c}_{gn}|^2|n\rangle\langle n|\ tr_a|g\rangle\langle g| - \bar{c}_{gn}\bar{s}_{gn}^*|n\rangle\langle n+1|\ tr_a|g\rangle\langle e| \\
&\quad - \bar{c}_{gn}^*\bar{s}_{gn}|n+1\rangle\langle n|\ tr_a|e\rangle\langle g| + |\bar{s}_{gn}|^2|n+1\rangle\langle n+1|\ tr_a|e\rangle\langle e| \\
&= |\bar{c}_{gn}|^2|n\rangle\langle n|\langle g|g\rangle - \bar{c}_{gn}\bar{s}_{gn}^*|n\rangle\langle n+1|\langle e|g\rangle \\
&\quad - \bar{c}_{gn}^*\bar{s}_{gn}|n+1\rangle\langle n|\langle g|e\rangle + |\bar{s}_{gn}|^2|n+1\rangle\langle n+1|\langle e|e\rangle \\
&= |\bar{c}_{gn}|^2|n\rangle\langle n| + |\bar{s}_{gn}|^2|n+1\rangle\langle n+1| \quad;\quad \delta_{ij} = \begin{cases} 1, & \text{if } i=j \\ 0, & \text{if } i \neq j \end{cases} \\
&= \begin{pmatrix} |\bar{c}_{gn}|^2 & 0 \\ 0 & |\bar{s}_{gn}|^2 \end{pmatrix}.
\end{aligned}
\tag{3.2.18}
$$

We then evaluate the eigenvalues $(\eta_1,\ \eta_2)$ of the reduced density matrices $\hat{\bar{\rho}}_a, \hat{\bar{\rho}}_f$ in Eqs. (3.2.17) and (3.2.18) to obtain

$$
\{\eta_1, \eta_2\} = \left\{ |\bar{c}_{gn}|^2, |\bar{s}_{gn}|^2 \right\}
\tag{3.2.19a}
$$

and determine the quantum system entanglement degree $E(\hat{\bar{\rho}}_{gn})$ defined in Eq. (3.2.14) according to

$$
\begin{aligned}
E(\hat{\bar{\rho}}_{gn}) &= -\eta_1 \log_2 \eta_1 - \eta_2 \log_2 \eta_2 \\
&= -|\bar{c}_{gn}|^2 \log_2 |\bar{c}_{gn}|^2 - |\bar{s}_{gn}|^2 \log_2 |\bar{s}_{gn}|^2 .
\end{aligned}
\tag{3.2.19b}
$$

The values of the quantum system entanglement degree, $E(\hat{\bar{\rho}}_{gn})$, at different values of sum frequency, $\bar{\delta}$, while noting the definitions of Rabi frequency, $\bar{R}_{gn}$, and interaction parameters, $\bar{c}_{gn}, \bar{s}_{gn}$, are in the range [0,1] as presented in Chapter 4.

In addition, noting that reduced density operators are mixed states, we quantify the mixedness by determining the length of the Bloch vector along the z-axis according to

$$
r_z = tr(\hat{\bar{\rho}}_{a(f)}\hat{\sigma}_z) .
\tag{3.2.20}
$$

The length of the Bloch vector r_z in Eq. (3.2.20) solved and provided in Chaphter. 4 is found to be $r_z = 0$ or in the range $0 < r_z < 1$ at different sum frequency $\bar{\delta}$ values.

Recall that r_z falls in the closed range [0,1], where 0 quantifies the stationary transition qubit state $|\bar{\phi}_{gn}\rangle$ as a maximally mixed state and 1 as a pure state else partially mixed when $0 < r_z < 1$.

In general $E(\hat{\bar{\rho}}_{gn}) = 0$ quantifies the transition qubit state $|\bar{\phi}_{gn}\rangle$ as a product state corresponding to $r_z = 1$, and $E(\hat{\bar{\rho}}_{gn}) = 1$ as a maximally entangled state corresponding to $r_z = 0$ else as entangled $0 < E(\hat{\bar{\rho}}_{gn}) < 1$ corresponding to $0 < r_z < 1$.

3.2.2.2 Entanglement evolution in the AJC interaction mechanism

The general dynamics of AJC interaction is described by the general time evolving AJC qubit state vector, $|\overline{\Psi}_{gn}(t)\rangle$, in Eq. (3.2.11). Substituting $|\overline{\Psi}_{gn}(t)\rangle$ from Eq. (3.2.11) into Eq. (3.2.12a) and using the definitions of $|\psi_{gn}\rangle$, $|\bar{\phi}_{gn}\rangle$ in Eqs. (3.2.2) and (3.2.3), respectively, the density operator takes the general form

$$
\begin{aligned}
\hat{\bar{\rho}}_{gn}(t) &= \left\{ \cos^2(\overline{R}_{gn}t) + \bar{c}_{gn}^2 \sin^2(\overline{R}_{gn}t) \right\} |g,n\rangle\langle g,n| \\
&+ \left\{ i\,\bar{s}_{gn} \cos(\overline{R}_{gn}t) \sin(\overline{R}_{gn}t) - \bar{c}_{gn}\bar{s}_{gn} \sin^2(\overline{R}_{gn}t) \right\} |g,n\rangle\langle e,n+1| \\
&+ \left\{ -i\,\bar{s}_{gn} \cos(\overline{R}_{gn}t) \sin(\overline{R}_{gn}t) - \bar{c}_{gn}\bar{s}_{gn} \sin^2(\overline{R}_{gn}t) \right\} |e,n+1\rangle\langle g,n| \\
&+ \left\{ \bar{s}_{gn}^2 \sin^2(\overline{R}_{gn}t) \right\} |e,n+1\rangle\langle e,n+1| \ .
\end{aligned}
$$

$$(3.2.21)$$

The reduced density operator of the atom is determined by tracing $\hat{\bar{\rho}}_{gn}(t)$ in Eq. (3.2.21) over the field states, thus taking the form

$$
\hat{\bar{\rho}}_a(t) = tr_f(\hat{\bar{\rho}}_{gn}(t)) = \overline{P}_g(t)|g\rangle\langle g| + \overline{P}_e(t)|e\rangle\langle e| \tag{3.2.22}
$$

after introducing the general time evolving atomic state probabilities, $\overline{P}_g(t)$, $\overline{P}_e(t)$, obtained as

$$
\overline{P}_g(t) = \cos^2(\overline{R}_{gn}t) + \bar{c}_{gn}^2 \sin^2(\overline{R}_{gn}t) \quad ; \quad \overline{P}_e(t) = \bar{s}_{gn}^2 \sin^2(\overline{R}_{gn}t) \tag{3.2.23}
$$

where the dimensionless interaction parameters, $\bar{c}_{gn}$, $\bar{s}_{gn}$, are defined in Eq. (3.2.4) and the Rabi frequency takes the form

$$
\overline{R}_{gn} = \frac{1}{2}\sqrt{16\lambda^2(n+1) + \bar{\delta}^2} \ . \tag{3.2.24}
$$

The time evolving atomic ground state probability, $\overline{P}_g(t)$, is the probability of finding an atom in the atomic ground state, $|g\rangle$, up to a normalisation factor while, $\overline{P}_e(t)$, is the probability for an atom to make a transition from the atomic ground state, $|g\rangle$, to atomic excited state, $|e\rangle$, up to a normalisation factor.

It is clear from Eq. (3.2.23) that at $t = 0$, the atom is in the atomic ground state $|g\rangle$, i.e., $\overline{P}_g(0) = 1$ and $\overline{P}_e(0) = 0$. Whereas at $t > 0$, the atom will be in a coherent superposition of ground $|g\rangle$ and excited $|e\rangle$ states with probability $\overline{P}_g(t)$ and $\overline{P}_e(t)$ respectively. This means that in the presence of the n-photon field, the atom is driven from its ground state $|g\rangle$ to a superposition of excited $|e\rangle$ and ground $|g\rangle$ states and back again.

Expressing $\hat{\bar{\rho}}_a(t)$ in Eq. (3.2.22) in 2×2 matrix form

$$\hat{\bar{\rho}}_a(t) = \begin{pmatrix} \overline{P}_e(t) & 0 \\ 0 & \overline{P}_g(t) \end{pmatrix} \tag{3.2.25}$$

we determine the quantum system entanglement degree $E(t)$ defined in Eq. (3.2.14) as

$$E(t) = -tr\left(\begin{pmatrix} \overline{P}_e(t) & 0 \\ 0 & \overline{P}_g(t) \end{pmatrix} \begin{pmatrix} \log_2 \overline{P}_e(t) & 0 \\ 0 & \log_2 \overline{P}_g(t) \end{pmatrix} \right)$$

$$\tag{3.2.26}$$

which takes the final form

$$E(t) = -\overline{P}_e(t) \log_2 \overline{P}_e(t) - \overline{P}_g(t) \log_2 \overline{P}_g(t) . \tag{3.2.27}$$

At different values of sum frequency $\bar{\delta} = \delta + 2\omega$ and photon number n we plot $E(t)$ against time t. The evolution of $E(t)$ is in the range [0,1]. Value 0 signifies disentanglement, 1 maximum entanglement else if $0 < E(t) < 1$ entangled. Plots are presented as results in Chapter 4.

3.2.2.3 Teleportation in the AJC interaction

Application of the time evolving state vector in Eq. (3.2.11)

$$|\overline{\Psi}_{gn}(t)\rangle = e^{-i\omega t(n+\frac{3}{2})} \left\{ \cos(\overline{R}_{gn}t)|\psi_{gn}\rangle - i\sin(\overline{R}_{gn}t)|\overline{\phi}_{gn}\rangle \right\} \tag{3.2.11'}$$

at various values of sum frequency, $\bar{\delta}$, enables us to describe Rabi oscillations between the initial qubit states, $|\psi_{gn}\rangle = |g, n\rangle$, and transition qubit states, $|\overline{\phi}_{gn}\rangle = -\overline{c}_{gn}|g, n\rangle + \overline{s}_{gn}|e, n+1\rangle$, at Rabi frequencies, $\overline{R}_{gn}$, in Eq. (3.2.4)

$$\overline{R}_{gn} = 2\lambda\overline{A}_{gn} \quad ; \quad \overline{A}_{gn} = \sqrt{(n+1) + \frac{\bar{\delta}^2}{16\lambda^2}} \quad ; \quad \bar{\delta} = \delta + 2\omega . \tag{3.2.4'}$$

In the process, we expect to obtain a maximally entangled transition anti-symmetric atom-field qubit state (or singlet state) $|\Psi^-\rangle$. This state, just like the symmetric atom-field Bell state $|\Phi^+\rangle$ used in standard JC studies (presented in Sec. A.1.2.3 and [111, 112, 167, 168] as examples) is the teleportation channel and it is in Bob's (receiver) possession. If Alice (sender) wishes to send to Bob a maximally entangled two-atom anti-symmetric state (singlet state) then the complete state of the system will take the form of Eq. (1.8.1b) which in this case we write

$$|\overline{\psi}\rangle_{total} = |\Psi^-\rangle_{a_1,a_2} \otimes |\Psi^-\rangle_{b_1,b_2} \; . \tag{3.2.28}$$

An observer, Charlie, receives qubits-$a1$($b1$) from Alice and Bob states respectively and carries out Bell projection as defined in Eq. (1.8.2) in the form

$$P_\Sigma := \langle\Sigma|\Lambda\rangle|\Sigma\rangle \; . \tag{1.8.2'}$$

The results of Bell state measurement are sent to Bob (or Alice). If it takes the form

$$_{a_1,b_1}\langle\Psi^-|\overline{\psi}\rangle_{total} = \frac{1}{2}|\Psi^-\rangle_{a_2,b_2} \; , \tag{3.2.29}$$

no local rotations by Pauli operators in Eq. (1.3.6) are to be made. Alice and Bob now share a Bell pair. Else if Charles measures and obtains

$$
\begin{aligned}
_{a_1,b_1}\langle\Phi^+|\overline{\psi}\rangle_{total} &= -\frac{1}{2}|\Phi^+\rangle_{a_2,b_2} \quad ; \\
_{a_1,b_1}\langle\Phi^-|\overline{\psi}\rangle_{total} &= \frac{1}{2}|\Phi^-\rangle_{a_2,b_2} \quad ; \\
_{a_1,b_1}\langle\Psi^+|\overline{\psi}\rangle_{total} &= \frac{1}{2}|\Psi^+\rangle_{a_2,b_2} \; ,
\end{aligned}
\tag{3.2.30}
$$

local corrections given by Pauli operators, $\hat{\sigma}_x$, $\hat{\sigma}_y$, $\hat{\sigma}_z$, defined in Eq. (1.3.6) are performed by Bob (or Alice) after Charlie has communicated the results of measurement according to

$$
\begin{aligned}
-\frac{1}{2}\left[\hat{\sigma}_{x(b_2)}|\Phi^-\rangle_{a_2,b_2}\right] &= \frac{1}{2}|\Psi^-\rangle_{a_2,b_2} \quad ; \\
\frac{1}{2}\left[i\,\hat{\sigma}_{y(b_2)}|\Phi^+\rangle_{a_2,b_2}\right] &= \frac{1}{2}|\Psi^-\rangle_{a_2,b_2} \quad ; \\
\frac{1}{2}\left[\hat{\sigma}_{z(b_2)}|\Psi^+\rangle_{a_2,b_2}\right] &= \frac{1}{2}|\Psi^-\rangle_{a_2,b_2} \; .
\end{aligned}
\tag{3.2.31}
$$

Applying the maximal teleportation fidelity, Eq. (1.8.19a)

$$F_{\hat{\rho}} = \frac{2f_{\hat{\rho}} + 1}{3} \tag{1.8.19a'}$$

where, $f_{\hat{\rho}}$, is the fully entangled fraction defined earlier in Eq. (1.8.19b) in the form

$$f_{\hat{\rho}} = \max_{|\Psi\rangle}\langle\Psi|\hat{\rho}|\Psi\rangle = \left\{ tr\sqrt{\hat{\rho}_{expected}^{\frac{1}{2}}\hat{\rho}_{measured}\hat{\rho}_{expected}^{\frac{1}{2}}} \right\}^2 \ , \tag{1.8.19b'}$$

to the outcomes in Eqs. (3.2.29) and (3.2.31), each has a unit fidelity, a quarter chance to occur.

3.2.3 Hadamard gate operation in the AJC interaction

The normalised qubit state transition operators in Eq. (3.2.5) are the Hadamard gate operators for an atom in an initial excited, $|e\rangle$, and ground, $|g\rangle$, states respectively. We re-write here their explicit forms as

$$\hat{\bar{\varepsilon}}_g = \frac{\hat{\bar{A}}}{\overline{A}_{gn}} = \frac{2\left[\bar{\delta}\hat{s}_z + 2\lambda(\hat{a}\hat{s}_- + \hat{a}^\dagger\hat{s}_+) \right]}{\sqrt{16\lambda^2(n+1) + \bar{\delta}^2}} \quad ; \quad \overline{A}_{gn} = \frac{1}{4\lambda}\sqrt{16\lambda^2(n+1) + \bar{\delta}^2} \quad ;$$

$$\hat{\bar{\varepsilon}}_e = \frac{\hat{\bar{A}}}{\overline{A}_{en}} = \frac{2\left[\bar{\delta}\hat{s}_z + 2\lambda(\hat{a}\hat{s}_- + \hat{a}^\dagger\hat{s}_+) \right]}{\sqrt{16n\lambda^2 + \bar{\delta}^2}} \quad ; \quad \overline{A}_{en} = \frac{1}{4\lambda}\sqrt{16n\lambda^2 + \bar{\delta}^2} \quad ;$$

$$\overline{\alpha} = \frac{\bar{\delta}}{2\lambda} \quad ; \quad \hat{\bar{A}} = \overline{\alpha}\hat{s}_z + \hat{a}\hat{s}_- + \hat{a}^\dagger\hat{s}_+ \quad ; \quad \hat{a}|n\rangle = \sqrt{n}|n-1\rangle \quad ;$$

$$\hat{a}^\dagger|n\rangle = \sqrt{n+1}|n+1\rangle \quad ; \quad \hat{s}_+ = \hat{s}_x + i\hat{s}_y \quad ; \quad \hat{s}_- = \hat{s}_x - i\hat{s}_y \quad ;$$

$$\hat{s}_+|e\rangle = 0 \quad ; \quad \hat{s}_-|e\rangle = |g\rangle \quad ; \quad \hat{s}_+|g\rangle = |e\rangle \quad ; \quad \hat{s}_-|g\rangle = 0 \ . \tag{3.2.32}$$

Defining an initial state vector, $|e, n\rangle$, in which an atom in an excited state enters a field mode in a number (Fock) state, $|n\rangle$; $n \geq 1$, in this particular interaction, by application of $\hat{\bar{\varepsilon}}_e$ in Eq. (3.2.5) (or Eq. (3.2.32)) a qubit state transition as described earlier in Eq. (3.2.7) takes the form

$$\hat{\bar{\varepsilon}}_e|e, n\rangle = \overline{a}_{en}|e, n\rangle + \overline{b}_{en}|g, n-1\rangle = |\overline{\phi}_{en}\rangle \quad ; \quad \hat{\bar{\varepsilon}}_e|\overline{\phi}_{en}\rangle = |e, n\rangle \ . \tag{3.2.33}$$

Here, $\overline{a}_{en}, \overline{b}_{en}$, are the normalisation parameters. Applying the definitions of interaction

parameters, $\overline{c}_{en}$, $\overline{s}_{en}$, and Rabi frequency, $\overline{R}_{en}$ in Eq. (3.2.4), $\overline{a}_{en}$, $\overline{b}_{en}$ are obtained in respective explicit forms as

$$\overline{a}_{en} = \frac{\overline{\delta}}{2\overline{R}_{en}} = \frac{\overline{\delta}}{\sqrt{16n\lambda^2 + \overline{\delta}^2}} \quad ; \quad \overline{b}_{en} = \frac{2\lambda\sqrt{n}}{\overline{R}_{en}} = 4\lambda\sqrt{\frac{n}{16n\lambda^2 + \overline{\delta}^2}} \ .$$

(3.2.34)

Similarly, defining an initial state vector, $|g, n\rangle$, in which an atom in an initial ground state, $|g\rangle$, is in a field mode in a number state, $|n\rangle$; $n \geq 0$, application of $\hat{\overline{\varepsilon}}_g$ in Eq. (3.2.5) (or Eq. (3.2.32)) we obtain in this specific case the qubit state transition

$$\hat{\overline{\varepsilon}}_g |g, n\rangle = -\overline{p}_{gn}|g, n\rangle + \overline{q}_{gn}|e, n+1\rangle = |\overline{\phi}_{gn}\rangle \quad ; \quad \hat{\overline{\varepsilon}}_g |\overline{\phi}_{gn}\rangle = |g, n\rangle \ ,$$

(3.2.35)

where $\overline{p}_{gn}$, $\overline{q}_{gn}$ are the normalisation parameters obtained in explicit forms

$$\overline{p}_{gn} = \frac{\overline{\delta}}{2\overline{R}_{gn}} = \frac{\overline{\delta}}{\sqrt{16\lambda^2(n+1) + \overline{\delta}^2}} \quad ; \quad \overline{q}_{gn} = \frac{2\lambda\sqrt{n+1}}{\overline{R}_{gn}} = 4\lambda\sqrt{\frac{n+1}{16\lambda^2(n+1) + \overline{\delta}^2}} \ ,$$

(3.2.36)

while taking note of the standard definitions of interaction parameters, $\overline{c}_{gn}$, $\overline{s}_{gn}$, and Rabi frequency, $\overline{R}_{gn}$ in Eq. (3.2.4).

In Eqs. (3.2.33) and (3.2.35), $|e, n\rangle$, $|g, n\rangle$ and $|\overline{\phi}_{en}\rangle$, $|\overline{\phi}_{gn}\rangle$, are the AJC initial, transition qubit state vectors. Further, Eqs. (3.2.33) and (3.2.35) show clearly the reversibility property of the gate operations. It is also clear that the initial atomic states, $|e\rangle$, $|g\rangle$, are rotated to diagonal (Hadamard) basis states, $|+\rangle$, in Eq. (3.2.33) and, $|-\rangle$, in Eq. (3.2.35). The computation basis, $|e\rangle$, $|g\rangle$, is the eigenbasis for the spin in the z-direction, whereas the Hadamard basis, $|+\rangle$, $|-\rangle$, is the eigenbasis for the spin in the x-direction [49] as explained earlier in Sec. 1.7.1.

Here, we specify Hadarmard rotations for initial atomic basis states, $|g\rangle$, $|e\rangle$, entering field modes, $n \geq 0$, $n \geq 1$, respectively in general forms

$$|e\rangle \rightarrow \overline{a}_{en}|e\rangle + \overline{b}_{en}|g\rangle = |+\rangle \quad ; \quad |g\rangle \rightarrow \overline{q}_{gn}|e\rangle - \overline{p}_{gn}|g\rangle = |-\rangle \ .$$

(3.2.37a)

In this respect, in an initial single-photon $n = 1$, vacuum $n = 0$ field modes respectively and at sum frequency $\overline{\delta} = 4\lambda$, standard Hadamard rotations defined in Eq. (1.7.3) are

obtained, which we re-write in the form

$$|e\rangle \rightarrow \frac{|e\rangle + |g\rangle}{\sqrt{2}} = |+\rangle \quad ; \quad |g\rangle \rightarrow \frac{|e\rangle - |g\rangle}{\sqrt{2}} = |-\rangle \; . \tag{3.2.37b}$$

3.2.4 C-NOT gate operation in AJC interaction

In order to realise a C-NOT gate operation in this case, we note that the state evolution operator for an initial atomic ground state, $|g\rangle$, in an n-photon field mode, $|n\rangle$; $n \geq 0$, in the AJC interaction is generated by the time evolution operator in Eq. (3.2.9), which on substituting the Hamiltonian $\hat{\overline{H}}_g$ from Eq. (3.2.8) and dropping the factorisable global phase factor $e^{-i\omega t\left(n+\frac{3}{2}\right)\hat{\overline{I}}_g}$, defines the C-NOT gate operator in the AJC model $e^{-i\theta\hat{\overline{\varepsilon}}_g}$ in the general form in Eq. (3.2.6) which we re-write here for ease of reference

$$e^{-i\theta\hat{\overline{\varepsilon}}_g} = \cos(\theta)\hat{\overline{I}}_g - i\;\sin(\theta)\hat{\overline{\varepsilon}}_g \; . \tag{3.2.6'}$$

Similarly, for an initial atomic excited state, $|e\rangle$, in a n-photon field mode, $|n\rangle$; $n \geq 1$, a C-NOT gate operation in the AJC interaction is generated by the time evolution operator [12]

$$\hat{\overline{U}}_e(t) = e^{-i\omega t\left(n+\frac{1}{2}\right)}\left(\cos(\overline{R}_{en}t)\hat{\overline{I}}_e - i\sin(\overline{R}_{en}t)\hat{\overline{\varepsilon}}_e\right) \tag{3.2.38}$$

which on substituting the Hamiltonian $\hat{\overline{H}}_e$ from Eq. (3.2.8) and dropping the global phase factor $e^{-i\omega t\left(n+\frac{1}{2}\right)\hat{\overline{I}}_e}$, defines the requisite C-NOT gate operator $e^{i\varphi\hat{\overline{\varepsilon}}_e}$ defined in Eq. (3.2.6) in complete final form

$$e^{i\varphi\hat{\overline{\varepsilon}}_e} = \cos(\varphi)\hat{\overline{I}}_e + i\sin(\varphi)\hat{\overline{\varepsilon}}_e \; . \tag{3.2.6'}$$

The C-NOT gate process consists of a two-level atom as the control qubit, which constitutes a two-dimensional Hilbert space spanned by atomic excited, $|e\rangle$, and ground, $|g\rangle$, states as basis vectors. Two non-degenerate polarised cavity modes, C_a, C_b, make the target qubit. The target qubit is defined in two-dimensional Hilbert space spanned by the state vector, $|v\rangle_1 = |0_a, 1_b\rangle$, which indicates that mode a is in vacuum state and one photon is present in mode b, and the state vector, $|v\rangle_2 = |1_a, 0_b\rangle$, which expresses the presence of one photon in mode a when there is no photon in mode b.

An important feature of this approach lies in the fact that after the control qubit (atomic qubit) interacts with the respective cavity modes, C_a, C_b, they exit in the same state despite altering the state of the respective successive cavity modes thus describing

energy conservation. Further for it to work, there should never be more than a single photon in a cavity field. This means that Fock states, $|0\rangle$ and $|1\rangle$, of the cavity modes, are the two logical states. Therefore, the state transitions $|g, n\rangle \rightarrow |e, n + 1\rangle$ such that $n = 0$, followed by $|e, n\rangle \rightarrow |g, n - 1\rangle$ such that $n = 1$ will experience Rabi oscillations at Rabi frequencies $\overline{R}_{gn}$, $\overline{R}_{en}$. These Rabi oscillations will depend on the interaction time t of the atom and the cavity modes.

In actual experiments, the magnitude of the atomic velocity v_a [28, 169–171] is determined by taking into account the length L of the cavity and the interaction time t such that $t = \frac{L}{v_{atom}}$. Further, noting that in such set-ups the velocity can vary [120], we shall evaluate the actual *effect* of the magnitude of atomic velocity by taking the coupling parameter λ constant, i.e., the Rabi angles $\theta = \overline{R}_{gn}t$, $\varphi = \overline{R}_{en}t$ will be depend on λ and interaction time t. The final qubit state is then readily calculated considering the definitions of the AJC qubit state algebraic transition operations in Eq. (3.2.7) and the algebraic property on exponentiation of $\hat{\bar{\varepsilon}}_g$, $\hat{\bar{\varepsilon}}_e$ defined in Eq. (3.2.6).

Considering that the atom undergoes a cycle of Rabi oscillation due to interaction with cavity mode, accurate choice of interaction time will be important. In the process, qubit state transitions consistent with Eq. (3.2.6) and qubit state operations defined in Eq. (3.2.7) occur at specified interaction times. More precisely the target qubits made up of electromagnetic field should be flipped when the control qubit is in an initial ground state, $|g\rangle$, and remain unchanged if the control qubit is in an initial excited state, $|e\rangle$.

3.2.4.1 Success probability of the C-NOT gate operation

Consider the quantum circuit in Fig. 3.1 representing a schematic of a quantum computation protocol for the C-NOT gate described in Sec. 3.2.4, including a measurement process.
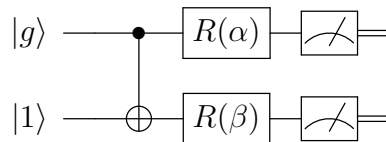
Figure 3.1: Measurement of outcome of C-NOT gate operation

Here, an atom in ground state, $|g\rangle$, enters a single-photon field mode, $|1\rangle$, as an example. The atom immediately evolves into a coherent superposition of excited, $|e\rangle$, and ground state, $|g\rangle$, a rotation specified by the Walsh-Hadamard gate as presented in

Eq. (3.2.37b)

$$|g\rangle \rightarrow \frac{1}{\sqrt{2}} (|e\rangle - |g\rangle) \tag{3.2.37'}$$

and so the combined product state is of the form

$$\frac{1}{\sqrt{2}} (|e\rangle - |g\rangle) \otimes |1\rangle = \frac{1}{\sqrt{2}} \left(e^{i\pi} |g, 1\rangle + |e, 1\rangle \right) . \tag{3.2.39a}$$

The qubits then entangle according to

$$\frac{1}{\sqrt{2}} \left(e^{i\pi} |g, 0\rangle + |e, 1\rangle \right) . \tag{3.2.39b}$$

This is described by the the C-NOT gate operation in the quantum circuit, where it flips the target qubit if and only if the control qubit is in an atomic ground state, $|g\rangle$. Note that the control qubits (atomic basis states $|e\rangle$, $|g\rangle$) after undergoing qubit state transitions in the two successive cavity modes, C_a and C_b respectively as specified by Eqs. (3.2.6) and (3.2.7), emerge in the same state $|e\rangle$ or $|g\rangle$. This explains why the qubits are in the summarised final form of Eq. (3.2.39b) without going into the standard AJC process we set out in Eqs. (3.2.6) and (3.2.7).

To measure the outcome of the gate operation we first apply unitary rotations in the clockwise direction $R(\alpha)$, $R(\beta)$ to the first and second qubits respectively in Eq. (3.2.39b) defined in the form

$$R(\alpha) = \begin{pmatrix} \cos(\alpha) & \sin(\alpha) \\ -\sin(\alpha) & \cos(\alpha) \end{pmatrix} \quad ; \quad R(\beta) = \begin{pmatrix} \cos(\beta) & \sin(\beta) \\ -\sin(\beta) & \cos(\beta) \end{pmatrix} . \tag{3.2.40}$$

The resulting state is determined according to

$$(R(\alpha) \otimes R(\beta)) \frac{1}{\sqrt{2}} (|e, 1\rangle - |g, 0\rangle)$$

$$= \frac{1}{\sqrt{2}} \left(\begin{pmatrix} \cos(\alpha) \\ -\sin(\alpha) \end{pmatrix} \otimes \begin{pmatrix} \sin(\beta) \\ \cos(\beta) \end{pmatrix} - \begin{pmatrix} \sin(\alpha) \\ \cos(\alpha) \end{pmatrix} \otimes \begin{pmatrix} \cos(\beta) \\ -\sin(\beta) \end{pmatrix} \right)$$

$$= \frac{1}{\sqrt{2}} \left(\begin{pmatrix} \cos(\alpha)\sin(\beta) \\ \cos(\alpha)\cos(\beta) \\ -\sin(\alpha)\sin(\beta) \\ -\sin(\alpha)\cos(\beta) \end{pmatrix} - \begin{pmatrix} \sin(\alpha)\cos(\beta) \\ -\sin(\alpha)\sin(\beta) \\ \cos(\alpha)\cos(\beta) \\ -\cos(\alpha)\sin(\beta) \end{pmatrix} \right)$$

$$\tag{3.2.41a}$$

which in the basis $\{|e, 0\rangle, |e, 1\rangle, |g, 0\rangle, |g, 1\rangle\}$ after applying the trigonometric identities

$$
\begin{aligned}
\sin(\alpha)\sin(\beta) &= \frac{\cos(\alpha - \beta) - \cos(\alpha + \beta)}{2} \\
\cos(\alpha)\cos(\beta) &= \frac{\cos(\alpha + \beta) + \cos(\alpha - \beta)}{2} \\
\sin(\alpha)\cos(\beta) &= \frac{\sin(\alpha + \beta) + \sin(\alpha - \beta)}{2} \\
\cos(\alpha)\sin(\beta) &= \frac{\sin(\alpha + \beta) - \sin(\alpha - \beta)}{2}
\end{aligned}
$$
(3.2.41b)

yields

$$
\frac{1}{\sqrt{2}}\left[-\sin(\alpha - \beta)\,|e, 0\rangle + \cos(\alpha - \beta)\,|e, 1\rangle - \cos(\alpha - \beta)\,|g, 0\rangle - \sin(\alpha - \beta)\,|g, 1\rangle\right] \ .
$$
(3.2.41c)

Defining the Rabi angle $\phi = \overline{R}\,\triangle\,t = (\alpha - \beta)$ we write Eq. (3.2.41c) in the form

$$
\frac{1}{\sqrt{2}}\left[-\sin(\phi)\,|e, 0\rangle + \cos(\phi)\,|e, 1\rangle - \cos(\phi)\,|g, 0\rangle - \sin(\phi)\,|g, 1\rangle\right]
$$
(3.2.41d)

Noting that (see Eq. (1.2.3)) $|e\rangle = \begin{pmatrix} 1 \\ 0 \end{pmatrix}$; $|g\rangle = \begin{pmatrix} 0 \\ 1 \end{pmatrix}$; $|0\rangle = \begin{pmatrix} 1 \\ 0 \end{pmatrix}$; $|1\rangle = \begin{pmatrix} 0 \\ 1 \end{pmatrix}$, the probability of measuring $|e, 0\rangle = \frac{1}{2}\sin^2(\phi)$. Similarly, the probability of measuring $|g, 1\rangle = \frac{1}{2}\sin^2(\phi)$. This means that the probability of the qubits collapsing to the same qubit value is

$$
P(|e, 0\rangle \cup |g, 1\rangle) = \sin^2(\phi) \ ,
$$
(3.2.42a)

and that of the qubits collapsing to different qubit values is

$$
P(|e, 1\rangle \cup |g, 0\rangle) = \cos^2(\phi) = 1 - \sin^2(\phi) \ .
$$
(3.2.42b)

Now since we are applying a two cavity mode to actualise the C-NOT gate, we apply the Bayes' theorem [172] that relates two conditional probabilities defined as

$$P(a|b) = \frac{P(b|a)P(a)}{P(b)} \; . \tag{3.2.43}$$

Defining cavity modes, a, b the conditional probability that the event in mode b occurs given that event a has occurred and are of the same qubit value is

$$P(a|b) = \frac{P(a \cap b)}{p(b)} \; , \tag{3.2.44a}$$

and the conditional probability that the event in mode a occurs given that event b has occurred and are of the same qubit value is

$$P(b|a) = \frac{P(b \cap a)}{p(a)} \; . \tag{3.2.44b}$$

It is clear from the definitions of Eqs. (3.2.44a), (3.2.44b) and the understanding of Bayes' theorem in Eq. (3.2.43) that

$$P(a \cap b) = P(b \cap a) = P(a|b)P(b) = P(b|a)P(a) \; . \tag{3.2.44c}$$

We now evaluate probability of success of the C-NOT process when the qubits collapse to the same qubit value according to

$$
\begin{aligned}
P_s &= \sin^2(\phi_a)\sin^2(\phi_b) = \sin^2(\phi_a)(1 - \cos^2(\phi_b)) \\
&= \sin^2(\phi_a) - \sin^2(\phi_a)\cos^2(\phi_b) \\
&= 1 - \cos^2(\phi_a) - \sin^2(\phi_a)\cos^2(\phi_b) \\
&= 1 - (\cos^2(\phi_a) + \sin^2(\phi_a)\cos^2(\phi_b)) \; .
\end{aligned}
$$
$$\tag{3.2.45}$$

Similarly, in the case of the qubits collapsing to different qubit values

$$
\begin{aligned}
P_s &= \cos^2(\phi_a)\cos^2(\phi_b) = \cos^2(\phi_a)(1 - \sin^2(\phi_b)) \\
&= \cos^2(\phi_a) - \cos^2(\phi_a)\sin^2(\phi_b) \\
&= 1 - \sin^2(\phi_a) - \cos^2(\phi_a)\sin^2(\phi_b) \\
&= 1 - (\sin^2(\phi_a) + \cos^2(\phi_a)\sin^2(\phi_b)) \; .
\end{aligned}
$$
$$\tag{3.2.46}$$

In this Thesis, we shall apply either Eq. (3.2.45) or (3.2.46) to determine success proba-
bility of the C-NOT gate operation between two successive cavity modes C_a, C_b.

3.3 AJC dynamics with field mode in an initial coherent state

Let us consider the field initially in a coherent state as defined in Eq. (1.5.6g) which we
re-write here in a general form ($t = 0$)

$$|\psi_n\rangle = e^{-\frac{|\alpha|^2}{2}} \sum_{n=0}^{\infty} \frac{|\alpha|^n}{\sqrt{n!}} |n\rangle \qquad (1.5.6g')$$

where, α, is the coherent amplitude, and a generalised initial atomic state, $|\psi_a\rangle$, prepared
in a superposition of excited, $|e\rangle$, and ground, $|g\rangle$, states in the form ($t = 0$)

$$|\psi_a\rangle = A |e\rangle + B |g\rangle \quad ; \quad A = \sqrt{\zeta} \quad ; \quad B = \sqrt{1 - \zeta} \qquad (3.3.1)$$

where the atom is initially in an excited states with probability ζ and ground state with
probability $1 - \zeta$. In Eq. (1.5.6g) (or Eq.(1.5.6g')) the states $|n\rangle$, $n = 0, 1.2, 3, ...$ of the
mode are the photon number (Fock) states.

The initial atom-field state, $|\psi_{an}\rangle_{AJC}$, is obtained as a direct product of atom and the
field states according to

$$|\psi_{an}\rangle_{AJC} = |\psi_a\rangle \otimes |\psi_n\rangle \ . \qquad (3.3.2)$$

Defining the mean photon number, $|\alpha|^2$, in the AJC interaction as

$$|\alpha|^2 = \langle \hat{a}\hat{a}^\dagger \rangle_{t=0} = \langle 1 + \hat{a}^\dagger \hat{a} \rangle_{t=0}, \qquad (3.3.3)$$

the exact solutions to the Schrödinger equation [10] for the initial atom-field system in

Eq. (3.3.2) in the AJC interaction, $|\overline{\Psi}_{an}(t)\rangle$, take explicit form $(t > 0)$

$$
\begin{aligned}
|\overline{\Psi}_{an}(t)\rangle \;=\; & \sum_{n=0}^{\infty} e^{-\frac{\alpha^2}{2}} \Bigg(\Big[A \frac{\alpha^n}{\sqrt{n!}} \, e^{-i\omega t\left(n+\frac{1}{2}\right)} (\cos(\overline{R}_{en}t) - i\overline{c}_{en}\sin(\overline{R}_{en}t)) - \\
& i\, B \frac{\alpha^{n-1}}{\sqrt{(n-1)!}} \overline{s}_{gn-1} \, e^{-i\omega t(n+\frac{1}{2})} \sin(R_{gn-1}t) \Big] |e\rangle + \\
& \Big[B \frac{\alpha^n}{\sqrt{n!}} \, e^{-i\omega t(n+\frac{3}{2})} (\cos(\overline{R}_{gn}t) + i\overline{c}_{gn}\sin(\overline{R}_{gn}t)) + \\
& i\, A \frac{\alpha^{n+1}}{\sqrt{(n+1)!}} e^{-i\omega t(n+\frac{3}{2})} \, \overline{s}_{en+1} \sin(\overline{R}_{en+1}t) \Big] |g\rangle \Bigg) \otimes |n\rangle \ .
\end{aligned}
$$

$$(3.3.4)$$

The final forms of Eq. (3.3.4) has been arrived at through Schmidt decomposition defined in Eq. (1.8.5) Sec. (1.8.2) and so the entanglement of the two interacting atom, field quantum systems is readily apparent.

To describe the evolution of the atom alone we introduce the reduced density matrix of the atom $\hat{\overline{\rho}}_a(t)$ by tracing $\hat{\overline{\rho}}_{an}(t)$ over the field states in the form

$$
\hat{\overline{\rho}}_a(t) = tr_f\left(|\overline{\Psi}_{an}(t)\rangle\langle\overline{\Psi}_{an}(t)|\right) \tag{3.3.5a}
$$

where for an atom in an initial ground state, $|g\rangle$, at any time $t > 0$ the state vector of the system, $|\overline{\Psi}_{gn}(t)\rangle$, in the AJC processe takes the form $(B = 1,\ A = 0)$

$$
\begin{aligned}
|\overline{\Psi}_{gn}(t)\rangle \;=\; & \sum_{n=0}^{\infty} e^{-\frac{\alpha^2}{2}} \Big[\Big(-i\, \frac{\alpha^{n-1}}{\sqrt{(n-1)!}} s_{gn-1} e^{-i\omega t(n+\frac{1}{2})} \sin(\overline{R}_{gn-1}t) \Big) |e\rangle + \\
& \frac{\alpha^n}{\sqrt{n!}} e^{-i\omega t(n+\frac{3}{2})} \left(\cos(\overline{R}_{gn}t) + i\,\overline{c}_{gn}\sin(\overline{R}_{gn}) \right) |g\rangle \Big] \otimes |n\rangle \ .
\end{aligned}
$$

$$(3.3.5b)$$

Applying Eq. (3.3.5a), the AJC reduced atomic density operator, $\hat{\overline{\rho}}_a^g(t)$, determined

from Eq. (3.3.5b) reduces to an explicit form

$$
\begin{aligned}
\hat{\bar{\rho}}_a^g(t) &= e^{-\alpha^2} \sum_{n=0}^{\infty} \left[\frac{\alpha^{2n}}{n!} \left(\cos^2(\overline{R}_{gn}t) + \bar{c}_{gn}^2 \sin^2(\overline{R}_{gn}t) \right) |g\rangle\langle g| \right. \\
&\quad + i\, \frac{\alpha^{2n-1}}{\sqrt{n!(n-1)!}}\, \bar{s}_{gn-1} e^{-i\omega t} \sin(\overline{R}_{gn-1}t)\left(\cos(\overline{R}_{gn}t) + i\bar{c}_{gn} \sin(\overline{R}_{gn}t) \right) |g\rangle\langle e| \\
&\quad - i\, \frac{\alpha^{2n-1}}{\sqrt{n!(n-1)!}}\, \bar{s}_{gn-1} e^{i\omega t} \sin(\overline{R}_{gn-1}t)\left(\cos(\overline{R}_{gn}t) - i\bar{c}_{gn} \sin(\overline{R}_{gn}t) \right) |e\rangle\langle g| \\
&\quad \left. + \frac{\alpha^{2(n-1)}}{(n-1)!}\, \bar{s}_{gn-1}^2 \sin^2(\overline{R}_{gn-1}t) |e\rangle\langle e| \right] \\
&= e^{-\alpha^2} \sum_{n=0}^{\infty} \left[\overline{P}_{gg}|g\rangle\langle g| + \overline{P}_{ge}|g\rangle\langle e| + \overline{P}_{eg}|e\rangle\langle g| + \overline{P}_{ee}|e\rangle\langle e| \right]
\end{aligned}
$$

$$(3.3.5c)$$

with the Rabi frequency and interaction parameters in the AJC process defined as

$$
\begin{aligned}
\overline{R}_{gn} &= \frac{\lambda}{2}\sqrt{4n+4+(\beta+2\xi)^2} \quad ; \quad \bar{c}_{gn} = \frac{(\beta+2\xi)}{\sqrt{4n+4+(\beta+2\xi)^2}} \\
\bar{s}_{gn} &= \sqrt{\frac{4(n+1)}{4n+4+(\beta+2\xi)^2}} \quad ; \quad \bar{\delta} = \delta + 2\omega \quad ; \quad \xi = \frac{\omega}{\lambda} \quad ; \quad \beta = \frac{\delta}{\lambda} \;.
\end{aligned}
$$

$$(3.3.5d)$$

3.3.1 Purity and atomic population inversion

We re-write the degree of purity defined in Eq. (1.3.16) in the form

$$
tr(\hat{\rho}_j^2(t)) = \frac{1}{2}\left[1 + (r_x^2(t) + r_y^2(t) + r_z^2(t)) \right] \quad ; \quad j : a(f)
\tag{1.3.16$'$}
$$

Recall that for pure states, $tr(\hat{\rho}_{a(f)}^2(t)) = 1$ in which the state-vector description of each individual system is possible. On the other hand for a two-level system a maximally mixed state corresponds to $tr(\hat{\rho}_{a(f)}^2(t)) = \frac{1}{2}$.

Defining the AJC time evolving Bloch vector, $\vec{r}(t) = \bar{r}_x(t)\hat{i} + \bar{r}_y(t)\hat{j} + \bar{r}_z(t)\hat{k}$, with

components in the AJC process, $\overline{r}_x(t)$, $\overline{r}_y(t)$, $\overline{r}_z(t)$, evaluated explicitly as

$$\overline{r}_x(t) = tr(\hat{\overline{\rho}}_a^g(t)\hat{\sigma}_x) = \sum_{n=0}^{\infty} e^{-\alpha^2} \frac{\alpha^{2n-1}}{\sqrt{n!(n-1)!}} \Big[2\overline{s}_{gn-1} \sin(\overline{R}_{gn-1}t) \cos(\overline{R}_{gn}t) \sin(\omega t)$$

$$-2\overline{s}_{gn-1}\overline{c}_{gn} \sin(\overline{R}_{gn-1}t) \sin(\overline{R}_{gn}t) \cos(\omega t) \Big]$$

$$\overline{r}_y(t) = tr(\hat{\overline{\rho}}_a^g(t)\hat{\sigma}_y) = \sum_{n=0}^{\infty} e^{-\alpha^2} \frac{\alpha^{2n-1}}{\sqrt{n!(n-1)!}} \Big[2\overline{s}_{gn-1} \sin(\overline{R}_{gn-1}t) \cos(\overline{R}_{gn}t) \cos(\omega t)$$

$$+2\overline{s}_{gn-1}\overline{c}_{gn} \sin(\overline{R}_{gn-1}t) \sin(\overline{R}_{gn}t) \sin(\omega t) \Big]$$

$$\overline{r}_z(t) = tr(\hat{\overline{\rho}}_a^g(t)\hat{\sigma}_z) = \sum_{n=0}^{\infty} e^{-\alpha^2} \Big[\frac{\alpha^{2(n-1)}}{(n-1)!}\overline{s}_{gn-1}^2 \sin^2(\overline{R}_{gn-1}t) - \frac{\alpha^{2n}}{n!} \Big(\cos^2(\overline{R}_{gn}t)$$

$$+\overline{c}_{gn}^2 \sin^2(\overline{R}_{gn}t) \Big) \Big],$$

$$(3.3.6)$$

we plot the degree of purity, $tr(\hat{\overline{\rho}}_a^2(t))$, considering the definition of interaction parameters and Rabi frequency in Eq. (3.3.5d).

In order to discuss the collapses and revival phenomenon, in relation to degree of entanglement, $S_a(t)$, and purity of states, $tr(\hat{\overline{\rho}}_a^2(t))$, we introduce atomic population inversion, $W(t)$, [34] defined as the difference between the excited and ground state probabilities according to

$$W(t) = tr\left(\hat{\sigma}_z \hat{\overline{\rho}}_a(t)\right)$$

$$= e^{-\alpha^2} tr\left[\begin{pmatrix} 1 & 0 \\ 0 & -1 \end{pmatrix} \begin{pmatrix} \sum_{n=0}^{\infty} \overline{P}_{ee}(t) & \sum_{n=0}^{\infty} \overline{P}_{eg}(t) \\ \sum_{n=0}^{\infty} \overline{P}_{ge}(t) & \sum_{n=0}^{\infty} \overline{P}_{gg}(t) \end{pmatrix} \right]$$

$$= e^{-\alpha^2} \sum_{n=0}^{\infty} \left(\overline{P}_{ee}(t) - \overline{P}_{gg}(t)\right) , \qquad (3.3.7a)$$

which takes the exact form as the z-component, $\overline{r}_z(t)$, in Eq. (3.3.6) of the AJC time evolving Bloch vector, $\vec{\overline{r}}$.

In addition since the AJC interaction is permanently detuned, the revival time, τ_R, of atomic population inversion is determined as established in [173] as

$$\tau_R \simeq \frac{\pi}{\sqrt{\frac{\overline{\delta}^2}{4\lambda^2} + (|\alpha|^2 + 1)} - \sqrt{\frac{\overline{\delta}^2}{4\lambda^2} + |\alpha|^2}} \quad ; \quad \overline{\delta} = \delta + 2\omega . \qquad (3.3.7b)$$

58

3.3.2   Entropy of Entanglement

Consideing the atomic subsystem, we apply the von Neumann entropy in Eq. (1.8.9) which we now define in terms of the length of the time evolving AJC Bloch vector, $\vec{r}(t)$, in complete form

$$S_a(t) = -\pi_1 \log_2 \pi_1 - \pi_2 \log_2 \pi_2 \quad ; \quad \pi_1 = \frac{1}{2}\left[1 + |\vec{r}(t)|\right] \; ; \; \pi_2 = \frac{1}{2}\left[1 - |\vec{r}(t)|\right] \; .$$

(3.3.8)

We then compute with ease the eigenvalues, π_1, π_2, considering the definitions of the AJC Bloch vector components in Eq. (3.3.6); interaction parameters and Rabi frequency in Eq. (3.3.5d). At various values of sum frequency, $\overline{\delta} = \delta + 2\omega$, and field intensity, $|\alpha|^2$, during the AJC process, we plot and analyse the dynamics of the von Neumann entropy for the atomic subsystem, $S_a(t)$, in Eq. (3.3.8) in relation to atomic population inversion (Rabi oscillations), $W(t)$, and purity of states, $tr(\hat{\rho}_a^2(t))$.

3.3.3   Photon statistics

In this section we present the approach adopted in analysis of the nature of photons during the AJC interaction processes.

3.3.3.1   Mean photon number

The initial average photon number [174], $|\alpha|^2$ is defined in Eq.(3.3.3). As time advances $(t > 0)$ the average photon number takes the form

$$\langle \hat{a}\hat{a}^\dagger \rangle_{\mathsf{t}} = tr\left[\hat{\overline{\rho}}_f(t)\,(\hat{a}\hat{a}^\dagger)\right] = tr\left[\hat{\overline{\rho}}_f(t)\left(1 + \hat{a}^\dagger\hat{a}\right)\right] \; .$$

(3.3.9)

The time evolving reduced density operators of the field, $\hat{\overline{\rho}}_f^g(t)$, in the AJC interaction is determined from Eq. (3.3.5b) by tracing $\hat{\overline{\rho}}_{gn}(t)$ over the atomic states according to

$$\hat{\overline{\rho}}_f^g(t) = tr_a(\hat{\overline{\rho}}_{gn}(t)) \quad ; \quad \hat{\overline{\rho}}_{gn}(t) = |\overline{\Psi}_{gn}(t)\rangle\langle\overline{\Psi}_{gn}(t)|$$

(3.3.10a)

to obtain

$$
\begin{aligned}
\hat{\bar{\rho}}_f^g(t) &= e^{-\alpha^2} \sum_{n=0}^{\infty} \left[\frac{\alpha^{2n}}{n!} \left(\cos^2(\overline{R}_{gn}t) + \overline{c}_{gn}^2 \sin^2(\overline{R}_{gn}t) \right) \right.\\
&\quad \left. + \frac{\alpha^{2(n-1)}}{(n-1)!} \overline{s}_{gn-1}^2 \sin^2(\overline{R}_{gn-1}t) \right] \otimes |n\rangle\langle n| .
\end{aligned}
\tag{3.3.10b}
$$

3.3.3.2 Mandel parameter

The Mandel Parameter defined in Eq. (1.4.1) is fundamental in characterising the quantum statistical properties of a system. We re-write it here in the form

$$
Q = \frac{\langle (\Delta \hat{\eta})^2 \rangle}{\langle \hat{\eta} \rangle} - 1 = \frac{\langle \hat{\eta}^2 \rangle - \langle \hat{\eta} \rangle^2}{\langle \hat{\eta} \rangle} - 1 \quad ; \quad \Delta \hat{\eta} = \sqrt{\langle \hat{\eta}^2 \rangle - \langle \hat{\eta} \rangle^2}
\tag{3.3.11}
$$

where, $\langle (\Delta \hat{\eta})^2 \rangle$, is the photon number variance, $\langle \hat{\eta} \rangle$, is the mean photon number and, $\hat{\eta} = \hat{a}\hat{a}^\dagger$, is anti-normal order operator of the number of particles (excitations).

Defining the mean square photon number $(t > 0)$

$$
\langle (\hat{a}\hat{a}^\dagger)^2 \rangle_{\mathtt{t}} = tr \left[\hat{\bar{\rho}}_f(t) \left(1 + \hat{a}^\dagger \hat{a} \right)^2 \right]
\tag{3.3.12}
$$

and considering the definition of the reduced density operator of the field in Eq. (3.3.10b) which we express in a compact form

$$
\begin{aligned}
\hat{\bar{\rho}}_f^g(t) &= \overline{J}_{gn}(t) \otimes |n\rangle\langle n| \quad ;\\
\overline{J}_{gn}(t) &= e^{-\alpha^2} \sum_{n=0}^{\infty} \left[\frac{\alpha^{2n}}{n!} \left(\cos^2(\overline{R}_{gn}t) + \overline{c}_{gn}^2 \sin^2(\overline{R}_{gn}t) \right) \right.\\
&\quad \left. + \frac{\alpha^{2(n-1)}}{(n-1)!} \overline{s}_{gn-1}^2 \sin^2(\overline{R}_{gn-1}t) \right] \quad ;\\
\hat{a}|n\rangle &= \sqrt{n}|n-1\rangle \quad ; \quad \hat{a}^\dagger|n\rangle = \sqrt{n+1}|n+1\rangle ,
\end{aligned}
\tag{3.3.13}
$$

the mean photon number defined in Eq. (3.3.9), mean square photon number defined in

Eq. (3.3.12) and hence the Mandel Q-parameter in Eq. (3.3.11) reduce to the forms

$$\langle \hat{\eta} \rangle = tr\left[\hat{\bar{\rho}}_f^g(t)(1 + \hat{a}^\dagger \hat{a})\right] = \overline{J}_{gn}(t)\langle n|(1 + \hat{a}^\dagger \hat{a})|n\rangle = (1 + n)\ \overline{J}_{gn}(t)\ ;$$

$$\langle \hat{\eta}^2 \rangle = tr\left[\hat{\bar{\rho}}_f^g(1 + \hat{a}^\dagger \hat{a})^2\right] = \overline{J}_{gn}(t)\langle n|(1 + \hat{a}^\dagger \hat{a})^2|n\rangle = (1 + n)^2\ \overline{J}_{gn}(t)\ ;$$

$$Q(t) = \frac{(1 + n)^2 \overline{J}_{gn}(t) - [(1 + n)\overline{J}_{gn}(t)]^2}{(1 + n)\overline{J}_{gn}(t)} - 1 = (1 + n)(1 - \overline{J}_{gn}(t)) - 1\ ,$$

$$(3.3.14)$$

after substituting the reduced field density operator in Eq. (3.3.10b) (or Eq. (3.3.13)).

We then plot the time evolution of $Q(t)$ in Eq. (3.3.14) for various values of sum frequency, $\overline{\delta} = \delta + 2\omega$, and field intensity, $|\alpha|^2$, noting the definitions of interaction parameters and Rabi frequency defined in Eq. (3.3.5d), and proceed to analyse the time evolution of $Q(t)$ during the AJC interaction, with focus on whether the nature of photons display Poissonian (coherent), super-Possonian (classical) or sub-Poissonian (nonclassical) statistics. For Poissonian $Q(t) = 0$, super-Poissonian $Q(t) > 0$ and sub-Poissonian $Q(t) < 0$.

3.4 AJC dynamics with field mode in an initial squeezed coherent state

Let us now consider when a field mode in an initial coherent squeezed state $|\alpha, \varsigma\rangle$ defined in Eq. (1.5.8a) is considered, which we re-write here in a general form

$$|\alpha, \varsigma\rangle = \overline{S}_n\ |n\rangle\ ;$$

$$\overline{S}_n = \frac{1}{\sqrt{\cosh(r)}}\ \exp\left[-\frac{1}{2}|\alpha|^2 - \frac{1}{2}\alpha^{*2}e^{i\theta}\tanh(r)\right]$$

$$\times\ \sum_{n=0}^{\infty} \frac{\left[\frac{1}{2}e^{i\theta}\tanh(r)\right]^{\frac{n}{2}}}{\sqrt{n!}}\ H_n\left[\gamma\left(e^{i\theta}\sinh(2r)\right)^{-\frac{1}{2}}\right]$$

$$(3.4.1a)$$

where r, ς is the squeeze, complex squeeze parameter in the form

$$\varsigma = r\ \exp(i\theta)\ ;\quad 0 \leq r < \infty\ ;\quad 0 \leq \theta \leq 2\pi\ ,\qquad (3.4.1b)$$

α the coherent amplitude and

$$\gamma = \alpha \cosh(r) + \alpha^* e^{i\theta} \sinh(r) \ . \tag{3.4.1c}$$

We define the average photon number, $\langle \hat{a}\hat{a}^\dagger \rangle$, for the squeezed state in Eq. (3.4.1a) in the form

$$|\alpha|^2 + \sinh^2(r) \tag{3.4.2}$$

such that if $|\alpha|^2 \gg \sinh^2(r)$, the coherent part of the state dominates the squeezed part.

The probability of finding n-photons $P(n)$ in the field during the AJC processes takes a general form

$$\begin{aligned}
P(n) &= |\langle n|\alpha,\varsigma\rangle|^2 \\
&= \frac{(\frac{1}{2}\tanh(r))^n}{n! \cosh(r)} \exp\left[-|\alpha|^2 - \frac{1}{2}\left(\alpha^{*2}e^{i\,\theta} + \alpha^2 e^{-i\,\theta}\right)\tanh(r)\right] \\
&\quad \times \left| H_n\left[\gamma\left(e^{i\,\theta}\sinh(2r)\right)^{-\frac{1}{2}}\right]\right|^2 \ .
\end{aligned} \tag{3.4.3}$$

If at $t = 0$, the atom is in a superposition of excited, $|e\rangle$, and, $|g\rangle$, state as defined in Eq. (3.3.1) and the field in an initial squeezed coherent state as defined in Eq. (3.4.1a) we easily obtain the initial atom-field state according to Eq. (3.3.2). When $B = 1$, $A = 0$, we determine as an example in the case of an atom in an initial ground state, $|g\rangle$, the AJC initial atom-field qubit state vector in the form

$$|\psi_{gn}\rangle_{AJC} = |\psi_g\rangle \otimes |\alpha,\varsigma\rangle \tag{3.4.4}$$

to obtain

$$|\psi_{gn}\rangle_{AJC} = \sum_{n=0}^{\infty} \overline{S}_n \, |g,n\rangle \ . \tag{3.4.5}$$

Here, we shall consider an initial squeezed coherent state with $\theta = 0$, and so $\varsigma = r$, α are real. This implies that the generalised squeezed coherent state, $|\alpha,\varsigma\rangle$, is now mapped onto $|\alpha,r\rangle$.

The exact solution $|\overline{\Psi}_{gn}(t)\rangle$ to the Schrödinger equation [10] for the AJC initial atom-field system in Eq. (3.4.5) takes the explicit form ($t > 0$)

$$
\begin{aligned}
|\overline{\Psi}_{gn}(t)\rangle &= e^{-\frac{i}{\hbar}\hat{\overline{H}}_g t}\,|g,n\rangle = \sum_{n=0}^{\infty}\Big[e^{-i\omega\left(n+\frac{3}{2}\right)t}\,\overline{S}_n\,\Big(\cos(\overline{R}_{gn}t) \\
&\quad + i\overline{c}_{gn}\sin(\overline{R}_{gn}t)\Big)|g\rangle - i e^{-i\omega\left(n+\frac{1}{2}\right)t}\,\overline{S}_{n-1}\,\overline{s}_{gn-1}\sin(\overline{R}_{gn-1})|e\rangle\Big]\otimes|n\rangle\ ; \\
\overline{R}_{gn} &= \frac{\lambda}{2}\sqrt{4n+4+(\beta+2\xi)^2}\quad;\quad \overline{c}_{gn} = \frac{(\beta+2\xi)}{\sqrt{4n+4+(\beta+2\xi)^2}} \\
\overline{s}_{gn} &= \sqrt{\frac{4(n+1)}{4n+4+(\beta+2\xi)^2}}\quad;\quad \overline{\delta} = \delta + 2\omega\quad;\quad \xi = \frac{\omega}{\lambda}\quad;\quad \beta = \frac{\delta}{\lambda}\ .
\end{aligned}
$$

$$(3.4.6)$$

The final form of Eq. (3.3.5d) has been arrived at through Schmidt decomposition [28] and so the two interacting atom, field quantum systems are entangled.

3.4.1 Photon statistics

We shall examine the nature of photon statistics during the AJC interaction by applying the Mandel Q-parameter defined in Eq. (3.3.11). The initial average photon number is of the form of Eq. (3.4.5). At any $t>0$, the mean, mean square photon number evolve in time according to Eqs. (3.3.9), (3.3.12).

The time evolving reduced density operator of the field $\hat{\overline{\rho}}_f^g(t)$ during the AJC interaction determined from Eq. (3.3.5d) is obtained explicitly as

$$
\begin{aligned}
\hat{\overline{\rho}}_f^g(t) &= tr_a(|\overline{\Psi}_{gn}(t)\rangle\langle\overline{\Psi}_{gn}(t)|) = \sum_{n=0}^{\infty}\Big[\overline{S}_n^2\Big(\cos^2(\overline{R}_{gn}t) + \overline{c}_{gn}^2\sin^2(\overline{R}_{gn}t)\Big) \\
&\quad + \overline{S}_{n-1}^2\,\overline{s}_{gn-1}^2\sin^2(\overline{R}_{gn-1}t)\Big]\otimes|n\rangle\langle n|\ .
\end{aligned}
$$

$$(3.4.7)$$

With the reduced field density operator in Eq. (3.4.7), mean, mean square photon number defined in Eqs. (3.3.9), (3.3.12) we easily evaluate $Q(t)$ in Eq. (3.3.11) in the following; Re-writing $\hat{\overline{\rho}}_f^g(t)$ in Eq. (3.4.7) and noting the actions of the annihilation,

creation operatiors $\hat{a}$, $\hat{a}^\dagger$ on the number state, $|n\rangle$, in the forms

$$\hat{\bar{\rho}}_f^g(t) = \overline{Z}_{gn}(t) \otimes |n\rangle\langle n| \quad ;$$

$$\overline{Z}_{gn}(t) = \sum_{n=0}^{\infty} \left[\overline{S}_n^2 \Big(\cos^2(\overline{R}_{gn}t) + \bar{c}_{gn}^2 \sin^2(\overline{R}_{gn}t) \Big) \right.$$

$$\left. + \overline{S}_{n-1}^2\, \bar{s}_{gn-1}^2 \sin^2(\overline{R}_{gn-1}t) \right] \quad ;$$

$$\hat{a}|n\rangle = \sqrt{n}|n-1\rangle \quad ; \quad \hat{a}^\dagger|n\rangle = \sqrt{n+1}|n+1\rangle \; , \tag{3.4.8}$$

the mean photon number defined in Eq. (3.3.9), mean square photon number defined in Eq. (3.3.12) and hence the Mandel Q-parameter in Eq. (3.3.11) reduce into the respective forms

$$\langle \hat{\eta} \rangle = tr\left[\hat{\bar{\rho}}_f^g(t)(1+\hat{a}^\dagger\hat{a})\right] = \overline{Z}_{gn}(t)\langle n|(1+\hat{a}^\dagger\hat{a})|n\rangle = (1+n)\,\overline{Z}_{gn}(t) \quad ;$$

$$\langle \hat{\eta}^2 \rangle = tr\left[\hat{\bar{\rho}}_f^g(1+\hat{a}^\dagger\hat{a})^2\right] = \overline{Z}_{gn}(t)\langle n|(1+\hat{a}^\dagger\hat{a})^2|n\rangle = (1+n)^2\,\overline{Z}_{gn}(t) \quad ;$$

$$Q(t) = \frac{(1+n)^2\overline{Z}_{gn}(t) - [(1+n)\overline{Z}_{gn}(t)]^2}{(1+n)\overline{Z}_{gn}(t)} - 1 = (1+n)(1-\overline{Z}_{gn}(t)) - 1 \; ,$$

$$\tag{3.4.9}$$

after substituting the reduced field density operator in Eq. (3.4.7) (or Eq. (3.4.8)).

At different values of r parameter. We then plot time evolution of the Mandel Q-parameter $Q(\tau)$ (where $\tau = \lambda t$ is the scaled time) for an initial atomic ground state, $|g\rangle$, in an initial squeezed coherent state while noting the definitions of interaction parameters and Rabi frequency defined in Eq. (3.4.6). For super-Poissonian photon statistics $Q(t) > 0$, sub-Poissonian $Q(t) < 0$ and Poissonian $Q(t) = 0$.

3.4.2 Evolution of atomic population inversion and entropy of entanglement

To describe the evolution of the atom alone we introduce the reduced density matrices of the atom by tracing the AJC density operator $\hat{\bar{\rho}}_{gn}(t)$ over the field states determined from Eq. (3.4.6) according to

$$\hat{\bar{\rho}}_a^g(t) = tr_f\left(|\overline{\Psi}_{gn}(t)\rangle\langle\overline{\Psi}_{gn}(t)|\right) \tag{3.4.10a}$$

taking explicit form

$$
\begin{aligned}
\hat{\bar{\rho}}_a^g(t) &= \sum_{n=0}^{\infty} \Big[\overline{S}_n^2 \Big(\cos^2(\overline{R}_{gn}t) + \bar{c}_{gn}^2 \sin^2(\overline{R}_{gn}t) \Big) |g\rangle\langle g| \\
&\quad + i\, \overline{S}_n\, \overline{S}_{n-1}\, \bar{s}_{gn-1} e^{-i\omega t} \sin(\overline{R}_{gn-1}t)\Big(\cos(\overline{R}_{gn}t) + i\bar{c}_{gn}\sin(\overline{R}_{gn}t) \Big)|g\rangle\langle e| \\
&\quad - i\, \overline{S}_n\, \overline{S}_{n-1}\, \bar{s}_{gn-1} e^{i\omega t} \sin(\overline{R}_{gn-1}t)\Big(\cos(\overline{R}_{gn}t) - i\bar{c}_{gn}\sin(\overline{R}_{gn}t) \Big)|e\rangle\langle g| \\
&\quad + \overline{S}_{n-1}^2\, \bar{s}_{gn-1}^2 \sin^2(\overline{R}_{gn-1}t)|e\rangle\langle e| \Big] \\
&= \sum_{n=0}^{\infty} \Big[\overline{P}_{gg}|g\rangle\langle g| + \overline{P}_{ge}|g\rangle\langle e| + \overline{P}_{eg}|e\rangle\langle g| + \overline{P}_{ee}|e\rangle\langle e| \Big] \;.
\end{aligned}
$$

(3.4.10b)

We then define the time evolving Bloch vector in the AJC interaction process, $\vec{\bar{r}}(t) = \bar{r}_x(t)\hat{i} + \bar{r}_y(t)\hat{j} + \bar{r}_z(t)\hat{k}$, with components obtained as $\bar{r}_x(t) = tr\left(\hat{\sigma}_x \hat{\bar{\rho}}_a^g(t) \right)$, $\bar{r}_y(t) = tr\left(\hat{\sigma}_y \hat{\bar{\rho}}_a^g(t) \right)$, $\bar{r}_z(t) = tr\left(\hat{\sigma}_z \hat{\bar{\rho}}_a^g(t) \right)$ taking respective explicit forms

$$
\begin{aligned}
\bar{r}_x(t) &= \sum_{n=0}^{\infty} \Big[\overline{S}_n\, \overline{S}_{n-1}\, \Big(2\bar{s}_{gn-1}\sin(\overline{R}_{gn-1}t)\cos(\overline{R}_{gn}t)\sin(\omega t) - 2\bar{s}_{gn-1}\bar{c}_{gn} \\
&\qquad \sin(\overline{R}_{gn-1}t)\sin(\overline{R}_{gn}t)\cos(\omega t) \Big) \Big] \;; \\
\bar{r}_y(t) &= \sum_{n=0}^{\infty} \Big[\overline{S}_n\, \overline{S}_{n-1}\Big(2\bar{s}_{gn-1}\sin(\overline{R}_{gn-1}t)\cos(\overline{R}_{gn}t)\cos(\omega t) + 2\bar{s}_{gn-1}\bar{c}_{gn} \\
&\qquad \sin(\overline{R}_{gn-1}t)\sin(\overline{R}_{gn}t)\sin(\omega t) \Big) \Big] \;; \\
\bar{r}_z(t) &= \sum_{n=0}^{\infty} \Big[\overline{S}_{n-1}^2\, \bar{s}_{gn-1}^2 \sin^2(\overline{R}_{gn-1}t) - \overline{S}_n^2\, \Big(\cos^2(\overline{R}_{gn}t) + \bar{c}_{gn}^2 \sin^2(\overline{R}_{gn}t) \Big) \Big] \;.
\end{aligned}
$$

(3.4.11)

We shall use the time evolving Bloch vector components in Eq. (3.4.11) to evaluate time evolution of atomic population inversion, $W(t)$, and the time evolution of the von Neumann entropy, $S_a(t)$, (as a measure of DEM).

The atomic population inversion, $W(t)$, [34] is defined as the difference between the

excited and ground state probabilities

$$
\begin{aligned}
W(t) &= tr\left(\hat{\sigma}_z \hat{\bar{\rho}}_a(t)\right) \\
&= tr\left[\begin{pmatrix} 1 & 0 \\ 0 & -1 \end{pmatrix} \begin{pmatrix} \sum_{n=0}^{\infty} \overline{P}_{ee}(t) & \sum_{n=0}^{\infty} \overline{P}_{eg}(t) \\ \sum_{n=0}^{\infty} \overline{P}_{ge}(t) & \sum_{n=0}^{\infty} \overline{P}_{gg}(t) \end{pmatrix}\right] \\
&= \sum_{n=0}^{\infty} \left(\overline{P}_{ee}(t) - \overline{P}_{gg}(t)\right) \ ,
\end{aligned}
\tag{3.4.12a}
$$

which is of the exact form as the z-component $\overline{r}_z(t)$ in Eq. (3.4.11) of the time evolving AJC Bloch vector.

As presented in Eq. (3.3.7b), the revival time, τ_R, of atomic population inversion, $W(t)$, is determined as established in [173] in the form

$$
\tau_R \simeq \frac{\pi}{\sqrt{\frac{\bar{\delta}^2}{4\lambda^2} + (|\alpha|^2 + 1)} - \sqrt{\frac{\bar{\delta}^2}{4\lambda^2} + |\alpha|^2}} \quad ; \quad \bar{\delta} = \delta + 2\omega
\tag{3.4.12b}
$$

since the AJC process is permanently detuned even at resonance, $\delta = 0$, i.e., $\bar{\delta} = 2\omega$.

Using the definitions of $\overline{r}_z(t)$ in Eq. (3.4.11), we plot $W(t)$ during the AJC processes. The atomic population inversion $W(t)$ evolves in time in the range $[-1, 1]$.

In order to discuss the collapses and revival phenomenon in relation to degree of entanglement we again apply the von Neumann entropy $S_a(t)$ in Eq. (3.3.8) (or (1.8.9)) defined in terms of the length of the time evolving AJC Bloch vector $\vec{r}(t)$. We again evaluate the eigenvalues π_1, π_2 considering the definition of the time evolving AJC Bloch vector components in Eq. (3.4.11).

Plots of $S_a(t)$ at different values of squeeze parameter r are then easily plotted. The DEM $S_a(t)$ evolves in time in the range $[0,1]$, i.e, $S_a(t) = 0$ quantifies disentanglement and consequently the atom, field quantum systems evolve to pure state, $S_a(t) = 1$ maximum entanglement consequently maximally mixed atom-field states else if $0 < S_a(t) < 1$ entangled and so partially mixed atom-field states.

CHAPTER 4
RESULTS

In this chapter, we present the results of the AJC interaction generated by the AJC Hamiltonian, $\overline{\hat{H}}$, in Eq. (3.1.4) and compare step-wise with the extensively studied JC interaction generated by the JC Hamiltonian, $\hat{H}$, in Eq. (3.1.3) including relevant cited references as provided in the appendices. To be exact, in Sec. 4.1 we present findings of the AJC interactions when a two-level atom interacts with a quantised field mode in Fock state, in Sec. 4.2 results of the AJC interactions when a field mode in an initial coherent state is considered and in Sec. 4.3 results of the AJC interactions when a field mode in an initial squeezed coherent state is considered.

4.1   AJC dynamics and application in QIP

4.1.1   Rabi oscillations

We begin by remarking that the QRM defined in Eq. (3.1.1) has two dynamical frames, specifically, the rotating frame (RF) and the counter(anti-)rotating frame (CRF). Dynamics in the RF is governed by the JC interaction mechanism and through a $U(1)$ symmetry transformation generated by the JC excitation number operator, $\hat{N}$, in Eq. (3.1.3), the QRM Hamiltonian in Eq. (3.1.1) is approximated by an effective JC Hamiltonian, $\hat{H}$, in Eq. (3.1.3) in a rotating wave approximation (RWA). In the RWA [15, 27, 175], the coupling strength, λ, is much weaker than the mode frequency, ω, i.e., $\lambda \leqslant |\omega|$. In this circumstances, if the qubit is close to resonance, $|\omega_0| - |\omega| \simeq 0$, and $|\omega_0 + \omega| \geqslant |\omega_0 - \omega|$ holds, the RWA can be applied. This implies neglecting terms that rotate at frequency $\omega_0 + \omega$, leading to the JC model. On the other hand, dynamics in the CRF is controlled by the AJC interaction mechanism through a $U(1)$ symmetry transformation generated by the conserved AJC excitation number, $\overline{\hat{N}}$, defined in Eq. (3.1.4). The QRM Hamiltonian is approximated by an effective AJC Hamiltonian, $\overline{\hat{H}}$, in Eq. (3.1.4) in the counter(anti) rotating wave approximation (CRWA) according to $|\omega_0 - \omega| \geqslant |\omega_0 + \omega|$. Here, we neglect terms that rotate at frequencies $\omega_0 - \omega$, leading to the AJC Hamiltonian in Eq. (3.1.4).

In order to expound on the aforementioned, theoretical and experimental designs of the full QRM dynamics has the CRF interpreted in the USC and DSC regimes [15, 175] during which the RWA is no longer valid (breaksdown) and so the CRT cannot be neglected. This is not the framework considered in this Thesis. Here, the exactly solvable AJC model

is studied independently and not in the full QRM. In the forthcoming, the dimensionless coupling parameter ratio $\frac{\lambda}{\omega}$, does not apply as discussed in the USC and DSC cases [15, 175], in the sense that it does not affect the dynamical evolution described by the time evolving state vector, $|\overline{\Psi}_{gn}(t)\rangle$, but only the fundamental dynamical features as we discuss in the following.

In the specific example starting with an atom in the ground state, $|g\rangle$, and the field mode in the vacuum state, $|0\rangle$, the basic qubit state vectors $|\psi_{g0}\rangle$ and $|\overline{\phi}_{g0}\rangle$, together with the corresponding entanglement parameters, are obtained by setting $n = 0$ in Eqs. (3.2.2) - (3.2.4) in the form

$$
\begin{aligned}
|\psi_{g0}\rangle &= |g,0\rangle \quad ; \quad |\overline{\phi}_{g0}\rangle = -\overline{c}_{g0}|g,0\rangle + \overline{s}_{g0}|e,1\rangle \; ; \\
\overline{c}_{g0} &= \frac{\overline{\delta}}{2\overline{R}_{g0}} \quad ; \quad \overline{s}_{g0} = \frac{2\lambda}{\overline{R}_{g0}} \quad ; \quad \overline{R}_{g0} = \frac{1}{2}\sqrt{16\lambda^2 + \overline{\delta}^2} \; ; \\
|g,0\rangle &= |g\rangle \otimes |0\rangle \quad ; \quad |e,1\rangle = |e\rangle \otimes |1\rangle \; .
\end{aligned}
\tag{4.1.1}
$$

The corresponding AJC Hamiltonian in Eq. (3.2.8) becomes $(n = 0)$

$$
\hat{\overline{H}}_g = \frac{3}{2}\hbar\omega\hat{\overline{I}}_g + \hbar\overline{R}_{g0}\hat{\overline{\varepsilon}}_g \; .
\tag{4.1.2}
$$

The time-evolving AJC state vector in Eq. (3.2.11) takes the form $(n = 0)$

$$
|\overline{\Psi}_{g0}(t)\rangle = e^{-i\frac{3}{2}\omega t}\left\{\cos(\overline{R}_{g0}t)|\psi_{g0}\rangle - i\sin(\overline{R}_{g0}t)|\overline{\phi}_{g0}\rangle\right\}
\tag{4.1.3}
$$

which describes Rabi oscillations at Rabi frequency, $\overline{R}_{g0}$, between the initial separable qubit state vector, $|\psi_{g0}\rangle$, and the entangled transition qubit state vector, $|\overline{\phi}_{g0}\rangle$.

The Rabi oscillation process is best described by the corresponding AJC Bloch vector which follows from Eq. (3.2.12g) in the form $(n = 0)$

$$
\vec{\overline{\rho}}_{g0}(t) = \left(0, -\sin(2\overline{R}_{g0}t), \cos(2\overline{R}_{g0}t)\right) \; .
\tag{4.1.4}
$$

(a) AJC   (b) JC

Figure 4.1: Rabi oscillations in the AJC interaction mechanism. Fig. 4.1(a): The Rabi oscillations for values of sum frequencies are shown by red ($\overline{\delta} = 5\lambda$; $\delta = \lambda$), black ($\overline{\delta} = 7\lambda$; $\delta = 3\lambda$) and blue ($\overline{\delta} = 4\lambda$; $\delta = \omega_0 - \omega = 0$). Fig. 4.1(b) [Rabi oscillations in the JC interaction extracted from Fig. A.1]: Blue circle is at resonance with frequency detuning $\delta = \omega_0 - \omega = 0$, red circle is for $\delta = \lambda$ and black circle $\delta = 3\lambda$

The time evolution of this AJC Bloch vector in Fig. 4.1(a) reveals that the Rabi oscillations between the basic qubit state vectors $|\psi_{g0}\rangle$, $|\overline{\phi}_{g0}\rangle$ in the AJC process, describe circles on which the states are distributed on the Bloch sphere.

In Fig. 4.1(a) we have plotted the AJC Rabi oscillation process with respective Rabi frequencies $\overline{R}_{g0}$ determined according to Eq. (4.1.1) for various values of sum frequency $\overline{\delta} = \omega_0 + \omega$. We have provided a comparison with plots of the corresponding JC process in Fig. 4.1(b) extracted from Fig. A.1 in Sec. A.2.1.

To facilitate the desired comparison of the AJC Rabi oscillation process with the standard JC Rabi oscillation process plotted in Fig. 4.1(b), we substitute the redefinition $\overline{\delta} = \omega_0 + \omega = \delta + 2\omega$ to express the Rabi frequency $\overline{R}_{g0}$ in Eq. (4.1.1) in the form

$$\overline{R}_{g0} = \frac{1}{2}\sqrt{16\lambda^2 + (\delta + 2\omega)^2}\,. \tag{4.1.5}$$

We have arbitrarily chosen the field mode frequency $\omega = 2\lambda$ ($\lambda = 0.5\omega$) such that for both AJC and JC processes in Figs. 4.1(a) and 4.1(b) (including plots in Fig. A.1) we vary only the detuning frequency $\delta = \omega_0 - \omega$. The resonance case $\delta = 0$ in the JC interaction now means $\overline{\delta} = 2\omega = 4\lambda$ in the AJC interaction.

For purposes of comparison, considering only three arbitrary values of frequency de-

tuning $\delta = \lambda$, 3λ, 0 and noting that λ and δ are both in units of frequency (s^{-1}) we easily determine $\overline{R}_{g0}$ in Eq. (4.1.5). We also use the general time evolving AJC state vector in Eq. (4.1.3),

$$|\overline{\Psi}_{g0}(t)\rangle = e^{-i\frac{3}{2}\omega t}\left\{\cos(\overline{R}_{g0}t)|\psi_{g0}\rangle - i\sin(\overline{R}_{g0}t)|\overline{\phi}_{g0}\rangle\right\} \qquad (4.1.3')$$

with $\overline{R}_{g0}$ as defined in Eq. (4.1.5) at values of $\overline{\delta} = 4\lambda$ ($\delta = 0$), 5λ ($\delta = \lambda$), 7λ ($\delta = 3\lambda$) to determine the coupled qubit state vectors $|\psi_{g0}\rangle$, $|\overline{\phi}_{g0}\rangle$ in Eq. (4.1.1) by setting $\overline{R}_{g0}t = \frac{\pi}{2}$, describing half cycle of Rabi oscillation as presented in Eqs. (4.1.6a) - (4.1.6c). In each case, we have an accumulated global phase factor which does not affect measurement results, but we have maintained them here in Eqs. (4.1.6a) - (4.1.6c) to explain the continuous time evolution over one cycle.

$$\delta = \lambda \quad ; \quad \overline{\delta} = 5\lambda \quad : \quad |g,0\rangle \rightarrow e^{-i\pi\frac{79}{82}}\left\{-\frac{5}{\sqrt{41}}|g,0\rangle + \frac{4}{\sqrt{41}}|e,1\rangle\right\} \rightarrow e^{-i\pi\frac{79}{41}}|g,0\rangle$$
$$(4.1.6a)$$

$$\delta = 3\lambda \quad ; \quad \overline{\delta} = 7\lambda \quad : \quad |g,0\rangle \rightarrow e^{-i\pi\frac{113}{130}}\left\{-\frac{7}{\sqrt{65}}|g,0\rangle + \frac{4}{\sqrt{65}}|e,1\rangle\right\} \rightarrow e^{-i\pi\frac{113}{65}}|g,0\rangle$$
$$(4.1.6b)$$

$$\delta = 0 \quad ; \quad \overline{\delta} = 4\lambda \quad : \quad |g,0\rangle \rightarrow e^{-i\pi}\left\{-\frac{1}{\sqrt{2}}|g,0\rangle + \frac{1}{\sqrt{2}}|e,1\rangle\right\} \rightarrow e^{-i\pi 2}|g,0\rangle \quad (4.1.6c)$$

The AJC Rabi oscillations for frequency detuning cases $\delta = \lambda, 3\lambda, 0$ are plotted as red, black and blue circles in Fig. 4.1(a), while the corresponding plots in the JC process are provided in Fig. 4.1(b)[or Fig. A.1] as a comparison. Here, Fig. 4.1(a) is a Bloch sphere entanglement [145] that corresponds to a 2-dimensional subspace of $\mathbb{C}^2 \otimes \mathbb{C}^2$ Span$\{|g,0\rangle, -\overline{c}_{g0}|g,0\rangle + \overline{s}_{g0}|e,1\rangle\}$ with $\overline{c}_{g0} = \frac{\overline{\delta}}{2\overline{R}_{g0}}$ and $\overline{s}_{g0} = \frac{2\lambda}{\overline{R}_{g0}}$ while Fig. 4.1(b) [or Fig. A.1] corresponds to a 2-dimensional subspace of $\mathbb{C}^2 \otimes \mathbb{C}^2$ Span$\{|e,0\rangle, c_{e0}|e,0\rangle + s_{e0}|g,1\rangle\}$ with $c_{e0} = \frac{\delta}{2R_{e0}}$ and $s_{e0} = \frac{2\lambda}{R_{e0}}$.

In Fig. 4.1 we observe:

(i) that due to the larger sum frequency $\overline{\delta} = \delta + 2\omega$ in the AJC interaction process as compared to the detuning frequency δ in the JC interaction process, the Rabi oscillation circles in the much faster AJC process are much smaller compared to the corresponding Rabi oscillation circles in the slower JC interaction process in

70

Fig. 4.1(b). This effect is in agreement with the assumption usually adopted to drop the AJC interaction components in the rotating wave approximation (RWA), noting that the fast oscillating AJC process averages out over time. We have demonstrated the physical property that the size of the Rabi oscillations curves decreases with increasing Rabi oscillation frequency by plotting the AJC oscillation curves for a considerably larger Rabi frequency $\overline{R}_{g0}$ where we have set the field mode frequency $\omega = 10\lambda(\lambda = 0.1\omega)$ in Fig. 4.2. It is clear in Fig. 4.2 that for this higher value of the Rabi frequency $\overline{R}_{g0}$ the Rabi oscillation curves almost converge to a point-like form
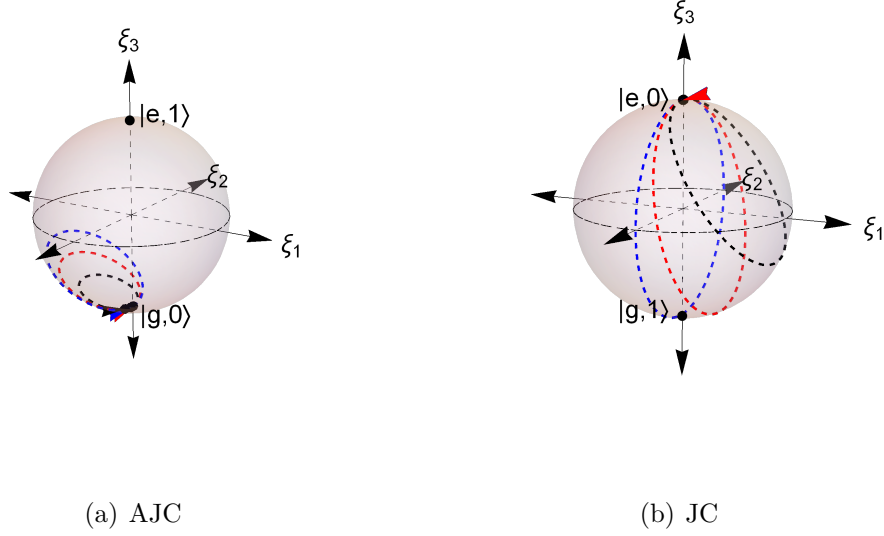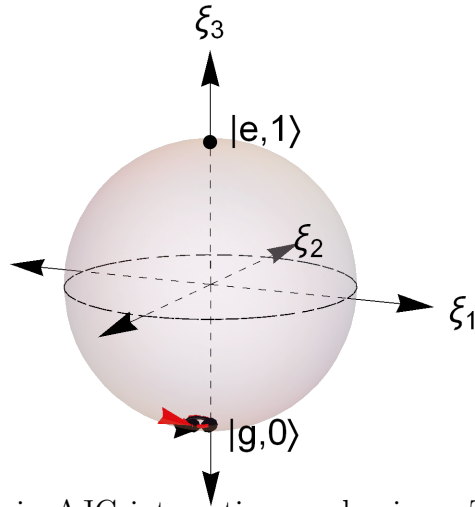

Figure 4.2: Rabi oscillations in AJC interaction mechanism. The Rabi oscillations for values of sum frequencies are shown by red ($\overline{\delta} = 21\lambda$; $\delta = \lambda$) and black ($\overline{\delta} = 23\lambda$; $\delta = 3\lambda$).

(ii) that Rabi oscillations in the AJC interaction process as demonstrated in Fig. 4.1(a) occur in the left hemisphere of the Bloch sphere while in the JC interaction process the oscillations occur in the right hemisphere as demonstrated in Fig. 4.1(b). This demonstrates an important physical property that the AJC interaction process occurs in the reverse sense relative to the JC interaction process;

(iii) an interesting feature that appears at resonance specified by $\delta = 0$. While in the JC model plotted in Fig 4.1(b) the Rabi oscillation at resonance $\delta = 0$ (blue circle) lies precisely on the yz-plane normal to the equatorial plane, the corresponding AJC Rabi oscillation (blue circle in Fig. 4.1(a)) is at an axis away from the yz-plane about the south pole of the Bloch sphere. This feature is due to the fact that the sum frequency $\overline{\delta} = 2\omega$ takes a non-zero value under resonance $\delta = 0$ such that the AJC oscillations maintain their original forms even under resonance.

71

We note that the qubit state transitions described by the Bloch vector in the AJC process (Fig. 4.1(a)) are blue sideband transitions characterised by the sum frequency $\bar{\delta} = \omega_0 + \omega = \delta + 2\omega$ according to the definition of the Rabi frequency $\overline{R}_{g0}$ in Eq. (4.1.5).

4.1.2 Entanglement analysis of basic qubit state vectors $|\psi_{g0}\rangle$ and $|\overline{\phi}_{g0}\rangle$ and teleportation in the AJC model

In this section we analyse the entanglement properties of the qubit state vectors, teleportation and the dynamical evolution of entanglement generated in the AJC interaction.

4.1.2.1 Entanglement properties

Let us start by considering the entanglement properties of the initial state $|\psi_{g0}\rangle$ which according to the definition in Eq. (4.1.1) is a separable pure state. The density operator of the qubit state vector $|\psi_{g0}\rangle = |g, 0\rangle$ is obtained as

$$\hat{\rho}_{g0} = |g, 0\rangle\langle g, 0| . \tag{4.1.7a}$$

Using the definition $|g, 0\rangle = |g\rangle \otimes |0\rangle$, we take the partial trace of $\hat{\rho}_{g0}$ in Eq. (4.1.7a) with respect to the field mode and atom states respectively, to obtain the respective atom and field reduced density operators $\hat{\rho}_a$, $\hat{\rho}_f$ in the form (subscripts $a \equiv atom$ and $f \equiv field$)

$$\hat{\rho}_a = tr_f(\hat{\rho}_{g0}) = |g\rangle\langle g| \quad ; \quad \hat{\rho}_f = tr_a(\hat{\rho}_{g0}) = |0\rangle\langle 0| \quad ; \quad |g\rangle = \begin{pmatrix} 0 \\ 1 \end{pmatrix} \quad ; \quad |0\rangle = \begin{pmatrix} 1 \\ 0 \end{pmatrix} \tag{4.1.7b}$$

which take explicit 2×2 matrix forms

$$\hat{\rho}_a = \begin{pmatrix} 0 & 0 \\ 0 & 1 \end{pmatrix} \quad ; \quad \hat{\rho}_f = \begin{pmatrix} 1 & 0 \\ 0 & 0 \end{pmatrix} . \tag{4.1.7c}$$

The trace of $\hat{\rho}_a, \hat{\rho}_a^2$ and $\hat{\rho}_f, \hat{\rho}_f^2$ of the matrices in Eq. (4.1.7c) are

$$tr(\hat{\rho}_a) = tr(\hat{\rho}_a^2) = tr\begin{pmatrix} 0 & 0 \\ 0 & 1 \end{pmatrix} = 1 \quad ; \quad tr(\hat{\rho}_f) = tr(\hat{\rho}_f^2) = tr\begin{pmatrix} 1 & 0 \\ 0 & 0 \end{pmatrix} = 1 . \tag{4.1.7d}$$

The unit trace determined in Eq. (4.1.7d) proves that the initial qubit state vector $|\psi_{g0}\rangle = |g, 0\rangle$ is a pure state (see Sec. 1.3.1).

Next, we substitute the matrix form of $\hat{\rho}_a$ and $\hat{\rho}_f$ from Eq. (4.1.7c) into Eq. (3.2.14) according to

$$
\begin{aligned}
S(\hat{\rho}_a) &= -tr(\hat{\rho}_a \log_2 \hat{\rho}_a) \\
&= -tr\left[\begin{pmatrix} 1 & 0 \\ 0 & 0 \end{pmatrix} \log_2 \begin{pmatrix} 1 & 0 \\ 0 & 0 \end{pmatrix}\right] = -tr\left[\begin{pmatrix} \log_2(1) & \log_2(0) \\ 0 & 0 \end{pmatrix}\right] = 0 \ ; \\
S(\hat{\rho}_f) &= -tr(\hat{\rho}_f \log_2 \hat{\rho}_f) \\
&= -tr\left[\begin{pmatrix} 0 & 0 \\ 0 & 1 \end{pmatrix} \log_2 \begin{pmatrix} 0 & 0 \\ 0 & 1 \end{pmatrix}\right] = -tr\left[\begin{pmatrix} 0 & 0 \\ \log_2(0) & \log_2(1) \end{pmatrix}\right] = 0 \ . \\
\Rightarrow E(\hat{\rho}_{g0}) &= S(\hat{\rho}_a) = S(\hat{\rho}_f) = 0 \ . \tag{4.1.7e}
\end{aligned}
$$

The equal von Neumann entanglement entropies in Eq. (4.1.7e) together with the property in Eq. (4.1.7d) quantifies the initial qubit state vector $|\psi_{g0}\rangle = |g, 0\rangle$ as a pure separable state, agreeing with the definition in Eq. (4.1.1).

We proceed to determine the entanglement properties of the (transition) qubit state vector $|\overline{\phi}_{g0}\rangle$ defined in Eq. (4.1.1). For parameter values $\delta = \lambda$, $\overline{\delta} = 5\lambda$ we ignore the phase factor in Eq. (4.1.6a), to write the transition qubit state vector in the form

$$
\delta = \lambda \quad ; \quad \overline{\delta} = 5\lambda : \quad |\overline{\phi}_{g0}\rangle = -\frac{5}{\sqrt{41}}|g, 0\rangle + \frac{4}{\sqrt{41}}|e, 1\rangle \ , \tag{4.1.8a}
$$

where again we note that $\lambda, \delta, \overline{\delta}$ are of units of frequency, per second (s^{-1}), hence the representation $\delta = \lambda$, $\overline{\delta} = 5\lambda$ is adopted in evaluation of the Rabi frequency $\overline{R}_{g0}$ and interaction parameters $\overline{c}_{g0}, \overline{s}_{g0}$ in Eqs. (4.1.1) and (4.1.5).

The corresponding density operator of the state in Eq. (4.1.8a) is

$$
\hat{\overline{\rho}}_{g0} = \frac{25}{41}|g, 0\rangle\langle g, 0| - \frac{20}{41}|g, 0\rangle\langle e, 1| - \frac{20}{41}|e, 1\rangle\langle g, 0| + \frac{16}{41}|e, 1\rangle\langle e, 1| \tag{4.1.8b}
$$

which takes the explicit 4×4 matrix form

$$
\hat{\overline{\rho}}_{g0} = \frac{1}{41}\begin{pmatrix} 0 & 0 & 0 & 0 \\ 0 & 16 & -20 & 0 \\ 0 & -20 & 25 & 0 \\ 0 & 0 & 0 & 0 \end{pmatrix} \tag{4.1.8c}
$$

with eigenvalues $\lambda_1 = 1$, $\lambda_2 = 0$, $\lambda_3 = 0$, $\lambda_4 = 0$. Applying Eq. (3.2.13), its von Neumann entropy

$$
\begin{aligned}
S(\hat{\bar{\rho}}_{g0}) &= -1 \log_2 1 - 0 \log_2 0 - 0 \log_2 0 - 0 \log_2 0 \\
&= 0
\end{aligned}
\tag{4.1.8d}
$$

quantifying the state $|\bar{\phi}_{g0}\rangle$ in Eq. (4.1.8a) as a bipartite pure state.

Taking the partial trace of $\hat{\bar{\rho}}_{g0}$ in Eq. (4.1.8b) with respect to the field mode and atom states respectively, we obtain the respective atom and field reduced density operators $\hat{\bar{\rho}}_a, \hat{\bar{\rho}}_f$ together with their squares in the form

$$
\begin{aligned}
\hat{\bar{\rho}}_a &= tr_f(\hat{\bar{\rho}}_{g0}) = \frac{25}{41}|g\rangle\langle g| + \frac{16}{41}|e\rangle\langle e| = \frac{1}{41}\begin{pmatrix} 16 & 0 \\ 0 & 25 \end{pmatrix} \quad ; \\
\Rightarrow \hat{\bar{\rho}}_a^2 &= \frac{625}{1681}|g\rangle\langle g| + \frac{256}{1681}|e\rangle\langle e| = \frac{1}{1681}\begin{pmatrix} 256 & 0 \\ 0 & 625 \end{pmatrix} \quad ; \\
\hat{\bar{\rho}}_f &= tr_a(\hat{\bar{\rho}}_{g0}) = \frac{25}{41}|0\rangle\langle 0| + \frac{16}{41}|1\rangle\langle 1| = \frac{1}{41}\begin{pmatrix} 25 & 0 \\ 0 & 16 \end{pmatrix} \quad ; \\
\Rightarrow \hat{\bar{\rho}}_f^2 &= \frac{625}{1681}|0\rangle\langle 0| + \frac{256}{1681}|1\rangle\langle 1| = \frac{1}{1681}\begin{pmatrix} 625 & 0 \\ 0 & 256 \end{pmatrix} \quad .
\end{aligned}
\tag{4.1.8e}
$$

The trace of $\hat{\bar{\rho}}_a^2$ and $\hat{\bar{\rho}}_f^2$ in Eq. (4.1.8e) gives

$$
tr(\hat{\bar{\rho}}_a^2) = tr(\hat{\bar{\rho}}_f^2) = \frac{881}{1681} < 1
\tag{4.1.8f}
$$

demonstrating that $\hat{\bar{\rho}}_a$ and $\hat{\bar{\rho}}_f$ are mixed states, satisfying the general property $tr(\hat{\rho}_{a(f)}^2) < 1$ for a mixed state $\hat{\rho}_{a(f)}$ as defined in Eq. (1.3.15).

To quantify the mixedness we determine the length of the Bloch vector along the z-axis as follows

$$
r_z = tr(\hat{\bar{\rho}}_a \hat{\sigma}_z) = tr(\hat{\bar{\rho}}_f \hat{\sigma}_z) = \frac{9}{41}
\tag{4.1.8g}
$$

which shows that the reduced density operators $\hat{\bar{\rho}}_a, \hat{\bar{\rho}}_f$ are non-maximally mixed states.

The eigenvalues (λ_1, λ_2) of $\hat{\bar{\rho}}_a$ and $\hat{\bar{\rho}}_f$ are $\left(\frac{16}{41}, \frac{25}{41}\right)$ and $\left(\frac{25}{41}, \frac{16}{41}\right)$ respectively, which on

substituting into Eq. (3.2.14), gives equal von Neumann entanglement entropies

$$E(\hat{\bar{\rho}}_{g0}) = S(\hat{\bar{\rho}}_a) = S(\hat{\bar{\rho}}_f) = -\frac{16}{41}\log_2\left(\frac{16}{41}\right) - \frac{25}{41}\log_2\left(\frac{25}{41}\right) = 0.964957 \qquad (4.1.8h)$$

Taking the properties in Eqs. (4.1.8d), (4.1.8f) - (4.1.8h) together clearly characterises the qubit state $|\bar{\phi}_{g0}\rangle$ in Eq. (4.1.8a) as an entangled bipartite pure state. However, since $S(\hat{\bar{\rho}}_a) = S(\hat{\bar{\rho}}_f) < 1$ the state is not maximally entangled. Similarly, the transition qubit state vector $|\bar{\phi}_{g0}\rangle = -\frac{7}{\sqrt{65}}|g,0\rangle + \frac{4}{\sqrt{65}}|e,1\rangle$ obtained for $\delta = 3\lambda$, $\bar{\delta} = 7\lambda$ in Eq. (4.1.6b) is an entangled bipartite pure state, but not maximally entangled.

Finally, we consider the resonance case $\delta = 0$, characterised by $\bar{\delta} = 4\lambda$ in the AJC model. Ignoring the phase factor in Eq. (4.1.6c) the transition qubit state vector $|\bar{\phi}_{g0}\rangle$ takes the form

$$\delta = 0 \quad ; \quad \bar{\delta} = 4\lambda : \quad |\bar{\phi}_{g0}\rangle = -\frac{1}{\sqrt{2}}|g,0\rangle + \frac{1}{\sqrt{2}}|e,1\rangle \ . \qquad (4.1.9a)$$

The corresponding density operator of the state in Eq. (4.1.9a) is

$$\hat{\bar{\rho}}_{g0} = \frac{1}{2}|g,0\rangle\langle g,0| - \frac{1}{2}|g,0\rangle\langle e,1| - \frac{1}{2}|e,1\rangle\langle g,0| + \frac{1}{2}|e,1\rangle\langle e,1| \qquad (4.1.9b)$$

which takes the explicit 4×4 matrix form

$$\hat{\bar{\rho}}_{g0} = \frac{1}{2}\begin{pmatrix} 0 & 0 & 0 & 0 \\ 0 & 1 & -1 & 0 \\ 0 & -1 & 1 & 0 \\ 0 & 0 & 0 & 0 \end{pmatrix} \qquad (4.1.9c)$$

with eigenvalues $\lambda_1 = 1$, $\lambda_2 = 0$, $\lambda_3 = 0$, $\lambda_4 = 0$. Applying Eq. (3.2.13) its von Neumann entropy

$$S(\hat{\bar{\rho}}_{g0}) = 0 \qquad (4.1.9d)$$

quantifying the state in Eq. (4.1.9a) as a bipartite pure state.

Taking the partial trace of $\hat{\bar{\rho}}_{g0}$ in Eq. (4.1.9b) with respect to the field mode and atom states respectively, we obtain the respective atom and field reduced density operators

$\hat{\bar{\rho}}_a, \hat{\bar{\rho}}_f$ together with their squares in the form

$$
\begin{aligned}
\hat{\bar{\rho}}_a &= tr_f(\hat{\bar{\rho}}_{g0}) = \frac{1}{2}|g\rangle\langle g| + \frac{1}{2}|e\rangle\langle e| \quad ; \quad \hat{\bar{\rho}}_a^2 = \frac{1}{4}|g\rangle\langle g| + \frac{1}{4}|e\rangle\langle e| \\
\hat{\bar{\rho}}_f &= tr_a(\hat{\bar{\rho}}_{g0}) = \frac{1}{2}|0\rangle\langle 0| + \frac{1}{2}|1\rangle\langle 1| \quad ; \quad \hat{\bar{\rho}}_f^2 = \frac{1}{4}|0\rangle\langle 0| + \frac{1}{4}|1\rangle\langle 1|
\end{aligned}
$$
$$(4.1.9e)$$

The trace of $\hat{\bar{\rho}}_a^2$ and $\hat{\bar{\rho}}_f^2$ in Eq. (4.1.9e) is

$$
tr(\hat{\bar{\rho}}_a^2) = tr(\hat{\bar{\rho}}_f^2) = \frac{1}{2} < 1 \tag{4.1.9f}
$$

which reveals that the reduced density operators $\hat{\bar{\rho}}_a, \hat{\bar{\rho}}_f$ are mixed states. To quantify the mixedness, we determine the length of the Bloch vector along the z-axis as follows

$$
r_z = tr(\hat{\bar{\rho}}_a \hat{\sigma}_z) = tr(\hat{\bar{\rho}}_f \hat{\sigma}_z) = 0 \tag{4.1.9g}
$$

showing that the reduced density operators $\hat{\bar{\rho}}_a$ and $\hat{\bar{\rho}}_f$ are maximally mixed states.

The eigenvalues (λ_1, λ_2) of $\hat{\bar{\rho}}_a$ and $\hat{\bar{\rho}}_f$ are $(\frac{1}{2}, \frac{1}{2})$ respectively which on substituting into Eq. (3.2.14), gives equal von Neumann entanglement entropies

$$
E(\hat{\bar{\rho}}_{g0}) = S(\hat{\bar{\rho}}_a) = S(\hat{\bar{\rho}}_f) = -\frac{1}{2}\log_2\left(\frac{1}{2}\right) - \frac{1}{2}\log_2\left(\frac{1}{2}\right) = 1 \tag{4.1.9h}
$$

The unit entropy determined in Eq. (4.1.9h) together with the properties in Eqs. (4.1.9d) - (4.1.9g) quantifies the transition qubit state determined at resonance $\delta = 0$ in Eq. (4.1.9a) (or Eq. (4.1.6c)) as a maximally entangled bipartite pure state. Due to this maximal entanglement property, we shall use the resonance transition qubit state $|\bar{\phi}_{g0}\rangle$ in Eq. (4.1.9a) to implement teleportation by an entanglement swapping protocol in Sec. 4.1.2.2 below.

Similar proof of entanglement of the AJC qubit states is easily achieved for all possible values of sum frequency parameter $\bar{\delta} = \omega_0 + \omega$, confirming that in the initial vacuum-field AJC interaction, reversible transitions occur only between a pure initial separable qubit state vector $|\psi_{g0}\rangle$ and a pure entangled qubit state vector $|\bar{\phi}_{g0}\rangle$.

This property of Rabi oscillations between an initial separable state and an entangled transition qubit state occurs in the general AJC interaction described by the general time evolving state vector $|\bar{\Psi}_{gn}(t)\rangle$ in Eq. (3.2.11).

It is of importance at this stage to mention about the qubit state transitions of an initial atom-field ground state $|g, 0\rangle$ in the JC interaction, i.e., an atom in ground state $|g\rangle$

in an initial vacuum field $|0\rangle$. To clarify, let us consider the definition of the time evolving qubit state vector $|\Psi_{gn}(t)\rangle$, Rabi frequency R_{gn} and interaction parameters c_{gn}, s_{gn} in the JC interaction defined for an initial atomic ground state in an n-photon field mode in the forms [12]

$$
\begin{aligned}
|\Psi_{gn}(t)\rangle &= e^{-i\omega t\left(n-\frac{1}{2}\right)}\left(\cos(R_{gn}t)|\psi_{gn}\rangle - i\sin(R_{gn}t)|\phi_{gn}\rangle\right) \quad ; \quad R_{gn} = 2\lambda A_{gn} \quad ; \\
A_{gn} &= \sqrt{n + \frac{\delta^2}{16\lambda^2}} \quad ; \quad c_{gn} = \frac{\delta}{2R_{gn}} \quad ; \quad s_{gn} = \frac{2\lambda\sqrt{n}}{R_{gn}} \quad ; \\
|\psi_{gn}\rangle &= |g, n\rangle \quad ; \quad |\phi_{gn}\rangle = -c_{gn}|g, n\rangle + s_{gn}|e, n-1\rangle ,
\end{aligned}
\tag{4.1.10}
$$

to describe the transitions between the stationary basic qubit state vectors $|\psi_{gn}\rangle$ and $|\phi_{gn}\rangle$ during time evolution of $|\Psi_{gn}(t)\rangle$ in Eq. (4.1.10). As an example, letting $\delta = 0$, λ; $R_{g0}t = \frac{\pi}{2}$; $\omega = 2\lambda$ we easily obtain

$$
\begin{aligned}
\delta = 0 \quad &: \quad |\Psi_{g0}(t = \infty)\rangle = 0 \quad ; \quad R_{g0} = 0 \quad ; \quad t = \infty \quad , \\
\delta = \lambda \quad &: \quad |g, 0\rangle \to e^{i\frac{3\pi}{2}}|g, 0\rangle \to e^{i3\pi}|g, 0\rangle .
\end{aligned}
\tag{4.1.11}
$$

We observe in the first case, $\delta = 0$, a closed state in the upper JC spectrum [10] while in the latter, $\delta = \lambda$, a clear free-evolution, i.e, the atom remains permanently in the atomic ground state $|g\rangle$ since it does not couple to the rotating field mode in vacuum state. Remember, the variation in the global phase has no physical meaning, indicating that the initial and transition states (at $\delta = \lambda$) in Eq. (4.1.11) effectively present the same physical system $|g, 0\rangle$.

These two cases provide the inherent difficulty in analysing the full QRM dynamics since the effective JC Hamiltonian cannot generate dynamical evolution when the atom is initially in ground state and in a vacuum field mode $|g, 0\rangle$, giving rise to the implementation of larger coupling regimes, the USC and DSC regimes. In these coupling regimes, the contribution of the counter(anti)-rotating (CRT) terms becomes salient and the dynamics of $|g, 0\rangle$ can be studied.

This fundamental result in Eq. (4.1.11) provides the justification of this study in the Fock space, where the dynamical evolution of the JC model in an initial vacuum field is fully demonstrated and specified strictly with the physical description of the effective JC Hamiltonian as that which drives the effective initial JC state vector $|e, 0\rangle$ to a time evolving entangled bipartite atom-field state. The AJC Hamiltonian on the other hand is that which drives the initial state vector $|g, 0\rangle$ to a time evolving entangled state as we have demonstrated. The reason why JC and AJC models are studied separately.

4.1.2.2 Teleportation in the AJC interaction mechanism

We now consider teleportation of entanglement, a process that uses entanglement swapping protocol as introduced in Sec. 3.2.2.3. Here, the state we want to teleport is a two-atom maximally entangled state in which we have assigned subscripts to distinguish the atomic qubit states in the form [176]

$$|\varphi\rangle_{12} = \frac{1}{\sqrt{2}}(|e\rangle_1|g\rangle_2 - |g\rangle_1|e\rangle_2) \tag{4.1.12}$$

and it is in Alice's possession. In another location Bob is in possession of a maximally entangled qubit state $|\overline{\phi}_{g0}\rangle$ generated in the AJC interaction in Eq. (4.1.6c) and expressed here as

$$\delta = 0 : |\overline{\phi}_{g0}\rangle \equiv |\Phi\rangle_{3x} = -\frac{1}{\sqrt{2}}|g\rangle_3|0\rangle_x + \frac{1}{\sqrt{2}}|e\rangle_3|1\rangle_x \tag{4.1.13}$$

where we have also assigned subscripts to the qubits in Eq. (4.1.13) to clearly distinguish them. More precisely the arbitrarily chosen subscript 3 specifies atomic qubits and x identifies field mode qubits that defines the maximally entangled state $|\Phi\rangle_{3x}$ in possession of the receiver (Bob).

An observer, Charlie, receives qubit-1 (in the state $|\varphi\rangle_{12}$, Eq. (4.1.12)) from Alice and qubit-x (in the state $|\Phi\rangle_{3x}$, Eq. (4.1.13)) from Bob. The entire state of the system

$$|\chi\rangle = |\varphi\rangle_{12} \otimes |\Phi\rangle_{3x} \tag{4.1.14a}$$

which on substituting $|\varphi\rangle_{12}$ and $|\Phi\rangle_{3x}$ from Eqs. (4.1.12), (4.1.13) and reorganizing takes the form

$$\begin{aligned}
|\chi\rangle &= \frac{1}{2}\Big[|\Psi^+\rangle_{1x}\left(\frac{|e\rangle_3|g\rangle_2 + |g\rangle_3|e\rangle_2}{\sqrt{2}}\right) + |\Psi^-\rangle_{1x}\left(\frac{|e\rangle_3|g\rangle_2 - |g\rangle_3|e\rangle_2}{\sqrt{2}}\right) \\
&\quad - |\Phi^-\rangle_{1x}\left(\frac{|g\rangle_3|g\rangle_2 - |e\rangle_3|e\rangle_2}{\sqrt{2}}\right) - |\Phi^+\rangle_{1x}\left(\frac{|g\rangle_3|g\rangle_2 + |e\rangle_3|e\rangle_2}{\sqrt{2}}\right)\Big]
\end{aligned}$$
$$\tag{4.1.14b}$$

after introducing the emerging Bell states obtained as

$$
\begin{aligned}
|\Psi^+\rangle_{1x} &= \frac{|e\rangle_1|1\rangle_x + |g\rangle_1|0\rangle_x}{\sqrt{2}} \quad ; \quad |\Psi^-\rangle_{1x} = \frac{|e\rangle_1|1\rangle_x - |g\rangle_1|0\rangle_x}{\sqrt{2}} \\
|\Phi^-\rangle_{1x} &= \frac{|e\rangle_1|0\rangle_x - |g\rangle_1|1\rangle_x}{\sqrt{2}} \quad ; \quad |\Phi^+\rangle_{1x} = \frac{|e\rangle_1|0\rangle_x + |g\rangle_1|1\rangle_x}{\sqrt{2}}
\end{aligned}
$$

$$(4.1.14\text{c})$$

Charlie performs Bell state projection between qubit-1 and qubit-x in Eq. (4.1.14c) (Bell state measurement (BSM)) and communicates his results to Bob which we have presented in Sec. 4.1.2.2.1 below.

4.1.2.2.1 Bell state measurement

Using $|\chi\rangle$ from Eq. (4.1.14b) and applying Eq. (1.8.2)

$$
P_\Sigma := \langle\Sigma|\Lambda\rangle|\Sigma\rangle \tag{1.8.2$'$}
$$

we obtain a Bell state projection outcome communicated to Bob in the form

$$
{}_{1x}\langle\Psi^-|\chi\rangle = \frac{1}{2}\left(\frac{|e\rangle_3|g\rangle_2 - |g\rangle_3|e\rangle_2}{\sqrt{2}}\right) = \frac{1}{2}|\Psi^-\rangle_{32} \tag{4.1.15a}
$$

The Bell state $|\Psi^-\rangle_{32}$ in Eq. (4.1.15a) is in the form of Alice's qubit in Eq. (4.1.12). Alice and Bob now have a Bell pair between qubit-2 and qubit-3. Similarly the other three Bell projections take the forms

$$
{}_{1x}\langle\Psi^+|\chi\rangle = \frac{1}{2}\left(\frac{|e\rangle_3|g\rangle_2 + |g\rangle_3|e\rangle_2}{\sqrt{2}}\right) = \frac{1}{2}|\Psi^+\rangle_{32} \tag{4.1.15b}
$$

$$
{}_{1x}\langle\Phi^-|\chi\rangle = \frac{1}{2}\left(\frac{|e\rangle_3|e\rangle_2 - |g\rangle_3|g\rangle_2}{\sqrt{2}}\right) = \frac{1}{2}|\Phi^-\rangle_{32} \tag{4.1.15c}
$$

$$
{}_{1x}\langle\Phi^+|\chi\rangle = -\frac{1}{2}\left(\frac{|e\rangle_3|e\rangle_2 + |g\rangle_3|g\rangle_2}{\sqrt{2}}\right) = -\frac{1}{2}|\Phi^+\rangle_{32} \tag{4.1.15d}
$$

For these case of Bell state projections in Eqs. (4.1.15b), (4.1.15c) and (4.1.15d) it will be necessary for Bob to perform local corrections to qubit-3 by Pauli operators

Table 4.1: Table showing how Bob applies an appropriate gate to his qubit based on BSM from Charlie during the AJC teleportation process.

$|\varphi\rangle_{12}$	$|\psi\rangle_{32}$	$UNITARY OPERATION$
$\frac{1}{\sqrt{2}}(|e\rangle_1|g\rangle_2 - |g\rangle_1|e\rangle_2)$	$\frac{1}{\sqrt{2}}(-|g\rangle_3|g\rangle_2 + |e\rangle_3|e\rangle_2)$	$-\hat{\sigma}_{x(atom3)} \otimes \hat{I}_{(atom2)}$
	$\frac{1}{\sqrt{2}}(-|g\rangle_3|g\rangle_2 - |e\rangle_3|e\rangle_2)$	$-i\hat{\sigma}_{y(atom3)} \otimes \hat{I}_{(atom2)}$
	$\frac{1}{\sqrt{2}}(|e\rangle_3|g\rangle_2 + |g\rangle_3|e\rangle_2)$	$\hat{\sigma}_{z(atom3)} \otimes \hat{I}_{(atom2)}$

Table A.1: Table showing how Bob applies an appropriate gate to his qubit based on BSM from Charlie during the JC teleportation process.

$|\kappa\rangle_{12}$	$|\epsilon\rangle_{32}$	$UNITARY OPERATION$
$\frac{1}{\sqrt{2}}(|e\rangle_1|e\rangle_2 + |g\rangle_1|g\rangle_2)$	$\frac{1}{\sqrt{2}}(|g\rangle_3|e\rangle_2 + |e\rangle_3|g\rangle_2)$	$\hat{\sigma}_{x(atom3)} \otimes \hat{I}_{(atom2)}$
	$\frac{1}{\sqrt{2}}(|g\rangle_3|e\rangle_2 - |e\rangle_3|g\rangle_2)$	$i\hat{\sigma}_{y(atom3)} \otimes \hat{I}_{(atom2)}$
	$\frac{1}{\sqrt{2}}(|e\rangle_3|e\rangle_2 - |g\rangle_3|g\rangle_2)$	$\hat{\sigma}_{z(atom3)} \otimes \hat{I}_{(atom2)}$

as shown in Tab. 4.1. We also see that the probability of measuring states $|\psi\rangle_{32}$ in Eqs. (4.1.15a)-(4.1.15d) in Charlie's lab is $p = \frac{1}{4}$ similar to that of $|\epsilon\rangle_{32}$ in the JC process in Tab. A.1 as determined in A.2.2.2. In general, by application of the entanglement swapping protocol (teleportation of entanglement), qubit-2 belonging to Alice and qubit-3 belonging to Bob despite never having interacted before became entangled. Further, we see that a maximally entangled *anti-symmetric* atom-field transition state $|\overline{\phi}_{g0}\rangle$ (in Eq. (4.1.6c)) easily generated in the AJC interaction, can be used in quantum information processing (QIP) protocols like entanglement swapping (teleportation of entanglement) which we have demonstrated in this work. Anti-symmetric quantum states [177] have an advantage over symmetric quantum states as their special features are particularly useful for implementing quantum mechanical key sharing protocol [61], quantum state sharing protocols and for comparing quantum states [178]. We note that it is not possible to generate such an entangled anti-symmetric state in the JC interaction starting with the atom initially in the ground state and the field mode in the vacuum state [12]. Recall that the JC interaction produces a meaningful physical effect, namely, spontaneous emission only when the atom is initially in the excited state $|e\rangle$ and the field mode in the vacuum state $|0\rangle$.

The emerging Bell states in Eq. (4.1.14c) and those determined after successful telepor-

tation, i.e., $|\Phi^{\pm}\rangle_{1x(32)}$, $|\Psi^{\pm}\rangle_{1x(32)}$ are maximally entangled two qubit states. The Bell states $|\Phi^{\pm}\rangle_{1x(32)}$ and $|\Psi^{+}\rangle_{1x(32)}$ are symmetric in the sense that if we exchange the subsystems $1 \leftrightarrow x$ $(3 \leftrightarrow 2)$ they remain the same, i.e, $|\Phi^{\pm}\rangle_{1x(32)} = |\Phi^{\pm}\rangle_{x1(23)}$, $|\Psi^{+}\rangle_{1x(32)} = |\Psi^{+}\rangle_{x1(23)}$. Conversely the Bell states $|\Psi^{-}\rangle_{1x(32)}$ are anti-symmetric in the sense that if the permutation of the subsystems are changed the anti-symmetric Bell states obtain a minus sign, i.e, $|\Psi^{-}\rangle_{1x(32)} = -|\Psi^{-}\rangle_{x1(23)}$.

Let us compare Bob's actions in Tab. 4.1 to that in Tab. A.1. To do this let us first express $-i\hat{\sigma}_y$ gate in Tab. 4.1 and $i\hat{\sigma}_y$ in Tab. A.1 in terms of $\hat{\sigma}_x$, $\hat{\sigma}_z$ gates.

The anti-commutator of the Pauli matrices $\hat{\sigma}_z$, $\hat{\sigma}_x$ is determined according to

$$
\begin{aligned}
\{\hat{\sigma}_z,\ \hat{\sigma}_x\} &= \hat{\sigma}_z\hat{\sigma}_x + \hat{\sigma}_x\hat{\sigma}_z \\
&= \begin{pmatrix} 1 & 0 \\ 0 & -1 \end{pmatrix}\begin{pmatrix} 0 & 1 \\ 1 & 0 \end{pmatrix} + \begin{pmatrix} 0 & 1 \\ 1 & 0 \end{pmatrix}\begin{pmatrix} 1 & 0 \\ 0 & -1 \end{pmatrix} \\
&= 0
\end{aligned}
$$

$$(4.1.16\mathrm{a})$$

and the commutator of the Pauli matrices $\hat{\sigma}_z$, $\hat{\sigma}_x$ is obtained as follows

$$
\begin{aligned}
[\hat{\sigma}_z,\ \hat{\sigma}_x] &= \hat{\sigma}_z\hat{\sigma}_x - \hat{\sigma}_x\hat{\sigma}_z \\
&= \begin{pmatrix} 1 & 0 \\ 0 & -1 \end{pmatrix}\begin{pmatrix} 0 & 1 \\ 1 & 0 \end{pmatrix} - \begin{pmatrix} 0 & 1 \\ 1 & 0 \end{pmatrix}\begin{pmatrix} 1 & 0 \\ 0 & -1 \end{pmatrix} = 2\begin{pmatrix} 0 & 1 \\ -1 & 0 \end{pmatrix} = 2i\begin{pmatrix} 0 & -i \\ i & 0 \end{pmatrix} \\
&= 2i\hat{\sigma}_y.
\end{aligned}
$$

$$(4.1.16\mathrm{b})$$

We can now express the anti-commutator relation in Eq. (4.1.16a) in the form

$$\hat{\sigma}_x\hat{\sigma}_z = -\hat{\sigma}_z\hat{\sigma}_x \qquad (4.1.16\mathrm{c})$$

and substitute in the commutator relation in Eq. (4.1.16b) to obtain

$$i\hat{\sigma}_y = \hat{\sigma}_z\hat{\sigma}_x\ . \qquad (4.1.16\mathrm{d})$$

Similarly, expressing the anti-commutator relation in Eq. (4.1.16a) in the form

$$\hat{\sigma}_z\hat{\sigma}_x = -\hat{\sigma}_x\hat{\sigma}_z \qquad (4.1.16\mathrm{e})$$

and substituting in Eq. (4.1.16b) we get

$$-i\hat{\sigma}_y = \hat{\sigma}_x \hat{\sigma}_z \ . \tag{4.1.16f}$$

As an addition, in Tab. 4.1, Bob applies a gate operation of $-\hat{\sigma}_x$ to qubit-3 in $|\psi\rangle_{32}$, which we can write in the form

$$-\hat{\sigma}_x = e^{i\pi}\hat{\sigma}_x \quad ; \quad -1 = e^{i\pi} \ . \tag{4.1.17}$$

With reference to Tab. 4.1, Eqs. (4.1.16a) - (4.1.16f) and Eq. (4.1.17), the following sequence of quantum gates is applied by Bob to qubit-3 in $|\psi\rangle_{32}$ to map $|\psi\rangle_{32}$ onto $|\varphi\rangle_{12}$ during the AJC process;

a)

$$\frac{1}{\sqrt{2}}\left(-|g\rangle_3|g\rangle_2 - |e\rangle_3|e\rangle_2\right) \xrightarrow{[\hat{\sigma}_x\hat{\sigma}_z]_{atom\ 3}\otimes\hat{I}_{atom\ 2}} \frac{1}{\sqrt{2}}\left(|e\rangle_3|g\rangle_2 - |g\rangle_3|e\rangle_2\right) \ , \tag{4.1.18a}$$

i.e, $-i\hat{\sigma}_y$ is equivalent to Bob applying $\hat{\sigma}_z$ gate followed by $\hat{\sigma}_x$ gate to qubit-3 in $|\psi\rangle_{32}$ in that order. Remember $\hat{I}_{atom\ 2}$ means doing nothing to qubit-2 in $|\psi\rangle_{32}$.

Looking closely at the JC process in Tab. A.1, $i\hat{\sigma}_y$ which is the same as applying $\hat{\sigma}_x$ then $\hat{\sigma}_z$ gates in that sequence to qubit-3 in $|\epsilon\rangle_{32}$

$$\frac{1}{\sqrt{2}}\left(|g\rangle_3|e\rangle_2 - |e\rangle_3|g\rangle_2\right) \xrightarrow{[\hat{\sigma}_z\hat{\sigma}_x]_{atom\ 3}\otimes\hat{I}_{atom\ 2}} \frac{1}{\sqrt{2}}\left(|e\rangle_3|e\rangle_2 + |g\rangle_3|g\rangle_2\right) \tag{4.1.18b}$$

maps the state $\frac{1}{\sqrt{2}}\left(|g\rangle_3|e\rangle_2 - |e\rangle_3|g\rangle_2\right)$ onto the symmetric Bell state $|\Phi^+\rangle_{32} = \frac{1}{\sqrt{2}}\left(|e\rangle_3|e\rangle_2 + |g\rangle_3|g\rangle_2\right)$. Here the order of gate operation is inverted relative to that during the local correction process to the received qubit in the AJC teleportation network.

Notice that a phase change π to the subsystem, qubit-3, in Eq. (4.1.18b) of the final corrected qubit state $|\Phi^+\rangle_{32} = \frac{1}{\sqrt{2}}\left(|e\rangle_3|e\rangle_2 + |g\rangle_3|g\rangle_2\right)$ followed by the gate operation defined in Eq. (4.1.18b) but taken in reverse order, i.e, $\hat{\sigma}_x$ followed by $\hat{\sigma}_z$ to qubit-3, defines the local correction process in Eq. (4.1.18a) to qubit-3 by Bob during the AJC teleportation of a two-atom entangled anti-symmetric state. A clear reverse measurement operation on Bob's qubit in the JC teleportation correction process

relative to the AJC case.

b)

$$\frac{1}{\sqrt{2}} \left(-|g\rangle_3 |g\rangle_2 + |e\rangle_3 |e\rangle_2 \right) \xrightarrow{[e^{i\pi}\hat{\sigma}_x]_{atom\ 3} \otimes \hat{I}_{atom\ 2}} \frac{1}{\sqrt{2}} \left(|e\rangle_3 |g\rangle_2 - |g\rangle_3 |e\rangle_2 \right) \ .$$

(4.1.18c)

This local correction means $-\hat{\sigma}_x$ is analogous to Bob applying $\hat{\sigma}_x$ gate followed by a phase change of π (see the phase factor $e^{i\pi}$) to qubit-3 in $|\psi\rangle_{32}$ in that order, noting that the relative phase induced in this superposition is physically important, i.e., $\frac{1}{\sqrt{2}} \left(|e\rangle_3 |g\rangle_2 + e^{i\pi} |g\rangle_3 |e\rangle_2 \right) = \frac{1}{\sqrt{2}} \left(|e\rangle_3 |g\rangle_2 - |g\rangle_3 |e\rangle_2 \right) \neq \frac{1}{\sqrt{2}} \left(|e\rangle_3 |g\rangle_2 + |g\rangle_3 |e\rangle_2 \right)$. One more time, $\hat{I}_{atom\ 2}$ does not change the state of qubit-2 in $|\psi\rangle_{32}$, i.e, no action to qubit-2 in $|\psi\rangle_{32}$.

The JC process in Tab. A.1 provides a local correction by Bob to the subsystem's qubit-3 in the form

$$\frac{1}{\sqrt{2}} \left(|g\rangle_3 |e\rangle_2 + |e\rangle_3 |g\rangle_2 \right) \xrightarrow{[\hat{\sigma}_x]_{atom\ 3} \otimes \hat{I}_{atom\ 2}} \frac{1}{\sqrt{2}} \left(|e\rangle_3 |e\rangle_2 + |g\rangle_3 |g\rangle_2 \right) \ .$$

(4.1.18d)

Fixating on Eq. (4.1.18d), spot that a phase change π on subsystem, $|g\rangle_3$, of the final symmetric qubit state $|\Phi^+\rangle = \frac{1}{\sqrt{2}} \left(|e\rangle_3 |e\rangle_2 + |g\rangle_3 |g\rangle_2 \right)$ will transform the final qubit state in Eq. (4.1.18d) to the original symmetric qubit state $|\Phi^-\rangle = \frac{1}{\sqrt{2}} \left(|e\rangle_3 |e\rangle_2 - |g\rangle_3 |g\rangle_2 \right)$ in Eq. (4.1.18c). In addition, if this is followed by applying a phase change of π after measuring $\hat{\sigma}_x$ on subsystem, qubit-3, will result into the final anti-symmetric qubit state $|\Psi^-\rangle = \frac{1}{\sqrt{2}} \left(|e\rangle_3 |g\rangle_2 - |g\rangle_3 |e\rangle_2 \right)$ in Eq. (4.1.18c). In this sense, the correction of qubit-3 in Bob's possession in the AJC teleportation process can be viewed as the inverse of the correction by Bob in JC teleportation process.

c)

$$\frac{1}{\sqrt{2}} \left(|e\rangle_3 |g\rangle_2 + |g\rangle_3 |e\rangle_2 \right) \xrightarrow{[\hat{\sigma}_z]_{atom\ 3} \otimes \hat{I}_{atom\ 2}} \frac{1}{\sqrt{2}} \left(|e\rangle_3 |g\rangle_2 - |g\rangle_3 |e\rangle_2 \right) \ .$$

(4.1.18e)

means that Bob applies $\hat{\sigma}_z$ gate to qubit-3 and involutory operator $\hat{I}_{atom\ 2}$ for no action to qubit-2 both in $|\psi\rangle_{32}$ Tab. 4.1.

The local correction by Bob in Tab. A.1 is defined according to

$$\frac{1}{\sqrt{2}}\left(|e\rangle_3|e\rangle_2 - |g\rangle_3|g\rangle_2\right) \xrightarrow{[\hat{\sigma}_z]_{atom\ 3} \otimes \hat{I}_{atom\ 2}} \frac{1}{\sqrt{2}}\left(|e\rangle_3|e\rangle_2 + |g\rangle_3|g\rangle_2\right).$$

(4.1.18f)

Here also, Bob applies $\hat{\sigma}_z$ gate to qubit-3 and involutory operator $\hat{I}_{atom\ 2}$ for no action to qubit-2 in $\frac{1}{\sqrt{2}}\left(|e\rangle_3|e\rangle_2 - |g\rangle_3|g\rangle_2\right)$.

Since the z-basis is the computational basis or the standard basis, i.e, $\{|g, 0\rangle, |e, 1\rangle\}_{AJC}, \{|e, 0\rangle, |g, 1\rangle\}_{JC}$ and is the only basis in which the aforementioned AJC, JC measurements are performed, explains the distinct forms of Eqs. (4.1.18e) and (4.1.18f) that express measurements of $\hat{\sigma}_z$ on subsystem qubit-3 for the states as defined.

4.1.2.2.2 Maximal teleportation fidelity

From Tab. 4.1

$$\begin{aligned}
\hat{\rho}_{expected} &= |\varphi_{12}\rangle\langle\varphi_{12}| \\
&= \frac{1}{2}\Big[(|e_1\rangle|g_2\rangle - |g_1\rangle|e_2\rangle)(\langle e_1|\langle g_2| - \langle g_1|\langle e_2|)\Big] \\
&= \frac{1}{2}\Big[|e_1, g_2\rangle\langle e_1, g_2| - |e_1, g_2\rangle\langle g_1, e_2| - |g_1, e_2\rangle\langle e_1, g_2| + |g_1, e_2\rangle\langle g_1, e_2|\Big] \\
&= \frac{1}{2}\begin{pmatrix} 0 & 0 & 0 & 0 \\ 0 & 1 & -1 & 0 \\ 0 & -1 & 1 & 0 \\ 0 & 0 & 0 & 0 \end{pmatrix}
\end{aligned}$$

(4.1.19)

$$
\begin{aligned}
\hat{\rho}_{measured} &= |\psi_{32}\rangle\langle\psi_{32}| \\
&= \frac{1}{2}\Big[(|e_3\rangle|g_2\rangle - |g_3\rangle|e_2\rangle)(\langle e_3|\langle g_2| - \langle g_3|\langle e_2|)\Big] \\
&= \frac{1}{2}\Big[|e_3,g_2\rangle\langle e_3,g_2| - |e_3,g_2\rangle\langle g_3,e_2| - |g_3,e_2\rangle\langle e_3,g_2| + |g_3,e_2\rangle\langle g_3,e_2|\Big] \\
&= \frac{1}{2}\begin{pmatrix} 0 & 0 & 0 & 0 \\ 0 & 1 & -1 & 0 \\ 0 & -1 & 1 & 0 \\ 0 & 0 & 0 & 0 \end{pmatrix}
\end{aligned}
$$

$$(4.1.20)$$

Substituting the results in Eq. (4.1.19) and Eq. (4.1.20) into the fully entangled fraction Eq. (1.8.19b)

$$
f_{\hat{\rho}} = \max_{|\Psi\rangle}\langle\Psi|\hat{\rho}|\Psi\rangle = \left\{tr\sqrt{\hat{\rho}_{expected}^{\frac{1}{2}}\hat{\rho}_{measured}\hat{\rho}_{expected}^{\frac{1}{2}}}\right\}^2 , \tag{1.8.19b'}
$$

we obtain

$$
f_{\hat{\rho}} = \left\{tr\begin{pmatrix} 0 & 0 & 0 & 0 \\ 0 & \frac{1}{2} & -\frac{1}{2} & 0 \\ 0 & -\frac{1}{2} & \frac{1}{2} & 0 \\ 0 & 0 & 0 & 0 \end{pmatrix}\right\}^2 = 1 . \tag{4.1.21}
$$

Substituting the value of the fully entangled fraction in Eq. (4.1.21) into Eq. (1.8.19a)

$$
F_{\hat{\rho}} = \frac{2f_{\hat{\rho}} + 1}{3} \tag{1.8.19a'}
$$

we get

$$
F_{\hat{\rho}} = \frac{2(1) + 1}{3} = 1 \tag{4.1.22}
$$

a maximal teleportation fidelity of unity, showing that the state was fully recovered, i.e Alice's qubit in Eq. (4.1.12) was successfully teleported to Bob. We obtain an equal outcome to all the other measured states. We have thus achieved qunatum teleportation using a maximally entangled qubit state generated in an AJC interaction, using the case

where the atom and field are initially in the absolute ground state $|g\rangle$, $|0\rangle$ as an example, noting that the classical limit of teleportation fidelity [65] is 0.75.

4.1.3 Evolution of entanglement in the AJC process

Utilising the definitions of the dimensionless parameters $\bar{c}_{gn}$, $\bar{s}_{gn}$ and the Rabi frequency $\overline{R}_{gn}$ in Eqs. $(3.2.4)$, $(3.2.24)$, we evaluate the atomic state probabilities $\overline{P}_g(t) = \cos^2(\overline{R}_{gn}t) + \bar{c}_{gn}^2 \sin^2(\overline{R}_{gn}t)$, $\overline{P}_e(t) = \bar{s}_{gn}^2 \sin^2(\overline{R}_{gn}t)$ in Eq. $(3.2.23)$ and plot the quantum system entanglement degree $E(\tau) = -\overline{P}_e(t)\log_2 \overline{P}_e(t) - \overline{P}_g(t)\log_2 \overline{P}_g(t)$ in Eq. $(3.2.27)$ against scaled time $\tau = \lambda t$ for arbitrarily chosen values of sum frequency $\bar{\delta} = 2\lambda$, 4λ, 5λ, 6λ, 7λ, 8λ and photon number $n = 0, 1, 2, 3, 6$ in Figs. 4.3 - 4.6 below.

(a) AJC   (b) JC
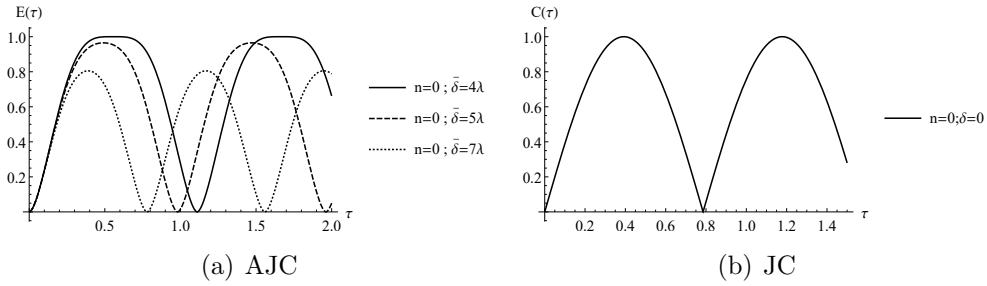
Figure 4.3: Degree of entanglement:Fig. (4.3(a)) DEM (E(τ)) against scaled time for sum frequency $\bar{\delta} = 4\lambda$, 5λ and 7λ when $n = 0$ while in Fig. (4.3(b)) [Fig. A.2 Appendix A] DEM (C(τ)) against scaled time τ at resonance $\delta = 0$ when $n = 0$.
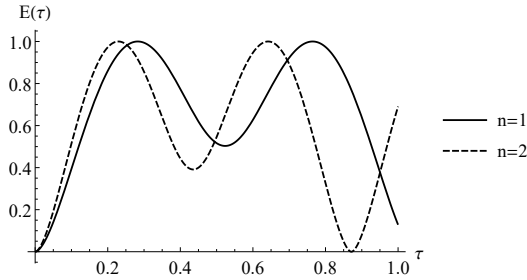
Figure 4.4: Degree of entanglement against scaled time for sum frequency $\bar{\delta} = 2\lambda$ when $n = 1$ and $n = 2$

(a) DEM
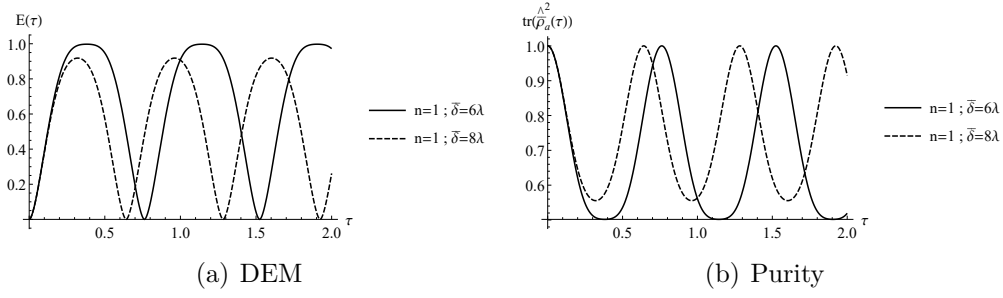
(b) Purity

Figure 4.5: Time evolution of DEM at increasing sum frequency $\overline{\delta}$ when the photon number n set constant and its effect on the degree of purity $tr(\hat{\overline{\rho}}_a^2(t))$. Fig. (4.5(a)), time evolution of $E(\tau)$ at $n = 1$; $\overline{\delta} = 6\lambda$, 8λ while Fig. (4.5(b)) is the corresponding time evolution of purity $tr(\hat{\overline{\rho}}_a^2(t))$ at $n = 1$; $\overline{\delta} = 6\lambda$, 8λ in the AJC process

(a) DEM
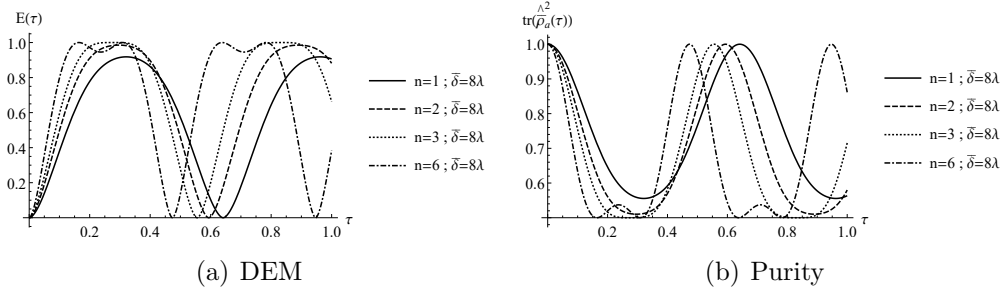
(b) Purity

Figure 4.6: Time evolution of DEM at increasing photon number n when the sum frequency detuning $\overline{\delta}$ set constant and its effect on the degree of purity $tr(\hat{\overline{\rho}}_a^2(t))$. Fig. (4.6(a)), time evolution of $E(\tau)$ at $n = 1, 2, 3, 6$; $\overline{\delta} = 8\lambda$ while Fig. (4.6(b)) is the corresponding time evolution of purity $tr(\hat{\overline{\rho}}_a^2(t))$ at $n = 1, 2, 3, 6$; $\overline{\delta} = 8\lambda$ in the AJC process

The graphs in Figs. 4.3(a) - 4.6 show the effect of photon number n and sum frequency $\overline{\delta} = \omega_0 + \omega$ on the dynamical behavior of quantum entanglement measured by the von Neumann entropy $E(\tau)$ (min $E(\tau) = 0$; max $E(\tau) = 1$). In the four figures, the phenomenon of entanglement sudden birth (ESB) and sudden death (ESD) is observed during the time evolution of entanglement similar to that observed in the JC model in Appendix. A and as obtained in [179–181]. In ESB there is an observed creation of entanglement where the initially un-entangled qubits are entangled after a very short time interval. For fairly low values of photon numbers n and sum frequency $\overline{\delta}$ as demonstrated in Fig. 4.4 for $\overline{\delta} = 2\lambda$ plotted when $n = 1$, $n = 2$, the degree of entanglement rises sharply to a maximum value of unity $(E(\tau)_{max})$ at an entangled state, stays at the maximum level for a reasonably short duration, decreases to a local minimum, then rises back to the

maximum value before falling sharply to zero $(E(\tau)_{min})$ at the separable state. The local minimum disappears for larger values of sum frequency $\overline{\delta} \geq 6\lambda$ at low photon number n and re-emerge at high photon number $n \geq 4$ (see Fig. 4.5(a) and Fig. 4.6(a)) as examples. However, in comparison to the resonance case $\delta = 0$ in the JC model in Fig. A.2 and [181] we notice a long-lived entanglement at $E(\tau)_{max} = 1$ in the cases of $\overline{\delta} = 4\lambda$ plotted when $n = 0$ in Fig. 4.3(a), $\overline{\delta} = 6\lambda$ plotted when $n = 1$ in Fig. 4.5(a) and $\overline{\delta} = 8\lambda$ plotted when $n = 3$ in Fig. 4.6(a) quantifying maximum entanglement before returning momentarily to a separable state. Agreeing precisely with the entanglement analysis example in Sec. 4.1.2.1, is the long-lived entanglement at $E(\tau)_{max} = 1$ in Fig. 4.3(a) determined for parameter values $\overline{\delta} = 4\lambda$ and $n = 0$. This is an important property since one of the Divincenzo criteria [89] set for efficient storage and processing of quantum information, is that long lived quantum states is a requirement in order to ensure long coherence times during computational process (quantum gate operations).

Further, in the JC model, the dynamics of $C(\tau)$ as shown in Figs. A.2 - A.5 and [179–181] has local minimums *only* when detuning is set at off-resonance $\delta \neq 0$ apart from special cases of maximum entanglement characterised by a long-lived entanglement at $C(\tau) = 1$ like in the case of $\delta = 4\lambda$ when $n = 0$ in Fig. A.3. The process of ESB and ESD then repeats periodically, consistent with Rabi oscillations between the qubit states.

In Fig. 4.3(a), it is clear that vacuum-field Rabi oscillations in the AJC interaction mechanism occur when an atom initially in ground state $|g\rangle$ is in a vacuum-field $n = 0$ in contrast to the JC interaction mechanism as shown in Figs. A.2 and A.3, where they only occur when an atom in an initial excited state $|e\rangle$ enters a vacuum-field $n = 0$.

An interesting entanglement property is observed in Fig. 4.3(a) and 4.5(a) where an increase in sum-frequency $\overline{\delta}$ results into a decrease in DEM measured by $E(\tau)$ at the same time increasing the frequency of oscillation of $E(\tau)$ similar to the JC case Fig. A.6(a) and in [182]. Plots of time evolution of purity $tr(\hat{\overline{\rho}}_a^2(\tau))$ in Fig. 4.5(b) confirms that the reduction in $E(\tau)$ is a consequence of the quantum system tending to pure state when the effect of sum frequency $\overline{\delta}$ is considered for small number of photons n similar to that discussed earlier in the JC examples in Fig. A.6 and [182]. We observe here, that the DEM can be increased by increasing the photon number n as demonstrated here in Fig. 4.6(a). Consequently, as shown in Fig. 4.6(b) the system tends to a maximally mixed state just like the JC case Fig. A.7 and in [180–182].

Although we have briefly mentioned earlier that sum frequency $\overline{\delta}$ results into an increase in frequency of oscillation of $E(\tau)$ we probe further its effect in detail with regard to the dynamics of $E(\tau)$. In Fig. 4.3(a) we set $\overline{\delta} = 4\lambda$, 5λ and 7λ when $n = 0$. As

discussed, it is clear from Fig. 4.3(a) that the frequency of oscillation of $E(\tau)$ increases with an increase in sum frequency $\bar{\delta} = \omega_0 + \omega$. As a comparison to the JC model discussed in Appendix. A, when detuning $\delta = \omega_0 - \omega$ is set at off resonance $\delta \neq 0$ results into a decrease in the frequency of oscillation of $C(\tau)$ as visualised in Fig. A.3 in comparison to the resonance case $\delta = 0$ Figs. A.2 . In Fig. A.4 at resonance $\delta = 0$ when $n = 1$ the period of $C(\tau)$ is shorter than at $\delta = \lambda$ when $n = 1$ in Fig. A.5. This phenomenon of reduction in frequency of oscillation of DEM in the JC model at off-resonance detuning, is also demonstrated clearly in [180–182].

Finally, in Fig. 4.4 and 4.6(a) sum-frequencies are kept constant at $\bar{\delta} = 2\lambda$ and $\bar{\delta} = 8\lambda$ respectively and photon number n is varied in each case. We clearly see that the frequency of oscillation of $E(\tau)$ increases with an increase in photon number n. This phenomenon in which the frequency of oscillation of DEM increases with an increase in photon number n is also observed in the JC model in Figs. A.4, A.5 and obtained in [180, 181].

4.1.4 Quantum C-NOT gate operations in the AJC interaction mechanism

It is important to note that in the AJC interaction [12], for a process starting from the state $|e, n\rangle$ where an atom in excited state $|e\rangle$ enters a n-photon field mode, the excited atom emits a positive energy photon, triggering the CR negative frequency field mode to absorb a negative energy photon causing a transition $|e, n\rangle \rightarrow |g, n - 1\rangle$; $n \geq 1$. On the other hand, a process starting from the state $|g, n\rangle$ where an atom in ground state $|g\rangle$ is in a n-photon field mode, the CR negative frequency field mode emits a negative energy photon, triggering the atom to absorb a positive energy photon, causing the transition $|g, n\rangle \rightarrow |e, n + 1\rangle$; $n \geq 0$.

Now, with reference to the AJC qubit state transition operators in Eq. (3.2.7) and the algebraic property on exponentiation of $\hat{\bar{\varepsilon}}_g$ defined in Eq. (3.2.6) which is the principal the AJC C-NOT gate operator in the case of an atom in an initial ground state $|g\rangle$, let us first consider when an atom initially in ground state $|g\rangle$ enters an electromagnetic cavity with mode a in vacuum state and a single photon in mode b. As stated earlier, this mode of interaction is possible because in the AJC interaction mechanism, an atom in an initial ground state $|g\rangle$ couples to the CR negative frequency component of the field mode in an initial vacuum state $|0\rangle$, spontaneously emitting a negative energy photon, thereby triggering Rabi oscillations at frequency $\bar{R}_{g0}$ between the atom (control qubit) and field mode (target qubit).

During the AJC interaction, we consider a case in which there should never be more than a single photon in the cavity field and so, the respective qubit state transitions will be

of the forms $|g, 0\rangle \rightarrow |e, 1\rangle$, $|e, 1\rangle \rightarrow |g, 0\rangle$. In addition, the atom-field coupling constant λ should be far much greater than the sum-frequency $\overline{\delta} = \omega_0 + \omega$, i.e., $(\lambda \gg \overline{\delta})$ so that the dimensionless coupling ratio $\frac{\lambda}{\overline{\delta}}$ becomes very large (NB: In view of the USC regime, the ratio $\frac{\lambda}{\overline{\delta}}$ is called the perturbative parameter and is defined within the perturbative region [183] of the USC regime where the contribution of CR terms become important. This ratio, however, does not apply here in this sense.).

In this respect, while the initial atomic ground state $|g\rangle$ is in the cavity initially in vacuum state $|0\rangle$, the field and the atom evolve according to

$$
\begin{aligned}
e^{-i\theta\hat{\overline{\varepsilon}}_g}|g, 0_a\rangle &= \cos(\theta)\, \frac{1}{\overline{A}_{g0}^2}(\overline{\alpha}\hat{s}_z + \hat{a}\hat{s}_- + \hat{a}^\dagger \hat{s}_+)^2 |g, 0_a\rangle \\
&\quad -i\sin(\theta)\, \frac{1}{\overline{A}_{g0}}(\overline{\alpha}\hat{s}_z + \hat{a}\hat{s}_- + \hat{a}^\dagger \hat{s}_+) |g, 0_a\rangle \quad ; \\
n &= 0 \quad ; \quad \hat{a}|n\rangle = \sqrt{n}|n-1\rangle \quad ; \quad \hat{a}^\dagger|n\rangle = \sqrt{n+1}|n+1\rangle \quad ; \\
\hat{s}_+ &= \hat{s}_x + i\hat{s}_y \quad ; \quad \hat{s}_- = \hat{s}_x - i\hat{s}_y \quad ; \\
\hat{s}_+|e\rangle &= 0 \quad ; \quad \hat{s}_-|e\rangle = |g\rangle \quad ; \quad \hat{s}_+|g\rangle = |e\rangle \quad ; \quad \hat{s}_-|g\rangle = 0 \\
\hat{\overline{A}} &= \overline{\alpha}\hat{s}_z + \hat{a}\hat{s}_- + \hat{a}^\dagger \hat{s}_+ \quad ; \quad \overline{A}_{gn} = \sqrt{(n+1) + \frac{\overline{\alpha}}{4}} \\
\overline{\alpha} &= \frac{\overline{\delta}}{2\lambda} \quad ; \quad \hat{\overline{\varepsilon}}_g = \frac{\hat{\overline{A}}}{\overline{A}_{gn}} \quad ; \quad \hat{\overline{I}}_g = \hat{\overline{\varepsilon}}_g^2 \quad\quad (4.1.23)
\end{aligned}
$$

which on applying the field mode operators $\hat{a}^\dagger$, $\hat{a}$, the atomic state transition operators $\hat{s}_+$, $\hat{s}_-$ in Eq. (4.1.23) and the parameter settings $\lambda \gg \overline{\delta}$ for a field mode in an initial vacuum state $n = 0$ we obtain from Eq. (3.2.4)

$$
\overline{A}_{gn} = \sqrt{(n+1) + \frac{\overline{\delta}^2}{16\lambda^2}} \quad\quad (3.2.4')
$$

$$
\overline{A}_{g0} \cong \sqrt{1 + 0} \cong 1 \quad ; \quad \frac{\overline{\delta}^2}{16\lambda^2} \cong 0 \quad ; \quad \lambda \gg \overline{\delta} \quad\quad (4.1.24)
$$

and Eq. (4.1.23) takes the reduced form

$$
e^{-i\theta\hat{\overline{\varepsilon}}}|g, 0_a\rangle = \cos(\theta)|g, 0_a\rangle - i\sin(\theta)|e, 1_a\rangle \, . \quad\quad (4.1.25)
$$

The qubit state transitions is now driven by positive and negative energy photon

absorption-emission process. It should be noted that if this condition was not met, in a completely off-resonant interaction the field mode frequency ω and the atomic transition frequency ω_0 would have been sufficiently detuned and so there would have been no transition between atomic basis states $|g\rangle$ and $|e\rangle$ during the interaction.

As stated in Sec. 3.2.4, the choice of atomic velocity is important in order to ensure that an atom in a cavity mode undergoes a Rabi oscillation cycle specified in an interaction time t. This means, if chosen so that in a time t, $\overline{R}_{g0}t = \pi$, we obtain

$$t = \frac{\pi}{\overline{R}_{g0}} \tag{4.1.26}$$

which is equal to half Rabi oscillation time. It therefore follows that the driving field is modulated according to

$$\theta \;=\; \overline{R}_{g0}t = 2\lambda\overline{A}_{g0}t = \pi. \tag{4.1.27}$$

Now since $\overline{A}_{g0} \cong 1$, the driving field modulation in Eq. (4.1.27) takes the final form

$$\theta = 2\lambda t = \pi \quad \Rightarrow \quad \theta = \lambda t = \frac{\pi}{2} \;, \tag{4.1.28}$$

and the evolution in Eq. (4.1.23) reduces to

$$|g, 0_a\rangle \rightarrow e^{-i\frac{\pi}{2}}|e, 1_a\rangle \tag{4.1.29}$$

We observe that the atom interacted with mode a and completed half of the Rabi oscillation, as a result, it contributed a photon to mode a by triggering the CR field to emit a negative energy photon and consequently evolved to excited state $|e\rangle$ by absorbing a positive energy photon. At this point it is important to note that there is a clear simultaneous excitation of both the atom and field states, as expected in the AJC interaction.

After the interaction time, the atom now in excited state $|e\rangle$ enters mode b containing a single photon in state $|1\rangle_b$. The interaction with mode b is obtained using Eqs. (3.2.7)

and (3.2.6) in the form

$$
e^{i\alpha\hat{\bar{\varepsilon}}_e}\left(e^{-i\frac{\pi}{2}}|e,1_b\rangle\right) \;\; \rightarrow \;\; e^{-i\frac{\pi}{2}}\Big[\cos(\alpha)\,\frac{1}{\overline{A}_{e1}^2}(\overline{\alpha}\hat{s}_z + \hat{a}\hat{s}_- + \hat{a}^\dagger\hat{s}_+)^2|e,1_b\rangle +
$$

$$
i\,\sin(\alpha)\,\frac{1}{\overline{A}_{e1}}(\overline{\alpha}\hat{s}_z + \hat{a}\hat{s}_- + \hat{a}^\dagger\hat{s}_+)|e,1_b\rangle\Big]\;;
$$

$$
n \;\;=\;\; 0\;\;;
$$

$$
\hat{s}_+|e\rangle \;\;=\;\; 0\;\;;\quad \hat{s}_-|e\rangle = |g\rangle\;\;;\quad \hat{s}_+|g\rangle = |e\rangle\;\;;\quad \hat{s}_-|g\rangle = 0
$$

$$
\hat{\overline{A}} \;\;=\;\; \overline{\alpha}\hat{s}_z + \hat{a}\hat{s}_- + \hat{a}^\dagger\hat{s}_+\;\;;\quad \overline{A}_{en} = \sqrt{n + \frac{\overline{\alpha}}{4}}
$$

$$
\overline{\alpha} \;\;=\;\; \frac{\overline{\delta}}{2\lambda}\;\;;\quad \hat{\bar{\varepsilon}}_e = \frac{\hat{\overline{A}}}{\overline{A}_{en}}\;\;;\quad \hat{\overline{I}}_g = \hat{\bar{\varepsilon}}_e^2 \tag{4.1.30}
$$

to obtain

$$
e^{-i\frac{\pi}{2}}|e,1_b\rangle = e^{-i\frac{\pi}{2}}\left[\cos(\alpha)|e,1_b\rangle + i\,\sin(\alpha)|g,0_b\rangle\right] \tag{4.1.31}
$$

after applying the field mode operators $\hat{a}^\dagger$, $\hat{a}$, the atomic state transition operators $\hat{s}_+$, $\hat{s}_-$ in Eq. (4.1.23) and the condition $\lambda \gg \overline{\delta}$.

With the set condition $\lambda \gg \overline{\delta}$, the Rabi frequency parameter $\overline{A}_{en}$ in Eq. (3.2.4) (or Eq. (4.1.30))

$$
\overline{A}_{en} = \sqrt{n + \frac{\overline{\delta}^2}{16\lambda^2}} \tag{3.2.4'},
$$

in the case of an atom in an initial excited state $|e\rangle$ interacting with an initial single-photon field mode $|1\rangle$ in the AJC process will assume a value

$$
\overline{A}_{e1} \cong \sqrt{1+0} \cong 1\;\;;\quad \frac{\overline{\delta}^2}{16\lambda^2} \cong 0\;. \tag{4.1.32}
$$

Here, Eq. (4.1.31) defines qubit state transitions driven by positive and negative photon emission-absorption process, a converse of that observed in Eq. (4.1.25).

In order to define the driving field modulation α in mode b, let the total interaction time be $t' = 2t$, such that t is equal to half Rabi oscillation times in modes a and b respectively, obtained as

$$
t = \frac{\pi}{\overline{R}_{g0}} = \frac{\pi}{\overline{R}_{e1}}\;. \tag{4.1.33}
$$

It follows that the total interaction time t' will take the form

$$t' = \frac{\pi}{\overline{R}_{g0}} + \frac{\pi}{\overline{R}_{e1}} = \frac{\pi(\overline{R}_{g0} + \overline{R}_{e1})}{\overline{R}_{g0}\overline{R}_{e1}} = 2t . \tag{4.1.34}$$

Re-organising Eq. (4.1.34) we obtain

$$\left(\frac{\overline{R}_{g0}\overline{R}_{e1}}{\overline{R}_{g0} + \overline{R}_{e1}}\right) t = \frac{\pi}{2} \tag{4.1.35a}$$

and define the resultant interaction time in mode b in the form

$$t = \frac{\pi}{2}\left(\frac{\overline{R}_{g0} + \overline{R}_{e1}}{\overline{R}_{g0}\overline{R}_{e1}}\right) . \tag{4.1.35b}$$

We can write Eq. (4.1.35a) in a compact form

$$\alpha = \overline{R}t = \frac{\pi}{2} \quad ; \quad \overline{R} = \left(\frac{\overline{R}_{g0}\overline{R}_{e1}}{\overline{R}_{g0} + \overline{R}_{e1}}\right) \tag{4.1.36}$$

after introducing a resultant Rabi frequency $\overline{R}$ as defined in Eq. (4.1.36).

Considering again an interaction where $\lambda \gg \overline{\delta}$, the Rabi frequency parameters $\overline{A}_{g0}$, $\overline{A}_{e1}$ as presented in Eqs. (4.1.24) and (4.1.32), will be of respective equal values $\overline{A}_{g0} = \overline{A}_{e1} \cong 1$.

We determine the Rabi frequencies $\overline{R}_{g0}$, $\overline{R}_{e1}$ according to [12]

$$\overline{R}_{g0} = 2\lambda\overline{A}_{g0} = 2\lambda \quad ; \quad \overline{R}_{e1} = 2\lambda\overline{A}_{e1} = 2\lambda. \tag{4.1.37}$$

Substituting $\overline{R}_{g0}$, $\overline{R}_{e1}$ in Eq. (4.1.37) into Eq. (4.1.36) we obtain

$$\alpha = \frac{(2\lambda)^2}{4\lambda}t = \frac{\pi}{2} . \tag{4.1.38}$$

The driving field modulation in Eq. (4.1.36) reduces to

$$\alpha = \lambda t = \frac{\pi}{2} \tag{4.1.39}$$

and the form of Eq. (4.1.31) results into an evolution

$$e^{-i\frac{\pi}{2}}|e, 1_b\rangle \to |g, 0_b\rangle . \tag{4.1.40}$$

The results in Eq. (4.1.40) shows that the atom evolves to ground state by emitting a

positive energy photon, causing the CR field to absorbs a negative energy photon initially in mode b, a simultaneous de-excitation of the atom and field states, as expected in the AJC process. The atom clearly performs a swapping of the electromagnetic field between the two field modes by controlled interaction.

When the atom in ground state $|g\rangle$, enters the electromagnetic cavity with mode b in vacuum state and a single-photon in mode a in that order, qubit state transitions take the same form as in Eqs. (4.1.29) and (4.1.40). That is, there will be simultaneous excitation of atom and field states during the qubit state transition $|g, 0_b\rangle \rightarrow e^{-i\frac{\pi}{2}}|e, 1_b\rangle$ followed by a qubit state transition that results into simultaneous de-excitation of qubit states $e^{-i\frac{\pi}{2}}|e, 1_a\rangle \rightarrow |g, 0_a\rangle$. This shows a clear swapping of the electromagnetic field between the two field modes a, b by controlled interaction when the atom is initially in the ground state $|g\rangle$.

When the atom in excited state $|e\rangle$ enters mode a in vacuum state, the atom propagates as a free wave without coupling to the field mode in vacuum state $|0\rangle$ [12], leaving the cavity without altering the state of the cavity-field mode. We recall that in an AJC process, an atom in an initial excited state $|e\rangle$ does not couple ($\lambda = 0$) to a free anti-rotating negative frequency field mode in an initial vacuum state $|0\rangle$.

The atom in excited state $|e\rangle$ then interacts with mode b containing a single photon-field as follows

$$e^{i\beta\hat{\bar{\varepsilon}}_e}|e, 1_b\rangle \rightarrow \cos(\beta)(\hat{a}\hat{s}_- + \hat{a}^\dagger\hat{s}_+)^2 |e, 1_b\rangle + i\sin(\beta)\ (\hat{a}\hat{s}_- + \hat{a}^\dagger\hat{s}_+)\ |g, 0_b\rangle$$

(4.1.41)

leading to

$$e^{i\beta\hat{\bar{\varepsilon}}_e}|e, 1_b\rangle \rightarrow \cos(\beta)|e, 1_b\rangle + i\sin(\beta)|g, 0_b\rangle \ .$$ (4.1.42)

After completing one Rabi oscillation in a time $t = \frac{2\pi}{R_{e1}}$ at Rabi frequency $\overline{R}_{e1} = 2\lambda\overline{A}_{e1} = 2\lambda$ since the Rabi frequency parameter $\overline{A}_{e1} \cong 1$ determined by considering the initial condition. This gives

$$\beta = \lambda t = \pi \ .$$ (4.1.43)

The form of Eq. (4.1.42) results into an evolution

$$|e, 1_b\rangle = e^{i\pi}|e, 1_b\rangle$$ (4.1.44)

We see in Eq. (4.1.44) that the atom in excited state $|e\rangle$ again leaves the cavity mode containing one photon without altering the state of the single-photon field mode.

When the atom in excited state $|e\rangle$ enters mode b in vacuum state followed by mode a containing a single-photon field mode, we observe a similar qubit state transition where in mode b the atom propagates as a free wave without coupling to the field mode followed by the transition $|e, 1_a\rangle \to e^{i\pi}|e, 1_a\rangle$ in mode a after one complete Rabi oscillation time.

From the results obtained, we conclude that the target qubit made up of the electromagnetic field remains unchanged if the control qubit, that is, the two-level atom, is initially in the excited state $|e\rangle$, while when the atom is in ground state $|g\rangle$, the cavity states $|0\rangle$ and $|1\rangle$ flip. We shall refer to this gate as the AJC C-NOT ($atom \to cavity$), i.e.,

$$AJC\ C-NOT\ |e,0\rangle \to |e,0\rangle = \begin{pmatrix} 1 \\ 0 \\ 0 \\ 0 \end{pmatrix} \quad ; \quad AJC\ C-NOT\ |e,1\rangle \to |e,1\rangle = \begin{pmatrix} 0 \\ 1 \\ 0 \\ 0 \end{pmatrix} \quad ;$$

$$AJC\ C-NOT\ |g,0\rangle \to |g,1\rangle = \begin{pmatrix} 0 \\ 0 \\ 0 \\ 1 \end{pmatrix} \quad ; \quad AJC\ C-NOT\ |g,1\rangle \to |g,0\rangle = \begin{pmatrix} 0 \\ 0 \\ 1 \\ 0 \end{pmatrix} ,$$

$$(4.1.45)$$

which we write in a compact matrix form

$$AJC\ C-NOT = \begin{pmatrix} 1 & 0 & 0 & 0 \\ 0 & 1 & 0 & 0 \\ 0 & 0 & 0 & 1 \\ 0 & 0 & 1 & 0 \end{pmatrix} . \qquad (4.1.46)$$

The form of the operator in Eq. (4.1.46) is of exact form as the standard C-NOT gate operator defined in Eq. (1.7.7) and [22, 23, 50] applied in the JC interactions.

It is important to note that the statistical properties of the cavity field are determined by the statistical properties of the atom that exits the cavity after coupling to the field during the specified interaction time.

4.1.4.1 Probability of success of the C-NOT gate

The qubit state transition operations during the C-NOT gate process, yielded qubit states with individual qubits having different qubit values. In this respect, the success

probability for the C-NOT gate is given by Eq. (3.2.46)

$$P_s = 1 - (\sin^2(\phi_a) + \cos^2(\phi_a)\sin^2(\phi_b)) \tag{3.2.46'}$$

In terms of the Rabi frequency we write Eq. (3.2.46) as

$$P_s = 1 - (\sin^2(\overline{R}_a \Delta t_a) + \cos^2(\overline{R}_a \Delta t_a)\sin^2(\overline{R}_b \Delta t_b)) \ . \tag{4.1.47}$$

For the case when the atom in the ground state $|g\rangle$ enters the electromagnetic cavity with field mode a in vacuum state followed by a single-photon field mode b we obtain the interaction parameters

$$\begin{aligned}
\overline{R}_a &= \overline{R}_{g0} = 2\lambda \quad ; \quad \Delta t_a = \frac{\pi}{\overline{R}_{g0}} = \frac{\pi}{2\lambda}, \\
\overline{R}_b &= \overline{R}_{e1} = 2\lambda \quad ; \quad \Delta t_b = \frac{\pi}{2}\frac{(\overline{R}_{g0} + \overline{R}_{e1})}{\overline{R}_{g0}\overline{R}_{e1}} = \frac{\pi}{2\lambda}
\end{aligned} \tag{4.1.48}$$

and when it enters a single-photon field mode a then proceeds to field mode b in vacuum state the interaction parameters reduce to

$$\begin{aligned}
\overline{R}_a &= \overline{R}_{e1} = 2\lambda \quad ; \quad \Delta t_a = \frac{\pi}{2}\frac{(\overline{R}_{e1} + \overline{R}_{g0})}{\overline{R}_{e1}\overline{R}_{g0}} = \frac{\pi}{2\lambda}, \\
\overline{R}_b &= \overline{R}_{g0} = 2\lambda \quad ; \quad \Delta t_b = \frac{\pi}{\overline{R}_{g0}} = \frac{\pi}{2\lambda}
\end{aligned} \tag{4.1.49}$$

which results in a unit probability of success $P_s = 1$ for the respective transitions.

Finally when the atom initially in excited state $|e\rangle$ enters mode a in vacuum state then a single-photon field mode b we obtain the interaction parameters

$$\begin{aligned}
\overline{R}_a &= \overline{R}_{e0} = 2\lambda \overline{A}_{e0} = 0 \quad ; \quad \overline{A}_{e0} = 0 \quad ; \quad \lambda = 0 \quad ; \quad \Delta t_a = \infty, \\
\overline{R}_b &= \overline{R}_{e1} = 2\lambda \overline{A}_{e1} = 2\lambda \quad ; \quad \overline{A}_{e1} \cong 1 \quad ; \quad \Delta t_b = \frac{2\pi}{\overline{R}_{e1}} = \frac{\pi}{\lambda}
\end{aligned}$$
$$\tag{4.1.50}$$

whereas when it enters a single-photon field mode a then mode b in vacuum state respec-

tively, the interactions parameters are

$$\begin{aligned}
\overline{R}_a &= \overline{R}_{e1} = 2\lambda\overline{A}_{e1} = 2\lambda \quad ; \quad \overline{A}_{e1} \cong 1 \quad ; \quad \Delta t_a = \frac{2\pi}{\overline{R}_{e1}} = \frac{\pi}{\lambda}, \\
\overline{R}_a &= \overline{R}_{e0} = 2\lambda\overline{A}_{e0} = 0 \quad ; \quad \lambda = 0 \quad ; \quad \overline{A}_{e0} = 0 \quad ; \quad \Delta t_a = \infty
\end{aligned}$$
$$(4.1.51)$$

which again gives a unit probability of success, for each transition.

We observe that success probabilities depend mainly upon the precise selection of the interaction times of the two-level atom with the successive cavity modes.

4.1.5 Hadamard logic gate in the AJC interaction mechanism

Let us now consider two examples specifying Hadamard rotations for initial atomic basis states $|g\rangle$, $|e\rangle$ entering field modes in initial vacuum and single-photon states $|0\rangle$, $|1\rangle$ respectively. The general form of the gate operators are defined in Eq. (3.2.32), Sec. 3.2.3 according to

$$\hat{\bar{\varepsilon}}_g = \frac{\hat{\overline{A}}}{\overline{A}_{gn}} = \frac{2\left[\,\bar{\delta}\hat{s}_z + 2\lambda(\hat{a}\hat{s}_- + \hat{a}^\dagger\hat{s}_+)\right]}{\sqrt{16\lambda^2(n+1) + \bar{\delta}^2}} \quad ; \quad \hat{\bar{\varepsilon}}_e = \frac{\hat{\overline{A}}}{\overline{A}_{en}} = \frac{2\left[\,\bar{\delta}\hat{s}_z + 2\lambda(\hat{a}\hat{s}_- + \hat{a}^\dagger\hat{s}_+)\right]}{\sqrt{16n\lambda^2 + \bar{\delta}^2}}$$
$$(3.2.32')$$

Applying $\hat{\bar{\varepsilon}}_g$ defined in Eq. (3.2.32) the single qubit Hadamard operator at sum frequency $\bar{\delta} = 4\lambda$ and $n = 0$ specified for an initial atomic ground state $|g\rangle$ reduces to the form

$$\begin{aligned}
\hat{\bar{\varepsilon}}_g &= \frac{1}{\sqrt{2}}\left(2\hat{s}_z + \hat{a}\hat{s}_- + \hat{a}^\dagger\hat{s}_+\right) \quad ; \quad \hat{s}_z = \frac{1}{2}\begin{pmatrix} 1 & 0 \\ 0 & -1 \end{pmatrix} \quad ; \\
\hat{s}_+ &= \hat{s}_x + i\,\hat{s}_y = \begin{pmatrix} 0 & 1 \\ 0 & 0 \end{pmatrix} \quad ; \quad \hat{s}_- = \hat{s}_x - i\,\hat{s}_y = \begin{pmatrix} 0 & 0 \\ 1 & 0 \end{pmatrix} \\
\hat{s}_x &= \frac{1}{2}\begin{pmatrix} 0 & 1 \\ 1 & 0 \end{pmatrix} \quad ; \quad \hat{s}_y = \frac{1}{2}\begin{pmatrix} 0 & -i \\ i & 0 \end{pmatrix} \\
\hat{a}|n\rangle &= \sqrt{n}|n-1\rangle \quad ; \quad \hat{a}^\dagger|n\rangle = \sqrt{n+1}|n+1\rangle \;.
\end{aligned}$$
$$(4.1.52)$$

Its action on an initial state vector $|g, 0\rangle$ is the qubit state transition $\hat{\bar{\varepsilon}}_g|g, 0\rangle$ which takes the explicit final form

$$\hat{\bar{\varepsilon}}_g|g, 0\rangle = -\frac{1}{\sqrt{2}}|g, 0\rangle + \frac{1}{\sqrt{2}}|e, 1\rangle \;. \qquad (4.1.53)$$

As expected the initial atomic ground state $|g\rangle$ is rotated to

$$|g\rangle \rightarrow \frac{1}{\sqrt{2}}(|e\rangle - |g\rangle) \ . \tag{4.1.54}$$

Notice that the rotation in Eq.(4.1.54) takes the exact standard form operated in terms of Pauli X,Z gates according to

$$
\begin{aligned}
\frac{1}{\sqrt{2}}(\hat{\sigma}_x + \hat{\sigma}_z)|g\rangle &= \frac{1}{\sqrt{2}} \left(\begin{pmatrix} 0 & 1 \\ 1 & 0 \end{pmatrix} + \begin{pmatrix} 1 & 0 \\ 0 & -1 \end{pmatrix} \right) \begin{pmatrix} 0 \\ 1 \end{pmatrix} = \frac{1}{\sqrt{2}} \begin{pmatrix} 1 & 1 \\ 1 & -1 \end{pmatrix} \begin{pmatrix} 0 \\ 1 \end{pmatrix} \\
&= \frac{1}{\sqrt{2}} \begin{pmatrix} 1 \\ -1 \end{pmatrix} = \frac{1}{\sqrt{2}} \left(\begin{pmatrix} 1 \\ 0 \end{pmatrix} - \begin{pmatrix} 0 \\ 1 \end{pmatrix} \right) \\
&= \frac{1}{\sqrt{2}}(|e\rangle - |g\rangle)
\end{aligned}
\tag{4.1.55}
$$

defining the action of a Hadamard operator

$$\hat{H} = \frac{1}{\sqrt{2}} \begin{pmatrix} 1 & 1 \\ -1 & 1 \end{pmatrix} \tag{4.1.56}$$

on an initial atomic ground state $|g\rangle$.

We now applying $\hat{\bar{\varepsilon}}_e$ in Eq. (3.2.32) at sum frequency $\bar{\delta} = 4\lambda$ and $n = 1$ specified for an initial atomic excited state $|e\rangle$ to obtain a Hadamard operator in the form

$$
\begin{aligned}
\hat{\bar{\varepsilon}}_e &= \frac{\hat{\bar{A}}}{A_{e1}} = \frac{1}{\sqrt{2}} \left(2\hat{s}_z + \hat{a}\hat{s}_- + \hat{a}^\dagger \hat{s}_+ \right) \quad ; \\
\hat{s}_+ &= \hat{s}_x + i\,\hat{s}_y = \begin{pmatrix} 0 & 1 \\ 0 & 0 \end{pmatrix} \quad ; \quad \hat{s}_- = \hat{s}_x - i\,\hat{s}_y = \begin{pmatrix} 0 & 0 \\ 1 & 0 \end{pmatrix} \\
\hat{s}_x &= \frac{1}{2} \begin{pmatrix} 0 & 1 \\ 1 & 0 \end{pmatrix} \quad ; \quad \hat{s}_y = \frac{1}{2} \begin{pmatrix} 0 & -i \\ i & 0 \end{pmatrix} \quad ; \quad \hat{s}_z = \frac{1}{2} \begin{pmatrix} 1 & 0 \\ 0 & -1 \end{pmatrix} \\
\hat{a}|n\rangle &= \sqrt{n}|n-1\rangle \quad ; \quad \hat{a}^\dagger|n\rangle = \sqrt{n+1}|n+1\rangle \ .
\end{aligned}
\tag{4.1.57}
$$

In this respect, the Hadamard operator $\hat{\bar{\varepsilon}}_e$ in Eq. (4.1.57) acts on an initial state vector $|e, 1\rangle$ resulting into a qubit state transition $\hat{\bar{\varepsilon}}_e|e, 1\rangle$ that assumes an explicit final form

$$\hat{\bar{\varepsilon}}_e|e, 1\rangle = \frac{1}{\sqrt{2}}|e, 1\rangle + |g, 0\rangle \ . \tag{4.1.58}$$

We clearly see that the initial atomic excited state $|e\rangle$ is rotated to

$$|e\rangle \rightarrow \frac{1}{\sqrt{2}}(|e\rangle + |g\rangle) \ . \tag{4.1.59}$$

Notice again that Eq. (4.1.59) is of exact form as that determined by direct application Pauli X, Z gate rotations according to

$$
\begin{aligned}
\frac{1}{\sqrt{2}}(\hat{\sigma}_x + \hat{\sigma}_z)|e\rangle &= \frac{1}{\sqrt{2}}\left(\begin{pmatrix} 0 & 1 \\ 1 & 0 \end{pmatrix} + \begin{pmatrix} 1 & 0 \\ 0 & -1 \end{pmatrix}\right)\begin{pmatrix} 1 \\ 0 \end{pmatrix} = \frac{1}{\sqrt{2}}\begin{pmatrix} 1 & 1 \\ 1 & -1 \end{pmatrix}\begin{pmatrix} 1 \\ 0 \end{pmatrix} \\
&= \frac{1}{\sqrt{2}}\begin{pmatrix} 1 \\ 1 \end{pmatrix} = \frac{1}{\sqrt{2}}\left(\begin{pmatrix} 1 \\ 0 \end{pmatrix} + \begin{pmatrix} 0 \\ 1 \end{pmatrix}\right) \\
&= \frac{1}{\sqrt{2}}(|e\rangle + |g\rangle)
\end{aligned}
\tag{4.1.60}
$$

defining the action of a Hadamard operator

$$\hat{H} = \frac{1}{\sqrt{2}}\begin{pmatrix} 1 & 1 \\ -1 & 1 \end{pmatrix} \tag{4.1.61}$$

on an initial atomic excited state $|e\rangle$.

The actions in Eqs. (4.1.53), (4.1.58) correspond to and agree with the standard quantum Hadamard gate operation of spin states. $\hat{\bar{\varepsilon}}_g, \hat{\bar{\varepsilon}}_e$ are indeed AJC Hadamard gate operators for interaction starting with atom initially in ground state $|g\rangle$ and excited state $|e\rangle$ respectively.

The Hadamard transformations in Eqs. (4.1.54) and (4.1.59) realised in the AJC interaction process (AJC model) agree precisely with the standard definition in Eq. (1.7.3).

4.2 AJC dynamics of a two-level atom interacting with field mode in an initial coherent state

We now analyse the time evolution of a two-level atom in a resonant $(\bar{\delta} = 2\omega)$, off-resonant $(\bar{\delta} = \delta + 2\omega)$ AJC interaction when the field mode in an initial coherent state is considered. Precisely, purity of states in relation to atom-field entanglement in this model is studied during time evolution of atomic population inversion. In addition, analysis of the quantum nature of the field system in the AJC interaction is presented. A comparison with the well known results of the JC process explained in detail in Appendix B is provided.

4.2.1 Time evolution of Field entropy, purity and atomic population inversion

Accordingly, to discuss the time evolution of the collapses and revival phenomenon $W(t)$ in relation to degree of entanglement $S_j(t)$ and consequently the degree purity $tr(\hat{\rho}_j^2(t))$ it is important to recall that for pure states $tr(\hat{\rho}_j^2) = 1$, $S_j(t) = 0$ and for maximally mixed states $tr(\hat{\rho}_j^2) = \frac{1}{2}$, $S_j(t) = 1$ where $j \equiv a(f)$.

Under resonance, the AJC, JC Rabi frequencies, $\overline{R}_{gn}$, R_{gn} and related interaction parameters $\overline{c}_{gn}$, $\overline{s}_{gn}$, c_{gn}, s_{gn} in Eqs. (3.3.5d), (B.1.7), which determine the evolution described by the respective time evolving Bloch vectors $\vec{\overline{r}}(t)$ in Eq. (3.3.6), $\vec{r}(t)$ in Eq. (B.1.8), take the forms

AJC:

$$\delta = 0; \quad \beta = 0 \quad : \quad \overline{R}_{gn} = \lambda\sqrt{n+1+\xi^2} \quad ; \quad \overline{c}_{gn} = \frac{\xi}{\sqrt{n+1+\xi^2}}$$

$$\overline{R}_{gn-1} = \lambda\sqrt{n+\xi^2} \quad ; \quad \overline{s}_{gn-1} = \sqrt{\frac{n}{n+\xi^2}} \qquad (4.2.1a)$$

JC:

$$\delta = 0; \quad \beta = 0 \quad : \quad R_{gn} = \lambda\sqrt{n} \quad ; \quad c_{gn} = 0$$

$$R_{gn+1} = \lambda\sqrt{n+1} \quad ; \quad s_{gn+1} = 1 . \qquad (4.2.1b)$$

It is immediately clear that under resonance, $\delta = 0$, $\beta = 0$, the JC Rabi frequency and related interaction parameters in Eq. (4.2.1b), are completely independent of frequency detuning parameter, while the AJC Rabi frequency and the related interaction parameters in Eq. (4.2.1a), depend explicitly on the residual detuning parameter, $\xi = \frac{\omega}{\lambda}$.

The physical consequence is that under resonance, the JC dynamics is completely independent of detuning, while the AJC dynamics is driven by internal residual detuning, $\xi = \frac{\omega}{\lambda}$. As a result, small or large values of the residual detuning parameters define strong coupling in the region, $0 < \xi < 1$, and weak coupling when, $\xi > 1$.

Applying Eq. (1.3.16) by substituting the time evolving AJC Bloch vector components $\overline{r}_x(t)$, $\overline{r}_y(t)$, $\overline{r}_z(t)$ defined in Eq. (3.3.6) we plot the time evolution of AJC degree of purity $tr(\hat{\overline{\rho}}_a^2(t))$ in Fig. 4.7(a) at $\delta = 0$, $|\alpha|^2 = 30$ and compare with that of JC degree of purity in Fig. 4.7(b) (Fig. B.1, Appendix B) at $\delta = 0$, $= |\alpha|^2 = 30$ respectively. For ease of comprehension, in the same figures we provide the respective AJC, JC time evolution of

atomic population inversion $W(t)$ defined in Eqs. (3.3.7a), (B.1.9a) which takes the same form as the z-components $\overline{r}_z(t)$, $r_z(t)$ in Eqs. (3.3.6), (B.1.8) of the time evolving AJC, JC Bloch vectors $\vec{\overline{r}}(t)$, $\vec{r}(t)$.
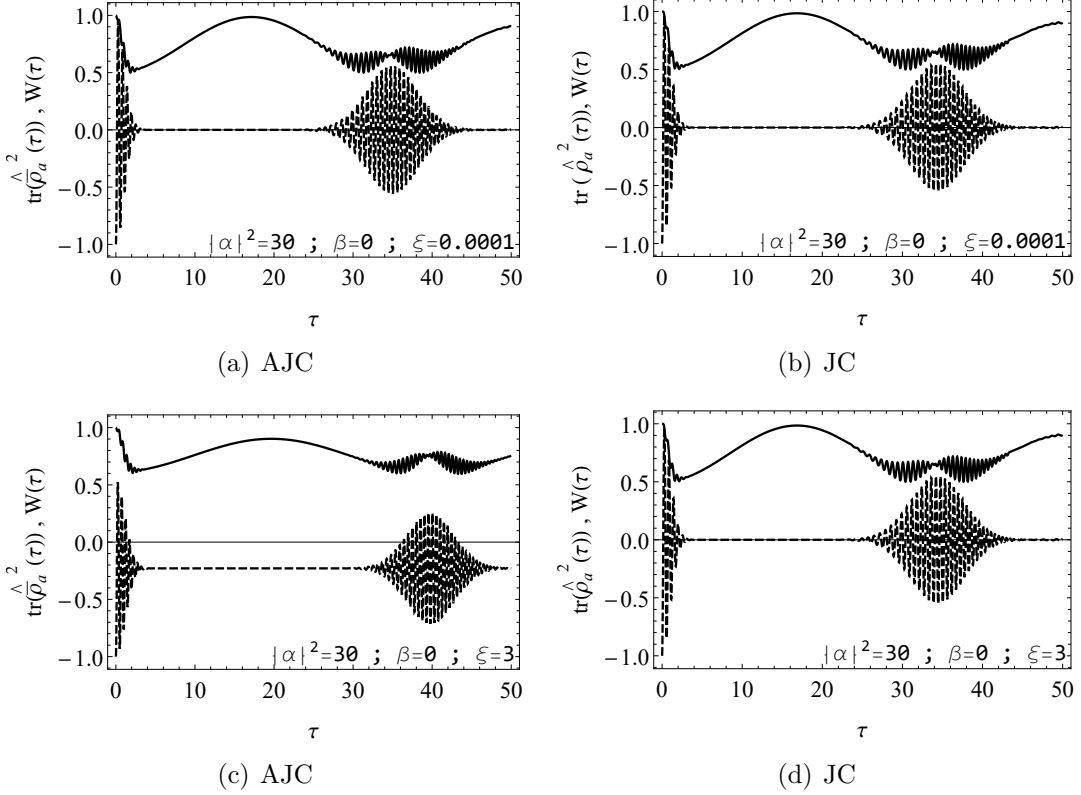
Figure 4.7: Time evolution of purity parameter and atomic population inversion. Fig. (4.7(a)) $tr(\hat{\overline{\rho}}_a^2(\tau))$, $W(\tau)$ at $\overline{\delta} = 2\xi\lambda = 0.0002\lambda$; $\beta = 0$, $\xi = 0.0001$ and $|\alpha|^2 = 30$ in the AJC process while Fig. (4.7(b)) (Fig. (B.1), Appendix B), the corresponding time evolution of $tr(\hat{\rho}_a^2(\tau))$, $W(\tau)$ at $\delta = \beta\lambda = 0$; $\beta = 0$, $\xi = 0.0001$ and $|\alpha|^2 = 30$ in the JC interaction.
Fig. (4.7(c)) $tr(\hat{\overline{\rho}}_a^2(\tau))$, $W(\tau)$ at $\overline{\delta} = 2\xi\lambda = 6\lambda$; $\beta = 0$, $\xi = 3$ and $|\alpha|^2 = 30$ in the AJC process while Fig. (4.7(d)) the corresponding time evolution of $tr(\hat{\rho}_a^2(\tau))$, $W(\tau)$ at $\delta = \beta\lambda = 0$; $\beta = 0$, $\xi = 3$ and $|\alpha|^2 = 30$ in the JC interaction.

We observe that in Figs. 4.7(a), 4.7(b), the AJC and JC evolutions are precisely similar. This is due to the fact that at very small residual detuning $\xi = 0.0001 \simeq 0$, the AJC and JC Rabi frequencies $\overline{R}_{gn}$, R_{gn} are nearly equal, giving the same form of dynamics.

As the residual detuning parameter, ξ, is increased to larger values, the dynamics of the AJC becomes significantly different from the JC dynamics at resonance, $\beta = 0$. This is illustrated in Figs. 4.7(c), 4.7(d) where the AJC evolution in Fig. 4.7(c) now reveals a

marked difference compared to the JC evolution in Fig. 4.7(d) since it is independent of ξ. We see that in the AJC plot in Fig. 4.7(c):

i) the atomic population inversion, $W(\tau)$, has gone significantly below zero, i.e., $W(\tau)$ has turned negative, meaning that, at larger $\xi = 3$, the AJC interaction generates more spin excitation in the ground state, $|g\rangle$, than in the excited state, $|e\rangle$

ii) the collapse period in the population inversion is longer, $\tau_R \simeq 34$, than in the corresponding JC evolution in Fig. 4.7(d) with, $\tau_R \simeq 26$

iii) the purity parameter, $tr(\hat{\bar{\rho}}_a^2(\tau))$, has increased towards the maximum value, $tr(\hat{\bar{\rho}}_a^2(\tau)) = 1$, showing that increasing the residual detuning parameter, ξ, to larger values in the AJC drives the atom towards a pure state as compared to the evolution in the JC in Fig. 4.7(d) which remains the same as in Fig. 4.7(b).

We then proceed to plot the dynamics of the von Neumann entropy $S_a(\tau)$ defined in Eq. (3.3.8) during the AJC processes and compare it to the widely-studied JC interaction presented here in Appendix B. To do this, we evaluate and substitute the eigenvalues $\pi_{1,2}$ defined in Eq. (3.3.8).

The plotted AJC DEM curves as measured by $S_a(t)$ at various values of field intensities $|\alpha|^2$ are in Figs. 4.8(a), 4.9(a) and 4.10(a) each for values of sum frequency $\overline{\delta} = \delta + 2\omega$; $\delta \geq 0$ whereas Figs. 4.8(b), 4.9(b) and 4.10(b) show the JC process DEM plots at resonance $\delta = 0$, off-resonance $\delta \neq 0$ at low, high field intensities $|\alpha|^2$ extracted as plotted in the extensively studied JC interaction in Appendix B.

(a) AJC

(b) JC

(c) AJC
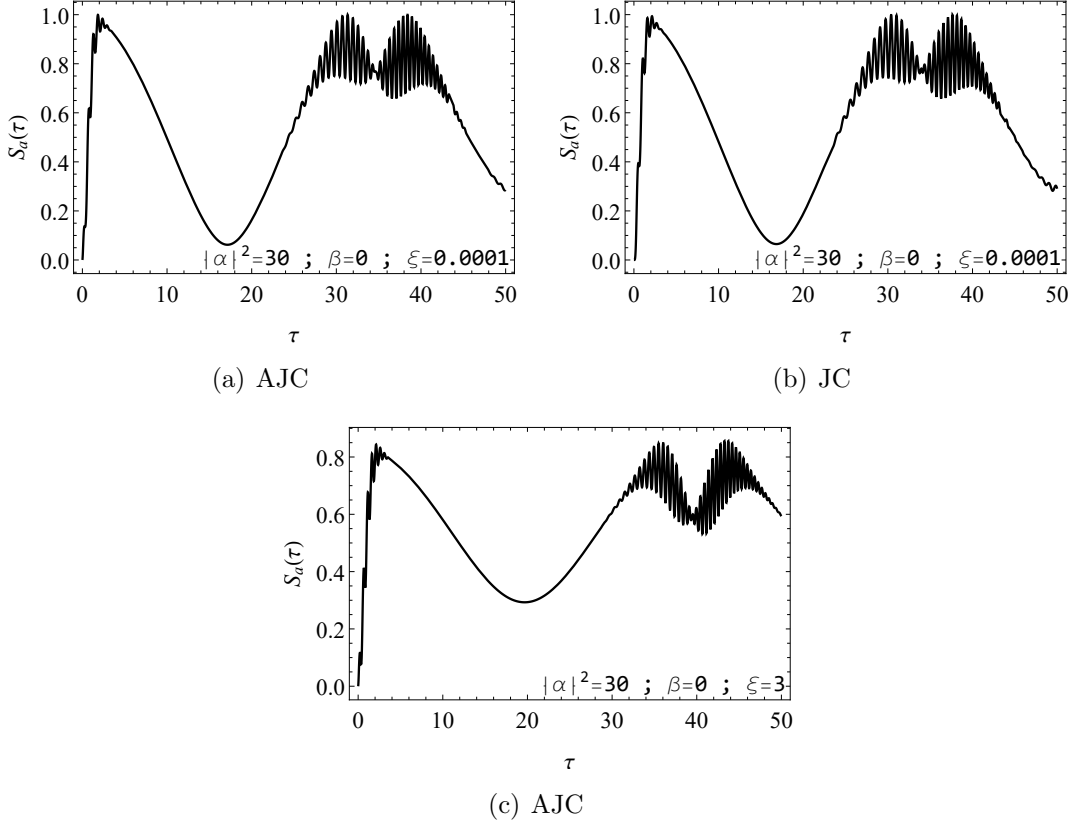
Figure 4.8: Time evolution of entropy of entanglement. Fig. (4.8(a)), $S_a(\tau)$ at $\overline{\delta} = 2\xi\lambda = 0.0002\lambda$; $\beta = 0$, $\xi = 0.0001$ and $|\alpha|^2 = 30$ in the AJC process while Fig. (4.8(b)) [Fig. B.2, Appendix B], is the corresponding $S_a(\tau)$ at $\delta = \beta\lambda = 0$; $\beta = 0$, $\xi = 0.0001$ and $|\alpha|^2 = 30$ in the JC interaction.
Fig. (4.8(c)), $S_a(\tau)$ at $\overline{\delta} = 2\xi\lambda = 6\lambda$; $\beta = 0$, $\xi = 3$ and $|\alpha|^2 = 30$ in the AJC interaction.

As explained in the case of atomic population inversion, $W(\tau)$, and purity parameter, $tr(\hat{\overline{\rho}}_a^2(\tau))$, we see that at resonance, setting a large residual detuning parameter, $\xi = 3$, as presented in our example in Fig. 4.8(c), the AJC DEM dynamics as measured by $S_a(\tau)$ becomes significantly different form the JC $S_a(\tau)$, dynamics at resonance, presented in Fig. 4.8(b). This is because, at very low residual detuning, $\xi = 0.0001 \simeq 0$, the AJC and JC Rabi frequencies, $\overline{R}_{gn}$, R_{gn}, are virtually equivalent, resulting in the same type of dynamics as visualised in Figs. 4.8(a) and 4.8(b).

With reference to the AJC curve in Fig. 4.8(c):

i) $S_a(\tau)$ decreases, and the values of $S_a(\tau)$ at the middle of collapse phase does not dip much towards zero, $S_a(\tau) = 0.3$, in comparison to $S_a(\tau) = 0.05$ in Figs. 4.8(a) and 4.8(b)

ii) that the observation in (i) above, means that in the AJC interaction at resonance, $\bar{\delta} = 2\omega = 2\xi\lambda$, increasing ξ, results in a general decrease in atom-field entanglement, $S_a(\tau) = 0.825$, in comparison to, $S_a(\tau) = 1$, in Figs. 4.8(a), 4.8(b) and a simultaneous increase in mixedness of the atom-field states.

(a) AJC

(b) JC
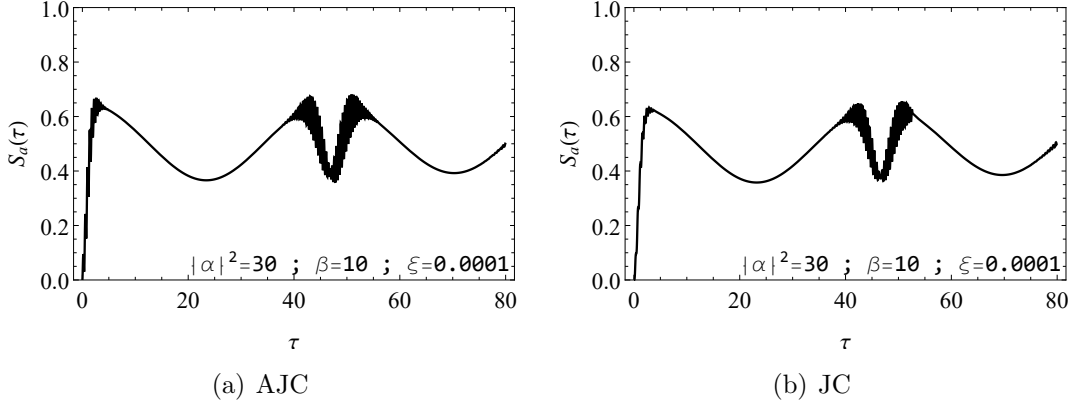
Figure 4.9: Time evolution of entropy of entanglement. Fig. (4.9(a)) is the time evolution of $S_a(\tau)$ at $\bar{\delta} = (\beta+2\xi)\lambda = 10.0002\lambda$; $\beta = 10$, $\xi = 0.0001$ and $|\alpha|^2 = 30$ in the AJC process while Fig. (4.9(b)) [Fig. B.3, Appendix B], $S_a(\tau)$ at $\delta = \beta\lambda = 10\lambda$; $\beta = 10$, $\xi = 0.0001$ and $|\alpha|^2 = 30$ in the JC interaction.

(a) AJC

(b) JC
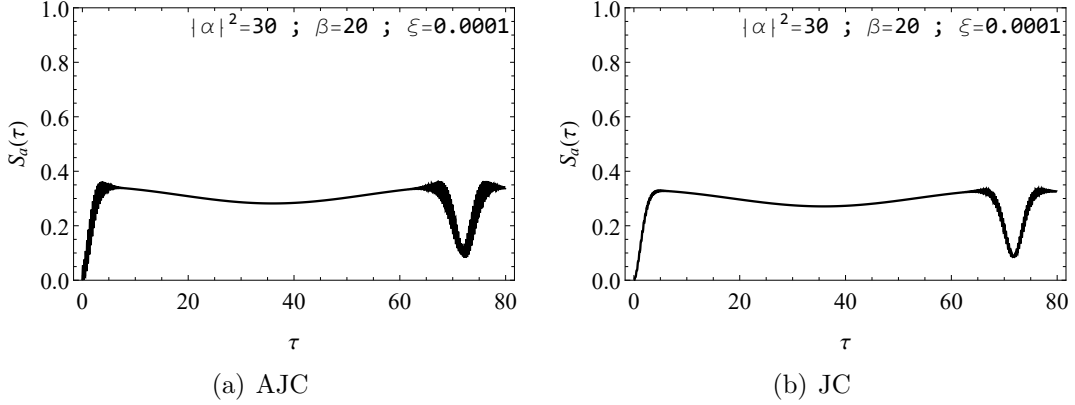
Figure 4.10: Time evolution of entropy of entanglement. Fig. (4.10(a)), time evolution of $S_a(\tau)$ at $\bar{\delta} = (\beta + 2\xi)\lambda = 20.0002\lambda$; $\beta = 20$, $\xi = 0.0001$ and $|\alpha|^2 = 30$ in the AJC process while Fig. (4.10(b)) [Fig. B.4, Appendix B] is the corresponding $S_a(\tau)$ at $\delta = \beta\lambda = 20\lambda$; $\beta = 20$, $\xi = 0.0001$ and $|\alpha|^2 = 30$ in the JC interaction.

Based on the preceding results in Figs. 4.7(a), 4.7(b), 4.8(a), 4.8(b), 4.9 and 4.10 we see that;

104

(i) at all time intervals, time evolution of the DEM, atomic population inversion, $S_a(\tau)$, $W(\tau)$, in the AJC interaction display behaviours agreeing and similar with earlier results in [173, 174, 184–186] and in Appendix B Figs. B.2, B.3 and B.4;

(ii) at `t>0` in a resonant AJC interaction $\bar{\delta} = 2\omega$; $\delta = 0$, Fig. 4.8(a), the value of the DEM as measured by the von Neumann entopy of entanglement, $S_a(\tau)$, presents highest initial value of unity at the collapse time [28], $\tau_c = \frac{1}{\sqrt{2}}$, defining maximum entanglement between the two-level atom and field just like its corresponding resonance case in the JC interaction, Fig. 4.8(b), set at $\delta = 0$ followed by an almost zero value of $S_a(\tau)$ at one half of the revival time as presented in Fig. 4.7, noting that the AJC process is at all times detuned at 2ω even at resonance $\delta = 0$.

During an off-resonant atom-field quantum systems interaction, the revival time, τ_R, of the atomic population inversion is approximated as established in [173], where here, we combine Eqs. (3.3.7b) (AJC) and (B.1.9c) (JC) in a general form

$$\tau_R \simeq \frac{\pi}{\sqrt{\frac{\triangle^2}{4\lambda^2} + (|\alpha|^2 + 1)} - \sqrt{\frac{\triangle^2}{4\lambda^2} + |\alpha|^2}} \quad ; \quad \triangle \equiv \delta, \bar{\delta} = \delta + 2\omega . \qquad (4.2.2)$$

Applying Eq. (3.3.7b) or (4.2.2) in the AJC process $\frac{\tau_R}{2} \simeq 17.3494$ and Eq. (B.1.9b) in the JC process, $\frac{\tau_R}{2} \simeq 17.20721$.

With reference to Figs. 4.7 and 4.8, the physical interpretation agreeing with [174, 184, 187–189] is that at `t>0` the atomic state will not be *pure* but at *one half* of the revival time, evaluated herein, the atom, (cavity) field quantum systems evolve simultaneously into pure state.

At the revival phases, $\tau_R \simeq 34.6989$ (AJC) , $\tau_R \simeq 34.4144$ (JC), as clearly visualised in Figs. 4.7 and 4.8, the DEM in the respective JC, AJC interaction mechanisms oscillates about a local minimum and maximum specifying that the field at the revival phase does not evolve to pure state [174];

(iii) touching on the revival times, τ_R, of the AJC, JC atomic population inversion in (ii) above, we conclude that despite the processes displaying similar patterns during time evolution of $W(\tau)$ and $S_a(\tau)$ they are of different forms due to different values of τ_R. This slight difference in τ_R in the AJC $W(\tau)$ plot in comparison to its corresponding JC case, is due to the residual detuning $\bar{\delta} = 2\omega = 2\xi\lambda$ present in the AJC interaction even at resonance, resulting in delay in revival of atomic inversion as presented;

(iv) in the permanently detuned AJC case in Fig. 4.9(a), just like its corresponding off-resonant JC interaction in Fig. 4.9(b) , the DEM measured by $S_a(\tau)$ displays low values at all time intervals in comparison to that in Fig. 4.8, after which $S_a(\tau)$ decreases further with every increase in frequency detuning δ in the JC process and sum frequency $\overline{\delta} = \delta + 2\omega$ in the AJC case as shown in Fig. 4.10. This means that entanglement between the two-level atom and the field decreases with every increase in sum frequency (AJC) and separately frequency detuning (JC) causing the atom to have less tendency to evolve to excited state, $|e\rangle$, from the ground state, $|g\rangle$.

Applying again Eq. (3.3.7b) or Eq. (4.2.2) to the AJC $S_a(\tau)$ plot in Fig. 4.9(a), we obtain half the revival time at $\frac{\tau_R}{2} \simeq 23.40431$ and the corresponding JC $S_a(\tau)$ curve in Fig. 4.9(b), $\frac{\tau_R}{2} = 23.40410$. Similarly the JC $S_a(\tau)$ curve presented in Fig. 4.10(a) gives $\frac{\tau_R}{2} \simeq 35.88870$ while the corresponding JC plot in Fig. 4.10(b) $\frac{\tau_R}{2} \simeq 35.88842$. It is clear that at these times $S_a(t)$ does not dip as much towards $S_a(\tau) = 0$ in comparison to the resonance cases in Fig. 4.8 accordant with [173]. Further, a clear delay in revival time of atomic inversion, τ_R, during all the AJC processes as a consequence of the additional residual detuning $2\omega = 2\xi\lambda$ is noted.

The reduction in $S_a(\tau)$ means that for large sum frequency $\overline{\delta} = \delta + 2\omega$ (AJC) and separately frequency detuning $\delta = \omega_0 - \omega$ (JC), the system tends to pure state at all time intervals during the interaction;

(v) during the AJC process in Figs. 4.9(a) and 4.10(a), rapid oscillations of $S_a(t)$ are observed at the collapse time $\tau_c = \frac{1}{\sqrt{2}}$ and the revival time, τ_R, in conformity with the prediction by Bloch and Siegert [86] that the CR frequency that yields a population oscillation of 2ω results into rapid spin-flipping operations due to entanglement of the interacting atom-field quantum systems. In contrast, it is clear that during the corresponding JC processes in Figs. 4.9(b) and 4.10(b), rapid oscillations are only at the revival phase and

(vi) during the AJC processes in Figs. 4.9(a) and 4.10(a), $S_a(\tau)$ records a slightly higher value than all the corresponding JC processes in Figs. 4.9(b) and 4.10(b).

4.2.2 Photon statistics

In this section we analyse the behavior/properties of photons in the AJC process where we applied the Mandel Q-Parameter in Eq. (3.3.11). Using the reduced density operator of the field mode $\hat{\overline{\rho}}_f^g(t)$ in Eq. (3.3.13) and the evaluations of mean $\langle \hat{\eta} \rangle$, mean

square $\langle \hat{\eta}^2 \rangle$ photon number in Eq. (3.3.14) we proceeded to plot the time evolution of the Mandel Q-parameter ($\tau = \lambda t$ is the scaled time) for an initial atomic ground state $|g\rangle$ and field mode, initial coherent state $|\alpha\rangle$. Plots of the AJC curves are provided in Figs. 4.11(a), 4.12(a), 4.13(a) and 4.14(a). We present a comparison with those of the corresponding JC process at resonance $\delta = 0$, off-resonance $\delta \neq 0$ at low, high field intensities $|\alpha|^2$ in Figs. 4.11(b) [Plotted in Fig. B.5], 4.12(b)[Plotted in Fig. B.6], 4.13(b)[Plotted in Fig. B.7] and 4.14(b)[Plotted in Fig. B.8] as determined in Appendix B.

(a) AJC

(b) JC

Figure 4.11: Time evolution of Mandel parameter. Fig. (4.11(a)) is the time evolution of $Q(\tau)$ at $\bar{\delta} = 2\xi\lambda = 0.0002\lambda$; $(\beta = 0)$, $\xi = 0.0001$ and $|\alpha|^2 = 6$ in the AJC process while Fig. (4.11(b)),$Q(\tau)$ at $\delta = \beta\lambda = 0$; $(\beta = 0)$ and $|\alpha|^2 = 6$ in the JC interaction plotted in Fig. B.5, Appendix B.

(a) AJC

(b) JC
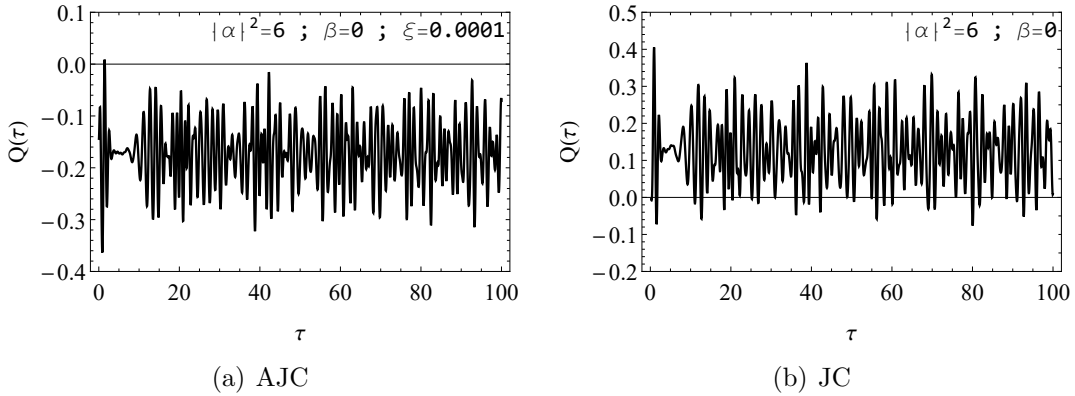
Figure 4.12: Time evolution of Mandel parameter. Fig. (4.12(a)) is the time evolution of $Q(\tau)$ at $\bar{\delta} = 2\xi\lambda = 0.0002\lambda$; $(\beta = 0)$, $\xi = 0.0001$ and $|\alpha|^2 = 30$ in the AJC process while Fig. (4.12(b))[Plotted in Fig. B.6, Appendix B],the corresponding $Q(\tau)$ at $\delta = \beta\lambda = 0$; $(\beta = 0)$ and $|\alpha|^2 = 30$ in the JC interaction.

(a) AJC

(b) JC

Figure 4.13: Time evolution of Mandel parameter. Fig. (4.13(a)) is the time evolution of $Q(\tau)$ at $\overline{\delta} = (\beta + 2\xi)\lambda = 20.0002\lambda; \beta = 20, \xi = 0.0001$ and $|\alpha|^2 = 30$ in the AJC process while Fig. (4.13(b)), is the corresponding $Q(\tau)$ at $\delta = \beta\lambda = 20\lambda; \beta = 20$ and $|\alpha|^2 = 6$ in the JC interaction plotted in Fig. B.7, Appendix B.

(a) AJC

(b) JC

Figure 4.14: Time evolution of Mandel parameter. Fig. (4.14(a)) is the corresponding time evolution of $Q(\tau)$ at $\overline{\delta} = (\beta + 2\xi)\lambda = 20.0002\lambda; \beta = 20, \xi = 0.0001$ and $|\alpha|^2 = 30$ in the AJC process while Fig. (4.14(b)), is the corresponding $Q(\tau)$ at $\delta = \beta\lambda = 20\lambda; \beta = 20$ and $|\alpha|^2 = 30$ in the JC interaction plotted in Fig. B.8 Appendix B.

From the plots in Figs. 4.11 - 4.14 we see that;

i) the photon statistics during the JC interaction is dominantly super-Poissonian as presented in Figs. 4.11(b), 4.12(b) and 4.14(b) consistent with the observation made in [190]. The only exception is in Fig. 4.13(b) where the nature of photons is dominantly sub-Poissonian. In this particular example a non-zero detuning $\delta \neq 0$ is introduced for a low mean photon number $|\alpha|^2$ and

ii) in the AJC plots in Figs. 4.11(a), 4.12(a), 4.13(a) and 4.14(a), the photon statistics

is dominantly sub-Poissonian and only exhibits negligibly small intervals of super-Poissonian statistics when the field intensity specified by $|\alpha|^2$ is increased during AJC atom, field resonant interaction $\overline{\delta} = 2\omega$; $\delta = 0$. For clarity, compare Figs. 4.11(a) and 4.12(a). This means that in the AJC interaction, the photon-number variance is much less than the average number of photons, $\langle(\Delta\hat{\eta})^2\rangle \ll \langle\hat{\eta}\rangle$, of the coherent field mode.

This dominant sub-Poissonian nature of photon field during the AJC process, is the cause of the observed slightly higher values of $S_a(t)$ recorded in Figs. 4.9(a) and 4.10(a) Sec. 4.2.1 consistent with [191].

We conclude here that the AJC process provides a signature sub-Poissonian photon statistics during the interaction, indicating that the photons in this particular interaction are naturally anti-bunched and maintains it despite variation of the field intensity and sum frequency as presented in our examples.

4.3 AJC dynamics of a two-level atom interacting with field mode in an initial squeezed coherent state

When the field mode in an initial squeezed coherent state is considered, we examine the temporal evolution of a two-level atom in a resonant, $\overline{\delta} = 2\omega$, off-resonant, $\overline{\delta} = \delta + 2\omega$, AJC interaction. In this model, the purity of states, $tr(\hat{\overline{\rho}}_a^2(t))$, in respect to atom-field entanglement, $S_a(t)$, is explored during the time evolution of atomic population inversion, $W(t)$. Furthermore, an examination of the quantum nature of the field system in the AJC interaction is provided by analysis of dynamics of the Mandel Q-parameter, $Q(t)$. A comparison with the well-known outcomes of the JC interaction provided in Appendix. C is included for ease of reference. Further, the considered residual detuning parameter, $\xi = 0.0001$ in Sec. 4.2.1 applies. In this regard, an exhaustive comparison is feasible, following the mathematical and physical interpretation provided therein.

4.3.1 Photon statistics

Referring to the reduced field density operator $\hat{\overline{\rho}}_f^g(t)$ in Eqs. (3.4.7), (3.4.8), interaction parameters, Rabi frequencies defined in Eq. (3.3.5d) and mean, mean square photon number defined in Eq. (3.4.9) we easily evaluate $Q(\tau)$ in Eq. (3.4.9) at resonance $\overline{\delta} = 2\omega$; $\delta = 0$, squeeze parameter values $r = 1, 1.3, 1.4, 1.5$ and field intensity $|\alpha|^2 = 40$. We then plot time evolution of the Mandel parameter $Q(\tau)$ (where $\tau = \lambda t$ is the scaled time) for an initial atomic ground state $|g\rangle$ and initial squeezed coherent state $|\alpha, r\rangle$

in Figs. 4.15(a), 4.16(a), 4.17(a) and 4.18(a). Plots of the corresponding JC process at resonance $\delta = 0$; $r = 1, 1.3, 1.4, 1.5$ and field intensity $|\alpha|^2 = 40$ are presented in Figs. 4.15(b) [Fig. C.1], 4.16(b) [Fig. C.2], 4.17(b)[Fig. C.3] and 4.18(b)[Fig. C.4] as determined in Appendix C.
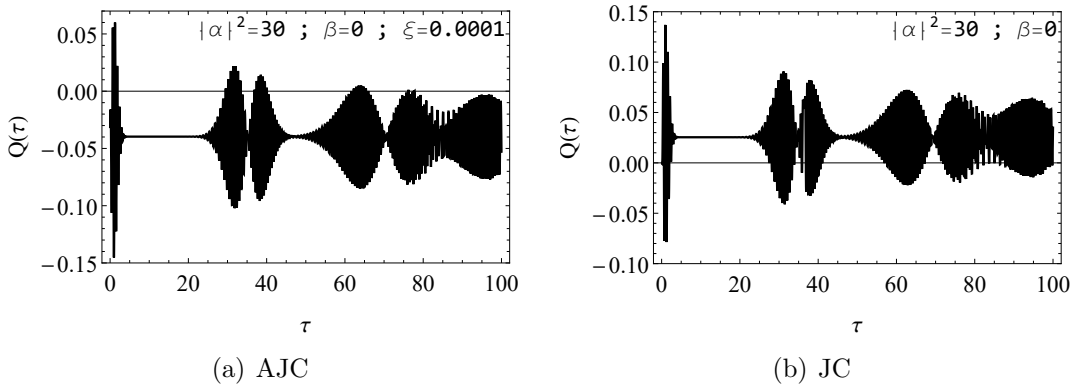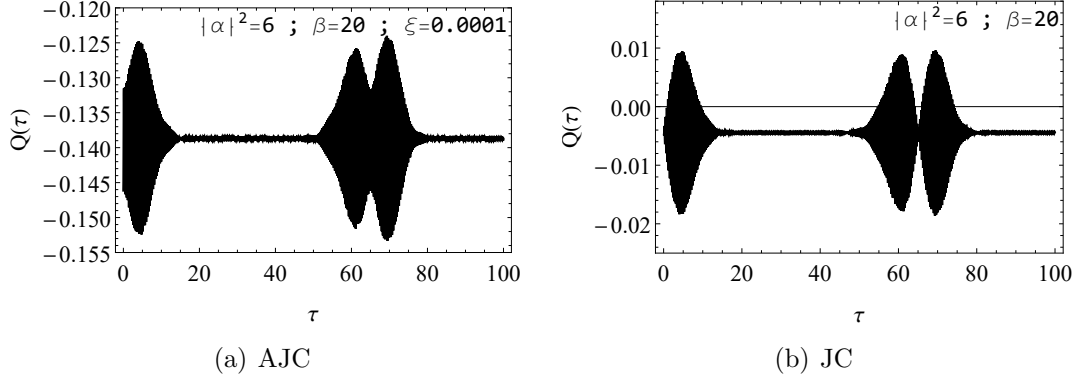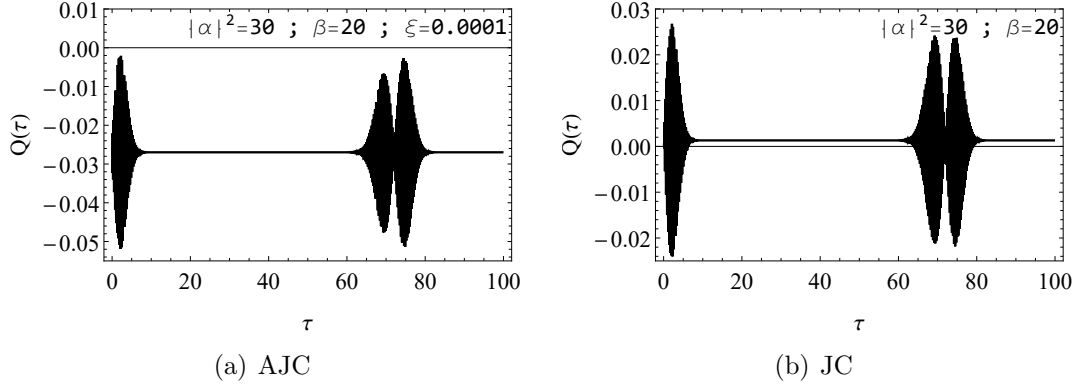

(a) AJC

(b) JC

Figure 4.15: Time evolution of Mandel parameter. Fig. (4.15(a)) is the time evolution of $Q(\tau)$ at $\overline{\delta} = 2\xi\lambda = 0.0002\lambda$; $\beta = 0$, $r = 1$, $\xi = 0.0001$ and $|\alpha|^2 = 40$ in the AJC process while Fig. (4.15(b))[Fig. C.1, Appendix C], is the corresponding plot of $Q(\tau)$ at $\delta = \beta\lambda = 0$; $\beta = 0$, $r = 1$ and $|\alpha|^2 = 40$ in the JC interaction.

(a) AJC

(b) JC
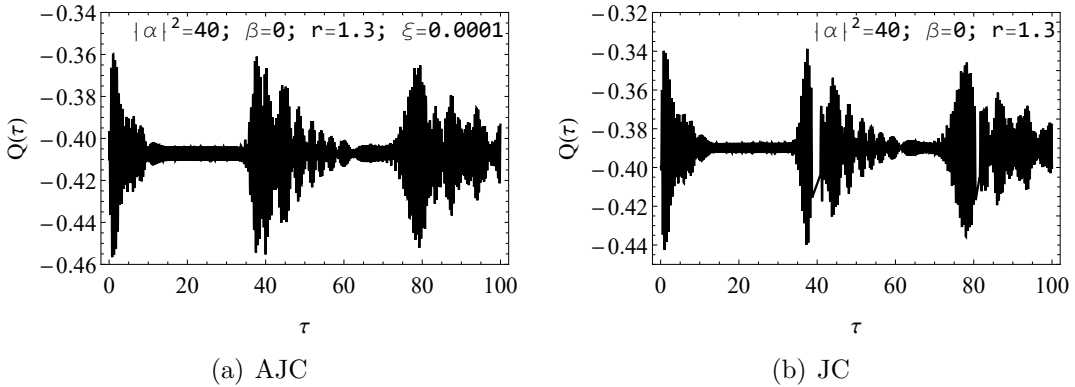
Figure 4.16: Time evolution of Mandel parameter. Fig. (4.16(a)) is the time evolution of $Q(\tau)$ at $\overline{\delta} = 2\xi\lambda = 0.0002\lambda$; $\beta = 0$, $r = 1.3$, $\xi = 0.0001$ and $|\alpha|^2 = 40$ in the AJC process while Fig. (4.16(b))[Fig. C.2, Appendix C], is the corresponding plot of $Q(\tau)$ at $\delta = \beta\lambda = 0$; $\beta = 0$, $r = 1.3$ and $|\alpha|^2 = 40$ in the JC interaction.
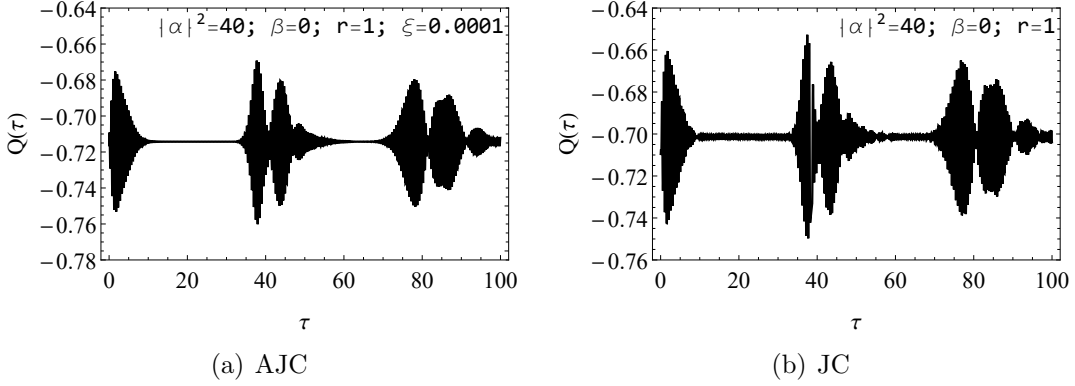
110

(a) AJC

(b) JC
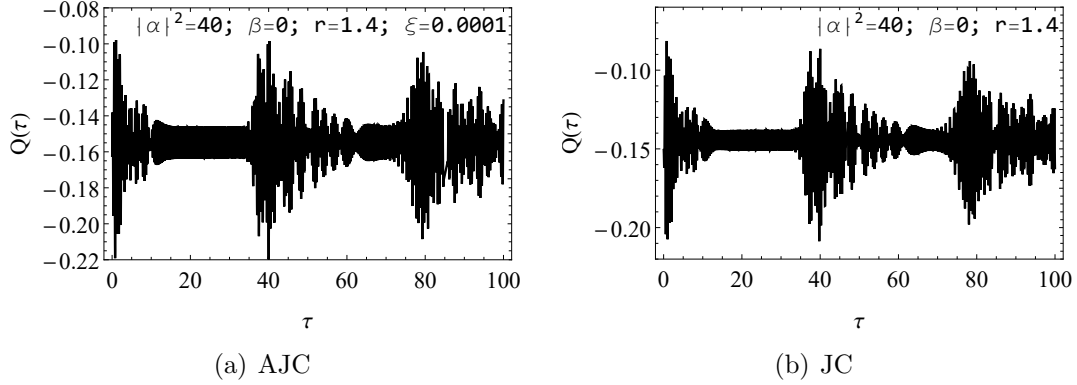
Figure 4.17: Time evolution of Mandel parameter. Fig. (4.17(a)) is the time evolution of $Q(\tau)$ at $\bar{\delta} = 2\xi\lambda = 0.0002\lambda$; $\beta = 0$, $r = 1.4$, $\xi = 0.0001$ and $|\alpha|^2 = 40$ in the AJC process while Fig. (4.17(b))[Fig. C.3, Appendix C], is the corresponding plot of $Q(\tau)$ at $\delta = \beta\lambda = 0$; $\beta = 0$, $r = 1.4$ and $|\alpha|^2 = 40$ in the JC interaction.

(a) AJC

(b) JC
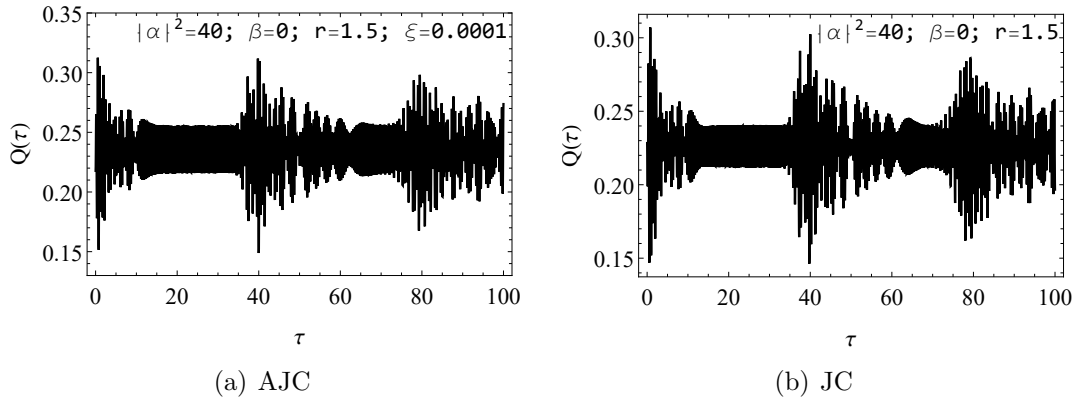
Figure 4.18: Time evolution of Mandel parameter. Fig. (4.18(a)) is the corresponding time evolution of $Q(\tau)$ at $\bar{\delta} = 2\xi\lambda = 0.0002\lambda$; $\beta = 0, r = 1.5$, $\xi = 0.0001$ and $|\alpha|^2 = 40$ in the AJC process while Fig. (4.18(b))[Fig. C.4, Appendix C], is the corresponding plot of $Q(\tau)$ at $\delta = \beta\lambda = 0$; $\beta = 0$, $r = 1.5$ and $|\alpha|^2 = 40$ in the JC interaction.

From the plots in Figs. 4.15 - 4.18 we see that;

(i) the photon statistics during the AJC interaction just like the JC interaction is dominantly sub-Poissonian at squeeze parameters $r = 1$ to $r = 1.4$ as presented in Figs. 4.15 - 4.17. The only exception is in Fig. 4.18 set at $r = 1.5$ where the photon statistics evolves to a dominant super-Poissonian from sub-Poissonian photon statistics;

(ii) in the AJC plots in Figs. 4.15(a), 4.16(a), 4.17(a) and 4.18(a), the pattern of the

111

time evolution of the Mandel parameter are similar to the corresponding JC cases in Figs. 4.15(b), 4.16(b), 4.17(b) and 4.18(a) but notable difference in thichkness at the collapse phase, revivals and revival peaks as visualised. However the evolutions of $Q(\tau)$ during the JC interactions in Figs. 4.15, 4.16 and 4.17 depict less negative values of $Q(\tau)$ than the corresponding AJC $Q(\tau)$ evolutions which are more negative. This means that the AJC process provides a reduced photon-number variance than the mean photon number of the squeezed coherent field mode, i.e., $\langle (\Delta \hat{n})^2 \rangle \ll \langle \hat{n} \rangle$. This implies that a more anti-bunched photon field mode, can be easily realised, during the AJC process than during the JC interaction.

We conclude at this point that the interaction feature of photon statistics at squeeze parameter, $1 \leq r \leq 1.4$, during the AJC process is similar to that realised during the corresponding JC interaction when an initial squeezed coherent field mode is considered. However, obtaining a more anti-bunched field mode in the AJC interaction is easier than in the analogous JC process as visualised, since the AJC $Q(\tau)$ values are more negative values than the related JC $Q(\tau)$ values.

4.3.2 Evolution of atomic population inversion and entropy of entanglement

As earlier stated, the z-component of the time evolving Bloch vector, $\vec{r}(t)$, is the difference of the time evolving excited state probability, $\overline{P}_{ee}(t)$, and time evolving ground state probability, $\overline{P}_{gg}(t)$, that defines atomic population inversion, $W(t)$. Applying the explicit definitions of the time evolving Bloch vector component $\overline{r}_z(t)$ in Eq. (3.4.11), we plot $W(t)$ in Figs. 4.19(a), 4.20(a) at $\overline{\delta} = 2\omega$; $\delta = 0, r = 1, 1.5, |\alpha|^2 = 40$ during the AJC interaction and compare with the JC interaction in Figs. 4.19(b)[Fig. C.5, Appendix C], 4.20(b)[Fig. C.6, Appendix C] at $\delta = 0, r = 1, 1.5, |\alpha|^2 = 40$ as determined in Appendix C.

(a) AJC

(b) JC
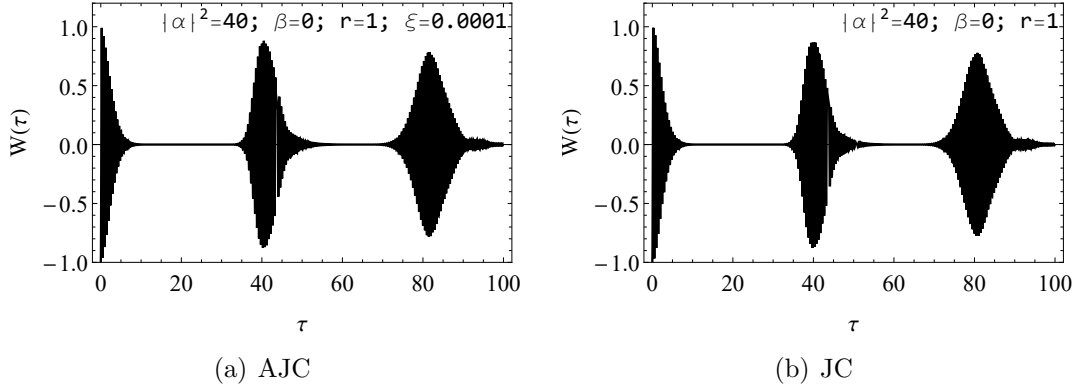
Figure 4.19: Time evolution of atomic population inversion. Fig. (4.19(a)) is the time evolution of $W(\tau)$ at $\overline{\delta} = 2\xi\lambda = 0.0002\lambda$; $\beta = 0, r = 1$, $\xi = 0.0001$ and $|\alpha|^2 = 40$ in the AJC process while Fig. (4.19(b))[Fig. C.5, Appendix C] is the corresponding plot of $W(\tau)$ at $\delta = \beta\lambda = 0$; $\beta = 0$, $r = 1$ and $|\alpha|^2 = 40$ in the JC interaction.


(a) AJC

(b) JC
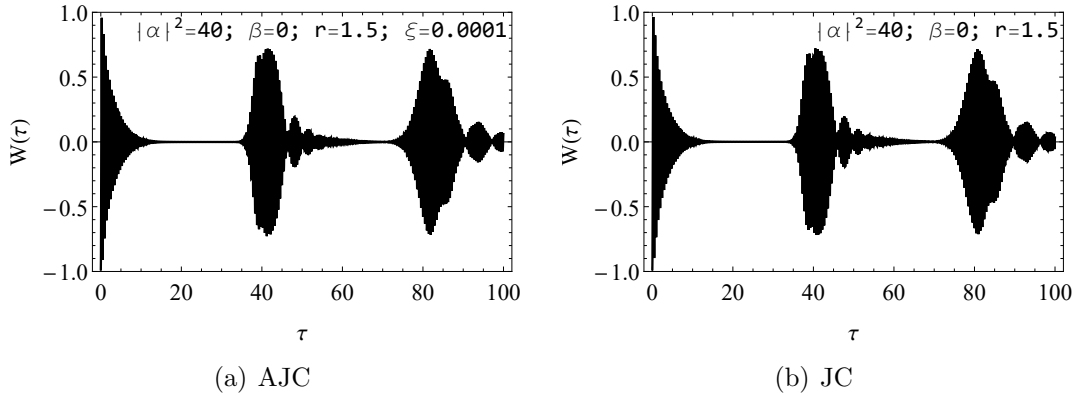
Figure 4.20: Time evolution of atomic population inversion. Fig. (4.20(a)) is the time evolution of $W(\tau)$ at $\overline{\delta} = 2\xi\lambda = 0.0002\lambda$; $\beta = 0$, $r = 1.5$, $\xi = 0.0001$ and $|\alpha|^2 = 40$ in the AJC process while Fig. (4.20(b))[Fig. C.6, Appendix C], is the corresponding plot of $W(\tau)$ at $\delta = \beta\lambda = 0$; $\beta = 0$, $r = 1.5$ and $|\alpha|^2 = 40$ in the JC interaction.

(a) AJC

(b) JC
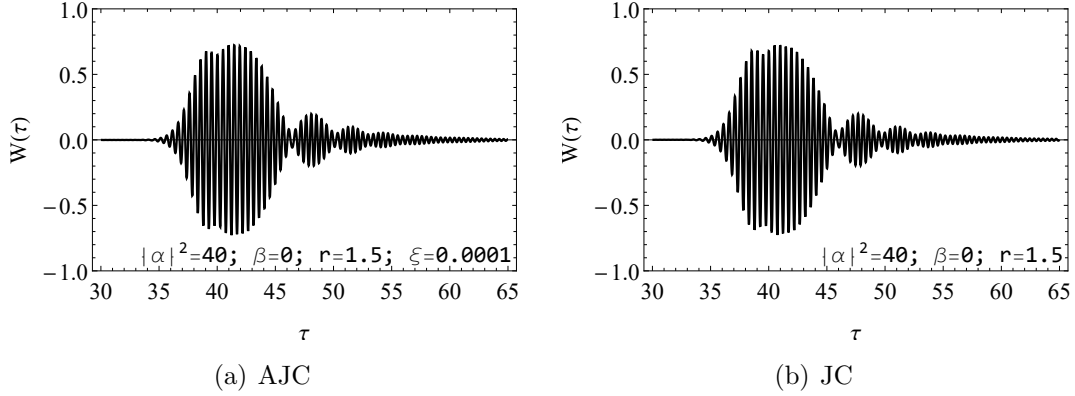
Figure 4.21: Time evolution of atomic population inversion (Ringing revivals).
Fig. (4.21(a)) is the time evolution of $W(\tau)$ at $\bar{\delta} = 2\xi\lambda = 0.0002\lambda$; $\beta = 0$, $r = 1.5$,
$\xi = 0.0001$ and $|\alpha|^2 = 40$ in the AJC process while Fig. (4.21(b))[Fig. C.7, Appendix C],
is the corresponding plot of $W(\tau)$ at $\delta = \beta\lambda = 0$; $\beta = 0$, $r = 1.5$ and $|\alpha|^2 = 40$ in the JC
interaction.

We proceed to plot the photon number distribution $P(n)$ defined in Eq. (3.4.3) at
$r = 1$, 1.5, $|\alpha|^2 = 40$ in Figs. 4.22(a), 4.22(b).

(a)

(b)
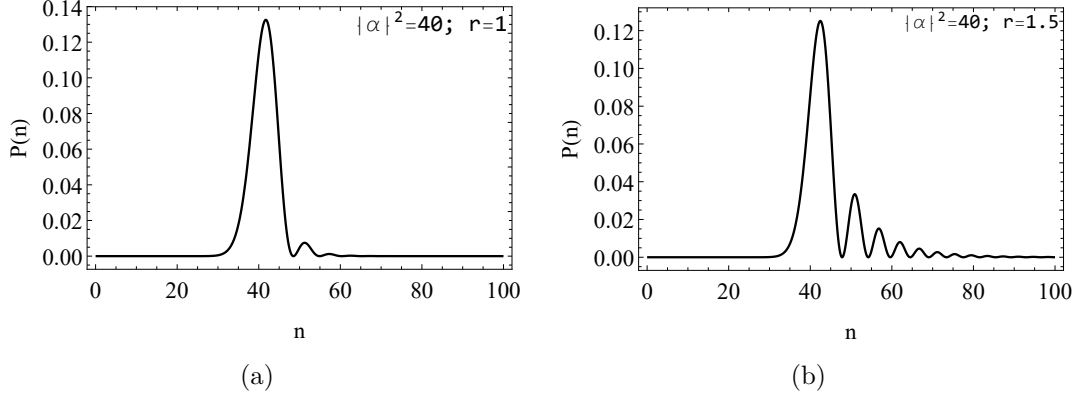
Figure 4.22: Photon number distribution $P(n)$. Fig. (4.22(a)) [Fig. C.8(a)], $P(n)$ at $r = 1$
and $|\alpha|^2 = 40$ while Fig. (4.22(b)) [Fig. C.8(b)] $P(n)$ at $r = 1.5$, $|\alpha|^2 = 40$

From the results in Figs. 4.19 - 4.22 we see:

i) that the time evolution of atomic population inversion during the AJC, JC processes
   appear similar in form. To investigate, let us determine their respective revival times,
   τ_R. As established in [192], we apply Eq. (B.1.9b) and express the field intensity
   formalism with regard to an initial squeezed coherent state, $\langle \hat{n} \rangle = |\alpha|^2 + \sinh^2(r)$.

114

The curve in Fig. 4.19(b) plotted in a resonant, $\delta = 0$, JC process and squeeze parameter, $r = 1$, has a revival time $\tau_R \simeq 40.41856$ while application of Eq. (3.3.7b) or Eq. (4.2.2) defined in [173] to the corresponding AJC resonant condition curve $\overline{\delta} = 0.0002\lambda$, squeeze parameter $r = 1$ plotted as presented in Fig. 4.19(a), we obtain $\tau_R \simeq 40.661292$. Similarly, Fig. 4.20(b) plotted in a resonant, $\delta = 0$, JC interaction, squeeze parameter $r = 1.5$, we apply Eq. (4.2.2) to obtain a revival time $\tau_R \simeq 41.93000$ while the corresponding AJC resonant condition plot 4.20(a) set at $\overline{\delta} = 0.0002\lambda$, squeeze parameter $r = 1.5$, application of Eq. (3.3.7b) or Eq. (4.2.2) yields a revival time $\tau_R \simeq 42.16408$. We see from these results that:

a) the atomic population inversion curves display the same pattern but are of distinct forms due to the different revival times, τ_R, and

b) there is an increase in revival time. This has two clear contributors. The first is an increase in squeeze parameter, r, which results in delay in revival of atomic inversion and second, the existance of the AJC residual infinitesimal detuning, $2\omega = 2\xi\lambda$, that causes the same effect of delaying revival in atomic inversion. A similar result was discussed in [17, 193], i.e, squeezing can be enhanced by increasing the squeeze parameter, r, or frequency detuning as its sum, $\overline{\delta} = \omega_0 + \omega$, (AJC) or difference, $\delta = \omega_0 - \omega$, (JC) ;

ii) that the oscillations at $r = 1.5$ in Figs. 4.20(b), 4.20(a) are more irregular at the collapse region than when $r = 1$ in Figs. 4.19(b), 4.19(a), commonly referred to as ringing revivals (see Fig. 4.21) in agreement with [17, 194], i.e., the collapse region is modulated or displays ringing different from the well known collapse region obtained when an initial coherent field is considered [28]. As explained in detail in [17, 194], the ringing is due to interference of the additional peaks (see Fig. 4.22) in the photon number distribution $P(n) = |\langle n|\alpha, r\rangle|^2$ observed during the AJC interaction and separately JC interaction (presented in Appendix. C), because the revivals produced by different peaks of $P(n)$ have different local mean photon numbers. In the process revivals due to individual peaks overlap but the effect of the resulting interference is to sharpen the ringing structure other than washing it away, i.e, the addition of each local peak in $P(n)$ adds an echo in $W(\tau)$ and the successive echoes brings further interference, which sharpens the echoes at earlier times and;

iii) in Fig. 4.19 sharpness of the revival regions during atomic population inversion which occur when the field is sub-Poissonian (see Fig. 4.15 at $r = 1$) accordant with [194], in comparison to the less pronounced and blunt peaks in Fig. 4.20 at $r = 1.5$. We

noted in our example in Fig. 4.18 plotted at $r = 1.5$ during the AJC, JC processes, that the field is super-Poissonian.

Accordingly, for purposes of completeness its important to visualise and discuss the collapses and revival phenomenon in relation to the DEM. Here the DEM is measured by the von Neumann entropy $S_a(t)$ defined in Eq. (3.3.8) in terms of the time evolving Bloch vector $\vec{r}(t)$ in the general form. Now, with the time evolving Bloch vector components explicitly defined in Eq. (3.4.11) we easily evaluate $S_a(t)$. The AJC process atomic entropy $S_a(\tau)$ ($\tau = \lambda t$ is the scaled time) plots are presented in Figs. 4.23(a) and 4.24(a) while the corresponding JC interaction plots at resonance $\delta = 0, r = 1, 1.5$, and field intensity $|\alpha|^2 = 40$ are shown in Figs. 4.23(b)[Fig. C.9, Appendix C] and 4.24(b)[Fig. C.10, Appendix C] as analysed in Appendix C.

| (a) AJC | (b) JC |

Figure 4.23: Time evolution of atomic entropy. Fig. (4.23(a)) is the time evolution of $S_a(\tau)$ at $\bar{\delta} = 2\xi\lambda = 0.0002\lambda$; $\beta = 0, r = 1$, $\xi = 0.0001$ and $|\alpha|^2 = 40$ in the AJC process while Fig. (4.23(b))[Fig. C.9, Appendix C], is the corresponding plot of $S_a(\tau)$ at $\delta = \beta\lambda = 0$; $\beta = 0$, $r = 1$ and $|\alpha|^2 = 40$ in the JC interaction.
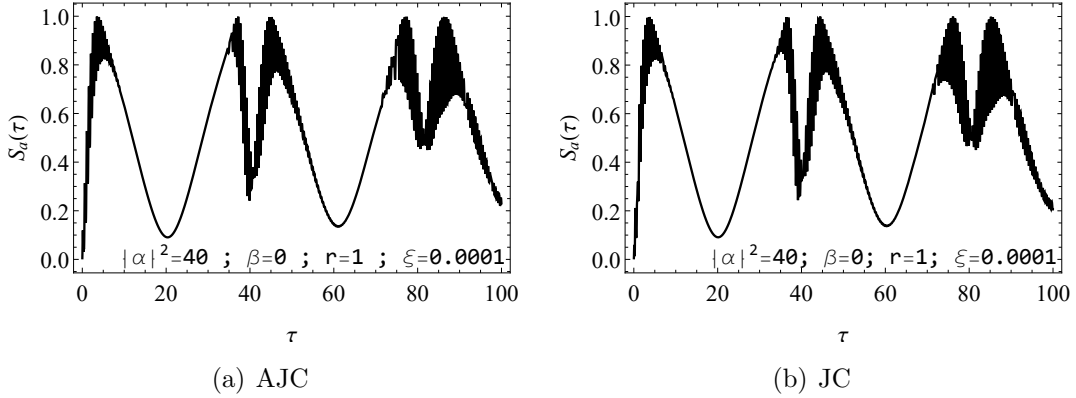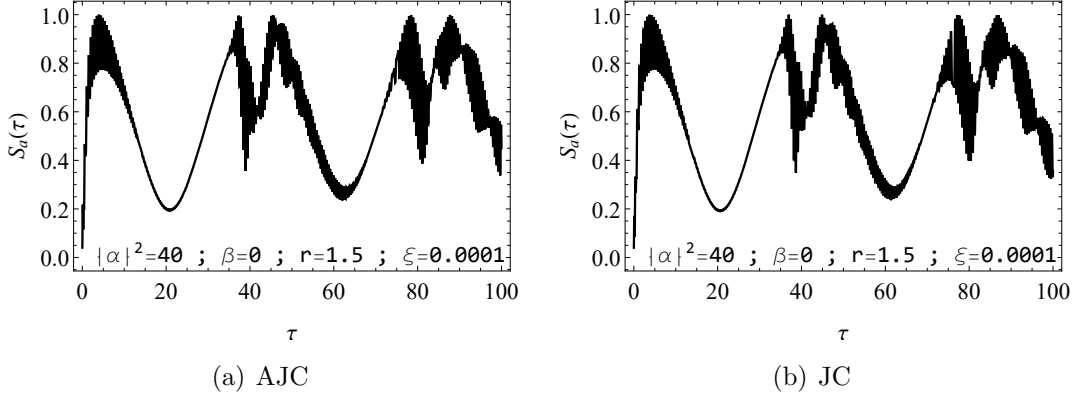
Figure 4.24: Time evolution of atomic entropy. Fig. (4.24(a)) is the time evolution of $S_a(\tau)$ at $\bar{\delta} = 2\xi\lambda = 0.0002\lambda$; $\beta = 0, r = 1.5$, $\xi = 0.0001$ and $|\alpha|^2 = 40$ in the AJC process while Fig. (4.24(b))[Fig. C.10, Appendix C], is the corresponding plot of $S_a(\tau)$ at $\delta = \beta\lambda = 0$; $\beta = 0$, $r = 1.5$ and $|\alpha|^2 = 40$ in the JC interaction.

Based on the results in Figs. 4.23 and 4.24;

i) we see that at a glance, we may not point out the exact revival times, due to the similar forms of the curves. We can however apply Eqs. (B.1.9b), (B.1.9c) or (3.3.7b) to establish the exact revival times, τ_R.

In Fig. 4.23(a) plotted in the AJC interactions, the the revival time is determined by applying Eq. (3.3.7b) or Eq. (B.1.9c) after substituting the field intensity form of an initial squeezed coherent state, $|\alpha|^2 + \sinh^2(r)$, to obtain $\tau_R \simeq 40.66129$. The corresponding revival time, τ_R, for the JC $S_a(\tau)$ curve in Fig. 4.23(b) is determined by apply Eq. (B.1.9b) after substituting the field intensity in the squeezed coherent state form, $|\alpha|^2 + \sinh^2(r)$, to obtain $\tau_R \simeq 40.41856$. We see that at these times, the value of $S_a(\tau)$ is approximately equal to that at half the revival times $\frac{\tau_R}{2}$, i.e, $S_a(\tau) \simeq 0.04$ in our example. This means that at these times $(\tau_R, \frac{\tau_R}{2})$ the atom-field states are entangled (mixed) when an initial squeezed coherent state is considered, accordant with [194]. In addition, as time advances, we note gradual increase in DEM and consequently the degree of mixedness since $S_a(t)$ records gradual increasing values with every increase in time. In addition, since the squeeze parameter is set at $r = 1$, we note that the delay in revival time during the AJC interaction in Fig. 4.23(a) in comparison to the JC curve in Fig. 4.23(b), is due to the effect of the residual detuning $\bar{\delta} = 2\omega = 2\xi\lambda$. Note here that ξ in the JC process is a phase, and it does not affect the dynamics of $S_a(\tau)$ as presented;

ii) that the behaviour in (i) is enhanced during the AJC and separately JC interaction set at $r = 1.5$ as presented in Fig. 4.24. The form of time evolution of $S_a(\tau)$ becomes more rapid with oscillations between $[\simeq 0.2, 1]$ characterising an increase in DEM (and so the degree of mixedness), consistent with [194]. It is now clear that the DEM (mixedness) increases with an increase in r;

iii) as demostrated in Fig. 4.23 set at $r = 1$, that the evolution of $S_a(\tau)$ during the AJC interaction and separately the corresponding JC interaction are of close form since the difference in revival time is negligibly small. A similar observation suffices at $r = 1.5$ as visualised in Fig. 4.24 and

iv) we observe ringing at periods after revivals, i.e, $\tau = 45$ and $\tau = 90$, reminiscent to that of the atomic population inversion discussed earlier. This is caused by the additional oscillations (peaks) in the photon number distribution $P(n)$ in Fig. 4.22(b), due to addition of more squeezed photons in the coherent field. This effect is observed in the AJC $S_a(\tau)$ dynamics in Fig. 4.24(a) and the corresponding JC $S_a(\tau)$ dynamics in Fig. 4.24(b) and in agreement with the findings determined separately in [193].

In conclusion, it is important to note that the time evolution atomic population inversion $W(\tau)$ graphs in Figs. 4.19, 4.20 and separately, the time evolution of atomic entropy $S_a(\tau)$ curves in Figs. 4.23, 4.24 depict similar respective patterns, however, they are of different forms with respect to different revival times, τ_R in $W(\tau)$, $S_a(\tau)$ dynamics. More precisely, the AJC $W(\tau)$, $S_a(\tau)$ evolutions, have longer revival times than that observed in the JC $W(\tau)$, $S_a(\tau)$ dynamics. Further, the field statistics in the AJC interaction in Figs. 4.15, 4.16 and 4.17 as measured by the time evolution of $Q(\tau)$, indicate that the field statistics in the AJC interaction is more anti-bunched than that in the JC interaction.

To facilitate the visualised comprehensive comparison, we intentionally set the dimensionless frequency ratio ξ at a very small value, so that the AJC resonant condition $\overline{\delta} = 2\omega = 2\xi\lambda$; $\delta = \beta\lambda = 0$, does not depart considerably from the JC resonant condition $\delta = 0$.

Under resonance, the explicit definitions of the Bloch vector components $\overline{r}_x(t)$, $\overline{r}_y(t)$, $\overline{r}_z(t)$ in Eq. (3.4.11), describing the AJC interaction while referring to the definitions of interaction parameters $\overline{c}_{gn}$, $\overline{s}_{gn-1}$, and Rabi frequency $\overline{R}_{gn}$, $\overline{R}_{gn-1}$ defined and determined in Eq. (3.3.5d) reduce to the form of Eq. (4.2.1a). Similarly, the corresponding Bloch vector components $r_x(t)$, $r_y(t)$, $r_z(t)$ describing the JC interaction as presented in Eq. (C.1.9) Appendix C while referring to the interaction parameters c_{gn}, s_{gn+1} and Rabi

frequency R_{gn}, R_{gn+1} defined and determined from Eq. (C.1.6), Appendix C take the form of Eq. (4.2.1b)

We see from Eq. (4.2.1a) that in a resonant atom-field AJC interaction interaction $\overline{\delta} = 2\omega = 2\xi\lambda$, the dimensionless frequency detuning ratio $\beta = \frac{\delta}{\lambda} = 0$; $\delta = 0$ and so the time-evolving Bloch vector components $\overline{r}_x(t)$, $\overline{r}_y(t)$, $\overline{r}_z(t)$ have only the photon number n, the dimensionless field mode frequency ratio $\xi = \frac{\omega}{\lambda}$, the mean photon number $|\alpha|^2$ and the squeeze parameter r as the variables while from Eq. (4.2.1b), in a resonant JC interaction $\delta = 0$, the mean photon number $|\alpha|^2$, the photon number n and the squeeze parameter r are the variables.

It therefore follows that the squeezing effect specified by the squeeze parameter r domiciled the interactions respectively since the mean photon number was set constant at $|\alpha|^2 = 40$.

We take note here that varying separately the mean photon number $|\alpha|^2$, sum frequency (frequency detuning) $\overline{\delta}(\delta)$ parameters also affects the degree of squeezing [195, 196], i.e., the squeezing effect is enhanced with each increase in $|\alpha|^2$, $\overline{\delta}$, δ. This means that as an alternate to variation in squeeze parameter r, keeping r constant while separately varying $|\alpha|^2$, δ, $\overline{\delta}$ upwards will result in strongly squeezed states or rather, squeezing effect.

In this thesis we considered one case; variation in the squeeze parameter r at a constant field intensity $|\alpha|^2 = 40$ and in a resonant AJC interaction $\overline{\delta} = 2\omega$ to make comparison with the corresponding JC interaction at resonance $\delta = 0$ clear. Recall that the AJC interaction always has a residual field mode frequency 2ω.

CHAPTER 5
DISCUSSION AND CONCLUSIONS

In this chapter discussion of results obtained in Chapter 4 is presented. In Secs. 5.1, 5.2 and 5.3 clear similarities and differences in quantum features of Rabi oscillations, entanglement and nature of field during the respective AJC, JC interaction is highlighted.

5.1 Two-level atom interacting with a field mode in Fock state

i) In Secs. 4.1.1 and A.2.1 of this thesis we analysed Rabi oscillations between basic stationary coupled atom-field AJC ($|\psi_{gn}\rangle$, $|\overline{\phi}_{gn}\rangle$), JC ($|\psi_{en}\rangle$, $|\phi_{en}\rangle$) qubit state vectors due to pure time evolving AJC ($|\overline{\Psi}_{gn}(t)\rangle$), JC ($|\Psi_{en}(t)\rangle$) qubit state vectors for an initial vacuum field $n = 0$ as an example. We simulated the Rabi oscillations of the pure time evolving coupled atom-field JC ($|\Psi_{en}(t)\rangle$), AJC ($|\overline{\Psi}_{gn}(t)\rangle$) qubit state vectors on a unit sphere referred to as the Bloch sphere in Figs. A.1, 4.1(a) and 4.2 using Mathematica software. We observed:

a) that Rabi oscillations in a cavity mode in an AJC interaction process, occur in the reverse sense relative to the JC interaction process;

b) with reference to Fig 4.2 that due to the larger sum frequency $\overline{\delta} = \omega_0 + \omega$ in the AJC interaction process as compared to detuning $\delta = \omega_0 - \omega$ in the JC interaction process, the Rabi oscillation circles in the much faster AJC process are much smaller compared to the corresponding Rabi oscillation circles in the slower JC interaction process. This observation agrees precisely with the assumption usually adopted in the RWA to drop the AJC coupling terms that simultaneously excite or de-excite atom and field, noting that the AJC interaction process averages out over time. These Rabi oscillation circles are due to precession of time evolving AJC Bloch vector $\vec{\overline{\rho}}_{gn}(t)$ and the time evolving JC Bloch vector $\vec{\rho}_{en}(t)$ respectively for $n = 0$ in our examples and;

c) in the same picture (Bloch sphere) we analysed JC, AJC resonant and off-resonant behaviour of Rabi oscillation circles. At resonance as visualised in Fig. A.1, the JC Bloch vector $\vec{\rho}_{en}(t)$ traces a path along the yz-plane. In the contrary since the AJC process is always detuned even at resonance $\overline{\delta} = 2\omega$, the Bloch vector $\vec{\overline{\rho}}_{gn}(t)$ precesses at an axis away from the yz-plane as visualised in Fig. 4.1(a). The off-resonant JC process depicted form of Rabi oscillation circles

similar to all the AJC cases as presented in Figs. A.1, 4.1(a). In this off-resonant condition, the JC, AJC Bloch vectors precess at an axis away from the yz-plane.

ii) We went further in Secs. 4.1.2.1and A.2.2.1 respectively to analyse entanglement properties of qubit state vectors $|\psi_{gn}\rangle$, $|\overline{\phi}_{gn}\rangle$ and $|\psi_{en}\rangle$, $|\phi_{en}\rangle$ generated in the AJC, JC interaction processes of a two-level atom and a single mode of quantised electromagnetic field, with the field mode in an initial vacuum state $n = 0$ as an example. We observed that the entanglement properties of basic AJC qubit state vectors $|\psi_{gn}\rangle$, $|\overline{\phi}_{gn}\rangle$ in Sec. 4.1.2.1 at all cases of sum frequency $\overline{\delta} = \omega_0 + \omega$ just like the JC process analysed in Sec. A.2.2.1 for qubit state vectors $|\psi_{en}\rangle$, $|\phi_{en}\rangle$ at off-resonance $\delta \neq 0$ depicted transition of qubit state vectors from initial separable (or product) qubit state vectors $|\psi_{en}\rangle$, $|\psi_{gn}\rangle$ to transition qubit state vectors $|\phi_{en}\rangle$, $|\overline{\phi}_{gn}\rangle$ that are entangled.

The *difference* is in the resonance $\delta = 0$, $\overline{\delta} = 2\omega$ JC, AJC interaction. The generated JC, AJC qubit state transitions $|\psi_{en}\rangle \rightarrow |\phi_{en}\rangle$, $|\psi_{gn}\rangle \rightarrow |\overline{\phi}_{gn}\rangle$ at resonance are; initial separable (product) qubit state $\rightarrow$ transition separable (product) qubit state (JC), initial separable product qubit state $\rightarrow$ entangled transition qubit state (AJC). This latter transition takes that consistent unique form because the AJC process remains detuned at a residual frequency $\overline{\delta} = 2\omega$ at resonance.

iii) In the AJC interaction process just like the JC interaction process, it is possible to generate maximally entangled transition qubit state vectors $|\overline{\phi}_{gn}\rangle$, $|\phi_{en}\rangle$ which are useful in QIP like quantum teleportation as teleportation channels which we demonstrated clearly in this Thesis in Secs. 4.1.2.2 and A.2.2.2.

iv) In Sec. 4.1.3 we studied the general dynamics of AJC interaction described by the general time evolving AJC qubit state vector $|\overline{\Psi}_{gn}(t)\rangle$. We observed that for different values of sum frequency parameter $\overline{\delta}$ and photon number n, the dynamical evolution of entanglement takes the same form as that of the JC interaction process in Sec. A.2.3 and references cited in this Thesis analysed for different values of frequency detuning parameter δ and photon number n. As analysed:

   a) in all the plots in Figs. 4.3(a) - 4.6 in the AJC and Figs. A.2 - A.5 in the JC process, entanglement sudden birth (ESB) and entanglement sudden death (ESD) are observed during time evolution of $E(\tau)$ and $C(\tau)$ respectively;

   b) an increase in sum-frequency parameter $\overline{\delta}$ in the AJC process and frequency detuning parameter δ in the JC process results into an increase in frequency of

oscillation DEM measures $E(\tau)$ and $C(\tau)$ respectively;

c) in all the plots in Figs. 4.3(a) - 4.6 in the AJC and Figs. A.2 - A.5 in the JC process an increase in photon number n also results into an increase in frequency of oscillation of DEM measures $E(\tau)$ and $C(\tau)$ respectively and

d) in the AJC, JC interaction processes in Secs. 4.1.3, A.2.3 as clearly demonstrated in Fig. 4.5(a) (AJC) in comparison to Fig. A.6(a) (JC), the DEM as measured by the von Neumann entropy $E(\tau)$ (AJC) and separately concurrence $C(\tau)$ (JC) decreases with an increase in sum frequency $\bar{\delta}$ (AJC), frequency detuning δ (JC) indicating gradual decrease in the degree of entanglement. The result of time evolution of purity of state $tr(\hat{\bar{\rho}}_a^2(\tau))$ in Fig. 4.5(b) (AJC) and separately $tr(\hat{\rho}_a^2(\tau))$ Fig. A.6(b) (JC) reveals that in the respective interactions the systems tend to pure state $tr(\hat{\rho}_a^2(\tau)) = tr(\hat{\bar{\rho}}_a^2(\tau)) = 1$, a point in which the state-vector description of the atom, field quantum systems is possible since $C(\tau) = E(\tau) = 0$. What is more, as visualised in Fig. 4.6(a) (AJC) and Fig. A.7(a) (JC), entanglement at a fixed sum frequency $\bar{\delta}$ (AJC), frequency detuning δ (JC) is enhanced by increasing photon number n. Where here the degree of purity $tr(\hat{\bar{\rho}}_a^2(\tau))$ in Fig. 4.6(b) (AJC) and separately $tr(\hat{\rho}_a^2(\tau))$ in Fig. A.7(b) (JC) provide a physical interpretation that the systems tend to maximally mixed states $tr(\hat{\rho}_a^2(\tau)) = tr(\hat{\bar{\rho}}_a^2(\tau)) = \frac{1}{2}$ during the respective AJC,JC processes, a point where maximum entanglement is realised $C(\tau) = E(\tau) = 1$.

However, there were *notable differences* on the dynamics of quantum entanglement as measured by $E(\tau)$ in the AJC process and $C(\tau)$ in the JC process.

a) To begin with, Fig. 4.3(a) in the AJC process clearly shows that vacuum-field Rabi oscillations in the AJC interaction mechanism occur when an atom initially in ground state $|g\rangle$ is in a vacuum-field $n = 0$ in contrast to the JC interaction mechanism demonstrated in Figs. A.2 and A.3 where vacuum field Rabi oscillations occur when an atom in an initial excited state $|e\rangle$ enters a vacuum-field $n = 0$.

b) The DEM in the JC process provided a unique feature, in that the frequency of oscillation of DEM as measured by concurrence $C(\tau)$ is higher at resonance $\delta = 0$ than off-resonance $\delta \neq 0$ as presented in Fig. A.2 in comparison to Fig. A.3. This is because an increase in frequency detuning δ minimises entanglement of the atom, field quantum systems. In the contrary, the AJC process which is at all times detuned, any increase in sum frequency $\bar{\delta}$ results in an increase in frequency

of oscillation of DEM as highlighted earlier. However in an initial vacuum field $n = 0$ for various values of sum frequency $\bar{\delta} = 5\lambda$, 7λ (AJC) corresponding to frequency detuning $\delta = \lambda$, 3λ (JC) chosen arbitrarily the frequency of oscillation of DEM in the AJC interaction process is higher (shorter periods) than that of the JC interaction process as presented in Fig. 4.3(a) (AJC) in comparison to Figs. A.2 and A.3 (JC). In addition, at resonance $\delta = 0$ (Fig. A.2), the JC process depicts shorter periods than the corresponding $\bar{\delta} = 4\lambda$ AJC curve of DEM in Fig. 4.3(a).

c) In the JC interaction process in comparison to the AJC interaction process in Figs. 4.3(a) - 4.6, local minimums occur *only* when frequency detuning is set at off-resonance $\delta \neq 0$ as shown in Figs. A.2 - A.5 except for the special cases like that of long-lived entanglement determined for parameter values $\delta = 4\lambda$, $n = 0$ in our example in Fig. A.3.

v) The results of unit fidelities in Secs. 4.1.2.2 and A.2.2.2 clearly showed that it is possible to carry out quantum teleportation in the AJC interaction process just like in the JC interaction process, noting that the classical limit is $\frac{2}{3}$ [65]. However, despite the fact that it is possible to generate a symmetric atom-field state in Sec. A.2.1 quantified as maximally entangled in Sec. A.2.2.1 and an anti-symmetric atom-field quantum state in Sec. 4.1.1 quantified as maximally entangled in Sec. 4.1.2.1, the anti-symmetric qubit states [177] have an advantage over symmetric quantum states since their qubits are distinct and so they are easy to detect and measure in an experiment. Due to their special features, anti-symmetric qubit states have recently been useful in implementing quantum mechanical key sharing protocol [61], quantum state sharing protocols and for comparing quantum states [178].

vi) Finally in quantum computing, measurement in Bell basis is fundamental as presented in Secs. 1.8 and 2.4. In practice as stated in Secs. 1.8 and 2.4, for a bipartite system of qubits, measurement in Bell basis involves applying a C-NOT gate to the qubits followed by a Hadamard gate to the first qubit which results into a measurement in computational basis. Here the C-NOT gate simply performs the act of un-entangling the previously entangled qubits. This allows the information to be converted from quantum information to a measurement of classical information.

In Secs. 4.1.4 we demonstrated that it is possible to implement an efficient quantum C-NOT gate in the AJC process as quantified by the ideal unit probabilities of success. This gate provided the same operation as the extensively implemented C-

NOT gates in the JC process since it flips the target qubit if and only if the atomic control qubit is in the computational basis state $|g\rangle$ but when the atomic control qubit is in the computational basis state $|e\rangle$ the target qubit remains unchanged. The gate operation was achieved by applying respective qubit state transition operations defined in the AJC sub-space spanned by normalised but non-orthogonal basic qubit state vectors and accurate choice of atom-field interaction times. Here, the control qubit was a two-level atom and the target qubit was made up of two non-degenerate and polarised cavities.

In Sec.4.1.5 we showed that it is possible to perform standard quantum Hadamard rotations to initial atomic computational basis states $\{|e\rangle,\ |g\rangle\}$ in the AJC process similar to those implemented in the extensively applied JC process detailed in Sec. 2.4. For a specified initial atomic state, this was achieved by setting a specific sum frequency and photon number in the AJC qubit state transition with the interaction component in the AJC Hamiltonian generating the state transitions.

5.2   Two-level atom interacting with a field mode in an initial coherent state

i) The photon statistics is dominantly sub-Poissonian during the AJC interaction as opposed to the dominantly super-Poissonian distribution during the JC process clearly showing that the field mode is naturally anti-bunched during the AJC process. It basically means that fully quantised light-matter interactions can easily be realised in the AJC process. The JC, AJC photon distributions are visualised by time evolution of the Mandel parameter in Figs. 4.11 - 4.14.

ii) From the results visualised in Figs. 4.7, 4.8 - 4.10 and 4.11 - 4.14:

a) considering first the resonance case examples ($\delta = 0$ (JC), $\bar{\delta} = 2\xi\lambda$ (AJC)) presented in Fig. 4.7 and Fig. 4.8, at $t > 0$, the first maximum of the DEM $S_a(t)$ is realised at the point when the respective atomic population inversions are just at the collapse phase ;

b) in both JC, AJC processes, at one-half of the revival time as demonstrated in Figs. 4.7 and 4.8 the DEM $S_a(t)$ reaches an almost zero degree and consequently while referring to the degree of purity $tr(\hat{\rho}_a^2(t))$ in Fig. 4.8 it is clear that the atom and the field systems evolve to pure state and;

c) an increase in frequency detuning δ (JC) and separately sum frequency $\overline{\delta}$ (AJC) as demonstrated in Figs. 4.8 - 4.10 leads to a decrease in DEM at all time intervals, however at one-half of the revival time the value of the DEM does not deep as much to $S_a(t) = 0$ in comparison to the resonance case in Fig. 4.8.

iii) For higher values of δ (JC), $\overline{\delta}$ (AJC) the DEM $S_a(t)$ in the AJC process is slightly higher than those of the JC process as shown here in Figs. 4.8 - 4.10. This is attributed to the quantum nature of the field during the AJC interaction discussed in (i).

5.3 Two-level atom interacting with a field mode in an initial squeezed coherent state

We analysed separately, the interaction of a two-level atom with a single mode of an initial squeezed coherent light during the AJC, JC processes, and the results in the respective interactions are consistent with earlier work cited in Sec. 4.3. As visualised, the nature of photon statistics and DEM take the same similar pattern during time evolution of atomic population inversion for values of squeeze parameter set in the range $[1, 1.5]$ but different forms. More precisely, the AJC $W(\tau)$, $S_a(\tau)$ dynamics generated longer revival times, τ_R, due to existence of residual detuning, 2ω, that delayed the revival of atomic inversion. Further, the AJC $Q(\tau)$ dynamics are more negative as visualised, than the corresponding JC $Q(\tau)$ dynamics, indicating that the AJC field statistics is more anti-bunched than its corresponding JC field statistics. An important quantum property, showing that there is a higher chance to generate single photons in the AJC interaction than in its correlated JC process.

What is more, at $r > 1.4$ the field system becomes dominantly super-Poissonian. We also observed that at a higher $r = 1.5$ the revival peaks during atomic population inversion becomes less pronounced, irregular and ringing revivals observed at an expected collapse phase. The ringing, is caused by addition of more squeezed photons in the coherent field, leading to increase oscillations in the photon number distribution $P(n)$. As a result, the individual peaks overlap and sharpens the ringing structure.

The DEM in the respective AJC, JC interactions, showed that it increases with every increase in r and interaction time $\tau = \lambda t$ albeit gradually, and so is the degree of mixedness.

CHAPTER 6
RECOMMENDATIONS

Owing to the impressive results obtained in analysis of the AJC model in this Thesis, we recommend a relevant method of detecting entangled states (Schrödinger Cats), AJC state engineering, practical implementation of quantum teleportation of qubits in the AJC model and in general, quantum technologies.

6.1 AJC State Engineering

In order to systematically implement the AJC Hamiltonian with a single-tuned blue-sideband interaction, the simulation process should involve AJC state preparation followed by unitary transformation and measurement.

The state of the whole system as an interaction of a two-level atom and a single photon where both the atom and the photon are initially in ground state $|g\rangle$, $|0\rangle$ will take the form of Eq. (3.2.11). In a field mode that keeps the cavity field with upto one photon, the main focus should be to determine the experimental values of the probability amplitudes

$$\alpha(t) = \cos(\overline{R}_{g0}t) \quad ; \quad \beta(t) = -i\sin(\overline{R}_{g0}t) \tag{6.1.1}$$

for the initial states $|\psi_{g0}\rangle$ and $|\overline{\phi}_{g0}\rangle$ in Eq. 3.2.11 and show their variation with time that has a direct correspondence to the Rabi frequency $\overline{R}_{g0}$ which is of the form

$$\overline{R}_{g0} = \frac{1}{2}\sqrt{16\lambda^2 + \overline{\delta}^2} \tag{6.1.2}$$

The measurement procedure can be easily implemented using efficient experimental schemes for manipulating quantum entanglement with atoms and photons in a cavity but strictly in the AJC model, during which process difficulties can be identified as appropriate. The most common scheme being CQED [92–94].

6.2 Detection of entangled states: analysis of statistical properties of atoms

In QED experiments, direct access to the field is not possible since they are trapped in the high Q cavities. The only way to study the statistical properties of the cavity field is

to analyse the statistical properties of the atom that exits after having been coupled to the field during the during the cavity crossing time [93, 94].

6.3   Entanglement Swapping

Entanglement swapping demonstrated in Sec. 4.1.2.2 can be realised in an experimental set-up through Bell state measurement. Initially, the two sets of entangled states in Eq. (4.1.12) and Eq. (4.1.13) are prepared. The entire state of the system then takes the form of Eq. (4.1.14b). The required Bell state measurement is achieved in this case by first applying the C-NOT gate to Charlies' qubits the followed by the Hadamard gate operation to qubit 1 also in Charlies' end. The processes of which we have elaborated clearly in Secs. 4.1.4.1 and 4.1.5. Here the results of Bell measurement are communicated to Bob by Charles.

The most recent and successful schemes are those that apply ion-traps in state preparation and gate operations [197–200]. We take note that the AJC process has an advantage of producing anti-symmetric states which again will provide an advantage of accurate state identification after measurement. While implementing this process step-wise in the AJC interaction, details of experimental design, procedures and difficulties can be provided as appropriate.

BIBLIOGRAPHY

[1] Rabi, I.I. On the process of space quantization. *Phys. Rev.*, 49(4):324, 1936.

[2] Rabi, I.I. Space quantization in a gyrating magnetic field. *Phys. Rev.*, 51(8):652, 1937.

[3] Braak, D. Integrability of the Rabi model. *Phys. Rev. Lett.*, 107(10):100401, 2011.

[4] Fox, A.M. *Quantum optics: An Introduction*, volume 15. Oxford University Press, 2006.

[5] Irish, E.K. Generalized rotating-wave approximation for arbitrarily large coupling. *Phys. Rev. Lett.*, 99(17):173601, 2007.

[6] Forn-Díaz, P., Lisenfeld, J., Marcos, D., Garcia-Ripoll, J.J., Solano, E., Harmans, C.J.P.M., and Mooij, J.E. Observation of the Bloch-Siegert shift in a qubit-oscillator system in the ultrastrong coupling regime. *Phys. Rev. Lett.*, 105(23):237001, 2010.

[7] Yoshihara, F., Fuse, T., Ashhab, S., Kakuyanagi, K., Saito, S., and Semba, K. Superconducting qubit–oscillator circuit beyond the ultrastrong-coupling regime. *Nat.Phys.*, 13(1):44–47, 2017.

[8] Jaynes, E.T. and Cummings, F.W. Comparison of quantum and semiclassical radiation theories with application to the beam maser. *Proc. IEEE*, 51(1):89–109, 1963.

[9] Omolo, J.A. Conserved excitation number and U(1)-symmetry operator for the anti-rotating (anti-Jaynes-Cummings) term of the Rabi Hamiltonian. *arXiv preprint arXiv:2103.06577*, 2021.

[10] Omolo, J.A. The anti-Jaynes-Cummings model is solvable: quantum Rabi model in rotating and counter-rotating frames; following the experiments. *arXiv preprint arXiv:2103.09546*, 2021.

[11] Omolo, J.A. Polariton and anti-polariton qubits in the Rabi model. *preprint Research Gate, DOI:10.13140/RG.2.2.11833.67683*, 2017.

[12] Omolo, J.A. Photospins in the quantum Rabi model. *preprint Research Gate, DOI: 10.13140/RG.2.2.27331.96807*, 2019.

[13] Chen, Q.-H., Wang, C., He, S., Liu, T., and Wang, K.-L. Exact solvability of the quantum Rabi model using Bogoliubov operators. *Phys. Rev. A*, 86(2):023822, 2012.

[14] Zhong, H., Xie, Q., Batchelor, M.T., and Lee, C. Analytical eigenstates for the quantum Rabi model. *J. Phys. A Math. Theor.*, 46(41):415302, 2013.

[15] Xie, Q., Zhong, H., Batchelor, M.T., and Lee, C. The quantum Rabi model: solution and dynamics. *J. Phys. A Math. Theor.*, 50(11):113001, 2017.

[16] Omolo, J.A. Symmetry conjugates and dynamical properties of the quantum Rabi model. *arXiv preprint arXiv:2112.12514*, 2021.

[17] Satyanarayana, M.V., Rice, P., Vyas, R., and Carmichael, H.J. Ringing revivals in the interaction of a two-level atom with squeezed light. *JOSA B*, 6(2):228–237, 1989.

[18] Moya-Cessa, H. and Vidiella-Barranco, A. On the interaction of two-level atoms with superpositions of coherent states of light. *J. Mod. Opt.*, 42(7):1547–1552, 1995.

[19] Yurke, B. and Stoler, D. Generating quantum mechanical superpositions of macroscopically distinguishable states via amplitude dispersion. *Phys. Rev. Lett.*, 57(1): 13, 1986.

[20] Gomes, A.F. and Vidiella-Barranco, A. Enhancement of Atom-Field Transfer of Coherence in a Two-Photon Micromaser Assisted by a Classical Field. *Appl. Math. Inf. Sci.*, 8(2):727, 2014.

[21] Agarwal, G.S. Vacuum-field Rabi oscillations of atoms in a cavity. *JOSA B*, 2(3): 480–485, 1985.

[22] Scherer, W. *Mathematics of Quantum Computing: An Introduction.* Springer Nature, 2019.

[23] Nielsen, M.A. and Chuang, I.L. *Quantum Computation and Quantum Information.* Cambridge University Press, 2010.

[24] Furusawa, A. and van Loock, P. *Quantum Teleportation and Entanglement: A Hybrid Approach to Optical Quantum Information Processing.* John Wiley & Sons, 2011.

[25] Mermin, N.D. *Quantum computer science: an introduction.* Cambridge University Press, 2007.

[26] Bloch, F. Nuclear induction. *Phys. Rev.*, 70(7-8):460, 1946.

[27] Allen, L. and Eberly, J.H. *Optical resonance and two-level atoms*, volume 28. Courier Corporation, 1987.

[28] Gerry, C. and Knight, P. *Introductory quantum optics.* Cambridge University Press, 2005.

[29] Mandel, L. Sub-poissonian photon statistics in resonance fluorescence. *Opt. lett.*, 4 (7):205–207, 1979.

[30] Teich, M.C. and Saleh, B.E.A. I photon bunching and antibunching. In *Progress in Optics*, volume 26, pages 1–104. Elsevier, 1988.

[31] Teich, M.C. and Saleh, B.E.A. Squeezed state of light. *Quant. Opt.*, 1(2):153, 1989.

[32] Mandel, L. and Wolf, E. *Optical coherence and quantum optics.* Cambridge University Press, 1995.

[33] Loudon, R. *The Quantum Theory of Light.* Oxford University Press, 1973.

[34] Scully, M.O., Zubairy, M.S., and others. *Quantum Optics.* Cambridge University Press, 1997.

[35] Bužek, V. and Quang, T. Generalized coherent state for bosonic realization of SU (2) Lie algebra. *J.Opt.Soc.B*, 6(12):2447–2449, 1989.

[36] Bužek, V. SU (1, 1) squeezing of SU (1, 1) generalized coherent states. *J.Mod.Opt.*, 37(3):303–316, 1990.

[37] Perelomov, A.M. *Generalized Coherent States and Their Applications.* Theoretical and Mathematical Physics. Springer Verlag, Berlin, 1987.

[38] Wodkiewicz, K. and Eberly, J.H. Coherent states, squeezed fluctuations, and the SU (2) and SU (1, 1) groups in quantum-optics applications. *J.Opt.Soc.B*, 2(3): 458–466, 1985.

[39] Zurek, W.H., Habib, S., and Paz, J.P. Coherent states via decoherence. *Phys. Rev. Lett.*, 70(9):1187, 1993.

[40] Glauber, R.J. The quantum theory of optical coherence. *Phys. Rev.*, 130(6):2529, 1963.

[41] Sudarshan, E.C.G. Equivalence of semiclassical and quantum mechanical descriptions of statistical light beams. *Phys. Rev. Lett.*, 10(7):277, 1963.

[42] Tipler, P.A. and Llewellyn, R. *Modern Physics.* Freeman, W.H., 5 edition, 2008.

[43] Orszag, M. *Quantum optics: including noise reduction, trapped ions, quantum trajectories, and decoherence.* Springer, 2016.

[44] Glauber, R.J. Coherent and incoherent states of the radiation field. *Phys. Rev.*, 131(6):2766, 1963.

[45] Klauder, J.R. Continuous-representation theory. I. postulates of continuous-representation theory. *J. Math. Phys.*, 4(8):1055–1058, 1963.

[46] Sakurai, J.J. *Modern Quantum Mechanics.* Benjamin/Cummings Publishing Company, Inc.: Menlo Park, CA, USA, 1985.

[47] Esteve, D., Raimond, J.-M., and Dalibard, J. *Quantum entanglement and information processing: lecture notes of the Les Houches Summer School 2003.* Elsevier, 2004.

[48] Williams, C.P. *Explorations in quantum computing.* Springer Science & Business Media, 2010.

[49] Gottesman, D. Fault-tolerant quantum computation with higher-dimensional systems. In *NASA International Conference on Quantum Computing and Quantum Communications*, pages 302–313. Springer, 1998.

[50] Barenco, A., Deutsch, D., Ekert, A., and Jozsa, R. Conditional quantum dynamics and logic gates. *Phys. Rev. Lett.*, 74(20):4083, 1995.

[51] Knill, E., Laflamme, R., Barnum, H., Dalvit, D., Dziarmaga, J., Gubernatis, J., Gurvits, L., Ortiz, G., Viola, L., and Zurek, W.H. Introduction to quantum information processing. *arXiv preprint quant-ph/0207171*, 2002.

[52] Braunstein, S.L., Mann, A., and Revzen, M. Maximal violation of Bell inequalities for mixed states. *Phys. Rev. Lett.*, 68(22):3259, 1992.

[53] Schilpp, P.A. *Albert Einstein.* Fine Communications, 2001.

131

[54] Einstein, A. *Albert Einstein, philosopher-scientist*, volume 502. Library of Living Philosophers, 1949.

[55] Schrödinger, E. Discussion of probability relations between separated systems. In *Mathematical Proceedings of the Cambridge Philosophical Society*, volume 31, pages 555–563. Cambridge University Press, 1935.

[56] Deutsch, D. Quantum theory, the Church–Turing principle and the universal quantum computer. *Proc. R. Soc. London A*, 400(1818):97–117, 1985.

[57] Deutsch, D. and Jozsa, R. Rapid solution of problems by quantum computation. *Proc. R. Soc. London A*, 439(1907):553–558, 1992.

[58] Grover, L.K. Quantum mechanics helps in searching for a needle in a haystack. *Phys. Rev. Lett.*, 79(2):325, 1997.

[59] Bennett, C.H., Brassard, G., Crépeau, C., Jozsa, R., Peres, A., and Wootters, W.K. Teleporting an unknown quantum state via dual classical and Einstein-Podolsky-Rosen channels. *Phys. Rev. Lett.*, 70(13):1895, 1993.

[60] Bennett, C.H., Bessette, F., Brassard, G., Salvail, L., and Smolin, J. Experimental quantum cryptography. *J. Cryptol.*, 5(1):3–28, 1992.

[61] Ekert, A.K. Quantum cryptography based on Bell's theorem. *Phys. Rev. Lett.*, 67 (6):661, 1991.

[62] Jennewein, T., Simon, C., Weihs, G., Weinfurter, H., and Zeilinger, A. Quantum cryptography with entangled photons. *Phys. Rev. Lett.*, 84(20):4729, 2000.

[63] Einstein, A., Podolsky, B., and Rosen, N. Can quantum-mechanical description of physical reality be considered complete? *Phys. Rev.*, 47(10):777, 1935.

[64] Bell, J.S. On the Einstein Podolsky Rosen Paradox. *Physics (Long Island City, N.Y.)*, 1(03), 1965.

[65] Marinescu, D.C. *Classical and quantum information*. Academic Press, 2011.

[66] Salart, D., Baas, A., Branciard, C., Gisin, N., and Zbinden, H. Testing the speed of 'spooky action at a distance'. *Nature*, 454(7206):861–864, 2008.

[67] Zbinden, H., Brendel, J., Tittel, W., and Gisin, N. Experimental test of relativistic quantum state collapse with moving reference frames. *J. Phy. A Math. Gen.*, 34 (35):7103, 2001.

[68] Kamefuchi, S., International Symposium "Foundations of Quantum Mechanics in the Light of New Technology", Japan, M., and Nihon B.G. *Proceedings of the International Symposium Foundations of Quantum Mechanics in the Light of New Technology: Central Research Laboratory, Hitachi, Ltd., Kokubunji, Tokyo, Japan, August 29-31, 1983.* Physical Society of Japan, 1984.

[69] Jaeger, G. *Entanglement, information, and the interpretation of quantum mechanics.* Springer Science & Business Media, 2009.

[70] Peres, A. Separability criterion for density matrices. *Phys. Rev. Lett.*, 77(8):1413, 1996.

[71] Chuang, I.L. and Nielsen, M.A. Prescription for experimental determination of the dynamics of a quantum black box. *J. Mod. Opt.*, 44(11-12):2455–2467, 1997.

[72] von Neumann, J. *Mathematical foundations of quantum mechanics: New edition.* Princeton University Press, 2018.

[73] Wootters, W.K. Entanglement of formation and concurrence. *Quantum Inf. Comput.*, 1(1):27–44, 2001.

[74] Abdel-Khalek, S. Dynamics of a moving five-level atom interacting with cavity fields. *J. Russ. Laser*, 32(1):86–93, 2011.

[75] Bennett, C.H., DiVincenzo, D.P., Smolin, J.A., and Wootters, W.K. Mixed-state entanglement and quantum error correction. *Phys. Rev. A*, 54(5):3824, 1996.

[76] Bennett, C.H., Bernstein, H.J., Popescu, S., and Schumacher, B. Concentrating partial entanglement by local operations. *Phys. Rev. A*, 53(4):2046, 1996.

[77] Wootters, W.K. Entanglement of formation of an arbitrary state of two qubits. *Phys. Rev. Lett.*, 80(10):2245, 1998.

[78] Hill, S. and Wootters, W.K. Entanglement of a pair of quantum bits. *Phys. Rev. Lett.*, 78(26):5022, 1997.

[79] Życzkowski, K., Horodecki, P., Sanpera, A., and Lewenstein, M. Volume of the set of separable states. *Phys. Rev. A*, 58(2):883, 1998.

[80] Vidal, G. and Werner, R.F. Computable measure of entanglement. *Phys. Rev. A*, 65(3):032314, 2002.

[81] Horodecki, M., Horodecki, P., and Horodecki, R. General teleportation channel, singlet fraction, and quasidistillation. *Phys. Rev. A*, 60(3):1888, 1999.

[82] Casanova, J., Romero, G., Lizuain, I., Juan J. García-Ripoll, and Solano, E. Deep strong coupling regime of the Jaynes-Cummings model. *Phys. Rev. Lett.*, 105(26): 263603, 2010.

[83] De Liberato, S. Light-matter decoupling in the deep strong coupling regime: The breakdown of the Purcell effect. *Phys. Rev. Lett.*, 112(1):016401, 2014.

[84] Niemczyk, T., Deppe, F., Huebl, H., Menzel, E.P., Hocke, F., Schwarz, M.J., Garcia-Ripoll, J.J., Zueco, D., Hümmer, T., Solano, E., and others. Circuit quantum electrodynamics in the ultrastrong-coupling regime. *Nat. Phys.*, 6(10):772–776, 2010.

[85] Ciuti, C., Bastard, G., and Carusotto, I. Quantum vacuum properties of the intersubband cavity polariton field. *Phys. Rev. B*, 72(11):115303, 2005.

[86] Bloch, F. and Siegert, A. Magnetic resonance for nonrotating fields. *Phys. Rev.*, 57 (6):522, 1940.

[87] Rubino, E., McLenaghan, J., Kehr, S.C., Belgiorno, F., Townsend, D., Rohr, S., Kuklewicz, C.E., Leonhardt, U., König, F., and Faccio, D. Negative-frequency resonant radiation. *Phys. Rev. Lett.*, 108(25):253901, 2012.

[88] McLenaghan, J. and König, F. Few-cycle fiber pulse compression and evolution of negative resonant radiation. *New J. Phys.*, 16(6):063017, 2014.

[89] DiVincenzo, D.P. Two-bit gates are universal for quantum computation. *Phys. Rev. A*, 51(2):1015, 1995.

[90] Frisch, R. and Segre, E. On the adjustment of the direction of quantization. *Z. Physik*, 80:610416, 1933.

[91] Arakawa, Y., Finley, J., Gross, R., Laussy, F., Solano, E., Vuckovic, J., and others. Focus on cavity and circuit quantum electrodynamics in solids. *New J. Phys*, 17: 010201, 2015.

[92] Raimond, J.-M., Brune, M., and Haroche, S. Manipulating quantum entanglement with atoms and photons in a cavity. *Rev. Mod. Phys.*, 73(3):565, 2001.

[93] Hinds, E.A. Cavity Quantum Electrodynamics. In Bates, D. and Bederson, B, editors, *Advances in Atomic, Molecular, and Optical Physics*, volume 28, pages 237–289. Academic Press, New York, 1991.

[94] Haroche, S. and Kleppner, D. Cavity Quantum Electrodynamics. *Phys. Today*, 42 (1):24–30, 1987.

[95] Jacak, L., Hawrylak, P., and Wojs, A. *Quantum dots*. Springer Science & Business Media, 2013.

[96] Kouwenhoven, L. and Marcus, C. Quantum dots. *Phys. World*, 11(6):35, 1998.

[97] Loss, D. and DiVincenzo, D.P. Quantum computation with quantum dots. *Phys. Rev. A*, 57(1):120, 1998.

[98] Cirac, J.I. and Zoller, P. Quantum computations with cold trapped ions. *Phys. Rev. Lett.*, 74(20):4091, 1995.

[99] Blatt, R. and Roos, C.F. Quantum simulations with trapped ions. *Nat. Phys.*, 8 (4):277–284, 2012.

[100] Leibfried, D., Blatt, R., Monroe, C., and Wineland, D. Quantum dynamics of single trapped ions. *Rev. Mod. Phys.*, 75(1):281, 2003.

[101] Blais, A., Gambetta, J., Wallraff, A., Schuster, D.I., Girvin, S.M., Devoret, M.H., and Schoelkopf, R.J. Quantum-information processing with circuit quantum electrodynamics. *Phys. Rev. A*, 75(3):032329, 2007.

[102] Petersson, K.D., McFaul, L.W., Schroer, M.D., Jung, M., Taylor, J.M., Houck, A.A., and Petta, J.R. Circuit quantum electrodynamics with a spin qubit. *Nature*, 490(7420):380–383, 2012.

[103] Solano, E. The dialogue between quantum light and matter. *Physics*, 4:68, 2011.

[104] Pedernales, J.S., Lizuain, I., Felicetti, S., Romero, G., Lamata, L., and Solano, E. Quantum Rabi model with trapped ions. *Sci. Rep.*, 5(1):1–7, 2015.

[105] Miller, R., Northup, T. E., Birnbaum, K. M., Boca, A.D.B.A., Boozer, A.D., and Kimble, H.J. Trapped atoms in cavity QED: coupling quantized light and matter. *J. Phys. B*, 38(9):S551, 2005.

135

[106] Haroche, S. and Raimond, J.-M. *Exploring the quantum: atoms, cavities, and photons.* Oxford University Press, 2006.

[107] Walther, H., Varcoe, B.T.H., Englert, B.-G., and Becker, T. Cavity quantum electrodynamics. *Rep. Prog. Phys.*, 69(5):1325, 2006.

[108] Häffner, H., Roos, C.F., and Blatt, R. Quantum computing with trapped ions. *Phys. Rep.*, 469(4):155–203, 2008.

[109] Devoret, M.H. and Schoelkopf, R.J. Superconducting circuits for quantum information: an outlook. *Science*, 339(6124):1169–1174, 2013.

[110] Bouwmeester, D., Pan, J.-W., Mattle, K., Eibl, M., Weinfurter, H., and Zeilinger, A. Experimental quantum teleportation. *Nature*, 390(6660):575–579, 1997.

[111] Boschi, D., Branca, S., De Martini, F., Hardy, L., and Popescu, S. Experimental realization of teleporting an unknown pure quantum state via dual classical and Einstein-Podolsky-Rosen channels. *Phys. Rev. Lett.*, 80(6):1121, 1998.

[112] Shi, B.-S., Jiang, Y.-K., and Guo, G.-C. Probabilistic teleportation of two-particle entangled state. *Phys. Lett. A*, 268(3):161–164, 2000.

[113] Lee, H.-W. Total teleportation of an entangled state. *Phys. Rev. A*, 64(1):014302, 2001.

[114] Ghosh, S., Kar, G., Roy, A., Sarkar, D., and Sen, U. Entanglement teleportation via Bell mixtures. *Phys. Rev. A*, 66(2):024301, 2002.

[115] Lee, J., Min, H., and Oh, S.D. Multipartite entanglement for entanglement teleportation. *Phys. Rev. A*, 66(5):052318, 2002.

[116] Lu, H. and Guo, G.-C. Teleportation of a two-particle entangled state via entanglement swapping. *Phys. Lett. A*, 276(5-6):209–212, 2000.

[117] Chimczak, G., Tanaś, R., and Miranowicz, A. Teleportation with insurance of an entangled atomic state via cavity decay. *Phys. Rev. A*, 71(3):032316, 2005.

[118] Bell, J.S. On the Einstein Podolsky Rosen paradox. *Physics Physique Fizika*, 1(3): 195, 1964.

[119] Greenberger, D.M., Horne, M.A., and Zeilinger, A. Bell's theorem, Quantum Theory, and Conceptions of the Universe, 1989.

[120] Hagley, E., Maitre, X., Nogues, G., Wunderlich, C., Brune, M., Raimond, J.-M., and Haroche, S. Generation of Einstein-Podolsky-Rosen pairs of atoms. *Phys. Rev. Lett.*, 79(1):1, 1997.

[121] Turchette, Q.A., Wood, C.S., King, B.E., Myatt, C.J., Leibfried, D., Itano, W.M., Monroe, C., and Wineland, D.J. Deterministic entanglement of two trapped ions. *Phys. Rev. Lett.*, 81(17):3631, 1998.

[122] Roos, C.F., Lancaster, G.P.T., Riebe, M., Häffner, H., Hänsel, W., Gulde, S., Becher, C., Eschner, J., Schmidt-Kaler, F., and Blatt, R. Bell states of atoms with ultralong lifetimes and their tomographic state analysis. *Phys. Rev. Lett.*, 92(22): 220402, 2004.

[123] Georgescu, I. Nobel Prize 2012: Haroche & Wineland. *Nat.Phys.*, 8(11):777–777, 2012.

[124] Schirber, M. Nobel prize: Quantum Entanglement Unveiled. *Physics*, 15:153, 2022.

[125] Mielnik, B. Geometry of quantum states. *Commun. Math. Phys.*, 9(1):55–80, 1968.

[126] Mielnik, B. Theory of filters. *Commun. Math. Phys.*, 15(1):1–46, 1969.

[127] Mielnik, B. Generalized quantum mechanics. *Commun. Math. Phys.*, 37(3):221–256, 1974.

[128] Brody, D.C. and Hughston, L.P. Geometric quantum mechanics. *J. Geom. Phys.*, 38(1):19–53, 2001.

[129] Mielnik, B. and Rosas-Ortiz, O. Quantum mechanical laws. *Fundamentals of Physics Volume*, 1:255–326, 2009.

[130] Mielnik, B. Convex geometry: a travel to the limits of our knowledge. In *Geometric Methods in Physics*, pages 253–264. Springer, 2013.

[131] Mielnik, B. Evolution loops. *J. Math. Phys.*, 27(9):2290–2306, 1986.

[132] Fernández C., David J., and Mielnik, B. Controlling quantum motion. *J. Math. Phys.*, 35(5):2083–2104, 1994.

[133] Fernández, D.J. and Rosas-Ortiz, O. Inverse techniques and evolution of spin-12 systems. *Phys. Lett. A*, 236(4):275–279, 1997.

[134] Emmanouilidou, A., Zhao, X.-G., Ao, P., and Niu, Q. Steering an eigenstate to a destination. *Phys. Rev. Lett.*, 85(8):1626, 2000.

[135] Rosas-Ortiz, O. Quantum control of two-level systems, IOP conf. *Proc. 185*, 485, 2004.

[136] Rezakhani, A.T. and Zanardi, P. General setting for a geometric phase of mixed states under an arbitrary nonunitary evolution. *Phys. Rev. A*, 73(1):012107, 2006.

[137] Bengtsson, I. and Zyczkowski, K. *Geometry of Quantum States: An Introduction to Quantum Entanglement.* Cambridge University Press, 2006.

[138] von Neumann, J. *Mathematical Foundations of Quantum Mechanics: Translated from the German Ed. by Robert T. Beyer.* Princeton University Press, 1955.

[139] Enríquez, M., Reyes, R., and Rosas-Ortiz, O. A note on the geometry of the quantum states of a two-level atom in external radiation fields. *J. Phys. Conf. Ser.*, 512(1):012021, 2014.

[140] Osterloh, A., Siewert, J., and Uhlmann, A. Tangles of superpositions and the convex-roof extension. *Phys. Rev. A*, 77(3):032310, 2008.

[141] Lohmayer, R., Osterloh, A., Siewert, J., and Uhlmann, A. Entangled three-qubit states without concurrence and three-tangle. *Phys. Rev. Lett.*, 97(26):260502, 2006.

[142] Gamel, O. Entangled Bloch spheres: Bloch matrix and two-qubit state space. *Phys. Rev. A*, 93(6):062320, 2016.

[143] Mäkelä, H. and Messina, A. N-qubit states as points on the Bloch sphere. *Phys. Scr.*, 2010(T140):014054, 2010.

[144] Martin, J., Giraud, O., Braun, P.A., Braun, D., and Bastin, T. Multiqubit symmetric states with high geometric entanglement. *Phys. Rev. A*, 81(6):062347, 2010.

[145] Boyer, M., Liss, R., and Mor, T. Geometry of entanglement in the Bloch sphere. *Phys. Rev. A*, 95(3):032308, 2017.

[146] Regula, B. and Adesso, G. Geometric approach to entanglement quantification with polynomial measures. *Phys. Rev. A*, 94(2):022324, 2016.

[147] Regula, B. and Adesso, G. Entanglement quantification made easy: Polynomial measures invariant under convex decomposition. *Phys. Rev. Lett.*, 116(7):070504, 2016.

[148] Deutsch, D.E. Quantum computational networks. *Proc R. Soc. London A*, 425 (1868):73–90, 1989.

[149] Raussendorf, R. and Briegel, H.J. A one-way quantum computer. *Phys. Rev. Lett.*, 86(22):5188, 2001.

[150] Barenco, A., Bennett, C.H., Cleve, R., DiVincenzo, D.P., Margolus, N., Shor, P., Sleator, T., Smolin, J.A., and Weinfurter, H. Elementary gates for quantum computation. *Phys. Rev. A*, 52(5):3457, 1995.

[151] Shi, Y. Both Toffoli and controlled-NOT need little help to do universal quantum computation. *arXiv preprint quant-ph/0205115*, 2002.

[152] Boykin, P.O., Mor, T., Pulver, M., Roychowdhury, V., and Vatan, F. A new universal and fault-tolerant quantum basis. *Inf. Process. Lett.*, 75(3):101–107, 2000.

[153] Domokos, P., Raimond, J.-M., Brune, M., and Haroche, S. Simple cavity-QED two-bit universal quantum logic gate: The principle and expected performances. *Phys. Rev. A*, 52(5):3554, 1995.

[154] Vitali, D., Giovannetti, V., and Tombesi, P. Quantum Gates and Networks with Cavity QED Systems. In *Macroscopic Quantum Coherence and Quantum Computing*, pages 235–244. Springer, 2001.

[155] Saif, F., Ul Islam, R., and Javed, M. Engineering quantum universal logic gates in electromagnetic-field modes. *J. Russ. Laser Res.*, 28(5):529–534, 2007.

[156] Dai, H., Fu, S., and Luo, S. Atomic nonclassicality in the Jaynes-Cummings model. *Phys. Lett. A*, 384(12):126371, 2020.

[157] Haroche, S. Nobel Lecture: Controlling photons in a box and exploring the quantum to classical boundary. *Rev. Mod. Phys.*, 85(3):1083, 2013.

[158] Wineland, D.J. Nobel Lecture: Superposition, entanglement, and raising Schrödinger's cat. *Rev. Mod. Phys.*, 85(3):1103, 2013.

[159] Mandel, L. Non-classical states of the electromagnetic field. *Phys. Scripta*, 1986 (T12):34, 1986.

[160] Arecchi, F.T., Courtens, E., Gilmore, R., and Thomas, H. Atomic coherent states in quantum optics. *Phys. Rev. A*, 6(6):2211, 1972.

[161] Zhang, W.-M. and Gilmore, R. Coherent states: Theory and some applications. *Rev. Mod. Phys.*, 62(4):867, 1990.

[162] Giraud, O., Braun, P., and Braun, D. Quantifying quantumness and the quest for Queens of Quantum. *New J. Phys.*, 12(6):063005, 2010.

[163] Bohnet-Waldraff, F., Braun, D., and Giraud, O. Quantumness of spin-1 states. *Phys. Rev. A*, 93(1):012104, 2016.

[164] Kiesel, T., Vogel, W., Christensen, S.L., Béguin, J.-B., Appel, J., and Polzik, E.S. Atomic nonclassicality quasiprobabilities. *Phys. Rev. A*, 86(4):042108, 2012.

[165] Oszmaniec, M. and Kuś, M. On detection of quasiclassical states. *J. Phys. A*, 45 (24):244034, 2012.

[166] Dai, H. and Luo, S. Information-theoretic approach to atomic spin nonclassicality. *Phys. Rev. A*, 100(6):062114, 2019.

[167] Gottesman, D. and Chuang, I.L. Demonstrating the viability of universal quantum computation using teleportation and single-qubit operations. *Nature*, 402(6760): 390–393, 1999.

[168] Nielsen, M.A., Knill, E., and Laflamme, R. Complete quantum teleportation using nuclear magnetic resonance. *Nature*, 396(6706):52–55, 1998.

[169] Phoenix, S.J.D. and Barnett, S. M. Non-local Interatomic Correlations in the Micromaser. *J. Mod. Opt.*, 40(6):979–983, 1993.

[170] KUDRYAVTSEV, I.K and KNIGHT, P.L. Atomic entaglement and Bell's inequality violation. *J. Mod. Opt.*, 40(9):1673–1679, 1993.

[171] Freyberger, M., Aravind, P.K., Horne, M.A., and Shimony, A. Proposed test of bell's inequality without a detection loophole by using entangled Rydberg atoms. *Phys. Rev. A*, 53(3):1232, 1996.

[172] Barnett, S. *Quantum Information*, volume 16. Oxford University Press, 2009.

[173] Bužek, V., Moya-Cessa, H., Knight, P.L., and Phoenix, S.J.D. Schrödinger-cat states in the resonant Jaynes-Cummings model: Collapse and revival of oscillations of the photon-number distribution. *Phys. Rev. A*, 45(11):8190, 1992.

[174] Phoenix, S.J.D. and Knight, P.L. Fluctuations and entropy in models of quantum optical resonance. *Ann. Phys.*, 186(2):381–407, 1988.

[175] Dingshun, L.V., Shuoming A.N., Liu, Z., Zhang, J.-N., Pedernales, J.S., Lamata, L., Solano, E., and Kim, K. Quantum simulation of the quantum rabi model in a trapped ion. *Phys. Rev. X*, 8(2):021027, 2018.

[176] Sousa, E.H.S. and Roversi, J.A. Selective engineering for preparing entangled steady states in cavity QED setup. *Quantum Rep.*, 1(1):63–70, 2019.

[177] Jex, I., Alber, G., Barnett, S. M., and Delgado, A. Antisymmetric multi-partite quantum states and their applications. *Fortschritte der Physik: Progress of Physics*, 51(2-3):172–178, 2003.

[178] Barnett, S.M., Chefles, A., and Jex, I. Comparison of two unknown pure quantum states. *Phys. Lett. A*, 307(4):189–195, 2003.

[179] Mohammadi, M. and Jami, S. Time evolution of entanglement and trace distance in an atom-cavity system described with random walk and non-random walk states. *Optik*, 181:582–587, 2019.

[180] Liu, X.-J., Lu, J.-B., Zhang, S.-Q., Liu, J.-P., Li, H., Liang, Y., Ma, J., Weng, Y.-J., Zhang, Q.-R., Liu, H., and others. The nonlinear Jaynes-Cummings model for the multiphoton transition. *Int. J. Theor. Phys.*, 57(1):290–298, 2018.

[181] Zhang, S.-Q., Lu, J.-B., Liu, X.-J., Liang, Y., Li, H., Ma, J., Liu, J.-P., and Wu, X.-Y. Quantum Entanglement of the Multiphoton Transition Jaynes-Cummings Model. *Int. J. Theor. Phys.*, 57(1):279–289, 2018.

[182] Abdel-Khalek, S., Quthami, M., and Ahmed, M.M.A. Effects of detuning and atomic motion parameter on the dynamical behavior of the entanglement between two-level atom and SU(1, 1) quantum system. *Opt. Rev.*, 22(1):25–32, 2015.

[183] Rossatto, D.Z., Villas-Bôas, C.J., Sanz, M., and Solano, E. Spectral classification of coupling regimes in the quantum rabi model. *Phys. Rev. A*, 96(1):013849, 2017.

[184] Gea-Banacloche, J. Collapse and revival of the state vector in the Jaynes-Cummings model: An example of state preparation by a quantum apparatus. *Phys. Rev. Lett.*, 65(27):3385, 1990.

[185] Phoenix, S.J.D. and Knight, P.L. Establishment of an entangled atom-field state in the Jaynes-Cummings model. *Phys. Rev. A*, 44(9):6023, 1991.

[186] Phoenix, S.J.D and Knight, P.L. Comment on "collapse and revival of the state vector in the Jaynes-Cummings model: An example of state preparation by a quantum apparatus". *Phys. Rev. Lett.*, 66(21):2833, 1991.

[187] Gea-Banacloche, J. Atom-and field-state evolution in the Jaynes-Cummings model for large initial fields. *Phys. Rev. A*, 44(9):5913, 1991.

[188] Gea-Banacloche, J. A new look at the Jaynes-Cummings model for large fields: Bloch sphere evolution and detuning effects. *Opt. Commun.*, 88(4-6):531–550, 1992.

[189] Shore, B.W. and Knight, P.L. "The Jaynes–Cummings Revival". In Grandy,Jr., W.T. and Milonni, P.W., editors, *Physics and Probability : Essays in Honour of Edwin T. Jaynes*, pages 15–32. Cambridge University, Press, 1993.

[190] Dung, H. T., Shumovsky, A.S., and Bogolubov Jr., N.N. Antibunching and sub-Poissonian photon statistics in the Jaynes-Cummings model. *Opt. Commun.*, 90 (4-6):322–328, 1992.

[191] Shatha, A. A. and Berrada, K. and Abdel-Khalek, S. Entanglement and photon statistics of two dipole–dipole coupled superconducting qubits with Kerr-like nonlinearities. *Results Phys.*, 16:102978, 2020.

[192] Eberly, J.H., Narozhny, N.B., and Sanchez-Mondragon, J.J. Periodic Spontaneous Collapse and Revival in a Simple Quantum Model. *Phys. Rev. Lett.*, 44(20):1323–1325, 1980.

[193] Subeesh, T., Sudhir, V., Ahmed, A.B.M., and Satyanarayana, M.V. Effect of Squeezing on the Atomic and the Entanglement Dynamics in the Jaynes-Cummings Model. *arXiv preprint arXiv:1203.4792*, 2012.

[194] Moya-Cessa, H. and Vidiella-Barranco, A. Interaction of squeezed light with two-level atoms. *J. Mod. Opt.*, 39(12):2481–2499, 1992.

[195] Kukliński, J.R. and Madajczyk, J.L. Strong squeezing in the Jaynes-Cummings model. *Phys. Rev. A*, 37(8):3175, 1988.

[196] Meystre, P. and Zubairy, M.S. Squeezed states in the Jaynes-Cummings model. *Phys. Lett. A*, 89(8):390–392, 1982.

[197] Riebe, M., Monz, T., Kim, K., Villar, A. S., Schindler, P., Chwalla, M., Hennrich, M., and Blatt, R. Deterministic entanglement swapping with an ion-trap quantum computer. *Nat. Phys.*, 4(11):839–842, 2008.

[198] Riebe, M. *Preparation of entangled states and quantum teleportation with atomic qubits.* Ph.D. thesis, Leopold-Franzens-Universität Innsbruck, 2005.

[199] Riebe, M., Kim, K., Schindler, P., Monz, T., Schmidt, P.O., Körber, T.K., Hänsel, W., Häffner, H., Roos, C.F., and Blatt, R. Process tomography of ion trap quantum gates. *Phys. Rev. Lett.*, 97(22):220407, 2006.

[200] Schmidt-Kaler, F., Häffner, H., Gulde, S., Riebe, M., Lancaster, G.P.T., Deuschle, T., Becher, C., Hänsel, W., Eschner, J., Roos, C. F., and others. How to realize a universal quantum gate with trapped ions. *Appl. Phys. B*, 77(8):789–796, 2003.

[201] Hill, S. and Wootters, W.K. Entanglement of a Pair of Quantum Bits. *Phys. Rev. Lett.*, 78:5022–5025, 1997.

[202] Rieffel, E.G. and Polak, W.H. *Quantum computing: A gentle introduction.* MIT Press, 2011.

[203] Van Meter, R. *Quantum networking.* John Wiley & Sons, 2014.

[204] Żukowski, M., Zeilinger, A., Horne, M.A., and Ekert, A.K. "event-ready-detectors"Bell experiment via entanglement swapping. *Phys. Rev. Lett.*, 71(26): 4287, 1993.

[205] Megidish, E., Halevy, A., Shacham, T., Dvir, T., Dovrat, L., and Eisenberg, H.S. Entanglement swapping between photons that have never coexisted. *Phys. Rev. Lett.*, 110(21):210403, 2013.

[206] Pan, J.-W., Bouwmeester, D., Weinfurter, H., and Zeilinger, A. Experimental entanglement swapping: entangling photons that never interacted. *Phys. Rev. Lett.*, 80(18):3891, 1998.

[207] Bose, S., Vedral, V., and Knight, P.L. Multiparticle generalization of entanglement swapping. *Phys. Rev. A*, 57(2):822, 1998.

[208] Tanaś, R. and Ficek, Z. Entangling two atoms via spontaneous emission. *J. Opt. B: Quantum Semiclassical Opt.*, 6(3):S90, 2004.

[209] Paschotta, Rüdiger and others. *Encyclopedia of laser physics and technology*, volume 1. Wiley Online Library, 2008.

[210] Yoshie, T., Scherer, A., Hendrickson, J., Khitrova, G., Gibbs, H.M., Rupper, G., Ell, C., Shchekin, O.B., and Deppe, D.G. Vacuum Rabi splitting with a single quantum dot in a photonic crystal nanocavity. *Nature*, 432(7014):200–203, 2004.

APPENDICES

APPENDIX A
JC DYNAMICS: FIELD MODE IN AN INITIAL FOCK (NUMBER) STATE

We provide in this appendix the methodology and results of the dynamics generated by the JC Hamiltonian $\hat{H}$ in Eq. (3.1.3) when a two-level atom interacts with a field mode in Fock state. The arbitrarily chosen field mode frequency $\omega = 2\lambda$ and various values of frequency detuning $\delta = \omega_0 - \omega$ as parameters in analysis of the AJC dynamics in Sec. 4.1 are maintained in Sec. A.2 to facilitate the desired comparison.

A.1 Methodology

Following the physical property established in [9], only a two-level atom in an initial excited state $|e\rangle$ entering a field mode in Fock state that is initially in vacuum state couples to the rotating positive frequency field component during the JC interaction process. In this respect, applying the state transition operator $\hat{A}$ from Eq. (3.1.3) to the initial atom-field n-photon excited state vector $|e, n\rangle$, the basic qubit state vectors $|\psi_{en}\rangle$ and $|\phi_{en}\rangle$ are determined in the form ($n = 0, 1, 2, ...$) [12]

$$|\psi_{en}\rangle = |e, n\rangle \quad ; \quad |\phi_{en}\rangle = c_{en}|e, n\rangle + s_{en}|g, n+1\rangle \qquad (A.1.1)$$

with dimensionless interaction parameters c_{en}, s_{en} and Rabi frequency R_{en} defined as

$$c_{en} = \frac{\delta}{2R_{en}} \quad ; \quad s_{en} = \frac{2\lambda\sqrt{n+1}}{R_{en}} \quad ; \quad R_{en} = 2\lambda A_{en}$$

$$A_{en} = \sqrt{(n+1) + \frac{\delta^2}{16\lambda^2}} \quad ; \quad \delta = \omega_0 - \omega \qquad (A.1.2)$$

where we have introduced detuning $\delta = \omega_0 - \omega$ to redefine α in Eq. (3.1.3).

The qubit state vectors in Eq. (A.1.1) satisfy the qubit state transition algebraic operations

$$\hat{A}|\psi_{en}\rangle = A_{en}|\phi_{en}\rangle \quad ; \quad \hat{A}|\phi_{en}\rangle = A_{en}|\psi_{en}\rangle . \qquad (A.1.3)$$

In the JC qubit subspace spanned by normalised but non-orthogonal basic qubit state vectors $|\psi_{en}\rangle, |\phi_{en}\rangle$ the basic qubit state transition operator $\hat{\varepsilon}_e$ and identity operator $\hat{I}_e$

are introduced according to the definition

$$\hat{\varepsilon}_e = \frac{\hat{A}}{A_{en}} \quad ; \quad \hat{I}_e = \frac{\hat{A}^2}{A_{en}^2} \quad \Rightarrow \quad \hat{\varepsilon}_e^2 = \hat{I}_e \tag{A.1.4}$$

which on substituting into Eq. (A.1.3) generates the basic qubit state transition algebraic operations

$$\hat{\varepsilon}_e|\psi_{en}\rangle = |\phi_{en}\rangle \quad ; \quad \hat{\varepsilon}_e|\phi_{en}\rangle = |\psi_{en}\rangle \quad ; \quad \hat{I}_e|\psi_{en}\rangle = |\psi_{en}\rangle \quad ; \quad \hat{I}_e|\phi_{en}\rangle = |\phi_{en}\rangle . \tag{A.1.5}$$

The algebraic properties $\hat{\varepsilon}_e^{2k} = \hat{I}_e$ and $\hat{\varepsilon}_e^{2k+1} = \hat{\varepsilon}_e$ easily gives the final property ($k = 0, 1, 2, ...$)

$$e^{i\theta\hat{\varepsilon}_e} = \cos(\theta)\hat{I}_e + i\sin(\theta)\hat{\varepsilon}_e \tag{A.1.6}$$

which is useful in evaluating the time-evolution operator.

The JC qubit Hamiltonian defined within the qubit subspace spanned by the basic qubit state vector vectors $|\psi_{en}\rangle, |\phi_{en}\rangle$ is then expressed in terms of the basic qubit state transition operators $\hat{\varepsilon}_e, \hat{I}_e$ in the form [12]

$$\hat{H}_e = \hbar\omega \left(n + \frac{1}{2} \right) \hat{I}_e + \hbar R_{en}\hat{\varepsilon}_e . \tag{A.1.7}$$

We use this form of the JC Hamiltonian to determine the general time-evolving state vector describing Rabi oscillations in the JC dynamics in Sec. A.1.1.

A.1.1 Rabi oscillations between the basic JC qubit state vector $|\psi_{en}\rangle$ and $|\phi_{en}\rangle$

The general dynamics generated by the JC Hamiltonian in Eq. (A.1.7) is described by a time evolving JC qubit state vector $|\Psi_{en}(t)\rangle$ obtained from the time-dependent Schrödinger equation in the form [12]

$$|\Psi_{en}(t)\rangle = \hat{U}_e(t)|\psi_{en}\rangle \quad ; \quad \hat{U}_e(t) = e^{-\frac{i}{\hbar}\hat{H}_e t} \tag{A.1.8}$$

where $\hat{U}_e(t)$ is the time evolution operator. Substituting $\hat{H}_e$ from Eq. (A.1.7) into Eq. (A.1.8) and applying appropriate algebraic properties [12], we use the relation in Eq. (A.1.6) to express the time evolution operator in its final form

$$\hat{U}_e(t) = e^{-i\omega t(n+\frac{1}{2})} \left\{ \cos(R_{en}t)\hat{I}_e - i\sin(R_{en}t)\hat{\varepsilon}_e \right\} \tag{A.1.9}$$

which we substitute into equation Eq. (A.1.8) and use the qubit state transition operations in Eq. (A.1.5) to obtain the time-evolving JC qubit state vector in the form

$$|\Psi_{en}(t)\rangle = e^{-i\omega t(n+\frac{1}{2})}\Big\{ \cos(R_{en}t)|\psi_{en}\rangle - i\sin(R_{en}t)|\phi_{en}\rangle\Big\} \ . \tag{A.1.10}$$

This time evolving state vector describes Rabi oscillations between the basic qubit states $|\psi_{en}\rangle$ and $|\phi_{en}\rangle$ at Rabi frequency R_{en}.

In order to determine the length of the Bloch vector associated with the state vector in Eq. (A.1.10), we introduce the density operator

$$\hat{\rho}_{en}(t) = |\Psi_{en}(t)\rangle\langle\Psi_{en}(t)| \tag{A.1.11a}$$

which we expand to obtain

$$
\begin{aligned}
\hat{\rho}_{en}(t) &= \cos^2(R_{en}t)|\psi_{en}\rangle\langle\psi_{en}| + \frac{i}{2}\sin(2R_{en}t)|\psi_{en}\rangle\langle\phi_{en}| - \frac{i}{2}\sin(2R_{en}t)|\phi_{en}\rangle\langle\psi_{en}| \\
&+ \sin^2(R_{en}t)|\phi_{en}\rangle\langle\phi_{en}| \ .
\end{aligned}
$$
$$\tag{A.1.11b}$$

Defining the coefficients of the projectors in Eq. (A.1.11b) as

$$
\begin{aligned}
\rho_{en}^{11}(t) &= \cos^2(R_{en}t) \quad ; \quad \rho_{en}^{12}(t) = \frac{i}{2}\sin(2R_{en}t) \quad ; \\
\rho_{en}^{21}(t) &= -\frac{i}{2}\sin(2R_{en}t) \quad ; \quad \rho_{en}^{22}(t) = \sin^2(R_{en}t)
\end{aligned}
$$
$$\tag{A.1.11c}$$

and interpreting the coefficients in Eq. (A.1.11c) as elements of a 2×2 density matrix $\hat{\rho}_{en}(t)$, which we express in terms of standard Pauli operator matrices I, σ_x, σ_y and σ_z in Eq. (1.3.6) as

$$\hat{\rho}_{en}(t) = \begin{pmatrix} \rho_{en}^{11}(t) & \rho_{en}^{12}(t) \\ \rho_{en}^{21}(t) & \rho_{en}^{22}(t) \end{pmatrix} = \frac{1}{2}\left(I + \vec{\rho}_{en}(t)\cdot\vec{\sigma}\right) \tag{A.1.11d}$$

where as defined in Sec. (1.3) $\vec{\sigma} = (\sigma_x, \sigma_y, \sigma_z)$ is the Pauli matrix vector and we have introduced the time-evolving Bloch vector $\vec{\rho}_{en}(t)$ obtained in the form

$$\vec{\rho}_{en}(t) = (\rho_{en}^x(t), \rho_{en}^y(t), \rho_{en}^z(t)) \tag{A.1.11e}$$

with components defined as

$$
\begin{aligned}
\rho_{en}^x(t) &= tr\left(\hat{\rho}_{en}(t)\sigma_x\right) = tr\begin{pmatrix} \frac{i}{2}\sin(2R_{en}t) & \cos^2(R_{en}t) \\ \sin^2(R_{en}t) & -\frac{i}{2}\sin(2R_{en}t) \end{pmatrix} = 0 \quad ; \\
\rho_{en}^y(t) &= tr\left(\hat{\rho}_{en}(t)\sigma_y\right) = tr\begin{pmatrix} -\frac{1}{2}\sin(2R_{en}t) & -i\cos^2(R_{en}t) \\ i\sin^2(R_{en}t) & -\frac{1}{2}\sin(2R_{en}t) \end{pmatrix} = -\sin(2R_{en}t) \quad ; \\
\rho_{en}^z(t) &= tr\left(\hat{\rho}_{en}(t)\sigma_z\right) = tr\begin{pmatrix} \cos^2(R_{en}t) & -\frac{i}{2}\sin(2R_{en}t) \\ -\frac{i}{2}\sin(2R_{en}t) & -\sin^2(R_{en}t) \end{pmatrix} = \cos(2R_{en}t).
\end{aligned}
$$

$$(A.1.11f)$$

The Bloch vector in Eq. (A.1.11e) takes the explicit form

$$
\vec{\rho}_{en}(t) = \Big(0,\, -\sin(2R_{en}t),\, \cos(2R_{en}t)\Big)
\tag{A.1.11g}
$$

which has unit length obtained easily as

$$
|\vec{\rho}_{en}(t)| = 1 \; .
\tag{A.1.11h}
$$

The property that the Bloch vector $\vec{\rho}_{en}(t)$ is of unit length (the Bloch sphere has unit radius), shows that the general time evolving state vector $|\Psi_{en}(t)\rangle$ in Eq. (A.1.10) is a pure state, as clearly explained in Sec. 1.3.1. The time evolution of this Bloch vector, describes geometric configuration of states in the Bloch sphere picture where here we adopt class 4 Bloch-sphere entanglement of a quantum rank-2 bipartite state [145, 147]. In this class of Bloch-sphere entanglement, only the initial state is separable and all the other states are entangled.

In this respect, we consider the specific example (which also applies to the general n-photon case) of an atom initially in excited state $|e\rangle$ entering a cavity with the field mode starting off in an initial vacuum state $|0\rangle$, such that the initial atom-field ground state is $|e, 0\rangle$.

A.1.2 Entanglement properties, teleportation of a two-atom maximally entangled state and dynamical evolution of entanglement generated in the JC interaction

In this section we demonstrate how to apply concurrence measure in analysis of entanglement properties of the JC qubit state vectors and the dynamical evolution of entanglement

generated in the JC interaction. We proceed further to present the algorithm of teleporting a two-atom Bell pair in the JC process, commonly referred to as teleportation of entanglement.

A.1.2.1 Entanglement properties of JC qubit states

As stated in Sec. 1.8.2, in quantum information, it is of interest to measure or quantify the entanglement of states. In a bipartite case, with two sub-systems A, B concurrence [23, 69, 77] is a good measure of entanglement in practical situations. From Eq. (1.8.12) (which we re-write here for ease of reference), for *pure* states of two spins, concurrence is defined as

$$C(|\psi_{AB}\rangle) = |\langle \psi_{AB} | \tilde{\psi}_{AB} \rangle| \qquad (1.8.12')$$

where we recall $|\tilde{\psi}_{AB}\rangle \equiv \hat{\sigma}_y^{\otimes 2} |\psi_{AB}^*\rangle$ is referred to as the 'spin-flipped' state vector.

Considering the initial stationary qubit state vector $|\psi_{en}\rangle$ in the JC interaction defined in Eq. (A.1.1) in the form

$$|\psi_{en}\rangle = |e, n\rangle = |e\rangle \otimes |n\rangle \ , \qquad (A.1.1')$$

we simply evaluate $|\tilde{\psi}_{en}\rangle = \hat{\sigma}_y^{\otimes 2} |\psi_{en}^*\rangle$ and hence $C(|\psi_{en}\rangle)$ in Eq. (1.8.12) and classify the state as either entangled or separable (product). We expect degree of entanglement (DEM) values as measured by $C(|\psi_{en}\rangle)$ to be in the range [0,1], since concurrence varies from 0 for a completely disentangled state to 1 for a maximally entangled state.

Further, concurrence can be expressed in terms of the minimum average pure-state concurrence where the required minimum is to be taken over all possible ways of decomposing the ensemble $\hat{\rho}_{AB}$ into a mixture of pure states $|\psi_{AB}\rangle$. In this respect from Eq. (1.8.13) (which again we re-write here for ease of reference), for a general two-spin state, concurrence is defined as

$$C(\hat{\rho}_{AB}) \ = \ \max\{0, \lambda_1 - \lambda_2 - \lambda_3 - \lambda_4\} \qquad (1.8.13')$$

where

$$\hat{\rho}_{AB} = |\psi_{AB}\rangle\langle\psi_{AB}| \quad ; \quad \hat{\tilde{\rho}}_{AB} = \hat{\rho}_{AB}(\hat{\sigma}_y^{\otimes 2})\hat{\rho}_{AB}^*(\hat{\sigma}_y^{\otimes 2}) \ . \qquad (A.1.12)$$

Here, λ_i are real square-roots of the eigenvalues of the density matrix $\hat{\tilde{\rho}}_{AB}$ in Eq. (A.1.12).

Now, the general form of the stationary transition qubit state vector $|\phi_{en}\rangle$ in the JC process is defined in Eq. (A.1.1). Substituting $|\phi_{en}\rangle$ in Eq. (A.1.1) into Eq. (1.3.10) the

density operator takes the form

$$
\begin{aligned}
\hat{\rho}_{en} &= |\phi_{en}\rangle\langle\phi_{en}| \\
&= |c_{en}|^2 \ |e,n\rangle\langle e,n| + c_{en}s_{en}^*|e,n\rangle\langle g,n+1| + s_{en}c_{en}^*|g,n+1\rangle\langle e,n| \\
&+ \ |s_{en}|^2 \ |g,n+1\rangle\langle g,n+1| \quad\quad\quad\quad\quad\quad\quad\quad\quad\text{(A.1.13a)}
\end{aligned}
$$

which we express explicitly in a generalised matrix form as

$$
\hat{\rho}_{en} = \begin{pmatrix} |c_{en}|^2 & 0 & 0 & c_{en}s_{en}^* \\ 0 & 0 & 0 & 0 \\ 0 & 0 & 0 & 0 \\ s_{en}c_{en}^* & 0 & 0 & |s_{en}|^2 \end{pmatrix} \quad\quad\text{(A.1.13b)}
$$

to evaluate eigenvalues λ_i of $\hat{\tilde{\rho}}_{en} = \hat{\rho}_{en}(\hat{\sigma}_y^{\otimes 2})\hat{\rho}_{en}^*(\hat{\sigma}_y^{\otimes 2})$ in Eq. (A.1.12) for states determined at different values of frequency detuning δ and quantify their entanglement using Eq. (1.8.13) while taking note of the definitions of interaction parameters c_{en}, s_{en} and Rabi frequency R_{en} in Eq. (A.1.2).

The DEM values measured by $C(\hat{\rho}_{en})$ are in the range [0,1]. The concurrence measure of the DEM is 0 for a completely disentangled state, 1 for a maximally entangled state and $0 < C(\hat{\rho}_{en}) < 1$ for an entangled state.

A.1.2.2 Entanglement evolution in the JC interaction mechanism

The DEM using concurrence measure which was formulated as a convex measure to amount the DEM for two qubits in pure states by Wooters and Hill [201] is defined as $(a \equiv atom, f \equiv field)$

$$
C(t) = \sqrt{2(1 - tr(\hat{\rho}_j^2))} \quad ; \quad j : a(f) \quad\quad\quad\text{(A.1.14)}
$$

where $\hat{\rho}_j$, is the reduced density operator.

Here, the general dynamics of the JC interaction is described by the general time-evolving qubit state vector $|\Psi_{en}(t)\rangle$ in Eq. (A.1.10). Substituting $|\Psi_{en}(t)\rangle$ from Eq. (A.1.10) into Eq. (A.1.11a) and using the definitions of $|\psi_{en}\rangle$ and $|\phi_{en}\rangle$ in Eq. (A.1.1)

the density operator takes the form

$$
\begin{aligned}
\hat{\rho}_{en}(t) &= \{\cos^2(R_{en}t) + c_{en}^2 \sin^2(R_{en}t)\}|e,n\rangle\langle e,n| + \{is_{en}\cos(R_{en}t)\sin(R_{en}t) \\
&+ c_{en}s_{en}\sin^2(R_{en}t)\}|e,n\rangle\langle g,n+1| + \{-is_{en}\cos(R_{en}t)\sin(R_{en}t) \\
&+ c_{en}s_{en}\sin^2(R_{en}t)\}|g,n+1\rangle\langle e,n| + \{s_{en}^2\sin^2(R_{en}t)\}|g,n+1\rangle\langle g,n+1| .
\end{aligned}
$$

$$(A.1.15a)$$

The reduced density operator of the atom $\hat{\rho}_a(t)$ is determined by tracing $\hat{\rho}_{en}(t)$ in Eq. (A.1.15a) over the field states thus taking the form

$$
\begin{aligned}
\hat{\rho}_a(t) = tr_f(\hat{\rho}_{en}(t)) &= P_e(t)|e\rangle\langle e| + P_g(t)|g\rangle\langle g| \\
&= \begin{pmatrix} P_e(t) & 0 \\ 0 & P_g(t) \end{pmatrix}
\end{aligned}
$$

$$(A.1.15b)$$

after introducing the general time-evolving atomic state probabilities $P_e(t)$ and $P_g(t)$ obtained as

$$
P_e(t) = \cos^2(R_{en}t) + c_{en}^2\sin^2(R_{en}t) \quad ; \quad P_g(t) = s_{en}^2\sin^2(R_{en}t) .
$$

$$(A.1.15c)$$

Plots of time evolution of the DEM measured by $C(t)$, are then easily generated after substituting Eq. (A.1.15b) into Eq. (A.1.14) for different parameter values of frequency detuning δ and photon number n.

Here, the DEM measure $C(t)$ evolves in time within the range [0,1], where a value nought defines a completely disentangled state (product) and unity a maximally entangled state.

A.1.2.3   Teleportation in the JC interaction

The maximally entangled atom-field state determined in Sec. A.1.2.1 is expected to be a symmetric atom-field Bell pair defined in Sec. 1.8 in the form $|\Phi^+\rangle$. This maximally entangled atom-field state acts as the teleportation channel and it will be in possession of a receiver (Bob) in a remote location. Assuming a sender (Alice) would wish to send to Bob a maximally entangled two-atom symmetric state, the total state of the system

takes the form ($a \equiv Alice, b \equiv Bob$)

$$|\psi\rangle_{total} = |\Phi^+\rangle_{a_1,a_2} \otimes |\Phi^+\rangle_{b_1,b_2} \ . \tag{A.1.16}$$

To actualise teleportation of entanglement, an observer (Charlie) will be responsible for carrying out the Bell state measurement (projection) process (Sec. 1.8, Eq. (1.8.2)) defined as [22]

$$P_\Sigma := \langle \Sigma | \Lambda \rangle | \Sigma \rangle \tag{1.8.2'}$$

and communicate the results to Bob (or Alice).

In this respect, Alice sends qubit a_1 to Charlie and Bob sends to him qubit b_1. Charlie carries out Bell measurement defined in Eq. (1.8.2). If he obtains

$$_{a_1,b_1}\langle \Phi^+ | \psi \rangle_{total} = \frac{1}{2} |\Phi^+\rangle_{a_2,b_2} \ , \tag{A.1.17}$$

Alice and Bob have a Bell pair between qubit a_2 and b_2. To quantify probability of success in the teleporation process, we apply teleportation fidelity [81] as a measure of closeness of two quantum states defined for any two-qubit state $\hat\rho$ in the form of Eq. (1.8.19a)

$$F_{\hat\rho} = \frac{2f_{\hat\rho} + 1}{3} \tag{1.8.19a'}$$

where $f_{\hat\rho}$ is the fully entangled fraction defined as [75] Eq. (1.8.19b)

$$f_{\hat\rho} = \max_{|\Psi\rangle} \langle \Psi | \hat\rho | \Psi \rangle = \left\{ tr \sqrt{\hat\rho_{expected}^{\frac{1}{2}} \hat\rho_{measured} \hat\rho_{expected}^{\frac{1}{2}}} \right\}^2 \ . \tag{1.8.19b'}$$

The measurement of Eq. (A.1.17) provides a unit fidelity $F_{\hat\rho} = 1$ with a quarter chance of occurring. This means that the teleported state is identical to that sent by Alice and so, Alice's qubit was successfully teleported to Bob.

The other three Bell projection outcomes take the respective forms

$$
\begin{aligned}
_{a_1,b_1}\langle \Phi^- | \psi \rangle_{total} &= \frac{1}{2} |\Phi^-\rangle_{a_2,b_2} \quad ; \\
_{a_1,b_1}\langle \Psi^- | \psi \rangle_{total} &= -\frac{1}{2} |\Psi^-\rangle_{a_2,b_2} \quad ; \\
_{a_1,b_1}\langle \Psi^+ | \psi \rangle_{total} &= \frac{1}{2} |\Psi^+\rangle_{a_2,b_2} \ ,
\end{aligned}
\tag{A.1.18}
$$

and so local corrections given by Pauli operators $\hat\sigma_x$, $\hat\sigma_y$, $\hat\sigma_z$ defined in Eq. (1.3.6) are

performed by Bob (or Alice) after Charlie has communicated the results of measurement according to

$$
\begin{aligned}
\frac{1}{2}\left[\hat{\sigma}_{z(b_2)}|\Phi^-\rangle_{a_2,b_2}\right] &= \frac{1}{2}|\Phi^+\rangle_{a_2,b_2} \quad ; \\
-\frac{1}{2}\left[i\hat{\sigma}_{y(b_2)}|\Psi^-\rangle_{a_2,b_2}\right] &= \frac{1}{2}|\Phi^+\rangle_{a_2,b_2} \quad ; \\
\frac{1}{2}\left[\hat{\sigma}_{x(b_2)}|\Psi^+\rangle_{a_2,b_2}\right] &= \frac{1}{2}|\Phi^+\rangle_{a_2,b_2} \quad .
\end{aligned}
\tag{A.1.19}
$$

We see from Eq. (A.1.19) that each measurement has a quarter chance to occur and a unit fidelity as expected.

A.2 Results: JC dynamics and application in quantum information processing (QIP)

A.2.1 Rabi oscillations

We now proceed to demonstrate the time evolution of the Bloch vector $\vec{\rho}_{en}(t)$ in Eq. (A.1.11g) which in effect describes the geometric configuration of states. We have adopted class 4 Bloch-sphere entanglement of a quantum rank-2 bipartite state [145, 147] to bring a clear visualisation of this interaction.

In the specific example starting with an atom in the excited state $|e\rangle$ and the field mode in the vacuum state $|0\rangle$ the basic qubit state vectors $|\psi_{e0}\rangle$ and $|\phi_{e0}\rangle$, together with the corresponding entanglement parameters, are obtained by setting $n = 0$ in Eqs. (A.1.1) and (A.1.2) in the form

$$
\begin{aligned}
|\psi_{e0}\rangle &= |e,0\rangle \quad ; \quad |\phi_{e0}\rangle = c_{e0}|e,0\rangle + s_{e0}|g,1\rangle \quad ; \\
c_{e0} &= \frac{\delta}{2R_{e0}} \quad ; \quad s_{e0} = \frac{2\lambda}{R_{e0}} \quad ; \quad R_{e0} = \frac{1}{2}\sqrt{16\lambda^2 + \delta^2} \quad ; \\
|e,0\rangle &= |e\rangle \otimes |0\rangle \quad ; \quad |g,1\rangle = |g\rangle \otimes |1\rangle \quad .
\end{aligned}
\tag{A.2.1}
$$

The corresponding Hamiltonian in Eq. (A.1.7) becomes ($n = 0$)

$$
\hat{H}_e = \frac{1}{2}\hbar\omega\hat{I}_e + \hbar R_{e0}\hat{\varepsilon}_e \quad .
\tag{A.2.2}
$$

The time-evolving state vector in Eq. (A.1.10) takes the form $(n = 0)$

$$|\Psi_{e0}(t)\rangle = e^{-\frac{i\omega t}{2}} \left\{ \cos(R_{e0}t)|\psi_{e0}\rangle - i\sin(R_{e0}t)|\phi_{e0}\rangle \right\} \qquad (A.2.3)$$

which describes Rabi oscillations at frequency R_{e0} between the initial qubit state vector $|\psi_{e0}\rangle$ and the transition qubit state vector $|\phi_{e0}\rangle$.

The Rabi oscillation process is best described by the corresponding Bloch vector which follows from Eq. (A.1.11g) in the form $(n = 0)$

$$\vec{\rho}_{e0}(t) = (0, -\sin(2R_{e0}t), \cos(2R_{e0}t)) \ . \qquad (A.2.4)$$

In the present work, for various values of frequency detuning $\delta = \lambda$, 2λ, 3λ, 4λ, 0 and field mode frequency $\omega = 2\lambda$ we use the general time evolving state vector in Eq. (A.2.3), with Rabi frequency R_{e0} as defined in Eq. (A.2.1) to determine the coupled qubit state vectors $|\psi_{e0}\rangle$, $|\phi_{e0}\rangle$ in Eq. (A.2.1) by setting $R_{e0}t = \frac{\pi}{2}$, describing half cycle of Rabi oscillation as presented below. In each case we have an accumulated global phase factor which does not affect measurement results [23, 202, 203], but we have maintained them here in Eqs. (A.2.5a)-(A.2.5e) to explain the continuous time evolution over one cycle.

$$\delta \ = \ 0 \ : \ |e,0\rangle \to e^{-i\pi\frac{3}{4}}|g,1\rangle \to e^{-i\pi\frac{3}{2}}|e,0\rangle \qquad (A.2.5a)$$

$$\delta \ = \ \lambda \ : \ |e,0\rangle \to e^{-i\pi\frac{25}{34}}\left\{\frac{1}{\sqrt{17}}|e,0\rangle + \frac{4}{\sqrt{17}}|g,1\rangle\right\} \to e^{-i\pi\frac{25}{17}}|e,0\rangle$$
$$(A.2.5b)$$

$$\delta \ = \ 2\lambda \ : \ |e,0\rangle \to e^{-i\pi\frac{7}{10}}\left\{\frac{1}{\sqrt{5}}|e,0\rangle + \frac{2}{\sqrt{5}}|g,1\rangle\right\} \to e^{-i\pi\frac{7}{5}}|e,0\rangle$$
$$(A.2.5c)$$

$$\delta \ = \ 3\lambda \ : \ |e,0\rangle \to e^{-i\pi\frac{7}{10}}\left\{\frac{3}{5}|e,0\rangle + \frac{4}{5}|g,1\rangle\right\} \to e^{-i\pi\frac{7}{5}}|e,0\rangle$$
$$(A.2.5d)$$

$$\delta = 4\lambda \quad : \quad |e,0\rangle \rightarrow e^{-i\pi\frac{7}{10}}\left\{\frac{1}{\sqrt{2}}|e,0\rangle + \frac{1}{\sqrt{2}}|g,1\rangle\right\} \rightarrow e^{-i\pi\frac{7}{5}}|e,0\rangle$$

<div align="right">(A.2.5e)</div>

In Fig. A.1 we have plotted the JC Rabi oscillation process with respective Rabi frequencies R_{e0} determined according to Eq. (A.2.1) for arbitrary values of frequency detuning $\delta = \omega_0 - \omega$.
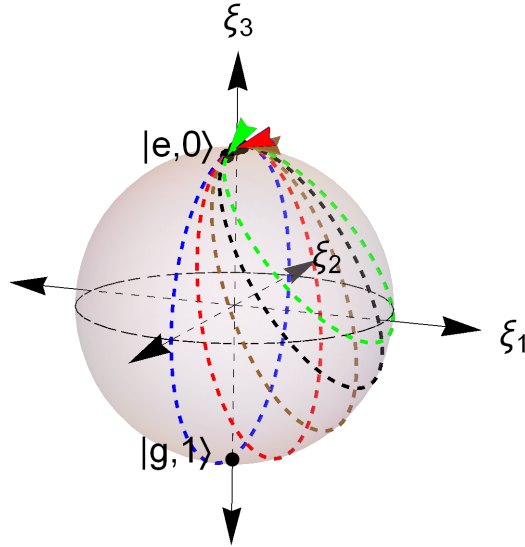

Figure A.1: Rabi oscillations in JC interaction mechanism. Here, blue circle is at resonance with frequency detuning $\delta = \omega_0 - \omega = 0$, red circle is for $\delta = \lambda$, brown circle $\delta = 2\lambda$, black circle $\delta = 3\lambda$ and green circle $\delta = 4\lambda$.

The JC Rabi oscillations for cases $\delta = \lambda, 2\lambda, 3\lambda, 4\lambda, 0$ are plotted as red, brown, black, green and blue circles in Fig. A.1. Here, Fig. A.1 is a Bloch sphere entanglement [145] that corresponds to a 2-dimensional subspace of $\mathbb{C}^2 \otimes \mathbb{C}^2$
Span$\{|e,0\rangle, c_{e0}|e,0\rangle + s_{e0}|g,1\rangle\}$ with $c_{e0} = \frac{\delta}{2R_{e0}}$ and $s_{e0} = \frac{2\lambda}{R_{e0}}$, where we recall that, in the JC interaction the initial atom-field ground state with the field mode in the vacuum state is $|e,0\rangle$.

The geometric configuration of the state space demonstrated on the Bloch-sphere in Fig. A.1 determined using the approach in [12] agrees precisely with that determined using the semi-classical approach in [139] corresponding to a 2-dimensional subspace of $\mathbb{C}^2$ Span $\{|e\rangle, |g\rangle\}$. In the approach [139], at resonance where frequency detuning $\delta = 0$ the atomic population is inverted from excited state $|e\rangle$ to ground state $|g\rangle$ and the Bloch-vector $\vec{r} = (\sin(\theta)\cos(\phi), \sin(\theta)\sin(\phi), \cos(\theta))$ describes a path along the yz-plane on the Bloch-sphere. For other values of frequency detuning, the atom evolves from excited

state $|e\rangle$ to a linear superposition of excited state $|e\rangle$ and ground state $|g\rangle$ and back to excited state $|e\rangle$ and the Bloch-vector $\vec{r}$ describes a circle about the north pole of the Bloch-sphere.

The time evolution of this JC Bloch vectors $\vec{\rho}_{e0}$ reveals that the Rabi oscillations between the basic qubit state vectors $|\psi_{e0}\rangle$, $|\phi_{e0}\rangle$ describe circles on which the states are distributed on the Bloch sphere as we have demonstrated.

A.2.2 Entanglement analysis of basic qubit state vectors $|\psi_{e0}\rangle$ and $|\phi_{e0}\rangle$ and teleportation in the JC model

In this section we analyse the entanglement properties of the JC qubit state vectors, dynamical evolution of entanglement and teleportation of a two-atom singlet state generated in the JC interaction.

A.2.2.1 Entanglement properties

Let us start by considering the entanglement properties of the initial state $|\psi_{e0}\rangle$ which according to the definition in Eq. (A.2.1) is a separable pure state. In this context

$$|\tilde{\psi}_{e0}\rangle = \hat{\sigma}_y^{\otimes 2}|\psi_{e0}^*\rangle = \hat{\sigma}_y^{\otimes 2}(|e\rangle \otimes |0\rangle) = i|g\rangle \otimes i|1\rangle \tag{A.2.6}$$

which on substituting into Eq. (1.8.12) we obtain

$$C(|\psi_{e0}\rangle) = |\langle \psi_{e0}|\tilde{\psi}_{e0}\rangle| = |-\langle e|g\rangle\langle 0|1\rangle| = 0 \tag{A.2.7}$$

quantifying the state in Eq. (A.2.1) (or the initial qubit state in Eq. (A.2.5a)) as a pure product state $|e\rangle \otimes |0\rangle$. Similarly, ignoring the global phase factor in Eq. (A.2.5a), the transition qubit state $|\phi_{e0}\rangle = |g, 1\rangle$ obtained at resonance $\delta = 0$ is a pure product state $|g\rangle \otimes |1\rangle$.

We now proceed to determine the entanglement property of the transition qubit state vector $|\phi_{e0}\rangle$ obtained at frequency detuning $\delta = \lambda$ in Eq. (A.2.5b). Ignoring the global phase factor in Eq. (A.2.5b), the transition qubit state $|\phi_{e0}\rangle$ takes the form

$$\delta = \lambda \quad : \quad \frac{1}{\sqrt{17}}|e, 0\rangle + \frac{4}{\sqrt{17}}|g, 1\rangle \tag{A.2.8}$$

The corresponding density operator of the state in Eq. (A.2.8) is

$$\hat{\rho}_{e0} = |\phi_{e0}\rangle\langle\phi_{e0}| = \frac{1}{17}|e,0\rangle\langle e,0| + \frac{4}{17}|e,0\rangle\langle g,1|\frac{4}{17}|g,1\rangle\langle e,0| + \frac{16}{17}|g,1\rangle\langle g,1| \quad \text{(A.2.9)}$$

which takes the explicit 4×4 matrix form

$$\hat{\rho}_{e0} = \frac{1}{17}\begin{pmatrix} 1 & 0 & 0 & 4 \\ 0 & 0 & 0 & 0 \\ 0 & 0 & 0 & 0 \\ 4 & 0 & 0 & 16 \end{pmatrix} \quad \text{(A.2.10)}$$

and $\hat{\tilde{\rho}}_{e0}$ by applying the definition in Eq. (A.1.12) is

$$\hat{\tilde{\rho}}_{e0} = \hat{\rho}_{e0}(\hat{\sigma}_y^{\otimes 2})\hat{\rho}_{e0}^*(\hat{\sigma}_y^{\otimes 2}) \quad \text{(A.2.11)}$$

which takes the explicit 4×4 matrix form

$$\hat{\tilde{\rho}}_{e0} = \frac{1}{289}\begin{pmatrix} 32 & 0 & 0 & 8 \\ 0 & 0 & 0 & 0 \\ 0 & 0 & 0 & 0 \\ 128 & 0 & 0 & 32 \end{pmatrix}. \quad \text{(A.2.12)}$$

The eigenvalues of the matrix in Eq (A.2.12) are

$$\lambda_1 = \frac{64}{289}, \ \lambda_2 = 0, \ \lambda_3 = 0, \ \lambda_4 = 0 \ . \quad \text{(A.2.13)}$$

Substituting the eigenvalues in Eq. (A.2.13) into Eq. (1.8.13) we obtain

$$C(\hat{\rho}_{e0}) = \max\left\{0, \sqrt{\frac{64}{289}}\right\} = \frac{8}{17} < 1 \quad \text{(A.2.14)}$$

quantifying the transition qubit state in Eq. (A.2.8) (or Eq. (A.2.5b)) as an entangled state but not maximally entangled since $C(\hat{\rho}_{e0}) < 1$. Similarly, the transition qubit states $|\phi_{e0}\rangle = \frac{1}{\sqrt{5}}|e,0\rangle + \frac{2}{\sqrt{5}}|g,1\rangle$ obtained for frequency detuning $\delta = 2\lambda$ in Eq. (A.2.5c) and $|\phi_{e0}\rangle = \frac{3}{5}|e,0\rangle + \frac{4}{5}|g,1\rangle$ obtained for frequency detuning $\delta = 3\lambda$ in Eq. (A.2.5d) are entangled but not maximally entangled.

Finally we consider the case of frequency detuning $\delta = 4\lambda$. Once again ignoring the

global phase factor in Eq. (A.2.5e), the transition qubit state vector takes the form

$$\delta = 4\lambda \quad : \quad \frac{1}{\sqrt{2}}|e,0\rangle + \frac{1}{\sqrt{2}}|g,1\rangle \ . \tag{A.2.15}$$

The corresponding density operator of the state in Eq. (A.2.15) is

$$\hat{\rho}_{e0} = \frac{1}{2}|e,0\rangle\langle e,0| + \frac{1}{2}|e,0\rangle\langle g,1| + \frac{1}{2}|g,1\rangle\langle e,0| + \frac{1}{2}|g,1\rangle\langle g,1| \ . \tag{A.2.16}$$

The explicit 4×4 matrix forms of $\hat{\rho}_{e0}$ in Eq. (A.2.16) and $\hat{\tilde{\rho}}_{e0}$ by applying the definition in Eq. (A.1.12) are of the form

$$\hat{\rho}_{e0} = \frac{1}{2}\begin{pmatrix} 1 & 0 & 0 & 1 \\ 0 & 0 & 0 & 0 \\ 0 & 0 & 0 & 0 \\ 1 & 0 & 0 & 1 \end{pmatrix} \quad ; \quad \hat{\tilde{\rho}}_{e0} = \frac{1}{2}\begin{pmatrix} 1 & 0 & 0 & 1 \\ 0 & 0 & 0 & 0 \\ 0 & 0 & 0 & 0 \\ 1 & 0 & 0 & 1 \end{pmatrix} \ . \tag{A.2.17}$$

The eigenvalues of $\hat{\tilde{\rho}}_{e0}$ in Eq. (A.2.17) are

$$\lambda_1 = 1, \ \lambda_2 = 0, \ \lambda_3 = 0, \ \lambda_4 = 0 \tag{A.2.18}$$

which on substituting into Eq. (1.8.13) we obtain

$$C(\hat{\rho}_{e0}) = \max\{0,1\} = 1 \ . \tag{A.2.19}$$

The unit concurrence determined in Eq. (A.2.19) reveals that the transition qubit state vector in Eq. (A.2.15) (or Eq. (A.2.5e)) determined at frequency detuning $\delta = 4\lambda$ is a maximally entangled bipartite pure state.

A similar proof of entanglement of the JC qubit states is easily achieved for all possible values of frequency detuning parameter $\delta = \omega_0 - \omega$. In general, in an initial vacuum-field JC interaction and $\delta \neq 0$ (off-resonance) reversible transitions occur *only* between a pure initial separable qubit state vector and an entangled transition qubit state vector while at resonance when $\delta = 0$ reversible transitions occur *only* between pure initial and transition separable qubit state vectors. These properties of Rabi oscillations occurs in the general JC interaction described by the general time evolving state vector $|\Psi_{en}(t)\rangle$ in Eq. (A.1.10).

A.2.2.2 Teleportation in the JC interaction mechanism

In the present work we consider an interesting case of quantum teleportation by applying entanglement swapping protocol (teleportation of entanglement) [204–207] where the teleported state is itself entangled. The state we want to teleport is a two-atom maximally entangled state in which we have assigned subscripts to distinguish the atomic qubit states in the form [208]

$$|\kappa\rangle_{12} = \frac{1}{\sqrt{2}} \left(|e\rangle_1 |e\rangle_2 + |g\rangle_1 |g\rangle_2 \right) \tag{A.2.20}$$

and it is in Alice's possession. In another location, Bob is in possession of a maximally entangled qubit state $|\phi_{e0}\rangle$ generated in the JC interaction in Eq. (A.2.5e) and expressed as

$$|\zeta\rangle_{3x} = \frac{1}{\sqrt{2}} |e\rangle_3 |0\rangle_x + \frac{1}{\sqrt{2}} |g\rangle_3 |1\rangle_x \tag{A.2.21}$$

where we also assign subscripts to the qubits in Eq. (A.2.21) in order to clearly distinguish them.

An observer, Charlie, receives qubit-1 from Alice and qubit-x from Bob. The entire state of the system

$$|\xi\rangle = |\kappa\rangle_{12} \otimes |\zeta\rangle_{3x} \tag{A.2.22a}$$

which on substituting $|\kappa\rangle_{12}$ and $|\zeta\rangle_{3x}$ from Eqs. (A.2.20), (A.2.21) and reorganising takes the form

$$
\begin{aligned}
|\xi\rangle \;=\; \frac{1}{2}\Big[& |\Phi^+\rangle_{1x} \left(\frac{|e\rangle_3 |e\rangle_2 + |g\rangle_3 |g\rangle_2}{\sqrt{2}} \right) + |\Phi^-\rangle_{1x} \left(\frac{|e\rangle_3 |e\rangle_2 - |g\rangle_3 |g\rangle_2}{\sqrt{2}} \right) \\
- \; & |\Psi^-\rangle_{1x} \left(\frac{|e\rangle_3 |g\rangle_2 - |g\rangle_3 |e\rangle_2}{\sqrt{2}} \right) + |\Psi^+\rangle_{1x} \left(\frac{|e\rangle_3 |g\rangle_2 + |g\rangle_3 |e\rangle_2}{\sqrt{2}} \right) \Big]
\end{aligned}
\tag{A.2.22b}
$$

after introducing the emerging Bell states obtained as

$$
\begin{aligned}
|\Phi^+\rangle_{1x} &= \frac{|e\rangle_1 |0\rangle_x + |g\rangle_1 |1\rangle_x}{\sqrt{2}} \quad ; \quad |\Phi^-\rangle_{1x} = \frac{|e\rangle_1 |0\rangle_x - |g\rangle_1 |1\rangle_x}{\sqrt{2}} \\
|\Psi^-\rangle_{1x} &= \frac{|e\rangle_1 |1\rangle_x - |g\rangle_1 |0\rangle_x}{\sqrt{2}} \quad ; \quad |\Psi^+\rangle_{1x} = \frac{|e\rangle_1 |1\rangle_x + |g\rangle_1 |0\rangle_x}{\sqrt{2}} \; .
\end{aligned}
\tag{A.2.22c}
$$

Charlie performs Bell state projection between qubit-1 and qubit-x (Bell state measurement (BSM)) and communicates his results to Bob which we have presented in Sec. A.2.2.2.1 below.

A.2.2.2.1   Bell state measurement

BSM is realised at Charlie's end. Projection of a state $|\Lambda\rangle$ onto $|\Sigma\rangle$ is defined in Eq. (1.8.2) as [22]

$$P_\Sigma := \langle\Sigma|\Lambda\rangle\,|\Sigma\rangle\ . \tag{1.8.2'}$$

Using $|\xi\rangle$ form Eq. (A.2.22) and applying Eq. (1.8.2) we obtain a Bell state projection outcome communicated to Bob in the form

$$_{1x}\langle\Phi^+|\xi\rangle = \frac{1}{2}\left(\frac{|e\rangle_3|e\rangle_2 + |g\rangle_3|g\rangle_2}{\sqrt{2}}\right) = \frac{1}{2}|\Phi^+\rangle_{32}\ . \tag{A.2.23a}$$

The Bell state $|\Phi^+\rangle_{32}$ in Eq. (A.2.23a) is in the the form of Alice's qubit in Eq. (A.2.20). Alice and Bob now have a Bell pair between qubit-2 and qubit-3. Similarly, the other three Bell projections take the forms

$$_{1x}\langle\Phi^-|\xi\rangle \;=\; \frac{1}{2}\left(\frac{|e\rangle_3|e\rangle_2 - |g\rangle_3|g\rangle_2}{\sqrt{2}}\right) = \frac{1}{2}|\Phi^-\rangle_{32} \tag{A.2.23b}$$

$$_{1x}\langle\Psi^-|\xi\rangle \;=\; -\frac{1}{2}\left(\frac{|e\rangle_3|g\rangle_2 - |g\rangle_3|e\rangle_2}{\sqrt{2}}\right) = -\frac{1}{2}|\Psi^-\rangle_{32} \tag{A.2.23c}$$

$$_{1x}\langle\Psi^+|\xi\rangle \;=\; \frac{1}{2}\left(\frac{|e\rangle_3|g\rangle_2 + |g\rangle_3|e\rangle_2}{\sqrt{2}}\right) = \frac{1}{2}|\Psi^+\rangle_{32} \tag{A.2.23d}$$

For these cases of Bell state projections in Eqs. (A.2.23b) - (A.2.23d) it will be necessary for Bob to perform local corrections to qubit-3 by Pauli operators as shown in Tab. A.1. We also see that the probability of measuring states $|\epsilon\rangle_{32}$ in Eqs. (A.2.23a) - (A.2.23d) is $p = \frac{1}{4}$. In general, by application of entanglement swapping protocol (teleportation of entanglement), qubit-2 belonging to Alice and qubit-3 belonging to Bob despite never having interacted before became entangled. In addition we see that a maximally entangled *symmetric* atom-field transition qubit state $|\phi_{e0}\rangle$ (in Eq. (A.2.5e)) generated in the JC interaction can be used in quantum information processing (QIP) protocols like en-

tanglement swapping (teleportation of entanglement) which we have demonstrated here.

Table A.1: Table showing how Bob applies an appropriate gate to his qubit based on BSM from Charlie

$|\kappa\rangle_{12}$	$|\epsilon\rangle_{32}$	$UNITARY\ OPERATION$
$\frac{1}{\sqrt{2}}(|e\rangle_1|e\rangle_2 + |g\rangle_1|g\rangle_2)$	$\frac{1}{\sqrt{2}}(|g\rangle_3|e\rangle_2 + |e\rangle_3|g\rangle_2)$	$\hat{\sigma}_{x(atom3)} \otimes \hat{I}_{(atom2)}$
	$\frac{1}{\sqrt{2}}(|g\rangle_3|e\rangle_2 - |e\rangle_3|g\rangle_2)$	$i\hat{\sigma}_{y(atom3)} \otimes \hat{I}_{(atom2)}$
	$\frac{1}{\sqrt{2}}(|e\rangle_3|e\rangle_2 - |g\rangle_3|g\rangle_2)$	$\hat{\sigma}_{z(atom3)} \otimes \hat{I}_{(atom2)}$

A.2.2.2.2   Maximal teleportation fidelity

For any two-qubit state $\hat{\rho}$ the maximal fidelity is given in Eq. (1.8.19a) in the form [81]

$$F_{\hat{\rho}} = \frac{2f_{\hat{\rho}} + 1}{3} \tag{1.8.19a'}$$

where as defined in Eq. (1.8.19b) $f_{\hat{\rho}}$ is the fully entangled fraction in the form [75]

$$f_{\hat{\rho}} = \max_{|\Psi\rangle}\langle\Psi|\hat{\rho}|\Psi\rangle = \left\{ tr\sqrt{\hat{\rho}^{\frac{1}{2}}_{expected}\hat{\rho}_{measured}\hat{\rho}^{\frac{1}{2}}_{expected}} \right\}^2 \tag{1.8.19b'}$$

From Tab. A.1

$$
\begin{aligned}
\hat{\rho}_{expected} &= |\kappa_{12}\rangle\langle\kappa_{12}| \\
&= \frac{1}{2}\Big[(|e_1\rangle|e_2\rangle + |g_1\rangle|g_2\rangle)(\langle e_1|\langle e_2| + \langle g_1|\langle g_2|)\Big] \\
&= \frac{1}{2}\Big[|e_1,e_2\rangle\langle e_1,e_2| + |e_1,e_2\rangle\langle g_1,g_2| + |g_1,g_2\rangle\langle e_1,e_2| + |g_1,g_2\rangle\langle g_1,g_2|\Big] \\
&= \frac{1}{2}\begin{pmatrix} 1 & 0 & 0 & 1 \\ 0 & 0 & 0 & 0 \\ 0 & 0 & 0 & 0 \\ 1 & 0 & 0 & 1 \end{pmatrix}
\end{aligned}
\tag{A.2.24a}
$$

$$
\begin{aligned}
\hat{\rho}_{measured} &= |\epsilon_{32}\rangle\langle\epsilon_{32}| \\
&= \frac{1}{2}\Big[(|e_3\rangle|e_2\rangle + |g_3\rangle|g_2\rangle)(\langle e_3|\langle e_2| + \langle g_3|\langle g_2|)\Big] \\
&= \frac{1}{2}\Big[|e_3, e_2\rangle\langle e_3, e_2| + |e_3, e_2\rangle\langle g_3, g_2| + |g_3, g_2\rangle\langle e_3, e_2| + |g_3, g_2\rangle\langle g_3, g_2|\Big] \\
&= \frac{1}{2}\begin{pmatrix} 1 & 0 & 0 & 1 \\ 0 & 0 & 0 & 0 \\ 0 & 0 & 0 & 0 \\ 1 & 0 & 0 & 1 \end{pmatrix}
\end{aligned}
$$

$$\text{(A.2.24b)}$$

Substituting the results in Eq. (A.2.24a) and Eq. (A.2.24b) into the fully entangled fraction Eq. (1.8.19b) we obtain

$$
f_{\hat{\rho}} = \left\{ tr \begin{pmatrix} \frac{1}{2} & 0 & 0 & \frac{1}{2} \\ 0 & 0 & 0 & 0 \\ 0 & 0 & 0 & 0 \\ \frac{1}{2} & 0 & 0 & \frac{1}{2} \end{pmatrix} \right\}^2 = 1 \qquad \text{(A.2.24c)}
$$

Substituting the value of the fully entangled fraction into Eq. (1.8.19a) we get

$$
F_{\hat{\rho}} = 1 \qquad \text{(A.2.24d)}
$$

a maximal teleportation fidelity of unity, showing that the state was fully recovered, i.e Alice's qubit in Eq. (A.2.20) was successfully teleported to Bob. We obtain an equal outcome to all the other measured states. We have thus achieved teleportation using a maximally entangled qubit state generated in a JC interaction, using the case where the atom is initially in an excited state $|e\rangle$ and the field in an initial vacuum state $|0\rangle$ as an example.

A.2.3 Evolution of entanglement

Substituting $\hat{\rho}_a(t)$ in Eq. (A.1.15b) into Eq. (A.1.14) and using the standard definitions of c_{en}, s_{en} and R_{en} in Eq. (A.1.2) to evaluate the probabilities in Eq. (A.1.15c), we plot concurrence $C(\tau)$ Eq. (A.1.14) against scaled time $\tau = \lambda t$ at resonance where the frequency detuning $\delta = 0$, arbitrarily chosen values of non-resonant frequency detuning

$\delta = \lambda, 2\lambda, 3\lambda, 4\lambda$ and photon number $n = 0, 1, 2$ in Figs. A.2 - A.5. We note in Figs. A.2 - A.5 that the dynamical behaviour of quantum entanglement measured by concurrence is in the range $0 \leq C(\tau) \leq 1$, such that min $C(\tau) = 0$ and max $C(\tau) = 1$.
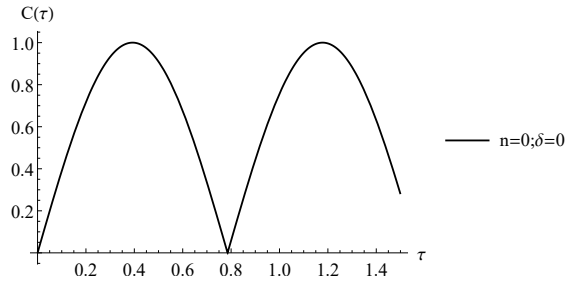

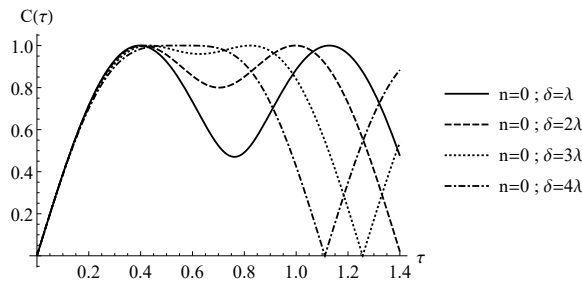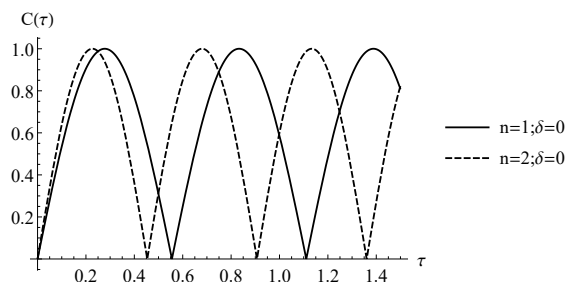Figure A.2: Concurrence $C(\tau)$ against scaled time τ at resonance $\delta = 0$ when $n = 0$.

Figure A.3: Concurrence $C(\tau)$ against scaled time τ at off-resonance $\delta = \lambda$, $\delta = 2\lambda$, $\delta = 3\lambda$ and $\delta = 4\lambda$ when $n = 0$.

Figure A.4: Concurrence $C(\tau)$ against scaled time τ at resonance $\delta = 0$ when $n = 1, 2$.
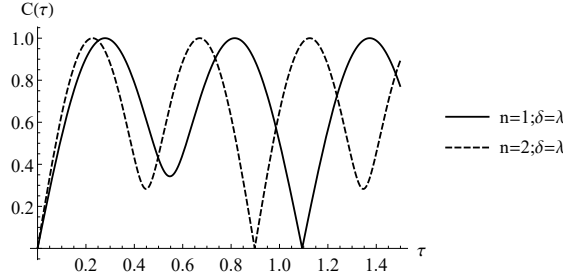
Figure A.5: Concurrence $C(\tau)$ against scaled time τ at off-resonance $\delta = \lambda$ when $n = 1,\ 2$.

(a) DEM
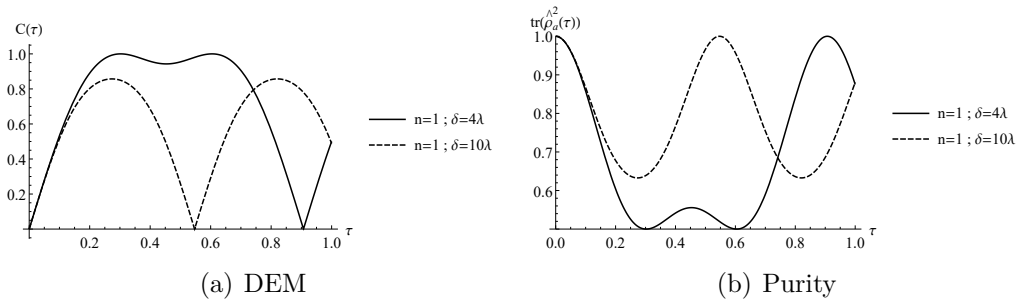
(b) Purity

Figure A.6: Time evolution of DEM at increasing frequency detuning δ when photon number n is set constant and its effect on the degree of purity $tr(\hat{\rho}_a^2(t))$. Fig. (A.6(a)), time evolution of concurrence $C(\tau)$ at $n = 1$; $\delta = 4\lambda$, 10λ while Fig. (A.6(b)) time evolution of purity $tr(\hat{\rho}_a^2(t))$ at $n = 1$; $\delta = 4\lambda$, 10λ in the JC process

(a) DEM
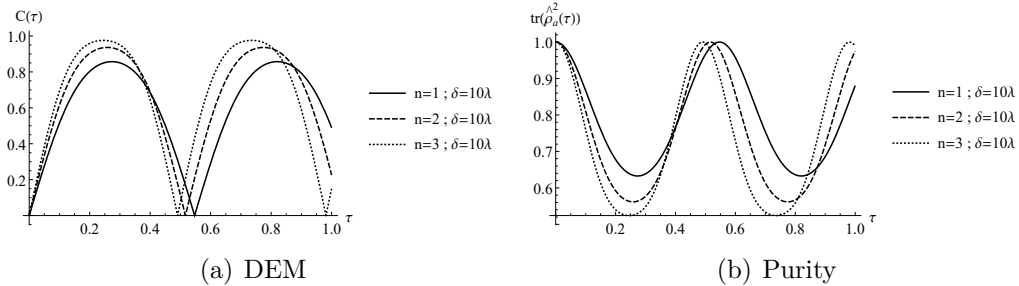
(b) Purity

Figure A.7: Time evolution of DEM at increasing photon number n when the frequency detuning δ set constant and its effect on the degree of purity $tr(\hat{\rho}_a^2(t))$. Fig. (A.7(a)), time evolution of concurrence $C(\tau)$ at $n = 1,\ 2,\ 3$; $\delta = 10\lambda$ while Fig. (A.7(b)) time evolution of purity $tr(\hat{\rho}_a^2(t))$ at $n = 1,\ 2,\ 3$; $\delta = 10\lambda$ in the JC process

Comparing Fig. A.2 and Fig. A.3 we observe that at resonance $\delta = 0$ the frequency of oscillation of $C(\tau)$ as shown in Fig. A.2 is higher than when detuning is set at off resonance $\delta \neq 0$ as demonstrated in Fig. A.3 for the specific cases of $\delta = \lambda,\ 2\lambda,\ 3\lambda,\ 4\lambda$.

In addition, Figs. A.2 and A.3 clearly show that there are Rabi oscillations even for the case when $n = 0$, commonly referred to as vacuum-field Rabi oscillations [8, 209, 210]. Further we observe in Fig. A.3, that despite the reduction in frequency of oscillation of $C(\tau)$ at off-resonance when $\delta \neq 0$ in comparison to the resonance case $\delta = 0$ in Fig. A.2, the frequency of oscillation of $C(\tau)$ increases with an increase in non-resonant frequency detuning $\delta \neq 0$. In the specific case of an initial photon number $n = 0$ and non-resonant frequency detuning $\delta = 4\lambda$ as demonstrated in Fig. A.3, we observe a long-lived entanglement at $C(\tau) = 1$. This agrees precisely with the result presented in Sec. A.2.2, where the transition qubit state vector obtained for parameter values $n = 0$ and $\delta = 4\lambda$ was determined to be maximally entangled (resulting into the long-lived entanglement) before returning momentarily to a separable state. What is more, with reference to Fig. A.3 it is evident that there is gradual vanishing of local minimums with increasing non-resonant frequency detuning $\delta \neq 0$ indicating enhancement of entanglement.

We now investigate the dynamics of $C(\tau)$ when the frequency detuning is set at resonance, off resonance $\delta = 0$, $\delta \neq 0$ while varying the photon number n. In Fig. A.4 we considered a resonance case $\delta = 0$ and varied the photon number n while in Fig. A.5, we set frequency detuning constant at $\delta = \lambda$ and varied the photon number n. In both cases, we observe that the frequency of oscillation of $C(\tau)$ increases with an increase in photon number n. Which means that the frequency of entangling the atom, field quantum systems increases with every increase in photon number n.

In Fig. A.6 we investigate the effect of increasing frequency detuning δ on the dynamics of concurrence $C(\tau)$ and consequently the degree of purity $tr(\hat{\rho}_a^2(t))$ when the photon number n is considered constant. In this respect, we set $n = 1$ and vary δ. We observe in Fig. A.6(a) that $C(\tau)$ records a lower value when $\delta = 10\lambda$ than when $\delta = 4\lambda$. The result in Fig. A.6(b) reveals that the decrease in $C(\tau)$ with every increase in δ at constant n is a consequence of the system tending to pure state. Further, with reference to Fig. A.7(a) we see that increasing the photon n increases the DEM as measured by $C(\tau)$ and consequently as demonstrated in Fig. A.7(b) the system tends to a maximally mixed state. This means that an increase in photon number n at a fixed frequency detuning δ results into an increase in the DEM of the atom, field quantum systems.

Finally in all the plots in Figs. A.2 - A.5, entanglement sudden birth (ESB) and entanglement sudden death (ESD) is observed during time evolution of $C(\tau)$. In ESB, there is an observed creation of entanglement where the initially un-entangled qubits are entangled after a very short time interval. Consequently DEM decreases and goes to zero over a short period of time, where the system returns momentarily to a separable state, i.e,

ESD. These findings in Sec. A.1.2.2 are consistent with those obtained in [179, 181, 182] as examples.

APPENDIX B

JC DYNAMICS: FIELD MODE IN AN INITIAL COHERENT STATE

In this appendix the methodology and results of the dynamics generated by the JC Hamiltonian $\hat{H}$ in Eq. (3.1.3) when a two-level atom interacts with a field mode initially in coherent state is presented. Various arbitrary values of field intensity $|\alpha|^2$, dimensionless field mode frequency ratio $\xi = \frac{\omega}{\lambda}$ and dimensionless frequency detuning ratio $\beta = \frac{\delta}{\lambda}$ chosen in the analysis of the AJC dynamics in Sec. 4.2 are adopted in Sec. B.2 to facilitate the desired comparison with the AJC dynamics.

B.1 Methodology

Let us consider the field initially in a coherent state as defined in Eq. (1.5.6g) which we re-write here in a general form ($t = 0$)

$$|\psi_n\rangle = e^{-\frac{|\alpha|^2}{2}} \sum_{n=0}^{\infty} \frac{|\alpha|^n}{\sqrt{n!}} |n\rangle \tag{B.1.1}$$

where α is the coherent amplitudes, and a generalised initial atomic state $|\psi_a\rangle$ prior to the JC interaction mechanisms prepared in a superposition of excited $|e\rangle$ and ground $|g\rangle$ states in the form ($t = 0$)

$$|\psi_a\rangle = A\,|e\rangle + B\,|g\rangle \quad ; \quad A = \sqrt{\zeta} \quad ; \quad B = \sqrt{1-\zeta} \tag{B.1.2}$$

where the atom is in an excited states with probability ζ and ground states with probability $1 - \zeta$. In Eq. (B.1.1) the states $|n\rangle$, $n = 0, 1.2, 3, ...$ of the mode are the photon number (Fock) states.

The initial atom-field state $|\psi_{an}\rangle_{JC}$ is obtained as a direct product of atom and the field states according to

$$|\psi_{an}\rangle_{JC} = |\psi_a\rangle \otimes |\psi_n\rangle . \tag{B.1.3}$$

Defining the mean photon number $|\alpha|^2$ as

$$|\alpha|^2 = \langle \hat{a}^\dagger \hat{a} \rangle_{t=0} \tag{B.1.4}$$

the exact solutions to the Schrödinger equation [10] for the initial atom-field system in Eq. (B.1.3) in the JC interaction $|\Psi_{an}(t)\rangle$ take the explicit form ($t > 0$)

$$
\begin{aligned}
|\Psi_{an}(t)\rangle &= \sum_{n=0}^{\infty} e^{-\frac{\alpha^2}{2}} \left(\left[A \frac{\alpha^n}{\sqrt{n!}} \, e^{-i\omega t\left(n+\frac{1}{2}\right)} (\cos(R_{en}t) - ic_{en}\sin(R_{en}t)) - \right. \right. \\
&\quad \left. i \, B \frac{\alpha^{n+1}}{\sqrt{(n+1)!}} s_{gn+1} \, e^{-i\omega t(n+\frac{1}{2})} \sin(R_{gn+1}t) \right] |e\rangle + \\
&\quad \left[B \frac{\alpha^n}{\sqrt{n!}} \, e^{-i\omega t(n-\frac{1}{2})} (\cos(R_{gn}t) + ic_{gn}\sin(R_{gn}t)) - \right. \\
&\quad \left. \left. -i \, A \frac{\alpha^{n-1}}{\sqrt{(n-1)!}} e^{-i\omega t(n-\frac{1}{2})} \, s_{en-1}\sin(R_{en-1}t) \right] |g\rangle \right) \otimes |n\rangle \qquad \text{(B.1.5)}
\end{aligned}
$$

The final form of Eq. (B.1.5) has been arrived at through Schmidt decomposition defined in Eq. (1.8.5) Sec. (1.8.2) and so the entanglement of the two interacting atom, field quantum systems is readily apparent.

To describe the evolution of the atom alone we introduce the reduced density matrices of the atom $\hat{\rho}_a(t)$ by tracing $\hat{\rho}_{an}(t)$ over the field states in the form

$$
\hat{\rho}_a(t) = tr_f \left(|\Psi_{an}(t)\rangle\langle\Psi_{an}(t)| \right) \qquad \text{(B.1.6a)}
$$

where for an atom in an initial ground state $|g\rangle$ at any time $t > 0$ the state vectors of the system $|\Psi_{gn}(t)\rangle$ in the JC processes take the form ($B = 1$, $A = 0$)

$$
\begin{aligned}
|\Psi_{gn}(t)\rangle &= \sum_{n=0}^{\infty} e^{-\frac{\alpha^2}{2}} \left[\left(-i \, \frac{\alpha^{n+1}}{\sqrt{(n+1)!}} s_{gn+1} e^{-i\omega t(n+\frac{1}{2})} \sin(R_{gn+1}t) \right) |e\rangle + \right. \\
&\quad \left. \frac{\alpha^n}{\sqrt{n!}} e^{-i\omega t(n-\frac{1}{2})} \left(\cos(R_{gn}t) + i \, c_{gn}\sin(R_{gn}) \right) |g\rangle \right] \otimes |n\rangle \qquad \text{(B.1.6b)}
\end{aligned}
$$

Applying Eq. (B.1.6a), the JC reduced atomic density operators $\hat{\rho}_a^g(t)$ determined from

Eqs. (B.1.6b) take explicit the form

$$
\begin{aligned}
\hat{\rho}_a^g(t) \;=\; & e^{-\alpha^2} \sum_{n=0}^{\infty} \Bigg[\frac{\alpha^{2n}}{n!} \Big(\cos^2(R_{gn}t) + c_{gn}^2 \sin^2(R_{gn}t) \Big) |g\rangle\langle g| \\
& +i \; \frac{\alpha^{2n+1}}{\sqrt{n!(n+1)!}} \; s_{gn+1} e^{i\omega t} \sin(R_{gn+1}t) \Big(\cos(R_{gn}t) + ic_{gn} \sin(R_{gn}t) \Big) |g\rangle\langle e| \\
& -i \; \frac{\alpha^{2n+1}}{\sqrt{n!(n+1)!}} \; s_{gn+1} e^{-i\omega t} \sin(R_{gn+1}t) \Big(\cos(R_{gn}t) - ic_{gn} \sin(R_{gn}t) \Big) |e\rangle\langle g| \\
& +\frac{\alpha^{2(n+1)}}{(n+1)!} \; s_{gn+1}^2 \sin^2(R_{gn+1}t)|e\rangle\langle e| \Bigg]
\end{aligned}
$$

$$\text{(B.1.6c)}$$

with the Rabi frequency and interaction parameters in the JC process defined as

$$
R_{gn} \;=\; \frac{\lambda}{2}\sqrt{4n+\beta^2} \quad;\quad c_{gn} = \frac{\beta}{\sqrt{4n+\beta^2}} \quad;\quad s_{gn} = 2\sqrt{\frac{n}{4n+\beta^2}} \quad;\quad \beta = \frac{\delta}{\lambda}
$$

$$\text{(B.1.7)}$$

B.1.1   Purity and atomic population inversion

We re-write the degree of purity defined in Eq. (1.3.16) in the form

$$
tr(\hat{\rho}_j^2(t)) = \frac{1}{2} \left[1 + (r_x^2(t) + r_y^2(t) + r_z^2(t)) \right] \quad;\quad j : a(f)
\tag{1.3.16'}
$$

Recall that for pure states, $tr(\hat{\rho}_{a(f)}^2(t)) = 1$ in which the state-vector description of each individual system is possible. On the other hand for a two-level system a maximally mixed state corresponds to $tr(\hat{\rho}_{a(f)}^2(t)) = \frac{1}{2}$.

Defining the JC time evolving Bloch vector $\vec{r}(t) = r_x(t)\hat{i} + r_y(t)\hat{j} + r_z(t)\hat{k}$ with com-

ponents $r_x(t)$, $r_y(t)$, $r_z(t)$ in the JC interaction evaluated in explicit form as

$$
\begin{aligned}
r_x(t) = tr(\hat{\rho}_a^g(t)\hat{\sigma}_x) &= \sum_{n=0}^{\infty} e^{-\alpha^2} \frac{\alpha^{2n+1}}{\sqrt{n!(n+1)!}} \Big[-2s_{gn+1} \sin(R_{gn+1}t) \cos(R_{gn}t) \sin(\omega t) \\
& \quad -2s_{gn+1}c_{gn} \sin(R_{gn+1}t) \sin(R_{gn}t) \cos(\omega t) \Big] \\
r_y(t) = tr(\hat{\rho}_a^g(t)\hat{\sigma}_y) &= \sum_{n=0}^{\infty} e^{-\alpha^2} \frac{\alpha^{2n+1}}{\sqrt{n!(n+1)!}} \Big[2s_{gn+1} \sin(R_{gn+1}t) \cos(R_{gn}t) \cos(\omega t) \\
& \quad -2s_{gn+1}c_{gn} \sin(R_{gn+1}t) \sin(R_{gn}t) \sin(\omega t) \Big] \\
r_z(t) = tr(\hat{\rho}_a^g(t)\hat{\sigma}_z) &= \sum_{n=0}^{\infty} e^{-\alpha^2} \Big[\frac{\alpha^{2(n+1)}}{(n+1)!} s_{gn+1}^2 \sin^2(R_{gn+1}t) - \frac{\alpha^{2n}}{n!} \Big(\cos^2(R_{gn}t) \\
& \quad + c_{gn}^2 \sin^2(R_{gn}t) \Big) \Big],
\end{aligned}
$$

$$(B.1.8)$$

we easily plot time evolution of the degree of purity $tr(\hat{\rho}_a^2(t))$ in the JC interaction considering the definition of interaction parameters and Rabi frequency in Eq. (B.1.7).

In order to discuss the collapses and revival phenomenon, in relation to degree of entanglement $S_f(t)$ and purity of states $tr(\hat{\rho}^2(t))$ we introduce atomic population inversion $W(t)$ [34] defined as the difference between the excited and ground state probabilities according to

$$
W(t) = tr(\hat{\sigma}_z \hat{\rho}_a(t)) \tag{B.1.9a}
$$

which takes the exact form as the z-component $r_z(t)$ in Eq. (B.1.8) of the JC time evolving Bloch vector.

The revival time of atomic population inversion, τ_R, at resonance $\delta = \omega_0 - \omega = 0$, is defined as [192]

$$
\tau_R = 2\pi \sqrt{|\alpha|^2} \,, \tag{B.1.9b}
$$

while in an off-resonant interaction, τ_R is approximated as [173]

$$
\tau_R \simeq \frac{\pi}{\sqrt{\frac{\delta^2}{4\lambda^2} + (|\alpha|^2 + 1)} - \sqrt{\frac{\delta^2}{4\lambda^2} + |\alpha|^2}} \,. \tag{B.1.9c}
$$

B.1.2 Entropy of Entanglement

Consideing the atomic subsystem, we apply the von Neumann entropy in Eq. (1.8.9) defined in terms of the length of the time evolving Bloch vector $\vec{r}(t)$, which we re-write here for ease of reference in the form

$$S_a(t) = -\pi_1 \log_2 \pi_1 - \pi_2 \log_2 \pi_2 \quad ; \quad \pi_1 = \frac{1}{2}\left[1 + |\vec{r}(t)|\right] ; \pi_2 = \frac{1}{2}\left[1 - |\vec{r}(t)|\right] \ .$$

$$(B.1.10)$$

We then compute with ease the eigenvalues π_1, π_2, considering the definition of the JC Bloch vector components in Eqs. (B.1.8) and interaction parameters, Rabi frequency in Eq. (B.1.7). At various values of frequency detuning δ and field intensity $|\alpha|^2$ we plot and analyse the dynamics of the von Neumann entropy for the atomic subsystem $S_a(t)$ in Eq. (3.3.8) in relation to atomic population inversion (Rabi oscillations) $W(t)$ and purity of states $tr(\hat{\rho}_a^2(t))$.

B.1.3 Photon statistics

In this section we present the approach adopted in analysis of the nature of photons during the JC interaction process.

B.1.3.1 Mean photon number

The initial average photon number in the normal order [174] $|\alpha|^2$ in the JC processes is defined in Eq.(B.1.4). As time advances ($t > 0$) the average photon number is of the form

$$\langle \hat{a}^\dagger \hat{a} \rangle_{\mathtt{t}} = tr\left[\hat{\rho}_f(t)\ \hat{a}^\dagger \hat{a}\right] \tag{B.1.11}$$

The time evolving reduced density operators of the field $\hat{\rho}_f^g(t)$ in the JC interaction is determined from Eqs. (B.1.6b) by tracing $\hat{\rho}_{gn}(t)$ over the atomic states according to

$$\hat{\rho}_f^g(t) = tr_a(\hat{\rho}_{gn}(t)) \quad ; \quad \hat{\rho}_{gn}(t) = |\Psi_{gn}(t)\rangle\langle\Psi_{gn}(t)| \tag{B.1.12a}$$

to obtain

$$\hat{\rho}_f^g(t) = e^{-\alpha^2} \sum_{n=0}^{\infty} \left[\frac{\alpha^{2n}}{n!} \left(\cos^2(R_{gn}t) + c_{gn}^2 \sin^2(R_{gn}t) \right) \right.$$
$$\left. \frac{\alpha^{2(n+1)}}{(n+1)!} s_{gn+1}^2 \sin^2(R_{gn+1}t) \right] \otimes |n\rangle\langle n| \qquad \text{(B.1.12b)}$$

B.1.3.2   Mandel parameter

The Mandel Parameter defined in Eq. (1.4.1) is fundamental in characterising the quantum statistical properties of a system. We re-write it here in the form

$$Q = \frac{\langle(\Delta\hat{\eta})^2\rangle}{\langle\hat{\eta}\rangle} - 1 \quad ; \quad \Delta\hat{\eta} = \sqrt{\langle\hat{\eta}^2\rangle - \langle\hat{\eta}\rangle^2} \qquad \text{(B.1.13)}$$

where $\langle(\Delta\hat{\eta})^2\rangle$ is the photon number variance, $\langle\hat{\eta}\rangle$ is the mean photon number and $\hat{\eta} \equiv \hat{a}^\dagger\hat{a}$ is the normal ordered operator of the number of particles (excitations).

Defining

$$\langle(\hat{a}^\dagger\hat{a})^2\rangle_{\mathtt{t}} = tr\left[\hat{\rho}_f(t) \ (\hat{a}^\dagger\hat{a})^2\right] \qquad \text{(B.1.14)}$$

and together with reduced field density operators in Eq. (B.1.12b), interaction parameters and Rabi frequencies defined in Eq. (B.1.7), and mean photon number defined in Eq. (B.1.11), we easily evaluate $Q(t)$ in Eq. (B.1.13) for various values of frequency detuning δ and field intensities $|\alpha|^2$. We then analyse the evolution of Q(t) during the interaction, with focus on whether the nature of photons display Poissonian (coherent), super-Possonian (classical) or sub-Poissonian (nonclassical) statistics. For Poissonian photon statistics $Q(t) = 0$, super-Poissonian $Q(t) > 0$ and sub-Poissonian $Q(t) < 0$.

B.2   Results: JC dynamics of a two-level atom interacting with field mode in an initial coherent state

We now analyse the time evolution of a two-level atom in a resonant, off-resonant JC interactions respectively when the field mode in an initial coherent state is considered. Precisely, purity of states in relation to atom-field entanglement in the models is studied during time evolution of atomic population inversion. In addition, a side by side analysis of the quantum nature of the field system in the JC and AJC interaction is presented.

B.2.1 Time evolution of Field entropy, purity and atomic population inversion

Accordingly, to discuss the time evolution of the collapses and revival phenomenon $W(t)$ in relation to degree of entanglement $S_j(t)$ and consequently the degree purity $tr(\hat{\rho}_j^2(t))$ it is important to recall that for pure states $tr(\hat{\rho}_j^2) = 1$, $S_j(t) = 0$ and for maximally mixed states $tr(\hat{\rho}_j^2) = \frac{1}{2}$, $S_j(t) = 1$ where $j \equiv a(f)$.

Applying Eq. (1.3.16) by substituting the time evolving JC Bloch vector components $r_x(t)$, $r_y(t)$, $r_z(t)$ defined in Eq. (B.1.8) we plot the time evolution of degree of purity $tr(\hat{\rho}_a^2(t))$ in Fig. B.1 at $\delta = 0$, $|\alpha|^2 = 30$ during the JC interaction. For ease of comprehension, in the same figures we provide the respective the time evolution of atomic population inversion $W(t)$ defined in Eq. (B.1.9a) which takes the same form as the z-component $r_z(t)$ of the time evolving JC Bloch vector $\vec{r}(t)$.
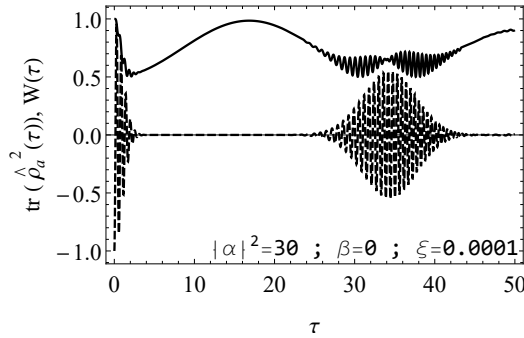
Figure B.1: Time evolution of purity parameter and atomic population inversion. $tr(\hat{\rho}_a^2(\tau))$, $W(\tau)$ at $\delta = \beta\lambda = 0$; $\beta = 0$, $\xi = 0.0001$ and $|\alpha|^2 = 30$ during the JC interaction.

We then proceed to plot the dynamics of the von Neumann entropy $S_a(\tau)$ defined in Eq. (B.1.10) during the JC process. To do this, we evaluate and substitute the eigenvalues π_1, π_2 defined in Eq. (B.1.10).

The JC process entropy of entanglement plots at resonance $\delta = 0$, off-resonance $\delta \neq 0$ at low, high field intensities $|\alpha|^2$ are shown in Figs. B.2, B.3 and B.4.
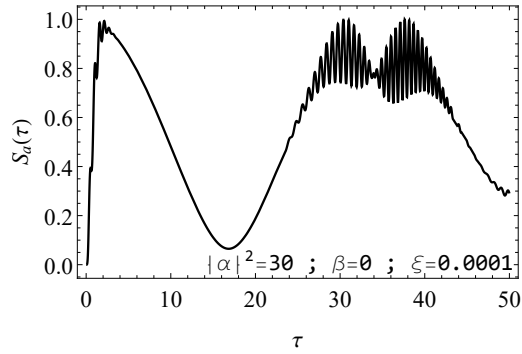
Figure B.2: Time evolution of entropy of entanglement. $S_a(\tau)$ at $\delta = \beta\lambda = 0$; $\beta = 0$, $\xi = 0.0001$ and $|\alpha|^2 = 30$ in the JC interaction.
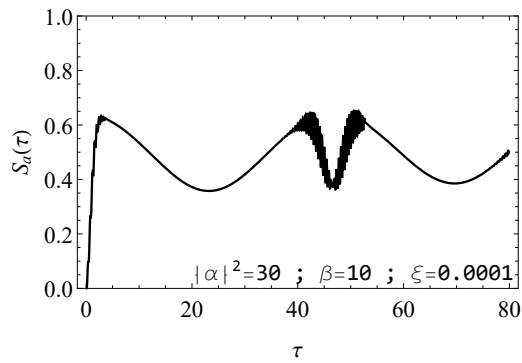

Figure B.3: Time evolution of entropy of entanglement. $S_a(\tau)$ at $\delta = \beta\lambda = 10\lambda$; $\beta = 10$, $\xi = 0.0001$ and $|\alpha|^2 = 30$ in the JC interaction.
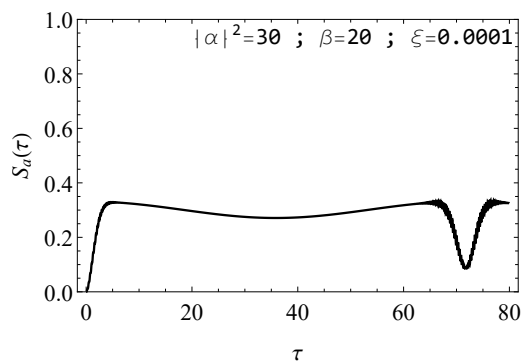

Figure B.4: Time evolution of entropy of entanglement. $S_a(\tau)$ at $\delta = \beta\lambda = 20\lambda$; $\beta = 20$, $\xi = 0.0001$ and $|\alpha|^2 = 30$ in the JC interaction.

Based on the preceding results in Figs. B.2, B.3 and 4.10(b) we see that;

i) at all time intervals, time evolution of the DEM, atomic population inversion $S_a(\tau)$, $W(\tau)$ in the JC interaction display behaviours conforming with earlier results in [173, 174, 184–186];

ii) at `t>0` in a resonant JC interaction $\delta = 0$, Fig. B.2, the value of the DEM $S_a(\tau)$ presents highest initial value of unity defining maximum entanglement between the two-level atom and field followed by an almost zero value of $S_a(\tau)$ at one half of the revival time as presented in Fig. B.1. With reference to Figs. B.1 and B.2, the physical interpretation agreeing with [174, 184, 187–189] is that at $t > 0$ the atomic state will not be *pure* but at *one half* of the revival time [192], $\frac{\tau_R}{2} = \pi\sqrt{|\propto|^2} \simeq 17.2$, the atom, (cavity) field quantum systems evolve simultaneously into pure state.

At the revival phases, $\tau_R = 2\pi\sqrt{|\alpha|^2} \simeq 34.4$, as clearly visualised in Figs. B.1 and B.2, the DEM in the JC interaction mechanisms oscillates about a local minimum and maximum specifying that the field at the revival phase does not evolve to pure state [174];

iii) in the off-resonant JC interaction process presented in Fig. B.3, the DEM $S_a(\tau)$ displays low values at all time intervals in comparison to that in Fig. B.2 which decreases further with every increase in frequency detuning δ and as visualised in Fig. B.4. This means that entanglement between the two-level atom and the field decreases with every increase in frequency detuning (JC).

During an off-resonant atom-field quantum systems interaction, the revival time τ_R of the atomic population inversion is approximated as [173]

$$\tau_R \simeq \frac{\pi}{\sqrt{\frac{\delta^2}{4\lambda^2} + (|\alpha|^2 + 1)} - \sqrt{\frac{\delta^2}{4\lambda^2} + |\alpha|^2}} \ . \tag{B.2.1}$$

Applying Eq. (B.2.1), we obtain half the revival time in Fig. B.3 at $\frac{\tau_R}{2} \simeq 23.4$ and that in Fig. B.4 at $\frac{\tau_R}{2} \simeq 35.9$. It is clear that at these times $S_a(t)$ does not dip as much towards $S_a(\tau) = 0$ in comparison to the resonance cases in Fig. B.2 accordant with [173]. This means that for large detuning (JC) and separately sum frequency (AJC), the system tends to pure state at all time intervals during the interaction and

iv) during the JC process in Figs. B.3 and B.4 rapid oscillations are occur at the revival phase τ_R and none at the collapse time [28] $\tau_c = \frac{1}{\sqrt{2}}$

B.2.2 Photon statistics

In this section we analyse the nature of photons during the JC processes. We proceed by plotting the time evolution of the Mandel Q parameter for an initial atomic ground state $|g\rangle$ interacting with a field mode in an initial coherent state. Plots of the JC process at resonance $\delta = 0$, off-resonance $\delta \neq 0$ at low, high field intensities $|\alpha|^2$ are presented in Figs. B.5, B.6, B.7 and B.8.
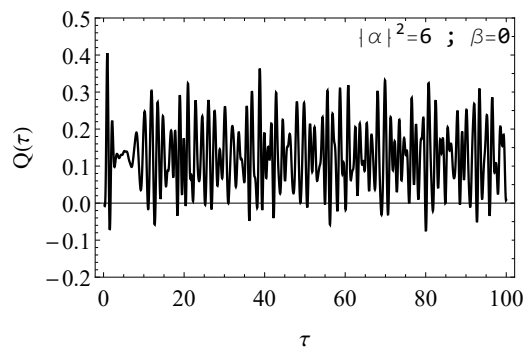

Figure B.5: Time evolution of Mandel parameter. $Q(\tau)$ at $\delta = \beta\lambda = 0$; $\beta = 0$ and $|\alpha|^2 = 6$ in the JC interaction.
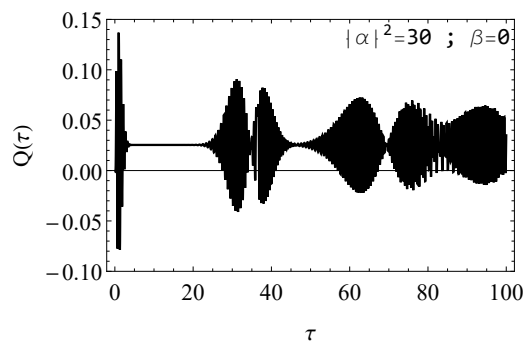
Figure B.6: Time evolution of Mandel parameter. $Q(\tau)$ at $\delta = \beta\lambda = 0$; $\beta = 0$ and $|\alpha|^2 = 30$ in the JC interaction.
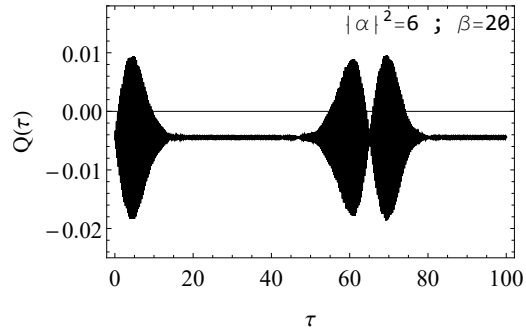
Figure B.7: Time evolution of Mandel parameter. $Q(\tau)$ at $\delta = \beta\lambda = 20\lambda$; $\beta = 20$ and $|\alpha|^2 = 6$ in the JC interaction.
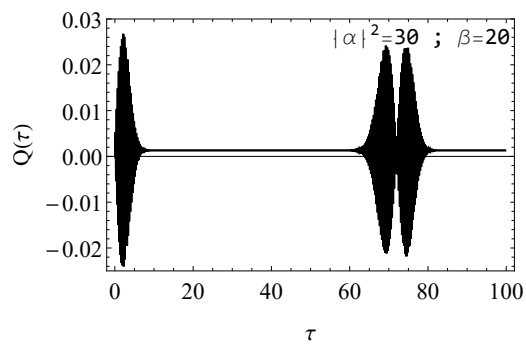
Figure B.8: Time evolution of Mandel parameter. $Q(\tau)$ at $\delta = \beta\lambda = 20\lambda$; $\beta = 20$ and $|\alpha|^2 = 30$ in the JC interaction.

From the plots in Figs. B.5 - B.8 we see that the photon statistics during the JC inter-action is dominantly super-Poissonian as presented in Figs. 4.11(b), 4.12(b) and 4.14(b) consistent with the observation made in [190]. The only exception is in Fig. 4.13(b) where the nature of photons is dominantly sub-Poissonian. In this particular example a non-zero detuning $\delta \neq 0$ is introduced for a low mean photon number $|\alpha|^2$.

APPENDIX C

JC DYNAMICS: FIELD MODE IN AN INITIAL SQUEEZED COHERENT STATE

We present the methodology and results of the JC dynamics generated by the JC Hamiltonian $\hat{H}$ in Eq. (3.1.3) when a two-level atom interacts with a field mode initially in a squeezed coherent state. Various values of squeeze parameter r, field intensity $|\alpha|^2$, dimensionless field mode frequency ratio $\xi = \frac{\omega}{\lambda}$ and dimensionless frequency detuning ratio $\beta = \frac{\delta}{\lambda}$ arbitrarily chosen in the analysis of the AJC dynamics in Sec. 4.3 are maintained at the same values in Sec. C.2 to guide a comprehensive comparison with the JC dynamics.

C.1 Methodology

Let us now consider when a field mode in an initial coherent squeezed state $|\alpha, \varsigma\rangle$ defined in Eq. (1.5.8a) is considered, which we re-write here in a general form

$$
\begin{aligned}
|\alpha, \varsigma\rangle &= \frac{1}{\sqrt{\cosh(r)}} \exp\left[-\frac{1}{2}|\alpha|^2 - \frac{1}{2}\alpha^{*2}e^{i\theta}\tanh(r)\right] \\
&\times \sum_{n=0}^{\infty} \frac{\left[\frac{1}{2}e^{i\theta}\tanh(r)\right]^{\frac{n}{2}}}{\sqrt{n!}} H_n\left[\gamma\left(e^{i\theta}\sinh(2r)\right)^{-\frac{1}{2}}\right] \otimes |n\rangle
\end{aligned}
$$

(C.1.1a)

where r, ς is the squeeze, complex squeeze parameter in the form

$$
\varsigma = r\,\exp(i\theta) \quad ; \quad 0 \leq r < \infty \quad ; \quad 0 \leq \theta \leq 2\pi \,,
$$

(C.1.1b)

α the coherent amplitudes and

$$
\gamma = \alpha\cosh(r) + \alpha^* e^{i\theta}\sinh(r) \,.
$$

(C.1.1c)

We define the average photon number $\langle \hat{a}^\dagger \hat{a} \rangle$ for the squeezed state in Eq. (C.1.1a) in the form

$$
|\alpha|^2 + \sinh^2(r)
$$

(C.1.2)

such that if $|\alpha|^2 \gg \sinh^2(r)$, the coherent part of the state dominates the squeezed part.

The probability of finding n-photons $P(n)$ in the field during the respective JC processes takes a general form

$$
\begin{aligned}
P(n) &= |\langle n|\alpha,\varsigma\rangle|^2 \\
&= \frac{(\frac{1}{2}\tanh(r))^n}{n!\cosh(r)} \exp\left[-|\alpha|^2 - \frac{1}{2}\left(\alpha^{*2}e^{i\,\theta} + \alpha^2 e^{-i\,\theta}\right)\tanh(r)\right] \\
&\times \left|H_n\left[\gamma\left(e^{i\,\theta}\sinh(2r)\right)^{-\frac{1}{2}}\right]\right|^2 .
\end{aligned}
\tag{C.1.3}
$$

If at $t = 0$, the atom is in a superposition of excited $|e\rangle$ and $|g\rangle$ state as defined in Eq. (B.1.2) and the field in an initial squeezed coherent state as defined in Eq. (C.1.1a) we easily obtain the initial atom-field state according to Eq. (B.1.3). When $B = 1$, $A = 0$, we determine as an example in the case of an atom in an initial ground state $|g\rangle$ the JC initial atom-field qubit state vector in the form

$$
|\psi_{gn}\rangle_{JC} = |\psi_g\rangle \otimes |\alpha,\varsigma\rangle
\tag{C.1.4}
$$

to obtain

$$
|\psi_{gn}\rangle_{JC} = \sum_{n=0}^{\infty} S_n\,|g,n\rangle \quad ; \quad \langle\hat{a}^\dagger\hat{a}\rangle_{t=0} = |\alpha|^2 + \sinh^2(r) .
\tag{C.1.5}
$$

Here, we shall consider an initial squeezed coherent state with $\theta = 0$, and so $\varsigma = r$, α are real. This implies that the squeezed coherent state $|\alpha,\varsigma\rangle$ is now mapped onto $|\alpha,r\rangle$.

The exact solution $|\Psi_{gn}(t)\rangle$ to the Schrödinger equation [10] for the JC initial atom-field system in Eq. (C.1.5) take the explicit form $(t > 0)$

$$
\begin{aligned}
|\Psi_{gn}(t)\rangle &= e^{-\frac{i}{\hbar}\hat{H}_g t}|g,n\rangle = \sum_{n=0}^{\infty}\left[S_n\,e^{-i\omega\left(n-\frac{1}{2}\right)t}\left(\cos(R_{gn}t)\right.\right. \\
&\left.\left. +ic_{gn}\sin(R_{gn}t)\right)|g\rangle - ie^{-i\omega\left(n+\frac{1}{2}\right)t}\,S_{n+1}\,s_{gn+1}\sin(R_{gn+1})|e\rangle\right]\otimes|n\rangle \;; \\
R_{gn} &= \frac{\lambda}{2}\sqrt{4n+\beta^2} \quad ; \quad c_{gn} = \frac{\beta}{\sqrt{4n+\beta^2}} \quad ; \quad s_{gn} = 2\sqrt{\frac{n}{4n+\beta^2}} \quad ; \quad \beta = \frac{\delta}{\lambda}
\end{aligned}
\tag{C.1.6}
$$

The final form of Eqs. (C.1.6) has been arrived at through Schmidt decomposition [28] and

so entanglement of the two interacting atom, field quantum systems is readily apparent.

C.1.1 Photon statistics

We shall examine the nature of photon statistics during the JC interaction by applying the Mandel Q parameter defined in Eq. (B.1.13). The initial average photon number is of the form of Eq. (C.1.5). At any $t > 0$, the mean, mean square photon number evolve in time according to Eqs. (B.1.11), (B.1.14).

The time evolving reduced density operators of the field $\hat{\rho}_f^g(t)$ during the JC interaction determined from Eqs. (C.1.6) is easily obtained as

$$\hat{\rho}_f^g(t) = tr_a(|\Psi_{gn}(t)\rangle\langle\Psi_{gn}(t)|) = \Big[S_n^2 \Big(\cos^2(R_{gn}t) + c_{gn}^2 \sin^2(R_{gn}t) \Big)$$
$$+ S_{n+1}^2 \, s_{gn+1}^2 \sin^2(R_{gn+1}t) \Big] \otimes |n\rangle\langle n| \tag{C.1.7}$$

With the reduced field density operator in Eq. (C.1.7), interaction parameters, Rabi frequencies defined in Eq. (C.1.6) and mean, mean square photon number defined in Eqs. (B.1.11), (B.1.14) we easily evaluate $Q(t)$ in Eq. (B.1.13) at different values of r parameter. We then plot time evolution of the Mandel Q parameter $Q(\tau)$ (where $\tau = \lambda t$ is the scaled time) for an initial atomic ground state $|g\rangle$ in an initial squeezed coherent state. As expected, for super-Poissonian photon statistics $Q(t) > 0$, sub-Poissonian $Q(t) < 0$ and Poissonian $Q(t) = 0$.

C.1.2 Evolution of atomic population inversion and entropy of entanglement

To describe the evolution of the atom alone we introduce the reduced density matrices of the atom by tracing the density operator $\hat{\rho}_{gn}(t)$ over the field states determined from Eq. (C.1.6) according to

$$\hat{\rho}_a^g(t) = tr_f \left(|\Psi_{gn}(t)\rangle\langle\Psi_{gn}(t)| \right) \tag{C.1.8a}$$

taking the explicit form

$$
\begin{aligned}
\hat{\rho}_a^g(t) \;=\; & \sum_{n=0}^{\infty} \Big[S_n^2 \Big(\cos^2(R_{gn}t) + c_{gn}^2 \sin^2(R_{gn}t) \Big) |g\rangle\langle g| \\
& + i\, S_n\, S_{n+1}\, s_{gn+1} e^{i\omega t} \sin(R_{gn+1}t) \Big(\cos(R_{gn}t) + i c_{gn}\sin(R_{gn}t) \Big) |g\rangle\langle e| \\
& - i\, S_n\, S_{n+1}\, s_{gn+1} e^{-i\omega t} \sin(R_{gn+1}t) \Big(\cos(R_{gn}t) - i c_{gn}\sin(R_{gn}t) \Big) |e\rangle\langle g| \\
& + S_{n+1}^2\, s_{gn+1}^2 \sin^2(R_{gn+1}t) |e\rangle\langle e| \Big] \; .
\end{aligned}
$$

$$\text{(C.1.8b)}$$

We then define the time evolving Bloch vector in the JC interaction $\vec{r}(t) = r_x(t)\hat{i} + r_y(t)\hat{j} + r_z(t)\hat{k}$ with components easily evaluated as $r_x(t) = tr\,(\hat{\sigma}_x \hat{\rho}_a^g(t))$, $r_y(t) = tr\,(\hat{\sigma}_y \hat{\rho}_a^g(t))$, $r_z(t) = tr\,(\hat{\sigma}_z \hat{\rho}_a^g(t))$ reducing to explicit forms

$$
\begin{aligned}
r_x(t) \;=\; & \sum_{n=0}^{\infty} \Big[S_n\, S_{n+1} \Big(- 2 s_{gn+1}\sin(R_{gn+1}t)\cos(R_{gn}t)\sin(\omega t) - 2 s_{gn+1} c_{gn} \\
& \sin(R_{gn+1}t)\sin(R_{gn}t)\cos(\omega t) \Big) \Big] \; ; \\
r_y(t) \;=\; & \sum_{n=0}^{\infty} \Big[S_n\, S_{n+1} \Big(2 s_{gn+1}\sin(R_{gn+1}t)\cos(R_{gn}t)\cos(\omega t) - 2 s_{gn+1} c_{gn} \\
& \sin(R_{gn+1}t)\sin(R_{gn}t)\sin(\omega t) \Big) \Big] \; ; \\
r_z(t) \;=\; & \sum_{n=0}^{\infty} \Big[S_{n+1}^2\, s_{gn+1}^2 \sin^2(R_{gn+1}t) - S_n^2 \Big(\cos^2(R_{gn}t) + c_{gn}^2 \sin^2(R_{gn}t) \Big) \Big] \; .
\end{aligned}
$$

$$\text{(C.1.9)}$$

We shall use the time evolving Bloch vector components in Eq. (C.1.9) to evaluate time evolution of atomic population inversion $W(t)$ and the time evolution of the von Neumann entropy $S_a(t)$ (as a measure of DEM).

The atomic population inversion $W(t)$ [34] is defined as the difference between the excited and ground state probabilities

$$W(t) = tr\,(\hat{\sigma}_z \hat{\rho}_a(t)) \qquad\qquad \text{(C.1.10)}$$

which is of the exact form as the z-component $r_z(t)$ in Eq. (C.1.9) of the time evolving JC Bloch vector.

Using the definition of $r_z(t)$ in Eq. (C.1.9), we plot $W(t)$ during the JC process. The

atomic population inversion $W(t)$ will be seen to evolve in time in the range $[-1, 1]$.

In order to discuss the collapses and revival phenomenon in relation to degree of entanglement we again apply the von Neumann entropy $S_a(t)$ in Eq. (B.1.10) (or (1.8.9)) defined in terms of the length of the time evolving Bloch vector $\vec{r}(t)$. We again evaluate the eigenvalues π_1, π_2 considering the definitions of the time evolving JC Bloch vector components in Eq. (C.1.9).

Plots of $S_a(t)$ at different values of squeeze parameter r are then easily plotted. The DEM $S_a(t)$ will evolve in time in the range $[0,1]$, i.e, $S_a(t) = 0$ quantifies disentanglement and consequently the atom, field quantum systems evolve to pure state, $S_a(t) = 1$ maximum entanglement consequently maximally mixed atom-field states else if $0 < S_a(t) < 1$ entangled and so partially mixed atom-field states.

C.2 Results: JC dynamics of a two-level atom interacting with field mode in an initial squeezed coherent state

C.2.1 Photon statistics

Referring to the reduced field density operators in Eq. (C.1.7), interaction parameters, Rabi frequencies defined in Eqs. (C.1.6) and mean, mean square photon number defined in Eqs. (3.3.9), (3.3.12) we easily evaluate $Q(t)$ in Eq. (3.3.11) at resonance $\delta = 0$ and field intensity $|\alpha|^2 = 40$. We then plot time evolution of the Mandel Q parameter $Q(\tau)$ (where $\tau = \lambda t$ is the scaled time) for an initial atomic ground state $|g\rangle$ in an initial squeezed coherent state. Plots of the JC process at resonance $\delta = 0$; $r = 1$, 1.3, 1.4, 1.5 and field intensity $|\alpha|^2 = 40$ are presented in Figs. C.1, C.2, C.3 and C.4.
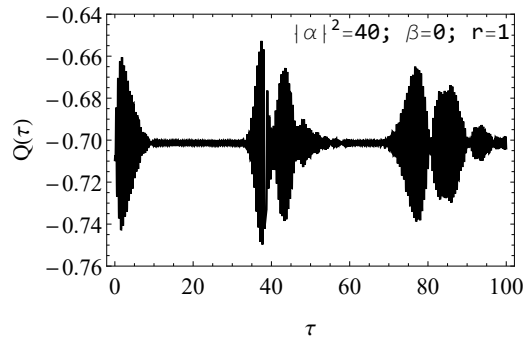

Figure C.1: Time evolution of Mandel parameter. $Q(\tau)$ at $\delta = \beta\lambda = 0$; $\beta = 0$, $r = 1$ and $|\alpha|^2 = 40$ in the JC interaction.
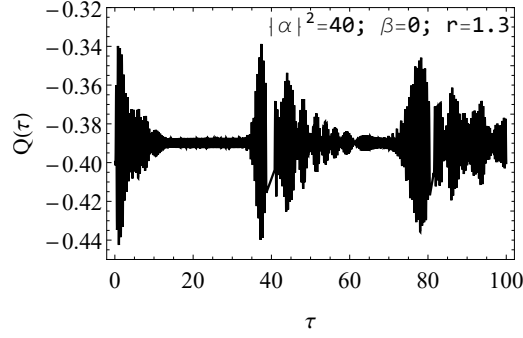
Figure C.2: Time evolution of Mandel parameter. $Q(\tau)$ at $\delta = \beta\lambda = 0$; $\beta = 0$, $r = 1.3$ and $|\alpha|^2 = 40$ in the JC interaction.
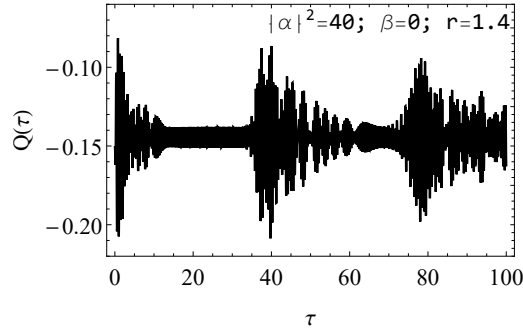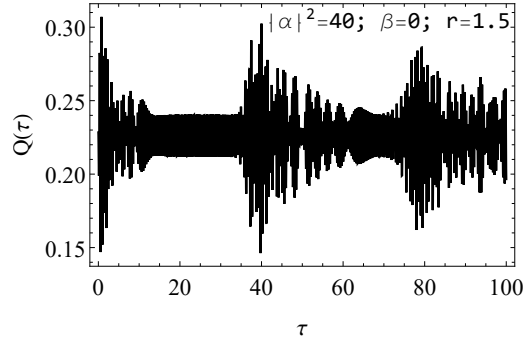

Figure C.3: Time evolution of Mandel parameter. $Q(\tau)$ at $\delta = \beta\lambda$; $\beta = 0$, $r = 1.4$ and $|\alpha|^2 = 40$ in the JC interaction.

Figure C.4: Time evolution of Mandel parameter. $Q(\tau)$ at $\delta = \beta\lambda = 0$; $\beta = 0$, $r = 1.5$ and $|\alpha|^2 + \sinh^2(r) = 40$ in the JC interaction.

From the plots in Figs. C.1 - C.4 we see that the photon statistics during the JC interaction is dominantly sub-Poissonian at squeeze parameters $r = 1$ to $r = 1.4$ as presented in Figs. C.1 - C.3. The only exception is in Fig. 4.18(b) set at $r = 1.5$ where

184

the photon statistics evolves to a dominant super-Poissonian from sub-Poissonian photon statistics. It is clear that the interaction feature of the nature of photon statistics is dependent on the squeeze parameter r accordant with earlier works in [28] [17, 194]. It was observed that squeezed coherent states exhibit photon antibunching effect within some limits, i.e., $r \leq 1.3$ similar to the findings herein which characterises nonclassical statistics of the field mode.

C.2.2   Evolution of atomic population inversion and entropy of entanglement

As earlier stated, the z-component of the time evolving Bloch vector is the difference of the time evolving excited state probability and time evolving ground state probability that defines atomic population inversion $W(t)$. Applying the explicit definition of the time evolving Bloch vector component $r_z(t)$ in Eq. (C.1.9), we plot $W(t)$ in Figs. C.5, C.6 at $\delta = 0, r = 1,$ 1.5, $|\alpha|^2 = 40$ during the JC interaction.
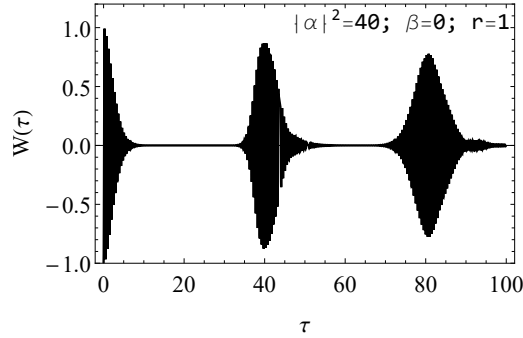

Figure C.5: Time evolution of atomic population inversion. $W(\tau)$ at $\delta = \beta\lambda = 0$; $\beta = 0$, $r = 1$ and $|\alpha|^2 = 40$ in the JC interaction.
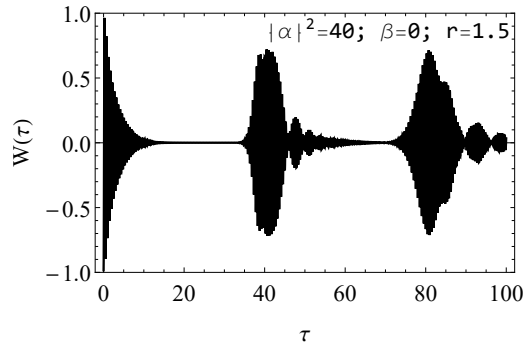

Figure C.6: Time evolution of atomic population inversion. $W(\tau)$ at $\delta = \beta\lambda = 0$; $\beta = 0$, $r = 1.5$ and $|\alpha|^2 = 40$ in the JC interaction.
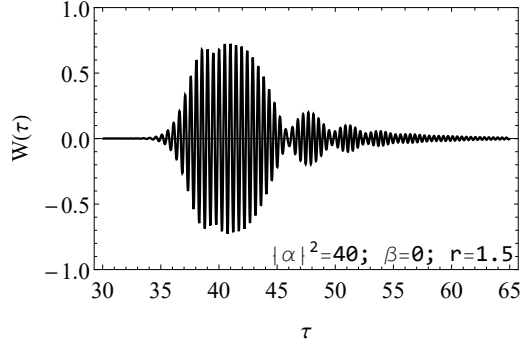
Figure C.7: Time evolution of atomic population inversion (Ringing revivals). $W(\tau)$ at $\delta = \beta\lambda = 0$; $\beta = 0$, $r = 1.5$ and $|\alpha|^2 = 40$ in the JC interaction.

We proceed to plot the photon number distribution P_n defined in Eq. (C.1.3) at $r = 1, 1.5$, $|\alpha|^2 = 40$ in Fig. C.8.

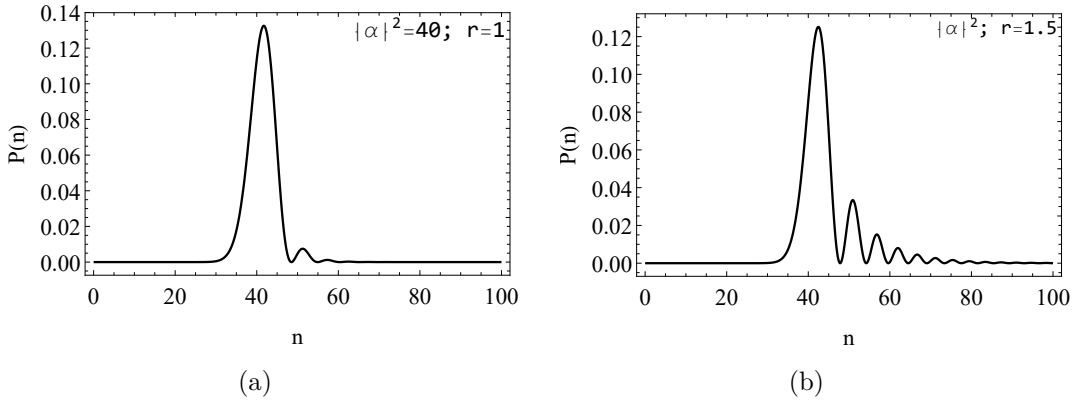(a)   (b)

Figure C.8: JC photon number distribution P_n. Fig. C.8(a), $P(n)$ at $r = 1$ and Fig. C.8(b) $P(n)$ at $r = 1.5$.

From the results in Figs. C.5 - C.8 we see:

i) that the oscillations at $r = 1.5$ in Fig. C.6 more irregular at the collapse region than when $r = 1$ in Fig. C.5, commonly referred to as ringing revivals (see Fig. C.7) in agreement with [17, 194], i.e., the collapse region is modulated or displays ringing different from the well known collapse region obtained when an initial coherent field is considered [28]. As explained in detail in [17, 194], the ringing is due to interference of the additional peaks (see Fig. C.8) the photon number distribution $P_n = |\langle n|\alpha, r\rangle|^2$ because the revivals produced by different peaks of P_n have different local mean photon numbers. In the process revivals due to individual peaks overlap but the effect of the resulting interference is to sharpen the ringing structure other

than washing it away, i.e, the addition of each local peak in P_n adds an echo in $W(\tau)$ and the successive echoes brings further interference, which sharpens the echoes at earlier times and;

ii) in Fig. C.5 sharpness of the revival regions during atomic population inversion which occur when the field is sub-Poissonian (see Fig. C.1 at $r = 1$) accordant with [194], in comparison to the less pronounced and blunt peaks in Fig. C.6 at $r = 1.5$. We noted in our example in Fig. C.4 plotted at $r = 1.5$ during the JC processes, that the field is super-Poissonian.

Accordingly, for purposes of completeness its important to visualise and discuss the collapses and revival phenomenon in relation to the DEM. Here the DEM is measured by the von Neumann entropy $S_a(t)$ defined in Eq. (3.3.8) in terms of the time evolving Bloch vector $\vec{r}(t)$ in the general form. Now, with the time evolving Bloch vector component explicitly defined in Eq. (C.1.9) we easily evaluate $S_a(t)$. The JC process atomic entropy $S_a(\tau)$ plots at resonance $\delta = \beta\lambda = 0$; $\delta = 0, r = 1, 1.5$, and field intensity $|\alpha|^2 = 40$ are shown in Figs. C.9 and C.10.
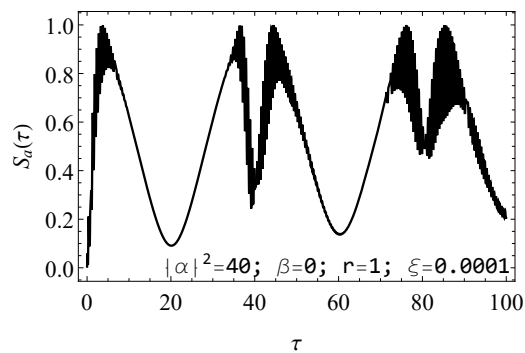

Figure C.9: Time evolution of atomic entropy. $S_a(\tau)$ at $\delta = \beta\lambda = 0$; $\beta = 0$, $r = 1$ and $|\alpha|^2 = 40$ in the JC interaction.
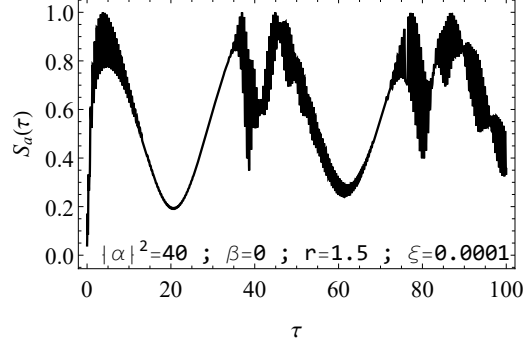
Figure C.10: Time evolution of atomic entropy. $S_a(\tau)$ at $\delta = \beta\lambda = 0$; $\beta = 0$, $r = 1.5$ and $|\alpha|^2 = 40$ in the JC interaction.

Based on the results in Figs. C.9 and C.10 we see;

i) in Fig. C.9 during the JC interaction, the value of $S_a(\tau)$ at the revival time [192] $\tau_R = 2\pi\sqrt{|\alpha|^2 + \sinh^2(r)}$ respectively, is approximately equal to that at half the revival times $\frac{\tau_R}{2}$, i.e, $S_a(\tau) \simeq 0.04$ in our example. This means that at these times $(\tau_R, \frac{\tau_R}{2})$ the atom-field states are entangled (mixed) when an initial squeezed coherent state is considered, accordant with [194]. In addition, as time advances, we note gradual increase in DEM and consequently the degree of mixedness since $S_a(t)$ records gradual increasing values with every increase in time and

ii) that the behaviour in (i) is enhanced during the JC interaction set at $r = 1.5$ as presented in Fig. C.10. The form of time evolution of $S_a(\tau)$ becomes more rapid with oscillations between $[\simeq 0.2, 1]$ characterising an increase in DEM (and so the degree of mixedness), consistent with [194]. It is now clear that the DEM increases with an increase in r.